Mathematical Modelling of the Dispersal and Fate of CES Discharge from the Boyer Mill in the Upper Derwent Estuary

Results of Part B

Final Report

J. Parslow, M. Herzfeld, J.R. Hunter, J.R. Andrewartha, P. Sakov, J. Waring

CSIRO
Hobart

March 2001

1 Introduction

The fate of effluent discharged by the pulp mill at Boyer has been previously modelled by CSIRO (Hunter and Andrewartha, 1990, Walker and Hunter, 1994, Hunter et al, 1998). This early modelling employed both a simple inverse box model (the "Enhanced Pritchard Model") of the estuary between New Norfolk and Sandy Bay, and a hydrodynamic model (now called "MECO") of the region between New Norfolk and Bridgewater.

The present study involves an investigation of the effects of the Combined Effluent Stream (CES) on the estuary above Bridgewater. The objectives are to:

- to determine the nature and extent of water exchange between the main channel and the mudflats/marshes,
- to assess the degree to which the CES interacts with these mudflats/marshes,
- to incorporate biogeochemical processes involving the key stressors identified in Stage 1 of the Ecological Risk Assessment (ERA) program (i.e. resin acids, dissolved oxygen (DO), nutrients and suspended particulate matter (SPM) into the mathematical model), and
- to predict concentrations of these key stressors, taking into account spatial and temporal variations.

Part A of this study, which was completed in December 1999 (Hunter and Parslow, 1999), had the following objectives:

- to undertake an assessment of the available models against study objectives,
- to evaluate alternative options for extending the current detailed hydrodynamic grid to cover wetlands in terms of feasibility and computational implications, and recommend one (or none),
- to assess the existing data for wetlands (bathymetry, tidal amplitude, salinity gradients) and its implications for implementing hydrodynamic or box models, and estimating or validating exchanges with wetlands,
- to recommend whether tracer release studies or other specific studies should be conducted to help quantify exchanges with wetlands, and
- to identify critical process studies and/or additional surveys which are required to model resin acid, nutrient, algal and DO distributions in the upper estuary and wetlands.

Hunter and Parslow (1999) made the following recommendations:

- that MECO be implemented for the Derwent Estuary between New Norfolk, at a resolution sufficient to describe, to a first approximation, flushing processes within the wetlands and between the wetlands and the main estuary channel,
- that a tracer study be implemented, in order to estimate exchange processes associated with the wetlands (this was not however implemented, but instead a 3-week salinity survey was carried out in the region of the wetlands in July 2000)
- that wind data be made available to assist the modelling (data from Boyer were provided to the Study),

- that water level data be provided from the Bureau of Meteorology gauge at New Norfolk and from the gauge at the Boyer mill,
- that additional bathymetry data be provided by the HEC, and
- that the ecological modelling be based on MECO (for resin acids) and on the box model, BM (for other constituents).

The present study therefore implements three models of the Upper Derwent Estuary in order to provide simulations of the effect of the CES. These models are:

- a hydrodynamic model (MECO) to provide simulations of transport and dispersal in the estuary,
- a model of resin acids (implemented within MECO), and
- a box model (BM) for the ecological modelling of other constituents.

Input data for the models (river flow, bathymetry, water level and winds) are described in Section 2.

It was determined that a tracer study would be expensive and would not necessarily yield useful estimates of the flushing of the wetlands. Instead, a 3-week salinity survey was carried in the region of the wetlands in June and July, 2000. This is described in Section 3.

Descriptions of the model formulations, calibration and validation, and model results are described in Sections 4, 5 and 6, respectively.

2 Input Data

2.1 River Flow

The estuary above the Boyer mill is primarily fed by the Derwent at Meadowbank, the Tyenna and various tributaries such as the Lachlan, which enters the river near New Norfolk. The Jordan enters the estuary below the Bridgewater causeway and so is not of concern for the present study. Previous modelling by CSIRO has used the following expression to estimate the river flow below the junction with the Lachlan River (i.e. in the vicinity of the Boyer mill):

$$\begin{aligned}\text{Flow below Lachlan} = &(\text{Flow in Derwent at Meadowbank}) \\ &+ 4.17 \text{ x } (\text{Flow in Tyenna at Newbury})\end{aligned} \qquad 2.1.1$$

Percentile values of this flow are shown in Table 2.1.1. The values in the third column indicate the flow used to drive the hydrodynamic and box models.

Table 2.1.1 : Flow statistics for Derwent Estuary below Lachlan for 1992 to 1999, inclusive.

Percentile	Flow (m^3s^{-1})	Assumed flow for modelling (m^3s^{-1})
5	43.63	45
50	90.80	90

2.2 Bathymetry

The bathymetry used for the modelling was a composite of data provided by the Hydro-Electric Corporation (HEC) in early 1993 (for a previous study of the Boyer outfall) and data provided by the HEC specifically for the present study. The latter data comprised some data collected about ten years ago, and data collected in 2000 specifically to improve our knowledge of the bathymetry over the wetlands. The total data set consisted of detailed bathymetry across 39 sections, referenced to the Australian Map Grid (AMG) and Australian Height Datum (AHD). Unfortunately, the vertical referencing of this data to AHD contained spurious and unexplained errors, such that depths over the wetlands did not agree with estimates made during surveys conducted for this study. Further, the calibration and validation exercise (Section 5) indicated a requirement that the cross-sectional area of the estuary should be increased in order to improve the model simulations. The following adjustments were therefore made to the bathymetry data:

- Each bathymetry point was adjusted, using the observed tide at Hobart and the time of the observation, to mean sea level. This adjustment removed much of the apparently spurious depth variability over the wetlands.
- A depth of 0.3 metres was subtracted from all bathymetry points over the wetlands to the west of the Bridgewater causeway. This improved the agreement between the defined bathymetry and estimates made during surveys conducted for the present study.

- A depth of 1 metre was added to all other bathymetry points. This adjustment was chosen as part of the calibration and validation exercise (Section 5).

The bathymetry data were interpolated onto the model grid used for the hydrodynamic model (see Section 4).

Figures 2.2.1 and 2.2.2 show the resultant bathymetry and cross-section locations for the whole model region and for the wetlands, respectively. Figures 2.2.3, 2.2.4, 2.2.5, 2.2.6, 2.2.7, 2.2.8, 2.2.9 and 2.2.10 show the observed bathymetry (after adjustment of water-level to the tide at Hobart - smooth line) and modelled (stepped line) bathymetry looking downstream at Sections 2B, 17, 19, 22, 68, 70, 76 and 92, respectively.

2.3 Water Level

Water level data were available from Hobart (provided by Hobart Ports), New Norfolk (provided by the Bureau of Meteorology) and Boyer (provided by Norske Skog). It was found that data previously provided by the Bureau of Meteorology for New Norfolk (and reported by Hunter and Parslow, 1999) contained major and unexplained errors, so that our previous estimate of tidal range at New Norfolk (Hunter and Parslow, 1999, p. 9) is incorrect. The data for New Norfolk to be described here (for the period 26/5/99 to 9/12/99) is believed to be satisfactory.

Data from these three locations were subject to tidal analysis. The heights of mean sea level, and the amplitudes (*h*) and phases (*g*) of the four major tidal constituents are shown in the following table:

Table 2.3.1. The mean sea level, and the amplitudes (*h*) and phases (*g*) of the four major tidal constituents for New Norfolk, Boyer and Hobart.

	New Norfolk	Boyer	Hobart
Mean sea level (m, relative to AHD)	0.01	0.14	0.00
O_1 amplitude (*h*, m)	0.13	0.15	0.14
O_1 phase (*g*, degrees)	57	71	53
K_1 amplitude (*h*, m)	0.20	0.19	0.21
K_1 phase (*g*, degrees)	88	96	86
M_2 amplitude (*h*, m)	0.28	0.29	0.23
M_2 phase (*g*, degrees)	247	282	249
S_2 amplitude (*h*, m)	0.02	0.01	0.01
S_2 phase (*g*, degrees)	153	197	200

The table shows that sea level at all three sites is very similar, indicating that, during a tidal cycle, the sea surface along the estuary remains approximately level.

In order to simplify subsequent analysis and interpretation, the hydrodynamic model was forced in such a way as to make the simulations periodic over one day. It was therefore necessary to generate a "synthesised" tide that is periodic over one day and yet captures the major features of the observed tide (e.g. the tidal range, the tidal period, the neap-spring cycle, the diurnal inequality, and the overall "shape" of the tidal curve). The resultant tide is composed only of the S_1 (exactly diurnal) and S_2

(exactly semidiurnal) constituents, with amplitudes and phases chosen to best approximate the neap and spring tides. These constants are shown in Table 2.3.2 and the corresponding tides over a 24 hour period are displayed in Figure 2.3.1.

Table 2.3.2 : The amplitudes (h) and phases (g) of the S_1 and S_2 constituents for the synthesised neap and spring tides.

	Neap	Spring
h(S_1, m)	0.061	0.346
h(S_2, m)	0.268	0.268
2 g (S_1, degrees)-g (S_2, degrees)	270	220

It should be noted that neap and spring tides simulated in this way have daily tidal ranges that are approximately the same as the 20-percentile and 80-percentile daily tidal ranges observed at Hobart.

2.4 Wind

As noted by Hunter and Parslow (1999), there are very few observations of wind in the model region. However, wind data has been collected at the Boyer mill for several years and, since the initiation of the Study, has become available in digital form. Wind data from Boyer has been provided at a 90-second time interval for the period 27 December 1999 to 26 September 2000, and has been analysed to provide representative scenarios for model forcing .

Firstly, the "average" axial direction of the modelled region of the Derwent Estuary was chosen as 60° True. Each wind vector was then selected by the quadrant into which it fell, defined by Table 2.4.1. The frequency of occurence, quoted as a percent, is also included in Table 2.4.1. Note that all wind directions are quoted as the degrees from true north toward which the wind blows, not the direction from which the wind is coming.

Table 2.4.1 : Definition of quadrants used in wind analysis.

Description	Quadrant Range (° True)	Frequency (%)
Down-river	15°-105°	58
Across-river (N)	285°-15°	14
Up-river	195°-285°	10
Across-river (S)	105°-195°	18

Since wind data sampled at a 90-second time interval shows considerable variability, it is important that any "average" or "typical" wind forcing is chosen with care. The wind stress and rate of mixing vary as the square and cube of the wind speed, respectively, so a simple average *underestimates* their overall effect. It was originally envisaged that a median wind in each quadrant would be used for model simulations, but it was found that driving a hydrodynamic model with the median wind produced too little mixing. The following table (Table 2.4.2) shows the statistics of various powers of the wind speed, resolved along the bisector of each quadrant (e.g. at 60° True for the down-river quadrant). The percent of the time that each wind is less than or equal to the average over all quadrants is included in Table 2.4.2. Note that the frequency of the median wind speed is not 50% since this quantity is a mean of the

median in each quadrant rather than the median of all samples. Table 2.4.2 indicates that the wind speed is less than the root mean cubed wind speed approximately three quarters of the time.

Table 2.4.2 : Statistics of various powers of the wind speed, resolved along the bisector of each quadrant. The last two columns represent the square root of the resolved component of the wind squared, and the cube root of the resolved component of the wind cubed, respectively.

	Median wind (ms^{-1})	Mean wind (ms^{-1})	Root mean $(wind)^2$ (ms^{-1})	Root mean $(wind)^3$ (ms^{-1})
Down-river	2.35	2.97	4.15	5.18
Across-river (N)	2.42	2.65	3.62	4.32
Up-river	2.93	3.20	4.00	4.60
Across-river (S)	2.42	3.17	4.60	5.74
Average over all quadrants	2.53	3.00	4.09	4.96
Frequency speed is less than average (%)	40	47	66	77

It should be noted that, although the vector-average wind speed (not shown above) is quite significant (about 1.7 ms^{-1} at 84° True), the average components in each quadrant are of similar magnitudes.

In order to ensure that mixing was adequately represented by the hydrodynamic model, root mean cubed wind data was used as forcing. Therefore, from the right-hand column of the above table, a wind speed of 5 ms^{-1} was chosen, irrespective of quadrant.

3 The Wetland Experiment

An experiment was carried out in the wetland region between 28 June and 24 July, 2000. The experiment involved deploying salinity sensors near the surface at a site over the wetlands (515710 E, 5268490 N), and at a nearby site in the main channel (516050 E, 5267850 N). It was hoped that a time lag between the salinity signals of the two sensors would give an indication of the flushing time of the wetlands. If the wetland behaves like a first-order linear low-pass filter, then the time lag of the wetland salinity is the same as the exponential time constant, or flushing time, of the wetland.

Unfortunately, during the period of the experiment, the vertical stratification of the water column in the vicinity of the sensors was large, inducing a large tidal variation in salinity. Since this effect depends on the *vertical* tidal displacement, it is indistinguishable from the effect of horizontal advection of salinity, which depends on the *horizontal* tidal displacement (the vertical and horizontal tidal displacements are in phase for a predominantly standing wave, as is found in the Derwent). Attempts were made to remove effects such as this that should be common to both sensors, using a multiple linear regression model forced by observables such as river flow, tides, tidally-averaged sea level, tidal range and wind. It was hoped that the resultant residuals would display a time lag indicative of the flushing time of the wetlands. This was only partially successful. The most complicated regression model, using all of the above observables as independent variables, removed about 48% and 25% of the variances of the salinity in the channel and wetland, respectively; a large amount of variability was unaccounted for. However, inspection of the resultant residuals indicated a time lag, or exponential flushing time, of around 5 hours, which is consistent with the estimates of Hunter and Parslow (1999; Section 2.5.5). Further discussion of the flushing time can be found in Hunter and Parslow (1999).

4 Description of Models

4.1 The Hydrodynamic Model

4.1.1 Introduction

The hydrodynamic model, MECO, was used to simulate transport and dispersal in the estuary. MECO is a three-dimensional, non-linear, variable-density hydrodynamic model developed by the CSIRO Division of Marine Research in Hobart. It is an upgraded version of the M3D model used in earlier simulations described by Walker and Hunter (1994).

MECO simulates three-dimensional distributions of velocity, temperature, salinity and concentrations of passive tracers, based on input fluxes of water, salt, heat and passive tracers, and forcing by winds, atmospheric pressure gradients and tides. The equations forming the basis of the model are similar to those described by Blumberg and Herring (1987), except that the model uses so-called "z" coordinates in the vertical to better represent stratified flows. The equations are solved using finite-difference techniques on a C-type grid (see, for example, Mesinger and Arakawa, 1976). The model has been described in more detail by Walker and Fandry (1994) and Walker and Waring (1998).

The hydrodynamic model was improved by including a higher order advection scheme (2^{nd} order flux form) with the TVD (total variation-diminishing) limiter of Leonard (1988) to decrease numerical diffusion whilst retaining monotinicity. This scheme resulted in a better representation of the vertical density structure in the water column and preserved density fronts associated with the propagating salt wedge. Horizontal diffusion was explicitly specified by the inclusion of a diffusion scheme cast in a flux form. Both the advection and diffusion schemes produced excellent mass conservation characteristics.

An improved boundary condition was developed for the Bridgewater open boundary and applied to tracers (temperature, salinity, resin acids) in the surface layer. This boundary condition preserved a memory of tracer concentrations from previous flood/ebb tidal cycles and applied these as boundary conditions for subsequent ebb/flood tides. In the absence of river flow, this condition would result in zero net tracer flux through the boundary over a perfectly symmetrical tidal cycle. Since the tide is semidiurnal, and typically non-symmetrical due to the combined effects of river runoff and frictional distortion, the tidal excursion in the flood/ebb may exceed the tidal excursion on the previous ebb/flood. Under these conditions, the tracer concentration on the boundary reverts to a constant (user specified) value.

4.1.2 Model Domain

The Derwent estuary extends for about 60 km, from New Norfolk at the landward end to the Iron Pot at the seaward end. From New Norfolk to a point a few kilometres upstream from Bridgewater, the estuary is about 150 to 250 m wide, with the main channel spanning most of the width. There exist large shallow bays (wetland areas) adjacent to the main channel directly upstream from Bridgewater. The Norske-Skog Mill site is located on the upper part of the estuary, about 5 km downstream from

New Norfolk. Here the estuary is relatively narrow and has depths ranging roughly between 5 and 15 m. The water column is usually strongly stratified, with a sharp interface between the relatively fresh surface water flowing downstream and the deeper saline water flowing upstream. The degree of stratification and the location of the end of the salt wedge depends on river flow. The most detailed description available of the upper estuary is that by Davies and Kalish (1989).

The model grid covers the upper Derwent Estuary between the bridge at New Norfolk and the causeway at Bridgewater. An orthogonal curvilinear grid is used, following a smooth approximation of the river centreline. The wetland area and main channel near Bridgewater are represented by an orthogonal polar grid to provide equal resolution in the long and cross river directions. This was merged with the orthogonal curvilinear grid upstream from the wetlands. The resolution of the grid in the long-river direction varies from about 110 m near new Norfolk and the Norske-Skog Mill site, to about 75 m near Bridgewater. The cross-river resolution varies smoothly from about 10 m at New Norfolk to about 55 m at the Bridgewater causeway. There are 172 cells in the long-river direction. For most of the river length, except the wetland area near Bridgewater, there are 9 cells across the river.

Vertically, the grid covers the entire depth range found in the upper estuary. There are 21 model layers, spaced 0.4 m apart between the surface and 4 m depth, and with gradually increasing spacing in the deeper parts of the model. For the range of flows studied, the halocline is always located in the top few metres of the water column where the vertical resolution is greatest. Depths of the bottom of each layer are given in Table 4.1.

Table 4.1 : Vertical Model Resolution.

Layer	Depth (m)	Layer	Depth (m)
20	0	10	4.0
19	0.4	9	4.45
18	0.8	8	5.0
17	1.2	7	5.7
16	1.6	6	6.6
15	2.0	5	7.75
14	2.4	4	9.2
13	2.8	3	11.0
12	3.2	2	13.2
11	3.6	1	15.85
		0	19

4.2 The Resin Acid Model

The resin acid model is directly coupled with the hydrodynamic model and simulations are performed on the same temporal and spatial scale. The source for these resin acids is the CES discharge at Boyer which can have variable flow rate and resin acid composition. The resin acid model predicts the concentrations in the water column over the whole estuary and the flux of resin acids to the sediments. Resin acids are subjected to the conservative processes of advection and mixing and the non-conservative processes outlined below.

4.2.1 Breakdown due to microbial decay.

Resin acids are divided into a labile (abietane-like) fraction, and a refractory (DHAA and pimarane) fraction, which each decay at a fixed rate.

4.2.2 Breakdown due to UV-B light.

There is evidence for enhanced breakdown of the labile resin acids under UV-B irradiation. At surface irradiances, the breakdown rate in laboratory studies (ERA Task 8) ranged from 0.7 d^{-1} to 3 d^{-1}. However, UV-B is strongly attenuated in the Derwent Estuary, due to both natural humics and the increased coloured organics introduced by the CES. At background river conditions, the estimated attenuation coefficient, Kd, for UV-B is about 10 m^{-1} and it is therefore assumed that UV-B attenuation is restricted to the surface cell. Since the breakdown rate is assumed to be proportional to UV-B, the disappearance rate of resin acids is estimated by multiplying UV-B breakdown rate, r_UVB, by the ratio of average to surface UVB in the surface cell, UVB_av. For a surface cell of depth ΔZ, this ratio is:

$$UVB\_av = \left[1 - \exp(-Kd.\Delta Z)\right]/(Kd.\Delta Z) \qquad 4.2.1$$

Given that the attenuation is very high, eqn. 4.2.1 can be reduced to:

$$UVB\_av = 1/(Kd.\Delta Z) \qquad 4.2.2$$

The estimated attenuation of UV-B due to CES is very high (Kd = 1080 m^{-1}) hence the additional effect of CES organics on attenuation is also included. This will have its primary effect within the mixing zone (defined as the region near the CES source where cross-river variability exists), but it will significantly increase attenuation down to 100:1 dilutions. The attenuating compounds introduced by CES are not modelled; however, as they are conservative any normalised conservative tracer can be used to estimate their effect on attenuation. In the model simulations, temperature is not subjected to surface or boundary heat fluxes and hence the elevated temperature of the CES discharge can be used as a conservative tracer of CES. The effective Kd in each surface cell is therefore computed as:

$$Kd = 10 + \frac{T - T_B}{T_{CES} - T_B} 1080 \qquad 4.2.3$$

where T is the model temperature, T_B is the background temperature in the model domain (i.e. temperature at time = 0) and T_{CES} is the temperature of the CES inflow. The computed attenuation is used to calculate UVB_av, and hence r_UVB*UVB_av, in each surface cell.

4.2.3 Aggregation / adsorption and settling.

A large proportion of the resin acids in the CES are dissolved, and the remainder are probably present as colloids, or adsorbed to other particles. Laboratory studies conducted to estimate separate adsorption / aggregation rates and settling rates were inconclusive. However, these studies indicate that the important process may be

adsorption of resin acids to particulate matter in the estuary, which then settles out, rather than aggregation of CES colloids.

Removal of dissolved fractions due to adsorption is achieved through fixed bulk adsorption rates to particles. If the disappearance rates in the laboratory studies are interpreted as adsorption rates, then the adsorption for the labile fraction at 20 psu is typically r_ads_20L = 0.25 d^{-1}, and for the refractory fraction at 20 psu r_ads_20R = 0.06 d^{-1}. Laboratory studies indicated that disappearance / adsorption rates were more or less proportional to salinity. However, this means that adsorption in the fresh surface layer is negligible. To allow for the possibility that part of the labile resin acid disappearance in the fresh layer is due to adsorption, we added a salinity independent adsorption rate r_ads_c. The total adsorption rate is then given by:

$$r\_ads = r\_ads\_c + r\_ads\_20\frac{S}{20} \qquad 4.2.4$$

where S is the salinity (psu).

Adsorption converts a neutrally buoyant or "dissolved" fraction into a particulate fraction which subsequently sinks. However, the settling rate is unknown and will have a major effect on the concentration and distribution of resin acids in the bottom layer. Due to the lack of data to conclusively partition dissolved loss into a breakdown and adsorption component, we have considered two alternative models. In the first, all the disappearance of labile dissolved tracer is assumed to be due to adsorption, while in the second, it is all attributed to breakdown. As this does not affect the dynamics of the dissolved fraction, but only the particulate fraction, we can treat both models simultaneously by simply adding a second labile particulate tracer. As the particulate tracers settle relatively quickly, the major impact is on the sedimenting flux of labile resin acids.

4.2.4 Adsorption to the bed sediment surface.

An additional process for removing resin acids is adsorption of resin acids directly to the bottom which is modelled as:

$$Sed\_flux = F\_ads\frac{D.u^{*}RES}{\upsilon} \qquad 4.2.5$$

where RES is the concentration of resin acids, D is the molecular diffusivity of resin acids, u* is the friction velocity and ν is the molecular viscosity. This formulation assumes resin acids are "sticky", i.e. the effective concentration on the surface is zero. The coefficient F_ads is an empirical constant which can be adjusted to allow for partial stickiness.

For typical values of D = 1.5E^{-9}, u* = 0.01 ms^{-1}, ν = 1.E^{-6}, sediment adsorption is equivalent to a sinking rate of approximately 1 m/day. This is unlikely to be a dominant process in the deeper channel but may be potentially important for the dissolved fraction in shallow areas.

4.2.5 Model Formulation.

The resin acid model requires five resin acid tracers: refractory dissolved (RDRA), labile dissolved (LDRA), refractory particulate (RPRA), labile particulate with no adsorption (LPRA) and labile particulate with adsorption (LPRA_A). The labile tracers are subject to breakdown. Dissolved tracers are converted to particulate tracers at the specified rates and particulate tracers are assigned a specified sinking rate.

These processes are written as:

$$\frac{\partial RDRA}{\partial t} = -r\_ads\_20R\frac{S}{20}RDRA \qquad 4.2.6$$

$$\frac{\partial RPRA}{\partial t} = r\_ads\_20R\frac{S}{20}RDRA \qquad 4.2.7$$

$$\frac{\partial LDRA}{\partial t} = -(r\_ads\_c + r\_ads\_20L\frac{S}{20})LDRA - rB.LDRA - r\_UVB.UVB\_av.LDRA \qquad 4.2.8$$

$$\frac{\partial LPRA}{\partial t} = -rB.LPRA - r\_UVB.UVB\_av.LPRA \qquad 4.2.9$$

$$\frac{\partial LPRA\_A}{\partial t} = (rB + r\_ads\_c + r\_ads\_20L\frac{S}{20})LDRA - rB.LPRA\_A - r\_UVB.UVB\_av.LPRA\_A \qquad 4.2.10$$

LPRA and RPRA are allowed to sink at a specified rate wP. LDRA and RDRA are subject to adsorption to the bed. Calibration parameters required for the resin acid model are summarised in Table 4.2.1.

Table 4.2.1 : Resin Acid Model Parameters

Variable	Description	Typical value	Units
rB	breakdown rate of labile resin acids	1*	d^{-1}
r_UVB	UVB breakdown rate at surface irradiance	2*	d^{-1}
Kd_riv	UVB attenuation in river	10**	m^{-1}
Kd_RES	UVB attenuation in CES	1080*	m^{-1}
r_ads_CL	Constant adsorption rate of labile RA	0 – 0.25*	d^{-1}
r_ads_20L	Adsorption rate of labile RA at S = 20 psu	0 - 0.25*	d^{-1}
r_ads_20R	Adsorption rate of refractory RA at S=20 psu	0.06*	d^{-1}
wP	Sinking rate of particulate RA	-****	$m.day^{-1}$
F_ads	Adsorption efficiency of bed	0 - 1***	-

* Task 8, Monash University
** Royle and Hart (1994)
*** John Hunter pers. comm.
**** Estimates unavailable; settling not included in the process study of Grace and Liang (2000a)

4.3 Transport (Box) Model

It is computationally too expensive to conduct biogeochemical and ecological model simulations within the hydrodynamic model implemented for the Derwent Estuary. The biogeochemical and ecological models not only include a large number of tracers and processes, but also need to be run over extended periods (at least several years). These models have been implemented within a coarse resolution transport model, or "box" model, BM. Physical exchanges within BM are derived from the hydrodynamic model output in the manner described below.

Horizontally, the box model represents the Estuary as a set of polygonal columns or boxes; each box contains a number of water column and sediment layers. An individual box and layer is referred to as a cell. Physically, each water column cell exchanges water with other cells. These exchanges represent effects of both advection and diffusion of material between cells in water column. BM implements the exchanges and accounts for corresponding changes in tracer concentrations. It also implements physical processes such as sources of tracers, sediment transport, exchange of material between sediment and water column, mixing within sediment, sources of water (river flow), precipitation and evaporation. As well as these physical exchanges, tracer concentrations within cells are modified by biogeochemical and ecological processes, described in section 4.4.

A more detailed description of BM is contained in the Port Phillip Bay (PPB) Environmental Study report (Walker, 1997). The most important functional distinction between the PPB and Derwent model versions is the "memory" boundary condition described later.

The model implemented for the Derwent consists of 24 boxes, with 22 "active" cells and 2 boundary cells (Fig. 4.3.1). The distance of the upstream edge and centre of each box from New Norfolk and the CES is shown in Table 4.3.1. The model laterally averages the main channel, and divides it lengthwise into 16 boxes, including 2 boundary boxes, one at New Norfolk (Box 0) and another at Bridgewater (Box 15). The larger northern wetlands are divided into 6 boxes (Boxes 16-21), and the southern wetlands into 2 boxes (Box 22 and 23).

Vertically, the model contains a maximum of 3 water column layers and 1 sediment layer. The stratified water column in the channel is generally divided into 3 water layers, while well-mixed wetland boxes have only 1 water layer. For more details on vertical water column geometry, see the section on exchange calculation.

Table 4.3.1 : Distances of Sub-regions from New Norfolk and the CES

Box Number	Distance from New Norfolk (m) (upstream box edge)	Distance from New Norfolk (m) (box centre)	Distance from CES (m) (upstream box edge)	Distance from CES (m) (box centre)
1	0	725	-5355	-4685
2	2163	3021	-3192	-2389
3	3838	4583	-1517	-827
4	5301	5952	-54	543
5	6674	7346	1320	1937
6	7982	8761	2628	3352
7	9416	9894	4062	4485
8	10576	11123	5222	5714
9	11908	12358	6554	6949
10	12878	13401	7524	7992
11	13859	14204	8505	8795
12	14651	14962	9297	9553
13	15456	15809	10102	10400
14	16238	16746	10884	11337
15	17158	17270	11804	11861

Negative values indicate the boundary is upstream

4.3.1 The “memory” boundary condition

In other applications such as Port Phillip Bay, it has been reasonable to assume that the estuarine outflow has negligible impact on tracer concentrations at the marine boundary, and marine boundary concentrations are fixed. However, the Port Phillip Bay transport model used a 24 hour time step, and averaged over the tidal cycle. Because of the short time scales of mixing and advection in the Derwent estuary, the box model used here has to resolve the tidal cycle. This creates a particular problem for the lower (Bridgewater) boundary condition (Fig. 4.3.1, box 15). (It also poses other significant challenges, discussed below under exchange calculation).

Averaged over a tidal cycle, the upper Derwent is a classic salt wedge estuary, with outflow at the surface and inflow at depth. This means that, on average, tracers in the bottom layer at Bridgewater are advected upstream in the model. These are mixed and transformed along with river and other loads in the upper estuary. These loads and transformations then determine the concentration in the surface layer leaving the estuary at Bridgewater.

Under the river flows modelled here, there is strong tidal exchange, and reversal of flow in all water column layers, at the Bridgewater boundary. The reversal of flow in the surface layer at Bridgewater means that surface boundary tracer concentrations are advected into the model at each flood tide. If a fixed surface boundary condition is used there, it is not necessarily consistent with loads and processes in the upper estuary, and results in distortion of tracer concentrations in the surface layer, at least within a tidal excursion or so of the boundary.

The problem arises from the artificial specification of a boundary half-way along the estuary. In practice, the surface water entering the model on the flood tide should have similar characteristics to the surface water leaving the model on the ebb tide. This has been accomplished via implementation of a “memory” boundary condition, which works as follows. The boundary cell is included in the transport calculations in a

modified way. At each model step, any water flowing from the model domain into the boundary cell is added to that cell, and the tracer concentrations in the cell adjusted accordingly. Water flowing from the boundary cell to the model domain carries the boundary cell tracer concentrations. The boundary cell volume is kept fixed at its initial value.

The result is that boundary cell concentrations track towards the average concentration leaving the model on the ebb tide. The time constant is determined by the volume of the boundary cell, which we treated as an adjustable parameter. A volume of 2.0E6 m^3 was found to give good results.

4.3.2 Deriving Box Model Exchanges : A New Inverse Technique

In the box model, volume exchanges between water column cells are externally specified, and define the circulation and mixing. These are derived from the hydrodynamic model output. Because of the coarse geometry of box models, and comparatively long time steps, these exchanges must average over time and space. Doing this realistically is always technically challenging.

For the Derwent model, it is particularly complicated because of the combination of tidal circulation in the wetlands, and intense vertical stratification with strong tidal modulation in the main channel. For any reasonable box model resolution, the strong river flow dictates use of a short time step, so that the water volume flushed through a cell in one time step does not exceed the cell volume. In addition, the almost complete flushing of the wetlands through the tidal cycle makes it impossible to average over the tidal cycle (as was done in Port Phillip Bay).

However, resolving the tidal cycle brings additional problems. In the hydrodynamic model, there are substantial tidally driven oscillations in the depth of the halocline. Resolving these required very thin layers (40 cm). In the much coarse 3-layer structure allowed by the box model, these fluctuations can result in unrealistic vertical numerical diffusion which wipes out vertical gradients in salinity and other tracers.

In the Port Phillip Bay study, a Lagrangian particle tracking technique was implemented in the hydrodynamic model to calculate the net exchanges of water between cells over the box model time step. This works quite well if the time step is long and tidally averaged. However, if the time step is short, the particle and corresponding volume exchanges may represent exchanges just across the boundary dividing two cells. Moreover, this exchange may subsequently be reversed as the tide reverses. But the box model implicitly smears the tracer associated with each exchange across the entire cell volume at each time step. This results in unrealistically high numerical diffusion.

To overcome this problem, we have developed a new variational inverse technique for calculating the box model exchanges from the hydrodynamic model. This approach builds on inverse techniques which have been applied previously to estimate box model exchanges from observed tracer (salinity) distributions. The problem there is to find a set of exchanges which best reproduce the observed salinity distribution. However, with only one tracer, the problem is underconstrained, except for the simplest circulations.

We have posed a comparable problem: estimate a set of exchanges for the box model which best reproduce tracer distributions produced by the hydrodynamic model. Here we have the luxury that we are not restricted to one tracer, and can use other conservative tracers, with different source-sink distributions in the hydrodynamic model, to better constrain the box model. The general formulation is: given tracer concentrations output by the hydrodynamic model in each box at every (box model) time step, find those box model exchanges that best reproduce these concentrations.

This inverse approach has a considerable advantage over particle tracking and other similar methods for calculating volume exchanges. It is essentially forced to choose exchanges which, when applied over time, compensate as far as possible for the numerical diffusion in the box model.

In formulating the inverse model, we can take advantage of the linearity of the (first-order, explicit) mixing scheme used in the Box Model. With the objective function defined as a quadratic function, the problem falls into the class of Quadratic Programming (QP) of Linear Optimisation Theory, for which there exist standard algorithms.

The QP problem has another useful feature: along with the equality constraints, it allows use of inequality constraints. The latter are necessary to ensure that the solution is physically sensible: all exchanges are positive and no cell discharges more water than it contains.

Another advantage of the inverse scheme adopted is that the forward version of the inverse model is identical to the transport model. Thus, it is possible to assess the outcome of the inverse model without running the box model: the current tracer values appearing at the inverse model run will be exactly reproduced during the following box model run.

4.3.3 Vertical Structure: An Isopycnal Box Model

It is customary to model salt-wedge estuaries as a 2-layer circulation. However, we found that models with fixed layer depths in each cell (either 2 or 3 layers) performed very badly. The problem is that, as the halocline depth varies over the tidal cycle, the salinity averaged over box model layers also varies substantially. Even with the inverse technique, it is not possible for the box model to reproduce these smeared tidal oscillations except through unrealistic horizontal and vertical exchanges.

The solution to this problem lies in allowing the box model layer depths to vary tidally along with the halocline. We fix the layer boundaries at chosen salinities, essentially turning the model into a crude isohaline or isopycnal model. For example, a three-layer model could have a fresh layer (0-4 PSU), a halocline layer (4-22 PSU) and a salt wedge layer (>22 PSU). We compute and store volumes and tracer concentrations in these cells at each time step, and modify the inverse model so the estimated exchanges reproduce the time-varying volumes as well as tracer concentrations.

4.3.4 Application to the Derwent

The inverse model application involves a number of choices for the user:
- setting values of individual exchanges (useful to set the river flow)
- setting weights for individual exchanges
- setting common and individual tracer weights
- setting tracer weights in individual cells proportional to 0^{th}, 1^{st} or 2^{nd} power of the cell volume
- scaling both exchanges and tracers
- scaling individual tracers
- using hydrodynamic input data in a periodic manner

In the Derwent, as well as salt, three additional conservative tracers were used: a "CES" tracer with source at CES discharge (Box 4); a "b17" tracer with two sources in Box 17, and a "b20" tracer with source in Box 20. These tracers were chosen so as to attempt to force the box model to reproduce the transport of CES tracers and the exchange between wetlands and channel predicted by the hydrodynamic model. The sources in Box 17 and Box 20 were chosen after some experimentation to provide useful constraints on box model exchanges. The tracer flux values were chosen to provide reasonable longitudinal gradients during the Inverse Model run without re-scaling.

For the upper Derwent, 2 vertical layers proved too crude to reproduce circulation both in the channel and in Wetlands. From the Hydrodynamic Model runs, the water flushing into the wetlands at high tide is mostly coming from the upper 1 m water layer in the channel. This level is substantially shallower than the halocline depth (typically from 2.5 to 3 m in the channel near the wetlands). As a result, the 2-layer model produces too high (by 1.5—2 PSU) salt concentration in the wetlands, which is a noticeable difference taking into account a typical salinity there of 1—6 PSU. Also, the 2-layer model produces lower (by about 2 PSU) salinity in bottom layer cells at the New Norfolk end, probably because of the bigger overall diffusion compared to the 3-layer model.

Overall, the 3-layer inverse model ran more reliably and produced a better fit than the 2-layer model. There was some penalty for the 3-layer model in terms of the CPU time, but it was still reasonable (about 2 hours on 800 MHz Pentium processor for an 11 day period with 30 minutes time step).

In terms of input data, the Inverse Model was run periodically on 1-day output of the Hydrodynamic Model (days 19.0—20.0 from the model start). It was run for 11 days with the last day exchanges being used later for the Box Model runs. The 10 days spin-up period was necessary to ensure that the Inverse Model had reached periodic state. (The model starts with zero tracer discrepancies, and it takes time to build up equilibrium values.)

The inverse model options (weights, salinities, etc) were tuned separately for each of the 12 physical scenarios modelled (see section 6.1), with typically 10 to 20 attempts required before the exchanges allowed the model to reproduce the observed tracers. The most important scenario-dependent parameters were the layer interface salinity levels (see Table 4.3.2).

Table 4.3.2. Salinities used to define layer interfaces for each physical model scenario (see section 6.1)

Tide	River flow, m3	Wind, direction	Salinity levels
NEAP	45	60	8, 23
NEAP	45	240	9, 22
NEAP	45	330	5, 22
NEAP	90	60	4.75, 24
NEAP	90	240	4, 21
NEAP	90	330	4.5, 20
SPRING	45	60	11, 23
SPRING	45	240	10, 23
SPRING	45	330	8, 23
SPRING	90	60	6, 22
SPRING	90	240	4, 21
SPRING	90	330	4, 21

For wind directions of 240° and 330°, there are sharp salinity variations in wetlands boxes 21, 22 and 23 that initially resulted in intermittent vertical splitting of these boxes into 2 layers at times while being 1-layer through the most part of the run. The current BM implementation does not allow changes in number of water column layers over time, so this splitting was prevented.

The choice of the upper interface value had a major influence on the Inverse Model run, so that at times a difference of 0.25 PSU could result in noticeable changes in the model outcome. For the second layer interface value, it was typical for changes by 1 PSU to be of little influence.

For all Inverse Model runs, a time step of 30 minutes was used. Reducing the time step to 15 minutes or increasing it to 60 minutes both resulted in bigger tracer discrepancies. This indicates that the time step of 30 minutes is near optimum for the cell size used.

To give preference to horizontal circulation, we reduced weights assigned to horizontal exchanges, typically to 0.2 (all other exchange weights were equal to 1 by default). Also, we set all but one exchange between Box 0 (New Norfolk boundary) and Box 1 to 0; the exchange between Box 0, upper layer and Box 1, upper layer was set either to 45 or 90 m3, depending on the required river flow. For better modelling of circulation in Wetlands, a number of exchanges across cell corners were added.

The weights for tracer discrepancies in a cell were set proportional to the cell volume. This weighting was found to provide most reliable results: making it independent of the cell volume results in too much influence from smaller cells, while making it proportional to cell volume squared overestimates the importance of cell size. This means that the inverse model is effectively fitted to reproduce tracer mass.

With this tuning, the inverse model reproduces the distribution of salinity and other hydrodynamic tracers quite well, given the substantial spatial and temporal averaging

involved. For example, errors in salinity in a model cell are typically around 0.3 PSU or less.

The inverse model approach to estimating box model exchanges, along with the isopycnal box model formulation which the inverse method makes possible, represent significant advances in our capacity to model coastal systems, especially those with strong vertical and temporal gradients.

4.4 Biogeochemical / Ecological Model

An overall goal of this modelling task is to help assess the impact of the CES discharge of stressors such as organic carbon, colour, and nutrients on the upper Derwent, and to provide some indication of the potential impacts of changes in CES composition which might result from secondary treatment.

To do this, we have used a general model of biogeochemical and ecological processes developed by CSIRO for estuaries and coastal waters. This model was initially developed for Port Phillip Bay, but has been substantially modified and improved in subsequent ongoing studies such as the National Land and Water Audit of Estuaries (NLWRA), and Gippsland Lakes. The approach adopted in developing this general model has been to seek robust, parsimonious but realistic representations of key chemical, physiological and ecological processes in coastal waters. This approach is currently being rigorously tested in the NLWRA, where we are attempting to model estuaries spanning the diverse range of geomorphological, hydrodynamic and ecological types found in Australia. The approach has an especial advantage for studies such as the current one of necessarily limited scope and duration, in that we are able to build on knowledge acquired in previous studies, reducing the dependence on local data and process studies for model calibration.

The model is implemented within the BM transport model described in the previous section. In this section, we start with a general overview of the biogeochemical model structure. A detailed technical description of the Port Phillip Bay model can be found in Murray and Parslow (1997). We then describe in some detail improvements to the model since 1997, focusing on those which are critical for the current study. We also discuss some particular additions to the model needed to deal with the upper Derwent and the CES discharge.

4.4.1 Model Overview

The model represents the cycling of nitrogen, phosphorous and carbon through both pelagic and benthic ecosystems. The Port Phillip Bay Study showed convincingly that, in shallow coastal embayments and estuaries, representation of both pelagic and benthic systems, and the coupling between them, is critical to understanding and predicting the response to nutrient loads (Murray and Parslow, 1997).

The ecological model has three modules: water column, sediment, and epibenthos. The water column module describes a simple planktonic food web. The model currently includes two phytoplankton functional groups: small phytoflagellates and large bloom-forming phytoplankton with nominal cell diameters of 5 μm and 20 μm

respectively. There are in turn two size classes of zooplankton which graze respectively on small and large phytoplankton. The model represents a range of forms of nonliving particulate and dissolved organic matter, as well as inorganic nutrient species, dissolved inorganic carbon (DIC) and dissolved oxygen.

The sediment module represents the breakdown of particulate and dissolved organic matter through microbial and detritivore activity which consumes oxygen and releases DIC and inorganic nutrients. The module includes the processes of nitrification and denitrification, which have been shown to play a pivotal role in nitrogen cycling in coastal systems (Harris et al., 1996). The module also includes benthic microalgae, which have now been shown to make a major contribution to primary production in many coastal systems.

The epibenthic module represents two functional classes of attached macrophytes: macroalgae, which take up nutrients from the water column, and seagrass, which take up nutrients from the sediment pore water.

A schematic view of nitrogen cycling through water column, sediment and epibenthic components is shown in Fig. 4.4.1. This cycle is similar to that represented in the Port Phillip Bay model (Murray and Parslow, 1997). However, there have been a number of substantial improvements in the model since that study, and these are now discussed in more detail.

4.4.2 Phosphorus Dynamics

The Port Phillip Bay model included phosphate as an explicit variable, but phosphorus participated in nutrient cycling as a "passive" tracer, always accompanying nitrogen at Redfield ratios. This was deemed adequate because phosphorus is always present at great excess in Port Phillip Bay.

The representation of phosphorus is substantially upgraded in the current model. First, phosphorus is now treated as a potentially limiting nutrient for plant growth along with nitrogen. The interaction between N and P in controlling plant growth is discussed further below. (Note that silicate has been dropped from the model in the version used here: silicate levels are quite high and saturating for phytoplankton growth in the upper Derwent.)

Second, adsorption-desorption interactions between dissolved inorganic P (DIP) and adsorbed particulate inorganic P (PIP) are now represented explicitly in both water column and sediments. The adsorption-desorption reaction is modelled so that the net adsorption flux is given by:

$$\frac{\partial PIP}{\partial t} = r\_ads\_P(P\_abs\_coeff.TSS.DIP - PIP) \qquad 4.4.1$$

Here r_ads_P (d^{-1}) controls the reaction rate, while P_abs_coeff ($m^3\ kg^{-1}$) determines the equilibrium between DIP and PIP. TSS is the concentration of suspended inorganic sediment ($kg\ m^{-3}$).

Third, the model now allows for variation in the N:P stoichiometry of organic matter depending on its origin. This is discussed further under stoichiometry below.

4.4.3 Plant growth

The PPBES model represented plant growth in a fairly traditional way, using Monod equations and half-saturation constants K_N to describe nutrient-limitation of plant growth, and a bilinear function incorporating a light-saturation intensity K_I to describe light-limitation. The "Law of the Minimum" was used to describe interactions among multiple limiting nutrients, while a multiplicative model was used to describe the interaction between nutrient and light limitation. The latter is known to underestimate plant growth when nutrients and light are co-limiting.

The plant growth module has subsequently been replaced by the so-called Chemical Reaction (CR) scheme developed by Baird and Emsley (1999). This scheme has substantial advantages over the PPBES scheme. First, it uses bio-physical formulations as far as possible to compute uptake rates. For example, it computes potential phytoplankton nutrient uptake rates as a function of far-field concentration and phytoplankton cell size and shape, assuming uptake is limited by the diffusive flux to the cell surface. ("Far-field" is used here in the sense of molecular diffusion to refer to the concentration at several cell radii.) Macroalgal potential nutrient uptake rates are computed using a model for the flux of nutrient across a turbulent boundary layer. Light capture by phytoplankton for photosynthesis is based on a model of optical cross-section, again based on cell size. The use of bio-physical formulations means that parameters such as K_N and K_I are derived from cell radius and fundamental physical laws, reducing the number of free parameters in the model.

Second, the CR scheme represents internal cell quotas for nitrogen, phosphorus and carbon, and assumes that growth rate depends on the product of factors proportional to internal cell quota. The scheme in principle allows cell quotas to be treated as dynamical variables and uptake to be decoupled from growth. However, in the current implementation, to reduce the number of model variables, quotas are assumed to adjust rapidly to changes in external concentration, and a quasi-steady-state relationship between external concentrations of DIN, DIP and light has been derived. This relationship has the substantial advantage over the multiplicative light-nutrient interaction used in PPBES that the initial slope of the growth rate vs concentration curve for one limiting factor is not reduced by other limiting factors.

A detailed description of the CR formulation is being prepared as a separate document (Baird et al, 2001).

4.4.4 O:C:N:P Stoichiometry

The model now explicitly represents the stoichiometry of all plant components, and distinguishes a Redfield O:C:N:P stoichiometry of 138:106:16:1 for phytoplankton and microphytobenthos from an Atkinson and Smith O:C:N:P stoichiometry of 716:550:30:1 for macrophytes. Zooplankton are assumed to have Redfield stoichiometry.

Allowing different stoichiometries complicates the treatment of detrital material. The model now includes two labile detrital pools: one of planktonic origin with Redfield stoichiometry (Lab_Det_Plank), and one of macrophyte origin with Atkinson stoichiometry (Lab_Det_Benth). It is assumed that by the time organic matter has been converted to refractory particulate detritus or refractory dissolved organic matter, its origin no longer affects breakdown rates. However, because there are different sources, with different stoichiometries, the model must separately represent DOC, DON and DOP, and Ref_Det_C, Ref_Det_N and Ref_Det_P, and allow these to vary independently, in order to conserve mass. This incidentally provides much more flexibility in representing catchment load composition.

4.4.5 Zooplankton Encounter Rates

Analogous to the bio-physical sub-models underpinning the CR scheme above, an encounter rate theory is now used to calculate zooplankton clearance rates, based on zooplankton and prey radius and zooplankton swimming speeds. While one can use a standard relationship between swimming speed and cell size, we allow swimming speed and therefore maximum clearance rate to be adjustable parameters.

4.4.6 Temperature Dependence

In the bio-physical sub-models discussed above, the temperature dependence of key physical and biochemical processes is accounted for.

4.4.7 Light attenuation

The PPBES model accounted for the specific attenuation due to phytoplankton and dissolved and particulate organic matter. The current model explicitly includes the attenuation due to suspended sediments (TSS). In some Australian catchments, the runoff is highly coloured due to high concentrations of humic material. This coloured dissolved organic matter (CDOM) can dominate light attenuation in estuaries, and cannot be accounted for simply in terms of total DOC or DON. The model assumes that CDOM is conservative in estuaries: under this assumption, its concentration can be computed from salinity. The attenuation due to CDOM in freshwater, K_C_fw, is prescribed as a model parameter.

The model now deals explicitly with both self-shading and light interactions among benthic plants. The model assumes a specific light absorption cross-section per unit biomass of macroalgae and seagrass. Self-shading is taken into account in computing light-limited growth rates, and this sets a bio-physical upper limit to seagrass and macroalgal standing stock. Further, it is assumed that macroalgae can overgrow seagrass, so light attenuation by macroalgae reduces light available to seagrass. The result is that the model predicts in a simple but effective way the loss of seagrass due to overgrowth by epiphytes under eutrophic conditions. Both seagrass and macroalgae are assumed to shade microphytobenthos.

4.4.8 Flocculation

Catchment runoff may contain loads of fine clay particles, which settle very slowly. Changes in surface chemistry associated with increasing salinity in estuaries lead to

flocculation and more rapid settling of these fine particles. This process is represented in the model by distinguishing two classes of fine inorganic sediment: unflocculated clay particles (TSS_unfloc), and flocculated particles (TSS_floc) with higher sinking rates. The model fixes two salinity thesholds, 6 and 10 PSU, and the conversion rate from TSS_unfloc to TSS_floc increases linearly from zero at the lower threshold to a maximum rate r_floc at the upper threshold.

Because these sediment fractions settle at different rates, the adsorbed inorganic P pool PIP is also divided into a PIP_unfloc and PIP_floc pool. Adsorption-desorption interactions of these fractions with DIP are modelled separately.

4.4.9 Labile Organic Carbon

The CES discharge includes large loads of labile organic carbon. The C:N and C:P ratios in the discharge are much larger than those in the labile detrital pools already present in the model, which are assumed to be generated by plankton or macrophytes. The model does include refractory DOC and POC pools, but these have long breakdown times, of the order of hundreds of days. We have therefore introduced two new labile organic carbon pools: Lab_DOC and Lab_POC, whose sole origin is assumed to be the CES discharge.

The breakdown kinetics of these pools is assumed to be linear, with a breakdown rate r_LOC which is temperature and potentially salinity (S) dependent. We also allow for adsorption of the Lab_DOC pool to form Lab_POC. Again, the adsorption kinetics are assumed to be first-order, and temperature and salinity dependent.

The local rate equations for these variables are therefore:

$$\frac{\partial Lab\_DOC}{\partial t} = -(r\_LOC + r\_LOC\_20\frac{S}{20})Lab\_DOC - (r\_ads\_DOC + r\_ads\_DOC\_20\frac{S}{20})Lab\_DOC \quad 4.4.2$$

$$\frac{\partial Lab\_POC}{\partial t} = -(r\_LOC + r\_LOC\_20\frac{S}{20})Lab\_POC + (r\_ads\_DOC + r\_ads\_DOC\_20\frac{S}{20})Lab\_DOC \quad 4.4.3$$

Lab_POC, like other particulate tracers, is assigned a sinking rate w_POC.

This representation of labile organic carbon is similar to the formulation used for labile resin acids, and is based partly on the experiments conducted as part of Task 8. These experiments are discussed further under model calibration.

The model does not treat bacteria explicitly in the breakdown of any of its detrital components. Where organic matter is primarily internally generated, it is reasonable to treat bacteria implicitly, and assume that bacterial biomass is low, that the modelled remineralization represents the net respiration by bacteria, and that the nutrients required by bacteria are supplied by the organic detritus itself. However, the CES discharge imposes quite a large load of labile POC and DOC on the estuary, without a

corresponding nutrient load. This could lead to a significant demand by bacteria for nutrients (nitrogen and phosphorus).

To allow for this, we have assumed that some fraction of the labile organic carbon removed is not respired to consume oxygen and produce CO_2, but instead is converted to bacterial biomass. For simplicity, this bacterial biomass is assigned to the detrital pool (Lab_Det_Plank), where it decays at a specified rate.

Associated with this production of bacterial biomass, there is an associated demand for dissolved inorganic nitrogen (DIN) and dissolved inorganic phosphorus (DIP) at the stoichiometry of Lab_Det_Plank (Redfield). This production is also potentially constrained by the availability of DIN and DIP. We have therefore made the production of bacterial biomass depend on DIN and DIP through a simple Monod, law of the minimum formulation:

$$Bacterial\ \ Prodn = F\_bact.min\left(\frac{DIN}{(KN\_bact + DIN)}, \frac{DIP}{(KP\_bact + DIP)}\right) .(r\_LOC + r\_LOC\_20\frac{S}{20})(Lab\_DOC + Lab\_POC) \quad 4.4.4$$

The associated demand for DIN (NOx, NH_3) and DIP (PO_4) is accounted for in the model.

4.4.10 Aerobic vs Anaerobic Respiration

The large oxygen demand imposed by the organic carbon load from the CES (or from natural sources) can lead to oxygen depletion in bottom waters or in sediments. Very low dissolved oxygen levels have been observed in bottom waters, and sediment flux measurements conducted in the upper Derwent as part of the ERA indicated that a substantial fraction of sediment respiration may be anaerobic. The model has been modified to divide the total net oxygen demand into aerobic and anaerobic fractions as follows. The total respiratory oxygen demand, Resp (mg O m^{-3} d^{-1}), is calculated as the sum of all respiratory processes. The aerobic respiration (and corresponding real oxygen demand), is calculated as:

$$Aer\_Resp = Resp\frac{Oxygen}{(KO\_aer + Oxygen)} \quad 4.4.5$$

where Oxygen is the dissolved oxygen in the water column or porewater, and KO_aer is the "half-saturation constant" for aerobic bacteria. KO_aer has been set to 100 mg m^{-3}. Provided this value is small compared with oxygen saturation (around 8000 mg m^{-3}), its precise value has almost no effect, except to determine the predicted low oxygen value in "anoxic" waters. Once waters become anoxic, the aerobic respiration is effectively determined by the rate at which physical transport (exchange of pore waters or advection and mixing) can supply oxygen. Because oxygen turns over very rapidly under these conditions, setting KO_aer much smaller forces the model to use very small time steps, increasing computation times to unacceptable levels.

5 Calibration and Validation

5.1 The Hydrodynamic Model

The hydrodynamic model was calibrated against salinity distributions extracted from the CSIRO Coastal Zone Program data set. Two calibration scenarios were produced corresponding to low (45 m^3s^{-1}, 5 percentile) and high (90 m^3s^{-1}, 50 percentile) river discharge conditions under the influence of a neap and mean tide (0.6 m and 0.9 m variation) respectively. Coastal Zone calibration data for low and high flow conditions are summarised in Table 5.1.1. Vertical sections along the river of the salinity distributions for these flow regimes is presented in Figures 5.1.1 and 5.1.2 respectively.

Table 5.1.1 : Calibration Data

	Low Flow	High Flow
CZP survey	5	7
Date	23 – 25 March 1993	14 – 15 October 1993
River flow	52 m^3s^{-1}	96 m^3s^{-1}
Tidal Range	0.5 m	0.9 m

The model was forced with flow through the open boundaries and a surface wind stress for the calibration scenarios. Wind direction was chosen as the most frequent, i.e. a down-river (60^{o}T) direction (see Table 2.4.1). A velocity profile, corresponding to the river flow at New Norfolk, was imposed at the upstream open boundary such that the cross-sectional integral of the velocity was equivalent to the imposed flow rate of 45 or 90 m^3s^{-1}. Non zero velocities through this boundary were restricted to the surface layer bounded by the free surface (time dependent) and a fixed pycnocline depth.

The tidal elevation measured at Hobart was imposed at the Bridgewater boundary and a constant wind was specified over the entire domain. Discharge was also included from the CES source with a specified temperature and salinity. The model estuary was started from rest with a fresh salinity distribution (0 psu) and temperature of 16^{o}C throughout. The model was allowed to run until a steady state was achieved. Model parameters for the calibration simulations are summarised in Table 5.1.2. Note that the pycnocline depths quoted specify the surface layer thickness for boundary condition input only, the model calculates the actual position of the pycnocline within the domain.

An empirical relation for the distance of steady state salt wedge penetration in the absence of mixing can be given as (Keulegan, 1957);

$$L \sim 2.5H\left[\frac{\sqrt{g'H^3}}{\upsilon}\right]^{\frac{1}{4}}\left[\frac{\sqrt{g'h}}{2U}\right]^{\frac{5}{2}} \quad \text{(m)} \qquad 5.1.1$$

where $g' = g\Delta\rho/\rho$ is the reduced gravity, H is the water depth, h is the thickness of the salt wedge, υ is the molecular viscosity and U is the velocity of the ambient flow. The inclusion of tides generates vertical velocity shear at the bottom boundary

resulting in enhanced mixing. This mixing increases the exchange of salt across the salt wedge interface and decreases the density contrast between the salt wedge and overlying water. It is observed from eqn. 5.1.1 that if $\Delta\rho$ decreases then the salt propagation length, L, also decreases, i.e. the inclusion of tidal activity is expected to result in less salt wedge penetration into the estuary. Equation 5.1.1 also indicates that salt wedge penetration will decrease with decreasing water depth, increasing river flow and decreasing salt wedge thickness.

These dependencies were certainly encountered whilst calibrating the hydrodynamic model. Salt wedge penetration dramatically receded under the influence of tides. However, once a partially stratified estuary was established by including tidal activity, little additional effect on the salt wedge was observed by changing the tidal range between neap (0.6 m) and spring (1.2 m). Bearing in mind that the system is highly non-linear, this suggests that some other process must limit salt penetration under partially stratified conditions.

Table 5.1.2 : Model Calibration Parameters

Parameter	Value
Vertical grid resolution	0.4 m
Pycnocline depth at Bridgewater boundary	-2m
Pycnocline depth at New Norfolk boundary	-3m
Temperature at Bridgewater boundary	16 ^{o}C
Temperature at New Norfolk boundary	16 ^{o}C
Salinity at Bridewater (surface)	6 psu
Salinity at Bridgewater (bottom)	30 psu
Salinity at New Norfolk boundary	0 psu
CES flow rate	0.7 m^3s^{-1}
CES temperature	30 ^{o}C
CES salinity	0 psu
Horizontal diffusivity	0.75 m^2s^{-1}
Horizontal viscosity	1.5 m^2s^{-1}
Wind	5.0 ms^{-1} 60^{o}T

Due to the limitations involved in discretizing a shallow irregular bathymetry in the presence of strong stratification, it was found necessary to deepen the bathymetry in the main channel by 1m in order to achieve a satisfactory salinity distribution and circulation throughout the estuary. This action was further vindicated by the uncertainty that existed in the hydrographic sections upon which the bathymetry was derived.

Vertical sections along the river of model salinity output are displayed in Figures 5.1.3, 5.1.4 and 5.1.5 for low flow-neap tide, high flow-neap tide and high flow-spring tide respectively. It can be observed that in Figures 5.1.4 and 5.1.5 a variation in tidal range does not impact on the salinity distribution, hence either of these salinity distributions may be compared to CZP survey 7 for calibration purposes.

Comparison of the field data (Figure 5.1.1 and 5.2.2) with model results (Figures 5.1.3 to 5.1.5) reveals the model successfully captures salt wedge penetration under low and high flow conditions, indicating the baroclinic circulation is well represented.

Predicted surface salinities at the Bridgewater boundary are also in good agreement with the field data, indicating that surface mixing is also well represented. The salt wedge receded as the flow rate increased, indicating that the barotropic – baroclinic interaction is successfully reproduced in the model. This is also evident in the field data, where the high flow salinity distribution is only capable of propagating the 20 psu contour to within 2km of New Norfolk, as compared to 25 psu in the low flow case. The high flow field data show residual high salinity pools in the deeper holes along the river which are not evident in the model simulations. This is due to spinning the model up from rest to steady state under high flow and not allowing any recession of the salt wedge once established, and is an example of the caution which must be applied when comparing field data obtained under non-steady conditions to steady state model output. The model satisfactorily reproduces the main features of the salinity distributions under low and high flow conditions.

5.2 The Resin Acid Model

Most of the resin acid model parameters are subject to very considerable uncertainty, as the laboratory experiments in Task 8 reported by Grace and Liang (2000a) yielded results which were inconclusive or at odds with observed mass balances in the estuary. It appears that breakdown and adsorption associated with the mixing of resin acids into the estuary differ significantly from those in the laboratory experiments. We have therefore been forced to estimate the model parameters by calibrating the model against field observations.

Crude mass fluxes of principal resin acid components at U16/17 were calculated from data obtained from the ERA Sampling Program 1999-2000. These flux measurements were based on the CES flow rates and resin acid composition outlined in Table 5.2.1.

Table 5.2.1 : Composition of CES.

Effluent Flow ($MLday^{-1}$)	Date	Total Resin Acids (μg/L)	Filtered Abietanes %	Filtered Refractory RA's %	Particulate Abietane RA's %	Particulate Refractory RA's %
39.8	24-Jul-00	2590	4	8	52	36
61.5	5-Jun-00	2950	6	11	51	32
65.4	17-Apr-00	3770	7	19	42	32
71.3	8-Mar-00	3470	6	11	52	32
72.2	18-Jan-00	6040	44	34	13	9
61.1	14-Dec-99	8720	34	32	23	11

Fluxes were expressed as a percentage of CES discharge retained at the sampling location, taking into account upstream flow in the bottom layer, and are summarised in Table 5.2.2. The fraction of the net downstream flux retained at U16/17 for total resin acids, excluding the high flow event on 24 July, ranged from 13% to 62%, with maximum amount retained at high river flows. For filtered abietanes, the quantity retained ranged from 2% to 50% with an average of 21%. For the filtered refractory component, the amount retained ranged from 41% to 146%, and averaged to 104%. Particulate abietane retention ranged from 2% to 8%, and averaged to 5%. Particulate refractory ranged from 0 to 56%, and averaged to 20%.

Table 5.2.2 : %CES load present in net downstream flux at U16/17.

Date	River Flow (m^3s^{-1})	Total Resin Acids (%)	Total Abietanes (%)	Total Refractory RA's (%)	Total Filtered Resin Acids (%)	Filtered Abietanes (%)	Filtered Refractory RA's (%)	Particulate Abietane RA's (%)	Particulate Refractory RA's (%)
24-Jul	187.2	65	33	106	318	220	374	17	48
5-Jun	111.8	32	10	63	110	50	145	5	36
17-Apr	53.8	13	5	21	46	24	54	2	6
8-Mar	59.0	16	3	34	89	8	134	2	0
18-Jan	28.5	15	2	31	19	2	41	6	0
14-Dec	71.6	62	17	122	82	23	146	8	56
Average*		28	7	54	69	21	104	5	20

*Average ignores 24-Jul. The river flow is so high that concentrations are very low, and errors are large.

These results indicate there is a loss of about 80% of filtered abietanes, 95% of particulate abietanes, 80% of particulate refractory, and 0% of filtered refractory. This is consistent with about an 80% loss of particulates due to sinking, and a 80% loss of abietanes due to breakdown. The dissolved refractory component is basically conservative. Note that there is substantial variation in composition of CES (see Table 5.2.1). In Jan 00 and Dec 99, the resin acid concentration is almost double other sampling occasions, and the additional material is almost all filterable (< 0.45 μm). This results in a large increase in the percent retained resin acids at U16/17.

In addition to the regular ERA field surveys, a special field study was conducted in November 2000. As well as measuring resin acids with more spatial resolution around the outfall, sediment traps were deployed at three locations downstream from the outfall. Unfortunately, at the time of this study, river flow was high (about 140 cumecs), and the fresh surface layer was deep, so that it was not possible to compare the observations directly with model predictions from the calibration scenarios at 45 and 90 cumecs. However, we have used the sediment trap results to derive sinking rates for comparison with values obtained by model calibration.

In deriving sinking rates from the sediment trap results, we have assumed that the particulate resin acids sink slowly in the surface layer, but rapidly once they reach the salt wedge. This is discussed further below, but the assumption is unavoidable given the very low concentrations of resin acids observed in the bottom layer. We assume that it is the freshwater sinking rate which is rate-limiting, and have estimated this by dividing the sediment trap flux by the overlying concentration in the surface layer. This source concentration was computed using measured concentrations at the surface and at a mid-depth level, close to the pycnocline. As the sediment traps were located approximately midway between the north bank and mid-river samples, a mean of these samples was taken as the concentration in the water column above the traps. Results are displayed in Table 5.2.3. Calculated settling rates are in the range of 0.2 to 4.2 m d^{-1}. The labile fraction generally settles faster than the refractory component. Note that these calculations assume all particulate matter entering the sediment traps is fresh material. Further evidence (Des Richardson, pers. comm.) suggests that much of the material in the sediment traps may have been resuspended material, and therefore the supplied settling rates should be treated with caution. However, the actual settling rates used in the model were obtained by calibrating to field data, hence these calculations do not influence the numerical simulations.

Table 5.2.3 : Estimated Particulate Settling Rates

LABILE PARTICULATE					
Station	Dissolved (mgm^{-3})	Deposition ($mgm^{-2}day^{-1}$)	Measurement Depth (m)	Salinity	Settling ($mday^{-1}$)
T4	28.3	52.97	0.5	0.1	1.87
T6	29.4	16.3	0.5	0.1	0.55
T7	2.8	5.5	0.5	0.1	2.0
T4	12.7	52.97	2.0	0.3	4.2
T6	7.0	16.3	2.4	0.3	2.3
T7	1.5	5.5	2.5	0.3	3.7
REFRACTORY PARTICULATE					
T4	87.2	43.8	0.5	0.1	0.5
T6	59.2	12.1	0.5	0.1	0.2
T7	11.1	7.5	0.5	0.1	0.68
T4	25.0	43.8	2.0	0.3	1.8
T6	31.5	12.1	2.4	0.3	0.38
T7	11.1	7.5	2.5	0.3	0.86

Mean labile settling velocity ~ $4x10^{-5}$ ms^{-1} (mid depth)
Mean refractory settling velocity ~ $1.2x10^{-5}$ ms^{-1} (mid depth)

The field data suggest that approximately 70% of total resin acids disappear from the water column between the discharge and U16/17. The expected travel time in the surface layer to U16/17 is very short, hence this degree of loss cannot be accounted for using the laboratory-based breakdown or adsorption/settling rates introduced in section 4.2, which predict removal of only a few percent in a few hours. It seems unlikely that any breakdown process could remove a large proportion of the resin acids, especially the refractory fraction which constitutes about half the input, in such a short time. It appears that settling and aggregation must be much more effective in the estuary than the laboratory experiments suggest, prompting the use of higher settling rates than anticipated.

The resin acid model was calibrated against the ERA Sampling Program 1999-2000 using CES data when discharge rates from the CES outfall corresponded to low flow, neap tide conditions. Two sampling dates fall into the category, viz. 17/4/00 and 7/3/00. The CES resin acid composition and flow characteristics for these surveys are summarised in Table 5.2.4. The CES resin acid composition and flow rate used in the model calibration was taken as that of 17 April 2000.

The concentrations of the resin acid components produced by the model were compared with data measured during these surveys (surface and bottom) at transects U18, U16/17 and U12. These transects consisted of north, south and mid-river stations (U12 excepted). Although the CES composition and flow characteristics are similar for the surveys, a degree of variability exists in the concentrations measured at these downstream stations. For calibration purposes the component concentrations at U18, U16/17 and U12 were expressed as a percent of the CES concentration for each acid fraction so that a measure of the variability could be established when comparisons were made to the model output. This procedure effectively places an upper and lower bound on the model resin acid concentrations. Note that the limit of detection of the resin acid measurements is around 0.02% CES, hence not too much

emphasis should be placed on model – field comparisons around concentrations of this magnitude.

Table 5.2.4 : CES Composition Characteristics

	Survey 17 April 2000	Survey 7 March 2000
CES flow (m^3s^{-1})	0.76	0.83
River flow (m^3s^{-1})	53.8	59.0
Labile filtered (μgL^{-1})	271	210
Labile particulate (μgL^{-1})	1572	1788
Refractory filtered (μgL^{-1})	718	377
Refractory particulate (μgL^{-1})	1211	1093
Total labile (μgL^{-1})	1843	1998
Total refractory (μgL^{-1})	1929	1470
Total resin acids (μgL^{-1})	3772	3468

The resin acid model parameters producing the best fit to field observations are summarised in Table 5.2.5 and comparisons of predicted and observed relative concentrations are presented in Figures 5.2.1 to 5.2.5. Sensitivity analyses revealed that a total loss of 2 d^{-1} for the labile dissolved fraction yields the optimum comparison to field observations. This results in acceptable concentrations in the surface near field at U18, but over-prediction at U16/17 and under-prediction at the Bridewater boundary at U12. It is considered that this calibration minimises the errors encountered at U16/17 and U12 whilst maintaining good near field predictions. The calibratable parameters outlined in Section 4.2 produced acceptable refractory resin acid distributions. Settling velocities were required to be higher for both particulate fractions. Note that the formulation of eqns. 4.2.9 and 4.2.10 will produce two distributions of labile particulate resin acids; one with zero adsorption and another with a salinity independent adsorption of 2 d^{-1}. The calibration comparisons for the particulate component including adsorption are displayed in Figure 5.2.6 for all sampling locations. Note that the field observations correspond to the straight lines in the plots, with the symbols N, M and S corresponding to north bank, mid-river and south bank sampling locations respectively. The model output is characterized by the undulating plots.

Table 5.2.5 : Resin Acid Calibration Parameters

Variable	Value	Units
rB (refractory)	0	d^{-1}
rB (labile)	2	d^{-1}
r_UVB	2	d^{-1}
Kd_riv	10	m^{-1}
Kd_RES	1080	m^{-1}
r_ads_CL	0	d^{-1}
r_ads_20L	0	d^{-1}
r_ads_20R	0.06	d^{-1}
wP_L	21.6	$m.day^{-1}$
wP_R	10.8	$m.day^{-1}$
F_ads	0.1	-

5.3 The Biogeochemical / Ecological Model

The CSIRO model used here is relatively complex and has a large number of potentially variable parameters. However, as noted in Section 4.4, the model has already been calibrated for a variety of other estuarine and coastal systems, and our goal has been to find process descriptions and parameters which are robust and transferable, and minimise the number of "tuned" parameters. Nonetheless, there are new parameters associated with processes included specifically for the CES, particularly the decay and adsorption of labile organic carbon. Moreover, as with each new system, the Derwent brings some unique characteristics eg a surface layer with very low salinities.

The primary data used to calibrate the model are the water column chemical measurements collected by Tasks 2A and 5A. Additional data have come from physiological process studies (Task 7) and benthic flux measurements and laboratory experiments (Task 8). Here, we first describe the field data sets which were simulated in model calibration, and then describe the calibration process against these data sets, including comparisons with flux and rate measurements obtained in process studies.

5.3.1 Data Sets and Forcing for Model Calibration

Tasks 2A and 5A measured a standard suite of physical and chemical variables in surface and bottom waters at 6 positions along the channel (CS, U20, U18/19, U18, U16/17, U12) and in waters at 6 sites in the wetlands on 7 occasions during the ERA. (At locations just downstream of the CES discharge (U18 and U16/17), cross-channel transects were conducted. These have been averaged for comparison with the box model predictions.) Concentrations in the CES discharge were also measured.

Four of those surveys have been used for model calibration. These were chosen primarily because the river flows at the time of those surveys (Table 5.3.1) approximate the river flows used in the hydrodynamic model scenarios, from which exchanges have been computed for the box model. The surveys on 23 November 99 and 14 December 99 correspond to river flows of 107 and 70 cumecs, which straddle the median flow scenario of 90 cumecs. The surveys on 7 March 2000 and 17 April 2000 correspond to river flows of 59 and 54 cumecs, and these have been simulated using the 5%ile river flow scenario with 45 cumecs. The other surveys had river flows which were much lower (January) or much higher (June, July) than the scenario flows.

For each of the 4 chosen calibration sets, it was necessary to provide data to force the model. The key data sets are upstream boundary conditions, downstream boundary conditions, CES loads, and New Norfolk STP loads.

The upstream boundary condition prescribes the concentrations of model variables in the river entering the estuary at New Norfolk. These have been derived from surface measurements at the control site CS, and are given in Table 5.3.1. In a number of cases, the measured concentration represents the sum of several model pools, and must be allocated across these.

It is assumed that measured DOC in the river is entirely refractory, and measured POC is primarily refractory. TN, TP, and inorganic nutrients are measured, but TN and TP were not divided into dissolved and particulate fractions. After subtracting NH_3 and NOx from TN, we have assumed that most of the remainder is (refractory) DON, with a small fraction, about 15%, Ref_Det_N. The SPM is assigned to unflocculated sediment, as the river is fresh. Chlorophyll a values were converted to model nitrogen units, and split 70:30 between large and small phytoplankton. Chlorophyll a data were not available for November and December and values for January and February of 1 mg Chl a m^{-3} were used.

Table 5.3.1. Derwent River boundary conditions used in model simulations for calibration and scenarios.

Variable	Units	Nov-23	Dec-14	Nov_Dec Scenario	Mar-07	Apr-17	Mar_Apr Scenario
River Flow	$m^3 s^{-1}$	107	72		59	54	
TSS_unfloc	g m^{-3}	4	1	2.5	4	7	5.5
DOC	mg m^{-3}	2800	3100	2950	2700	2200	2450
Ref_Det_C	mg m^{-3}	1260	160	710	37	37	37
Ref_Det_N	mg m^{-3}	22	33	27	37	23	30
Ref_Det_P	mg m^{-3}	2	1	1.5	2	2	2
DON	mg m^{-3}	132	230	181	232	108	170
DOP	mg m^{-3}	10	4	7	0	7	4
PO_4	mg m^{-3}	3	1	2	2	2	2
PO_4_ads	mg m^{-3}	0	0	0	0	0	0
NH_3	mg m^{-3}	6	6	6	6	6	6
NOx	mg m^{-3}	22	20	21	3	11	7
Large Phyto	mg N m^{-3}	5	5	5	7	7	7
Small Phyto	mg N m^{-3}	2	2	2	4	4	4
Oxygen	mg m^{-3}	9400	8900	9150	11700	10000	10850

Table 5.3.2. Bridgewater bottom layer boundary conditions used in model simulations for calibration and scenarios.

Variable	Units	Nov-23	Dec-14	Nov_Dec Scenario	Mar-07	Apr-17	Mar_Apr Scenario
TSS_floc	g m^{-3}	45	5	25	22	74	48
DOC	mg m^{-3}	1400	1700	1550	2600	2000	2300
Ref_Det_C	mg m^{-3}	984	84	534	0	84	42
Ref_Det_N	mg m^{-3}	10	10	10	10	10	10
Ref_Det_P	mg m^{-3}	2	0	1	0	0	0
DON	mg m^{-3}	171	192	182	147	253	200
DOP	mg m^{-3}	21	0	10.5	0	0	0
Lab_Det_Plank	mg m^{-3}	10	10	10	10	10	10
PO_4	mg m^{-3}	4	5	4.5	14	23	18.5
PO_4_ads	mg m^{-3}	4	0	2	0	51	5
NH_3	mg m^{-3}	36	36	36	36	36	36
NOx	mg m^{-3}	4	8	6	28	22	25
Large Phyto	mg N m^{-3}	7	7	7	7	7	7
Small Phyto	mg N m^{-3}	3	3	3	3	3	3
Oxygen	mg m^{-3}	7000	7000	7000	4100	7000	5550

In the same way, bottom observations at U12B were used to fix the downstream boundary conditions at Bridgewater (Table 5.3.2). (As discussed in Section 4.4, only concentrations in the bottom layer must be prescribed at the downstream boundary.)

Similar comments apply about the allocation of observed pools to model variables. Because bottom water in the lower estuary is likely to contain some labile organic matter, a small constant amount of TN has been allocated to labile detritus.

There is a large variation in both measured TP and dissolved PO_4 in bottom waters at the downstream boundary. Under these circumstances, allocation of the non-PO_4 TP pool between organic P and adsorbed inorganic P is somewhat arbitrary. We have adopted the strategy of assigning an adsorbed inorganic P pool which is in equilibrium with the TSS and PO_4 pools according to the model's P-adsorption formulation.

Contamination of samples resulted in unusable NH_3 data on these ERA surveys, so the NH_3 values used have had to be based on other data. The upstream boundary condition is the median value from long-term monitoring over the period 95-99. However, this long-term monitoring program did not sample the bottom layer at Bridgewater. The bottom value represents the median of a number of samples collected in the bottom layer downstream in the estuary and analysed by MAFRI. Use of either value for specific calibration runs is of course suspect. In calibration runs, it has only been possible to compare the predicted NH_3 concentrations with observations based on long-term monitoring (in the surface layer) or limited MAFRI measurements in the bottom layer.

Table 5.3.3. CES loads used in calibration runs.

Variable	**Units**	**Nov-23**	**Dec-14**	**Mar-07**	**Apr-17**
Lab_DOC	mg s-1	104800	125100	194200	165700
Lab_POC	mg s-1	0	8000	1960	192300
DOC	mg s-1	33600	44700	50000	120000
Ref_Det_C	mg s-1	2570	0	3700	0
DON	mg s-1	0	0	1857	870
Lab_Det_Plank	mg s-1	626	950	722	1880
PO_4	mg s-1	42	2	111	85
NH_3	mg s-1	144	54	182	155
NOx	mg s-1	16	13	36	43
Colour-Kd	$m^2\ s^{-1}$	72	72	80	80

The CES loads used in the simulations are shown in Table 5.3.3. The measured variables were POC, DOC, TN, TP, PO_4 (FRP), NH_3 and NO_x. An attempt was made to use measured BOD to allocate the POC and DOC between labile and refractory fractions for each survey, but this was very noisy and probably unreliable on a survey by survey basis. Instead we have used a typical value of 25% refractory organic carbon (Des Richardson, pers comm), and most of this has been assigned to the DOC pool. The ratio of POC and DOC, and the TOC values, vary widely among these surveys, with the April measurement in particular characterised by very large TOC and POC levels. Observed non_PO4 P was assumed to be present as labile detritus, and this was then used to estimate levels of labile detrital N (Lab_Det_Plank), assuming Redfield ratios. The remaining organic N was assigned to DON.

Both NH_3 and TN may be over-estimated in these measurements by NH_3 sample contamination, although typical levels of contamination, about 50 mg m^{-3}, are generally small compared with TN levels of 800 mg m^{-3} or higher.

The loads from New Norfolk STP are based on estimated annual loads of TN and TP provided by Coughanowr (1997). More recent estimates of loads could not be obtained for the ERA. The plant was described in 1996 as carrying out secondary treatment, so these loads are assumed to consist primarily of dissolved inorganic N and P. In these runs, loads of PO_4, NH_3 and NOx are assigned values of 255, 786 and 152 mg s^{-1} respectively.

The model requires the specification of daily average surface irradiance. According to Kirk (1983), clear sky daily insolation at the latitude of Hobart should be about 20 MJ m^{-2} d^{-1} in Mar-Apr, and 40 MJ m^{-2} d^{-1} in Nov-Dec. Allowing for a reduction due to cloud cover by about 40%, actual daily insolation should be about 12 in Mar-Apr and 24 in Nov-Dec. These values represent an average daily surface irradiance of about 140 and 280 W m^{-2} respectively. The model converts these values to estimates of sub-surface PAR by multiplying by 0.43.

5.3.2 Calibration against POC, DOC, Oxygen

We started by calibrating the organic carbon components of the model against observations of POC, DOC and dissolved oxygen. Because they are dominated by CES and river loads of organic carbon, these components behave moderately (though not entirely) independently of the rest of the biogeochemical cycle.

Comparisons of predicted and observed values of POC, DOC and dissolved oxygen in surface and bottom waters in the channel and wetlands are given for November, December, March and April in Fig. 5.3.1 to 5.3.4. In all these plots, the two lines plotted represent minimum and maximum predicted values over a 24 hour tidal cycle: ie the range of model predictions. As noted above, there is considerable variation in the CES loads of organic carbon fractions among the 4 surveys, and also considerable variation in river concentrations of POC. These variations provide considerable contrast across the 4 calibration surveys, which helps considerably in constraining model parameters.

The variation in surface DOC in the channel is controlled predominantly by the input from the CES, its dilution in the river flow, and the total disappearance rate, r_LOC + r_ads_DOC. A total disappearance rate of 2 d^{-1} gives reasonably good agreement with observations downstream of the discharge in all months (Fig. 5.3.1-4 a). The predicted increase above river concentrations at U18, just downstream of the discharge, is satisfactory in all months. The data at U16/17 in March and April suggest an even larger disappearance rate, but this would give poorer agreement at U18, and in November.

These disappearance rates are much higher than those reported by Grace and Liang (2000a) in Task 8 laboratory experiments with CES samples. Their disappearance rates in freshwater were generally very low, with a half-life of around 20 days. As for resin acids (5.2), the half-life of organic carbon in the estuary seems to be much shorter than laboratory experiments show.

With a disappearance rate of 2 d^{-1}, most of the Lab_DOC has disappeared by Bridgewater (box 15), and the predicted DOC there is predominantly refractory DOC from the river and the CES. The adoption of a refractory DOC fraction equal to 25%

of TOC load, and the assumption that river DOC is entirely refractory, generally leads to good agreement with surface DOC observations downstream at U12 (Box 15), and in the wetlands. In simulations where the CES DOC load was assumed to be entirely labile, predicted DOC concentrations in the wetlands and at U12 were generally too low.

DOC observations in the bottom layer are relatively uniform throughout the estuary. In the model, only a little of the CES DOC mixes into the bottom layer, and so the DOC concentration there is fixed predominantly by the Bridgewater boundary condition.

Having fixed a total disappearance rate for Lab_DOC, the next step is to allocate this between adsorption and remineralization. This allocation obviously has a significant effect on the predicted POC concentrations, but these are also affected by the assumed sinking rate for POC. On the other hand, the oxygen sag in surface waters downstream of the discharge provides a good constraint on the breakdown rate r_LOC. A value of 0.5 d^{-1} for r_LOC provides reasonable agreement with observations in all months (Fig. 5.3.1-4 c). Higher rates definitely lead to under-prediction of oxygen downstream of the discharge.

With an adsorption rate r_ads_DOC of 1.5 d^{-1} (ie 2 d^{-1} - 0.5 d^{-1}), a high sinking rate of at least 20 m d^{-1} for Lab_POC is required to match the POC concentrations in surface and bottom waters (Fig. 5.3.1-4 b). The chief constraint here is in April, when the CES load of lab_POC is very high. However, in other months, the high adsorption rate for Lab_DOC does result in production of a substantial amount of Lab_POC in the surface layer, and a high loss rate through sinking is required to match the low observed surface POC.

While POC in surface layers is reproduced reasonably well, there is a tendency to over-predict POC in the bottom layer. It is possible that sinking rates of POC in saline bottom waters are even higher than 20 m d^{-1}. Grace and Liang (2000a) reported higher disappearance rates under dilute saline conditions, and one might expect increased flocculation at higher salinities. The box model does not currently allow variable sinking rates. However, at 20 m d^{-1}, the residence time in the bottom layer is still very short, of order 3 hours. Net long-estuary currents in the bottom layer are low, and so underprediction of the sinking rate in this layer is unlikely to affect the sedimentation pattern for POC significantly.

The model tends to underpredict POC in the wetlands, quite significantly in some cases. Some of the observed POC values in the wetlands are much higher than those in surface waters upstream. It is likely that these are due to local resuspension by wind and wave action in very shallow waters. There has been no attempt to collect data or calibrate a sediment resuspension / transport model as part of the ERA. This would be a major undertaking in itself. The box model currently uses a constant low background level of sediment resuspension everywhere, and so is unable to reproduce the (intermittent) high resuspension rates in the wetlands.

Bottom oxygen concentrations are obviously of concern to managers, and represent the greatest challenge for the model. The predicted concentrations are controlled by a number of factors. Because vertical mixing is very weak, bottom oxygen is supplied

primarily by transport upstream from Bridgewater, and so the boundary condition there plays an important role. The low observed oxygen concentrations at Bridgewater in March result in reduced oxygen concentrations throughout the estuary upstream. Bottom oxygen in the bottom layer is consumed both by breakdown of organic matter in bottom waters, and by breakdown of organic carbon in the sediments. While labile organic matter from the CES discharge makes the dominant contribution in the water column, refractory POC can accumulate in the sediment and make a substantial contribution over time to oxygen consumption there.

The model generally reproduces bottom oxygen values reasonably well in November and December. It underpredicts bottom oxygen in the vicinity of the discharge in March. It predicts maximum drawdown of oxygen, to the point of bottom water anoxia, at and just upstream of the CES discharge in April, associated with the very high CES organic load then. Unfortunately, oxygen data were not collected in the upper estuary on that survey.

It should be noted that bottom oxygen observations were taken from profiles at around 5 to 6 m, rather than in deep holes in the estuary. The box model does not resolve these deep holes. If it did, and mixing between these holes and the overlying water was restricted (as would be expected), it is likely that the model would commonly predict anoxia in these holes.

There are a number of potential sources of error in these calibration simulations.

- The model is using standard river flows which only roughly approximate the observed flows. Moreover, the "observed" flows represent 3-day averages prior to the surveys; real flows vary on a range of time scales from hours to weeks.
- The model is being forced with boundary conditions and loads based on "snapshot" observations from surveys. There is considerable variation in many variables among surveys even one month apart; we do not know the time scales on which these vary, or how representative these snapshots might be of the period leading up to the calibration survey.
- The observations do not discriminate between some variables which play different dynamic roles in the model: we must guess at an allocation of these pools across variables when fixing boundary conditions.

The issue of temporal variability is a key concern. In each simulation, the model is being run to long-term quasi-steady state over five years, with constant physical forcing, boundary conditions and loads. We can distinguish several time scales in the model behaviour. Variables such as Lab_POC, Lab_DOC and surface oxygen have very short time scales, and reach quasi-steady state on time scales of a few days. Variables such as refractory POC and DOC in the water column have very long breakdown times, but their distribution is consequently controlled predominantly by physical mixing and advection, and so reaches quasi-steady state on time scales of 10 to 20 days (less in surface waters). However, bottom oxygen concentrations respond partly to the build-up of refractory POC in bottom sediments. This can take several years to reach quasi-steady state.

We can conclude that it is reasonable to compare predicted and observed concentrations in surface waters for individual surveys, and may be reasonable to compare predicted and observed POC and DOC in bottom waters, but that we should

be cautious in comparing predicted and observed bottom oxygen for individual surveys.

It was unclear at the start of the modelling exercise whether it would be possible to explain current levels of oxygen drawdown in bottom waters based solely on current loads, given the extremely large historical loads of organic carbon prior to the early 1990s. There is no indication in the model calibration that oxygen demand in sediments and bottom waters is consistently underestimated. (See also the discussion of sediment respiration rates below.) It appears that organic carbon from the historical loads has either been flushed from the estuary, or is sufficiently refractory that it contributes relatively little to sediment oxygen demand.

5.3.3 Calibration against Nitrogen, Phosphorus and Chlororophyll

We next set out to calibrate the model against the various fractions of nitrogen, phosphorus and Chlorophyll a. Comparison plots for November, December, March and April are given in Fig. 5.3.5 to 5.3.8.

As described in Section 4.4, the biogeochemical and ecological representation of nitrogen and phosphorous cycling is complex, and contains a large number of parameters. There is insufficient data for the Upper Derwent to calibrate this model starting from "scratch". However, based on other studies, we believe that the "standard" set of model processes and parameters provides a realistic and robust representation of nitrogen, phosphorous and carbon cycling in coastal systems. We have started from this parameter set, and only made changes in a few cases where the observations provide compelling reasons to do so.

Initial simulations for the four surveys all led to over-prediction of chlorophyll at Bridgewater and in the wetlands. The model contains two phytoplankton components: small phyto-flagellates and large phytoplankton (diatoms). Based on observations in Task 7 (Roberts et al, 2001), most of the observed biomass in surface waters at New Norfolk was allocated to large phytoplankton. In initial runs, large phytoplankton biomass doubled downstream at Bridgewater, and small phytoplankton increased four-fold.

There were no measurements of chlorophyll during the November and December surveys, and so it's possible that phytoplankton biomass did in fact increase downstream in those months. However, observations in February, March and April, and later in July, showed chlorophyll levels in surface waters to remain relatively constant or decline as these waters travelled downstream.

In the standard model, small phytoplankton are strongly regulated by grazing control by zooflagellates. Zooplankton biomass was not measured in surveys, and grazing dilution experiments in Task 7 did not succeed. In the initial runs, zooflagellate biomass was assigned a low value at the New Norfolk boundary, and small phytoplankton escaped grazing control. When the boundary value for zooflagellate biomass was increased to levels in equilibrium with the small phytoplankton biomass, the latter remained relatively constant.

In the standard model, large phytoplankton are not grazing controlled, and large phytoplankton biomass is normally controlled by either nutrient or light limitation. Sinking losses can also be significant in shallow waters. In the standard model, these phytoplankton are considered capable of rapid bloom formation, and are assigned a high maximum growth rate of 2 d^{-1}. In the Derwent, this maximum growth rate was reduced to 1.25 d^{-1} (the same as small phytoplankton), and the sinking rate increased from 0.5 to 1 m d^{-1}. With these changes, large phytoplankton biomass also remained relatively constant through the estuary (Fig. 5.3.5-8 f).

PvsI experiments conducted in Task 7 (Roberts et al, 2001) measured light-saturated photosynthetic rates of about 3 to 6 mg C mg Chl a^{-1} h^{-1}. For the C:Chl a ratio of 50:1 assumed by the model, and a 12:12 light:dark cycle, these rates correspond to maximum growth rates of about 0.8 to 1.6 d^{-1}, similar to those adopted in the model. In the surface layer, about 2 m thick, with predicted values of Kd downstream of the CES discharge around 2 m^{-1}, the mean light intensity is saturating for phytoplankton growth in the model. This is consistent with Ik values measured in Task 7 PvsI experiments. Bio-assay experiments in February and May 2000 suggested the possibility of both N and P limitation, but predominantly N limitation. However, these are yield experiments, and do not necessarily indicate the degree of proximate in situ nutrient limitation of growth at the time of sample collection. Nutrient-induced fluorescence transient (NIFT) experiments conducted in Task 7 suggested N limitation of growth in situ (Roberts et al, 2001).

The model allows for both nitrogen and phosphorus limitation of growth. The uptake rate at low nutrient concentrations is calculated using a bio-physical formulation based on diffusion to the cell surface, which we believe to be robust, and have not modified. The actual degree of nutrient limitation predicted by the model depends on nutrient levels, which in turn depend on other source and loss terms. We go on to discuss calibration against inorganic nutrients before returning to the issue of controls on phytoplankton growth and biomass.

In November and December, NOx values in the river are quite high, around 20 mg m^{-3}, and most of this disappears by the time surface waters reach Bridgewater and the wetlands above Bridgewater. The initial runs reproduced this pattern quite well because phytoplankton consumed surface nutrients. When phytoplankton growth was reduced in accordance with observed Chl a, the model over-predicted surface nitrate downstream. We then considered the potential role of bacterial biomass in removing inorganic nutrients, as described in Section 4.4.

The parameter F_bact represents the maximum proportion of labile organic carbon consumed by bacteria which is converted to labile organic matter. One might think of this as the growth efficiency of bacteria on labile organic carbon. However, it is possible that bacterial biomass is turning over rapidly, on time scales of hours or days. The model treats bacteria implicitly, and does not "see" this rapid turnover. F_bact actually represents the proportion converted to labile organic matter (Lab_Det_plank) with a turnover time of 10 days. It is possible that this is substantially less than the physiological growth efficiency.

F_bact was tuned so as to best reproduce the reduction in nitrate along the channel. Somewhat surprisingly, the best agreement was obtained for F_bact = 0.4, which is

very close to the maximum growth efficiency for bacteria. With this value, the model appeared to over-predict the rate of decline in nitrate in April (when the CES load of organic carbon was very high), and underpredict the rate of decline in December, when NOx fell sharply from U18/19 above the discharge to U18 and U16/17 below the discharge (Fig. 5.3.5-8 b).

It is possible that other mechanisms not captured in the model are responsible for part or all of this decline in NOx downsteam. The model does predict significant biomass of macroalgae and microphytobenthos in the wetlands, and this does result in further drawdown of nutrients there (see below). However, without bacterial uptake, this is insufficient to reproduce the observed nitrate levels at Bridgewater. The December data provide the strongest evidence that this disappearance is associated with the CES discharge.

Ammonia and NOx are treated by the model as interchangeable sources of dissolved inorganic nitrogen for both bacteria and phytoplankton. As discussed above, calibration of the model against ammonia observations is problematic - we can only compare predictions with historical data and data from later in the ERA. In general, the agreement between predicted and observed NH_3 in the surface layer is remarkably good, although the model does tend to overpredict NH_3 in surface waters at U20 and U18/19, upstream of the CES (Fig. 5.3.5-8c). In the model, ammonia is elevated there due to the assumed substantial load of ammonia from the New Norfolk STP. However, there is little evidence of this in the observations.

The model underpredicts NOx in bottom waters in November and December, but does better in March. The model does not allow for nitrification in the water column, and it is possible that this is proceeding in bottom waters.

The model reproduces bottom NH_3 values quite well in November and December, but over-predicts bottom NH_3 in March and April (Fig. 5.3.5-8 c). In keeping with observations of high denitrification efficiencies in benthic chamber studies in Task 8, the maximum denitrification efficiency in the model was increased to 0.85. The model still uses a rather crude semi-empirical model of denitrification based on Port Phillip Bay data, and it is possible that this model underestimates denitrification efficiencies in March and April. However, this is a period of low flow and maximum oxygen depletion in bottom waters, which one might expect to reduce denitrification efficiencies.

It is also possible that the overprediction of bottom NH_3 in March and April is due to the time scale issues discussed above. Under low flow conditions, there is more time for particulate organic N to settle into bottom waters and then accumulate in sediments. When the model is run for 5 years at a river flow of 45 cumecs (which is only a 5%ile flow), it may well result in over-prediction of organic nitrogen accumulation and remineralization.

When it is forced by the loads and boundary conditions described above, the model overpredicts surface PO_4 and TP in surface waters in all surveys (Fig. 5.3.5-8 d,e). This is most pronounced in March, when the observed TP and PO_4 is extremely low throughout the surface layer. Part of this over-prediction arises from the input into the model of a substantial PO_4 load from the New Norfolk STP. As in the case of NH_3,

there is no evidence for this load in the observations at U20 and U18/19, where concentrations of both TP and PO_4 are similar to or less than those at the control site. For comparison, and because of the lack of recent data on the STP load, we have shown model predictions of TP and PO_4 with the New Norfolk load set to zero in Fig. 5.3.9. Agreement is improved, and in some cases, eg PO_4 in November and December, is quite good, but in general the model still tends to overpredict PO_4 and TP in surface waters.

The most likely explanation for this is that the model underestimates the removal of PO_4 by adsorption to particles. However, since the model also overestimates TP, this adsorbed fraction must be rapidly removed by settling. The model includes standard equilibrium P-adsorption dynamics. In these dynamics, the ratio of adsorbed PO_4 to dissolved PO_4 is given by P_ads_coeff.TSS, with the model parameter P_ads_coeff having units of $m^3\ kg^{-1}$. In the model, this has been given a value of 30, based on previous calibration of the model in Gippsland Lakes. This value is already much higher (ie leads to more P adsorption) than the standard value of 1 or 2 recommended for freshwaters (Grace and Liang, 2000b).

Phosphorus-partitioning experiments were conducted as part of Task 8. Those experiments showed extremely high apparent P-partitioning coefficients in river waters, of order 8000 (Grace and Liang, 2000b)! These extremely high values result because there is apparently strong partitioning to the particulate phase, despite the very low TSS levels observed in river waters. Grace and Liang note that the adoption of standard values for this coefficient in waters of widely different TSS concentrations may not be reasonable. They also note that the apparent large P-partitioning coefficients they measured could have been due to rapid uptake of added trace PO_4 by P-limited phytoplankton.

The model also over-predicts phosphate and TP in bottom waters in March and April, and TP in bottom waters in November (Fig. 5.3.5-8 d). In November and April, this is exaggerated by very high boundary values of TP and (in April) DIP in bottom waters at Bridgewater (U12). There is no evidence for these high values further upstream, and it seems possible that these elevated measured values are not appropriate boundary conditions for the upper estuary, perhaps because of local spatial and temporal variation at U12.

Model agreement with observations might be improved by increasing P_ads_coeff further. However, it is difficult to justify this without a better understanding of P partitioning in both surface and bottom waters. As Grace and Liang (2000b) point out, this would require a much larger study than was possible in the ERA.

5.3.4 Comparison of model predictions against other ERA field data

In addition to the survey data, the ERA has yielded a number of other observations which can be compared with model predictions. We consider here sediment respiration, and biomass of microphytobenthos, macroalgae and seagrass.

Predicted levels of (aerobic) sediment respiration under current median CES loads have been plotted for both low flow and median flow scenarios in Fig. 6.3.4. Predicted median aerobic sediment respiration rates range from 40 to 120 mmol $O_2\ m^-$

^{2} d^{-1} under median flow conditions (Fig. 6.3.4 a), and 10 to 80 mmol O_2 m^{-2} d^{-1} under low flow conditions (Fig. 6.3.4 b). The benthic chamber studies measured oxygen consumption rates of 50 to 100 mmol m^{-2} d^{-1}.

There are two opposing controls on sediment respiration rates in the model. Total respiration measured as mmol CO_2 m^{-2} d^{-1} depends on the accumulated organic carbon in the sediments. In the channel, this shows a maximum under and just upstream of the CES. Very high total respiration rates are also predicted on the wetlands, due to accumulation of organic matter from seagrass and macroalgae. As sediments become more oxygen-stressed, aerobic respiration is limited by the flux of oxygen to the sediment. Under low flow conditions in the channel, oxygen is depleted in bottom waters, sediments become strongly oxygen depleted, and an increasing proportion of total respiration becomes anaerobic. Benthic chamber studies in February also found that a substantial fraction (about half on average) of total respiration was anaerobic (Nicholson and Longmore, 2000). The model also predicts lower sediment respiration rates under low flow conditions on the wetlands, but this occurs because nutrients are more limiting, and predicted benthic primary production is lower.

The model predicts microphytobenthic (ie benthic microalgal) biomass of around 90 to 120 mg Chl a m^{-2} in the wetlands under median flow (Fig. 6.3.12 a), and higher values, up to 180 mg Chl a m^{-2}, under low flow (Fig. 6.3.12 b). Predicted values are higher in model cells adjacent to the channel (17, 19, 21, 22 and 23), and lower in cells at the back of the northern wetlands. This is due to increased nutrient limitation at the back of the wetlands. Observed microphytobenthic biomass in the wetlands in Task 7 ranged from 60 mg Chl a m^{-2} in dense seagrass beds, up to 800 mg Chl a m^{-2} on bare substrate near the channel (Roberts et al., 2001). The model is unable to reproduce these extremely high values, but does not have the spatial resolution (nor, most likely, sufficient process detail) to predict the detailed mosaic spatial structure of seagrass beds and bare substrate. Microphytobenthos biomass predicted by the model represents a broad average over large spatial cells. Roberts et al. (2001) do not report estimates of mean MPB biomass over the wetlands. Task 2B_5B estimated that about 30% of the wetlands are covered by sparse seagrass, and 70% by dense seagrass. This implies a mean MPB biomass in November of 290 mg Chl a m^{-2} in November, about twice model estimates. However, the MPB biomass observed in Task 7 in earlier surveys in February, May and July 2000 was much lower than in November 2000, and more consistent with model estimates (Roberts et al., 2001).

Under low flow conditions, the model predicts microphytobenthic biomass in the channel of around 20 to 30 mg Chl a m^{-2} (Fig. 6.3.12 b), which compares very favourably with measured values. However, under median flow, the model predicts higher biomass values, up to 120 mg Chl a m^{-2} (Fig. 6.3.12 a). Predicted biomass in the channel is limited by light availability: the higher predicted biomass under median flow occurs because the “colour” contributed by the CES is diluted more, reducing light attenuation.

The model predicts seagrass biomass in the wetlands ranging from 1200 to 3000 g wet wt m^{-2} under median flow (Fig. 6.3.14 a), and 800 to 2500 g wet wt m^{-2} under low flow (Fig. 6.3.14 b). The increased biomass under median flow appears to be due to greater nutrient accumulation in wetlands sediments. Peak biomass values reported by

Tasks 2B_5B were about 3000 g wet wt m^{-2} in dense cover, with an overall mean value of 2200 g wet wt m^{-2}. This is remarkably close to the predicted values, given that no tuning of seagrass parameters was undertaken.

The predicted macroalgal biomass in the wetlands is low, about 150 to 200 g wet wt m^{-2} under median flow (Fig. 6.3.13 a), and 100 to 150 g wet wt m^{-2} under low flow (Fig. 6.3.13 b). In the model, macroalgal biomass in the wetlands is nutrient limited, while macroalgae do not grow in the channel in the current load scenarios, due to light limitation. In the real estuary, scour may also prevent macroalgal growth in the channel, but this effect is not represented in the model.

Given the uncertainties and approximations involved in setting boundary conditions and loads, and the approximations involved in running simplified physical scenarios, the calibrated model matches observations from the ERA study surprisingly well. Reaching this level of agreement has required only limited adjustment of existing parameters. The observations have provided reasonable constraints on new parameters associated with the fate of labile organic carbon from the CES.

Key areas of remaining uncertainty are:

- the controls on phytoplankton biomass in the surface layer;
- the nutrient load from the New Norfolk STP;
- the processes (most likely adsorption - desorption and sedimentation) controlling phosphate and TP concentrations in both surface and bottom layers;
- bacterial uptake of DIN and DIP associated with remineralization of labile organic carbon from the CES.

We discuss these further below in analysing the results of the model scenarios.

6 Scenarios

6.1 The Hydrodynamic Model

6.1.1 Introduction

The scenarios were chosen from the twelve combinations of the following forcing variables:

- River Flow (Two Options) : 5-percentile and 50-percentile flows of 45 and 90 m^3s^{-1} were chosen as described in Section 2.1

- Tidal Elevation at the Bridgewater Boundary (Two Options): Synthesised tidal elevations were defined for neaps and springs, as described in Section 2.3.

- Wind (Three Options): Winds of speed 5 ms^{-1} were chosen for wind directions (towards) of 60° True (down-river), 240° True (up-river) and 330° True (across-river (N)), as described in Section 2.4. Computational constraints prohibited four wind scenarios from being attempted and we chose to simulate a north cross river wind only. From a mixing and transport perspective the choice of cross river direction would not greatly affect the solutions owing to the narrow width of the channel. The wetlands, however, may experience differences and it was decided that a north cross river wind may promote more channel-wetland exchange.

6.1.2 Results

Salinity distributions on an along-river cross-section for the neap tide/45 m^3s^{-1}, neap tide/90 m^3s^{-1} and the spring tide/90 m^3s^{-1} scenarios for a 5 m^3s^{-1} wind with direction 60^oT can be viewed in Figures 5.1.3, 5.1.4 and 5.1.5 respectively. The surface salinity distribution at maximum ebb and flood flow over the wetland area for the neap tide/ 45 m^3s^{-1} and spring tide/90 m^3s^{-1} with 5 m^3s^{-1} 60^oT wind is displayed in Figures 6.1.1 to 6.1.4. Only conditions of neap tide/45 m^3s^{-1} and spring tide/90 m^3s^{-1}, corresponding to the least and most energetic forcing scenarios, are presented. The along river cross-sectional and wetland surface salinity distributions for these scenarios with 5 m^3s^{-1} 240^oT and 330^oT winds are presented in Figures 6.1.5 to 6.1.16.

6.1.3 Salt Wedge Variability

The salinity distributions for all scenarios exhibit the salt wedge propagation sensitivity to river flow and insensitivity to tidal range discussed in Section 5.1. The difference in upstream distance of where the 2 and 25 psu salinity contours intersect the surface and bottom respectively is used as an indicator of the variability between scenarios. Table 6.1.1 displays these approximate differences (in km) between high and low flow conditions. The salt wedge appears most sensitive to changes in river flow when the wind is in a down-river direction (60^oT). Table 6.1.2 shows the differences in position of these salinity contours between neap and spring tide conditions, demonstrating that the imposed tidal range does not greatly affect the salinity distribution.

Table 6.1.1 : Difference in Salt Wedge Position (km) between Flows.

The distance given (in km) is the distance from the Bridgewater boundary of where the 2psu or 25 psu intersects the surface or bottom respectively for the 90ms^{-1} scenarios subtracted from the distances these isohalines intersect the surface/bottom for the 45ms^{-1} scenarios.

Wind (^{o}T)	Neap Tide		Spring Tide	
	2 psu	25 psu	2 psu	25 psu
60	4.5	3	4.5	3.5
240	>1.5	1	>1.5	1.5
330	>2	1.5	>2	2.5

'>' indicates the contour receded past the Bridgewater boundary

Table 6.1.2 : Difference in Salt Wedge Position (km) between Tides.

The distance given (in km) is the distance from the Bridgewater boundary of where the 2psu or 25 psu intersects the surface or bottom respectively for the spring tide scenarios subtracted from the distances these isohalines intersect the surface/bottom for the neap tide scenarios.

Wind (^{o}T)	45 m^{3}s^{-1}		90 m^{3}s^{-1}	
	2 psu	25 psu	2 psu	25 psu
60	0	1	0	1
240	0	0	0	0.5
330	0	1	0	0.5

Finally the difference in salt wedge position between up-river and down-river wind directions (this corresponds to the most extreme differences) is summarised in Table 6.1.3. These results demonstrate that the salinity distribution, and associated circulation, is very sensitive to wind direction. The wind generates water transport in the surface layer which must be compensated by a flow in the lower layer to preserve continuity. If the wind blows down-river (60^{o}T) then the compensating flow in the bottom boundary layer is up-river, i.e. salt wedge propagation is aided by this compensating flow. The converse is true for an up-river wind, resulting in reduced salt wedge propagation. Note that wind induced surface currents are approximately 1/30 wind speed, hence a 5ms^{-1} wind corresponds to an ~0.17 ms^{-1} current. The cross sectional area of the New Norfolk boundary is ~ 84 x 3m, hence a 45 m^{3}s^{-1} river flow corresponds to mean velocities of ~ 0.18 ms^{-1} in the surface layer. These velocities are of the approximate magnitude as the surface wind induced current, and it is therefore not surprising that wind has an impact on the system of the same order as the river flow rate.

Table 6.1.3 : Difference in Salt Wedge Position (km) between 60^{o}T & 240^{o}T

The distance given (in km) is the distance from the Bridgewater boundary of where the 2psu or 25 psu intersects the surface or bottom respectively for the 240^{o}T wind scenarios subtracted from the distances these isohalines intersect the surface/bottom for the 60^{o}T wind scenarios.

Tide	45 m^{3}s^{-1}		90 m^{3}s^{-1}	
	2 psu	25 psu	2 psu	25 psu
Neap	6	7	>2	4.5
Spring	5.5	6	>2	4

6.1.4 Upwelling

Elevated surface salinities are observed over a small area approximately 0.5 to 1 km up-river from the Bridgewater boundary during the flood tide. An anti-clockwise eddy is generated near this boundary on the flood tide, and may generate topographically induced vertical flow resulting in upwelling of the deeper saline water to the surface. The magnitude of the eddy and location and strength of the upwelling vary with tidal amplitude, river flow and wind direction. The maximum salinity in this area may be used as an indicator for upwelling strength; maximum surface salinities for all scenarios are displayed in Table 6.1.4.

Table 6.1.4 : Maximum Surface Salinity at Bridgewater

Wind (^oT)	45 m^3s^{-1}		90 m^3s^{-1}	
	Neap	Spring	Neap	Spring
60	5.91	8.33	3.48	4.40
240	7.65	8.83	2.83	4.40
330	4.58	7.83	2.11	3.66

The largest salinities occur when the tidal pressure gradient is least opposed by the river head, i.e. the spring tide with 45 m^3s^{-1} flow. Furthermore, when the wind assists the flood tide (direction of 240 ^oT), maximum flow through the Bridgewater boundary is achieved and surface salinity attains the maximum across all scenarios. Conversely, when the tide is weak and river flow strong (neap tide with 90 m^3s^{-1} flow), the flood eddy is also weak leading to reduced upwelling and lower surface salinities. The upwelled salty water is generally advected counterclockwise in the eddy (e.g. Figures 6.1.2, 6.1.4, 6.1.7, 6.1.10 and 6.1.13) and the whole system relocates south-westwards to the wetland area south of the channel and on to the Bridgewater boundary as the tide turns. This upwelling event is also responsible for elevated salinities, in varying degrees, over the wetlands during the flood tide. Note that if a tracer is confined to the surface layer (e.g. resin acids) then this phenomenon acts to lower the tracer concentration in the surface layer on the flood tide by direct advection of low concentration tracer from the bottom.

6.2 The Resin Acid Model

6.2.1 Introduction

The resin acid loads in the CES discharge used in the scenario simulations differ from those in the calibration scenarios due to changes in mill and effluent treatment processes which resulted in a modified resin acid composition. Alum was previously used to remove resin acids from effluent resulting in the particulate fraction dominating the composition. As from September 2000 the mineral bentonite was used to adsorb resin acids from the effluent, thus removing particulate fraction and leaving the dissolved fraction dominant. The composition of resin acids in the CES for the scenario simulations is based on the 95 percentile concentrations measured in the CES since the process changes and is summarised in Table 6.2.1 (Des Richardson, pers. comm.);

Table 6.2.1 : Resin Acid Scenario CES Loads

Flow (m^3s^{-1})	Labile filtered (μgL^{-1})	Labile particulate (μgL^{-1})	Refractory filtered (μgL^{-1})	Refractory particulate (μgL^{-1})
0.65	1550	300	1550	300

6.2.2 Resin Acid Statistics

Statistics in the form of 5, 50 and 95 percentiles and maximum values (expressed as a percent of the CES load, % CES) are presented for eight model variables listed in Table 6.2.2 for a combined scenario situation. The combined scenario was obtained by assigning weights to each modelled scenario representing the frequency of occurence, and the contribution to the cumulative frequency from the individual scenarios was calculated using these scenario weights. If y_{ij} represents the value (% CES) of scenario i taken at time/cell location j, then these values and the corresponding scenario weights are first sorted in ascending order, e.g. $y_{ij}(k)$, k=1,N where N is the total number of obervations. The cumulative frequency up to the value $y_{ij}(k)$ is given by:

$$p(k) = \frac{\sum_{l=1}^{k} sw(l)}{\sum_{l=1}^{N} sw(l)} \qquad 6.2.1$$

where sw is the scenario weight. Hence to obtain the n^{th} percentile, first k is found such that p(k)=n then $y_{ij}(k)$ is equal to the percentile. The scenario weights are obtained by multiplying the frequency of tidal, river flow and wind variations, where:

1. tide : neap = 50%, spring = 50%
2. flow : 45 m^3s^{-1} = 10%, 90 m^3s^{-1} = 90%
3. wind : downstream (60°T) = 58%, cross-stream (330°T) = 32% , upstream (240°T) = 10%

In assigning these weights, we are forced to represent the full range of each forcing parameter by two or three values. Thus, we have treated the neap and spring tides as each representative of half the set of possible tides, and the 5%ile and 50%ile river flows as representing respectively the 0 to 10%ile, and > 10%ile ranges of river flows. The three wind scenarios were assigned weights according to the relative frequency for the respective wind quadrants; the weight assigned to the cross-stream wind scenario was taken as the sum of the frequencies of both north and south cross-stream quadrants (see Table 2.4.1).

Table 6.2.2 : Model Output Variables

Model Variable	Code	Units
Refractory dissolved resin acids	RDRA	% CES
Refractory particulate resin acids	RPRA	% CES
Labile dissolved resin acids	LDRA	% CES
Labile particulate resin acids (LDRA decay)	LPRA	% CES
Labile particulate resin acids (LDRA adsorption)	LPRA_A	% CES
Total resin acids (LDRA decay)	TOTAL	% CES
Total resin acids (LDRA adsorption)	TOTAL_A	% CES
Conservative CES tracer	CES TRACER	% CES

The model domain was subdivided vertically into 4 depth intervals of 1.2m and then from 4.8m to the bottom, and horizontally into the spatial discretization used in the box model (see Figure 4.3.1). Statistics for each variable in the combined scenario are presented for these sub-regions in Tables 6.2.13 to 6.2.20 and Figures 6.2.1 to 6.2.8. Surface plots (Figure 6.2.9) and vertical sections (Figures 6.2.11 to 6.2.14) through the mixing zone are also presented for total resin acids. The locations of the vertical sections are taken as the CES outfall, midway between the CES and U18, U18 and midway between U18 and U16/17 (Figure 6.2.10).

For comparison purposes surface and section plots of total resin acids for a typical scenario (neap tide/90 m^3s^{-1} with 240^{o}T wind) and an extreme scenario (spring tide/45 m^3s^{-1} with 240^{o}T wind) are included as Figures 6.2.15 to 6.2.24. The typical and extreme cases were chosen by obtaining the order statistics of the 95 percentile total resin acid concentration aggregated over the sub-region containing the CES (box 4) for each individual scenario, and then selecting the scenarios corresponding to the sample median and maximum. The extreme scenario is therefore one that promotes pooling of the CES (see section 6.2.3. below). The typical scenario is similar to the combined scenario but shows less cross-stream structure away from the CES source for the lower percentiles. The extreme scenario shows larger %CES concentrations throughout the mixing zone, however the median distribution is comparable to the 95 percentile distribution of the combined scenario.

Surface and sections of total resin acids with adsorption losses (TOTAL_A) for the combined scenarios are included as Figures 6.2.25 to 6.2.29. There exists considerable variability in the cross-stream structure of the resin acids in the mixing zone over a tidal cycle (e.g. Figure 6.2.30 (b) and (i)), with relatively uniform concentrations encountered on the flood tide and a strong cross-river gradient on the ebb. This variability is manifested in the 95 percentile and maximum plots in the form of suppressed cross-river structure.

6.2.3 Temporal and Spatial Variability

An analysis of the temporal distribution of the resin acids reveals that the resin acids pool around the effluent source on the flood tide and propagate down-river on the ebb

as a distinct pulse of high concentration (e.g. Figures 6.2.30 (a-l)). This results in a periodic trend in the concentration at any point downstream of the CES, with a lag in the time that maximum and minimum concentrations are observed between locations. Throughout the overall mixing zone, minimum concentrations are generally observed at the time of strongest ebb flow (~1200 hours) and maximum concentrations encountered around times of strongest flood flow (~0600 and 1800 hours). The maximum flood flow corresponds to the minimum current velocities in the mixing zone, as the tidal wave must overcome the barotropic gradient from the river discharge. These minimum currents lead to the least dilution of resin acids and hence maximum concentrations, and *vice versa* for the strongest ebb currents.

Table 6.2.4 shows the maximum % concentrations at U16/17 over a tidal cycle for each scenario. (Note; the number of significant figures these data are presented with is not intended to reflect the accuracy of the model, rather to allow unambiguous comparisons of results across scenarios.) It is observed that the maximum % CES concentration increases as the wind tends from down-river to up-river. Also, the spring tide scenarios exhibit greater concentrations than the neap tide for the same wind and flow, and low flow scenario concentrations are greater than high flows for the same wind and tidal range. These trends are related to how the physical forces driving the hydrodynamics (e.g. wind, tide and river flow) combine/oppose to determine the velocity at the time of strongest flood flow. For example, when a large tide and wind combine to oppose a small river flow (i.e. spring tide/45 m^3s^{-1}, 240^{o}T) the velocity at the CES on the flood is expected to be minimum leading to maximum pooling effect and % CES concentrations. Conversely, when the strongly flowing river and wind combine to oppose a small tide (neap tide/90 m^3s^{-1}, 60^{o}T), velocities at the CES are maximum and the pooling effect is expected to be smallest. These expectations can be verified in Table 6.2.4. Note that considerable variability exists in the concentrations in Table 6.2.4, with a three-fold difference between largest (3.492%) and smallest (1.057%) concentrations. The maximum surface RDRA concentration at U12 correlates with that at U16/17, with the largest concentration of 1.417% occurring in the spring tide/45 m^3s^{-1}, 240^{o}T scenario and smallest concentration of 0.661% in the neap/90 m^3s^{-1}, 60^{o}T scenario (Table 6.2.5).

Table 6.2.4 : Maximum RDRA % CES Concentrations at U16/17

Wind (^{o}T)	45 m^3s^{-1}		90 m^3s^{-1}	
	Neap	Spring	Neap	Spring
60	1.833	2.178	1.057	1.276
330	2.270	2.659	1.171	1.439
240	2.824	3.492	1.617	1.952

Table 6.2.5 : Maximum RDRA % CES Concentrations at U12

Wind (^{o}T)	45 m^3s^{-1}		90 m^3s^{-1}	
	Neap	Spring	Neap	Spring
60	1.099	1.150	0.661	0.639
330	1.354	1.355	0.752	0.757
240	1.401	1.417	0.845	0.966

The labile dissolved fraction exhibits a much reduced pooling effect, which is further attenuated closer to the Bridgewater boundary. In this case the non-conservative

losses (decay and adsorption) decrease the concentration by ~86% per day whereas the pulse is advected to the Bridgewater boundary within at least 21 hours of its formation (Table 6.2.6). Therefore the pooling effect must compete with the non-conservative losses, such that the fastest moving pulse combined with the greatest pooling concentration result in the largest concentrations at U12. This corresponds to the spring tide/45 m^3s^{-1}, 60°T scenario (0.129%, Table 6.2.7) with the smallest maximum % concentration of 0.022% occurring in the neap tide/45 m^3s^{-1}, 240°T scenario. Again there exists considerable variability in the maximum concentration, with the additional decay and adsorption losses contributing towards a six-fold difference between largest and smallest concentrations at U12. A direct correlation no longer exists between concentrations at U16/17 (Table 6.2.8) and U12 due to the extra losses of the labile component, i.e. the further a water parcel becomes from the source (the longer it remains in the river), the greater the impact of the non-conservative losses.

Table 6.2.6 : Travel Time of the Pulse to Bridgewater (hours)

Wind (°T)	45 m^3s^{-1}		90 m^3s^{-1}	
	Neap	Spring	Neap	Spring
60	22	23	21	21
240	44	42	23	22
330	34	34	23	21

Table 6.2.7 : Maximum LDRA % CES Concentrations at U12

Wind (°T)	45 m^3s^{-1}		90 m^3s^{-1}	
	Neap	Spring	Neap	Spring
60	0.087	0.129	0.099	0.121
240	0.022	0.034	0.061	0.089
330	0.056	0.070	0.094	0.106

Table 6.2.8 : Maximum LDRA % CES Concentrations at U16/17

Wind (°T)	45 m^3s^{-1}		90 m^3s^{-1}	
	Neap	Spring	Neap	Spring
60	0.967	1.061	0.624	0.727
240	0.697	0.966	0.770	0.806
330	0.977	0.981	0.630	0.730

The particulate resin acid fractions possess larger bottom concentrations than the dissolved fractions in the channel as a direct result of settling. Concentration generally decreases in the bottom layer with distance from the CES source. The dissolved fractions are predominantly confined to the surface layer in the main channel, due to the large density gradient through the pycnocline retarding mixing between surface and bottom waters. Near the Bridgewater boundary larger concentrations are observed in the bottom layer relative to the surface layer (i.e. the vertical distribution is more uniform) as a result of the large velocities and vertical velocity shear at the boundary leading to enhancing mixing in this region. Table 6.2.9 shows the bottom RDRA concentrations expressed as a percentage of the surface concentrations for stations U12, U16/17 and U18, from which it is observed that bottom concentrations in the channel at U18 and U16/17 are generally less than 4% of the surface concentrations whereas at Bridgewater (U12) concentrations can be as high as 38%. The resin acids mixed into the bottom layer are advected up-river within the salt wedge.

Table 6.2.9 : Bottom RDRA Concentration as a % CES of Top Concentration

Scenario	U12	U16/17	U18
Neap/45 60°T	22.1	3.9	3.5
Neap/45 240°T	16.9	1.1	0.7
Neap/45 330°T	17.9	2.7	2.2
Neap/90 60°T	23.2	3.3	2.6
Neap/90 240°T	7.8	0.6	0.4
Neap/90 330°T	16.6	2.8	2.4
Spring/45 60°T	36.1	4.3	3.6
Spring/45 240°T	16.7	1.4	0.9
Spring/45 330°T	26.7	3.1	2.3
Spring/90 60°T	38.1	3.6	2.7
Spring/90 240°T	11.0	1.2	0.7
Spring/90 330°T	29.1	3.2	2.7

6.2.4 Sedimentation Rates

Sedimentation rates for the RPRA, LPRA and LPRA_A particulate fractions are displayed in Figures 6.2.31, 6.2.32 and 6.2.33 for all scenarios. Considerable variability exists between the fractions and between scenarios. Generally the LPRA_A fraction has maximum deposition rates over the wetland area while the refractory fraction has maximum rates in the channel. The LPRA fraction consistently records maximum rates near the outfall, with very little deposition elsewhere. The LPRA_A component is consistently higher than the refractory by virtue of its larger settling rate combined with the increased concentration received through adsorption. The refractory component generally has maximum deposition upstream from the effluent source for down-river wind directions but near the Bridgewater boundary for up-river winds, particularly for the low flow scenarios. This is probably due to net transport of a greater proportion of particulate matter upstream as a result of larger upstream flow in the bottom layer under down-river winds (see Section 6.1.3). Maximum deposition rates for the particulate fractions are displayed in Tables 6.2.10 to 6.2.12. The refractory deposition rate is largest for down-river wind directions, with a maximum of 6.55 $mgm^{-2}day^{-1}$ for the spring tide, 45 m^3s^{-1} flow scenario. In this instance these rates occur upstream from the CES. The LPRA_A fraction records the largest deposition rate for labile resin acids over the wetlands with 10.45 $mgm^{-2}day^{-1}$ in the spring tide, 90 m^3s^{-1} cross-river wind scenario.

Table 6.2.10 : Maximum Deposition Rates, RPRA ($mgm^{-2}day^{-1}$)

Wind (°T)	45 m^3s^{-1}		90 m^3s^{-1}	
	Neap	Spring	Neap	Spring
60	5.68	6.55	2.09	2.54
240	4.21	4.66	0.61	0.88
330	3.51	4.44	1.31	1.61

Table 6.2.11 : Maximum Deposition Rates, LPRA ($mgm^{-2}day^{-1}$)

Wind (°T)	45 m^3s^{-1}		90 m^3s^{-1}	
	Neap	Spring	Neap	Spring
60	3.5	3.61	4.51	4.35
240	4.09	3.58	3.85	3.88
330	3.61	3.60	4.10	3.98

Table 6.2.12 : Maximum Deposition Rates, LPRA_A ($mgm^{-2}day^{-1}$)

Wind (^oT)	45 m^3s^{-1}		90 m^3s^{-1}	
	Neap	Spring	Neap	Spring
60	9.98	9.91	10.21	10.23
240	9.91	10.00	10.16	10.27
330	10.07	10.12	10.30	10.45

6.3 Biogeochemical / Ecological Model Scenarios.

6.3.1 Scenario Formulation

A key goal of the modelling study was to use the model to help assess the impact of the current CES on the estuary, and to assess the potential impact of future loads under a proposed secondary treatment regime. To meet this requirement, three CES load scenarios have been simulated: current (median) CES loads, zero CES loads, and secondary-treated (median) CES loads. The current and secondary-treatment CES loads are given in Table 6.3.1. Both are based on an assumed median flow of 56 ML d^{-1}.

Table 6.3.1. CES loads used in scenarios.

Variable	**Units**	**Current**	**Secondary Treatment**
Lab_DOC	mg s-1	105950	26488
Lab_POC	mg s-1	44200	11050
DOC	mg s-1	50050	12513
Ref_Det_C	mg s-1	0	0
DON	mg s-1	744	187
Lab_Det_Plank	mg s-1	1063	561
PO_4	mg s-1	29	33
adsorbed PO_4	mg s-1	0	472
NH_3	mg s-1	49	33
NOx	mg s-1	24	130
Colour-Kd	m^2 s^{-1}	65	65

The current values are based on median concentrations measured in the ERA. The assumptions discussed earlier have been used to allocate POC and DOC between refractory and labile fractions, and to allocate TP and TN to various inorganic and organic fractions. A median concentration of 75 mg m^{-3} for NH_3 has been used based on long-term monitoring prior to the ERA, because of contamination of samples during the ERA.

Loads under secondary treatment are based on results from trials held in the early 90s. It is assumed that secondary treatment would result in a 75% reduction in TOC. This has been applied equally to all fractions. The TN and TP loads have been allocated differently in the secondary treatment scenario. Under the current scenario, it was assumed that the non-PO_4 P was labile organic matter (Lab_Det_Plank), and that the organic N not accounted for by Lab_Det_Plank was DON. In the secondary treatment scenario, we assume that much of the organic matter has been broken down. We assume that 25% of the organic N is DON, and the remainder is Lab_Det__Plank N.

However, the TP load is much larger than can be accounted for by organic matter at close to Redfield ratios, and we assume that this excess P is adsorbed inorganic P.

The secondary-treated CES is obviously characterised by lower organic carbon loads. However, the TN load is substantially lower under secondary treatment. The NOx load is increased substantially in relative terms, but is still low in absolute terms. There is a large increase in TP load, which is assumed here to consist primarily of adsorbed inorganic P.

These three load scenarios have been run under the 12 physical scenarios described in section 6.1: 5%ile and 50%ile river flows, neap and spring tides, and three wind directions. The 5%ile river flow scenarios were run with New Norfolk and Bridgewater boundary conditions derived from ERA observations in Nov-Dec, and the 50%ile river flow scenarios with boundary conditions derived from ERA observations in Mar-Apr. These boundary conditions are given in Tables 5.3.1 and 5.3.2. This strategy was adopted partly because the model was calibrated against observations in these months, and partly because it allows some assessment of the impact of changes in CES loads against different chemical as well as physical forcing.

The 1996 New Norfolk STP loads were used in all scenario simulations.

6.3.2 Scenario Results

Summaries of model predictions under the three load scenarios are presented in Fig. 6.3.1 -14 for median (a) and 5%ile (b) river flows. Predictions are presented for DOC, POC, Oxygen, sediment respiration, TN, NOx, NH_3, TP, PO_4, SPM, Chl a, Microphytobenthos (MPB), Macroalgae and Seagrass. Tables 6.3.2 to 6.3.86 show these data for each variable and scenario in every box.

For each river flow, simulations were carried out under 6 physical scenarios (2 tide conditions times 3 wind directions). In each simulation, predicted concentrations in each cell were recorded at hourly intervals over a 24 h tidal cycle, after a 5 year "spin-up". We have combined results for these 6 tide-wind combinations in a manner similar to that described for resin acids in section 6.2. A combined cumulative frequency histogram of all 144 concentrations (6 scenarios times 24 hourly predictions for each scenario) concentrations was developed, with the frequency of individual observations from each physical scenario weighted by the scenario's relative likelihood of occurrence. The 5%ile, 50%ile and 95%ile values were then extracted from these combined cumulative histograms.

The relative weights used for tide and wind directions were the same as those used for resin acids in section 6.2: 50% each for neap and spring tide, and downstream wind 58%, cross-stream wind 32% , upstream wind 10%. The method differs from that used for resin acids, in that the two sets of scenarios corresponding to 5%ile and 50%ile river flow are dealt with separately. We chose to do this because the different river flow scenarios also correspond to different river loads and marine boundary conditions as well as different physical forcing, and may also be interpreted as representing different seasonal responses.

In Fig. 6.3.1-14, the median values are plotted with symbols and solid lines, while the 5%ile and 95%ile values are plotted as dashed lines.

The dominant effect of CES loads on DOC occurs in the surface layer, where predicted concentrations below the discharge decrease as one would expect with decreasing CES load (Fig. 6.3.1 a, b). Note however, that background DOC concentrations in the river are quite high. The increase above background in surface DOC predicted under secondary treatment represents only about 10% of river concentrations under median flow, and 20% under 5%ile flow. Relative impacts on DOC concentrations in the bottom layer are much smaller, about 5% under current loads, and 2% under secondary treatment.

Similar comments apply to POC. Under median flow conditions, the CES POC contributes about 50% of the POC in surface and bottom waters immediately downstream of the discharge under current conditions, and this reduces to about 20% under secondary treatment (Fig. 6.3.2 a). However, under low flow conditions, background river POC is much lower, and CES - derived POC dominates in both surface and bottom waters (Fig. 6.3.2 b). In surface waters, the CES signal diminishes downstream towards the wetlands, due to rapid sinking of CES-derived Lab_POC.

Within the wetlands, POC is higher in cells adjacent to the channel (17, 19, 21), and lower in cells at the back of the wetlands (18, 20, 22). This contrast is more evident in the upstream cells (17, 18, 19, 20). Under 5%ile flows, POC is higher in cell 17 under zero CES load than under current loads, due to increased local benthic production (see below).

The oxygen sag in surface waters downstream of the CES discharge is reduced as one would expect under secondary treatment and zero CES, but this sag is rather small in any case (maximum of about 600 mg O m^{-3}) (Fig. 6.3.3 a,b). The oxygen drawdown in bottom waters is much more significant. Note however that under median flow conditions, there is substantial drawdown in bottom oxygen even under zero CES loads, due to the long-term accumulation of riverine POC in sediments. In fact, it can be said that riverine carbon dominates over CES carbon as a cause of oxygen drawdown in bottom waters under median flow conditions (Fig. 6.3.3 a). This is due primarily to the large riverine load of Ref_Det_C in the median flow scenario, which is based in turn on the high POC concentrations observed in November 1999, at a river flow of 107 $m^3 s^{-1}$.

In the low flow scenario (Fig. 6.3.3 b), oxygen drawdown is very substantial, and dominated by CES loads. River loads of POC (based on observations in March and April of 2000) are very low (Table 5.3.2). Note that the oxygen drawdown does not scale linearly with CES load, and is almost as great under secondary treatment as under current loads. This occurs because oxygen consumption in the sediment is limited by oxygen supply. As bottom water oxygen levels are depleted, an increasing proportion of organic carbon breakdown in sediments is supported by anaerobic activity.

These effects on sediment oxygen consumption are shown in Fig. 6.3.4 a,b. Under median flow, where sediment carbon is primarily derived from riverine sources, benthic oxygen consumption actually increases in the channel bottom upstream when

CES loads are reduced, because oxygen availability increases (Fig. 6.3.4 a). Under 5%ile flow, where CES is the dominant source of carbon, benthic oxygen consumption is actually higher upstream under secondary treatment than under current loads (Fig. 6.3.4 b), for the same reason.

The results in Fig 6.3.3 b should be treated with some caution. If the river is as important a source of refractory POC as Fig. 6.3.2 a suggests, then this material will accumulate in sediments under periods of median or higher flow, and drive sediment respiration even under periods of low flow. Oxygen consumption and drawdown under low flow with zero CES loads is therefore likely to be much greater than suggested in Fig. 6.3.3 b and Fig. 6.3.4 b.

TN behaves quite similarly under median and low flow (Fig. 6.3.5 a, b), and shows relatively small and consistent effects of CES discharge. TN is dominated by high concentrations of DON in river inputs. The current CES discharge boosts these by about 10% under median flow, and by about 15% under 5%ile flow. The effect is diminished under secondary treatment (TN loads are almost halved under secondary treatment - Table 6.3.1). Effects of CES on TN in the wetlands are small, and the pattern is again dominated by low values in cells at the back of the wetlands.

The nitrate (NOx) results (Fig. 6.3.6 a,b) show an interesting interaction between carbon and nitrogen loads. Predicted NOx values in surface and bottom waters are lowest under current CES loads, because of the bacterial uptake of DIN in the model associated with the high labile organic carbon load (discussed in section 5.3). Under secondary treatment, CES NOx loads are increased and labile organic carbon loads reduced by 75%. The reduced bacterial uptake almost accounts for the increased NOx input, so that predicted NOx concentrations in surface waters downstream of the discharge are similar under zero CES and secondary treatment loads, and substantially higher than those predicted under current loads.

The NOx load from the CES is relatively minor compared with the river load, even under secondary treatment, and NOx concentrations in surface waters are dominated by river concentrations. River concentrations of NOx are higher under median flow (Nov-Dec) than low flow (Mar-Apr) conditions, and this is reflected in NOx concentrations in surface waters throughout the estuary. In particular, NOx is much lower in wetlands under the 5%ile flow for all CES loads. Predicted NOx concentrations in bottom waters are dominated by the Bridgewater boundary concentration, which is higher under low flow conditions.

Ammonia behaves quite similarly to NOx (Fig. 6.3.7). The dominant effect of the current CES on surface waters is the uptake of NH_3 by bacteria growing on labile organic carbon, so that predicted surface NH_3 values are lowest under current loads, and higher under secondary-treated and zero loads. Remineralization of the TN load which sediments out from the CES discharge increases bottom water NH_3 concentrations, so these are highest under current loads, lower under secondary loads (where TN is reduced) and least under zero loads. This effect is reinforced by reduced denitrification efficiencies in bottom waters under high CES loads.

The CES NH_3 load into surface waters is again less than other loads, although in this case the New Norfolk STP contributes more than the river. Surface concentrations

upstream are higher under low flow, because the STP load suffers less dilution. NH_3 concentrations in the wetlands are substantially higher under zero or secondary treated CES loads, primarily because of the reduced bacterial uptake. Under current loads, bacterial uptake is more effective under low flow conditions, and wetland concentrations are lower under these conditions, despite the higher concentrations upstream.

Total phosphorus (TP) results are shown in Fig. 6.3.8 a, b. The CES load is highest under secondary treatment, and increases background TP in the vicinity of the discharge by about 50% under median flow, and 100% under low flow. However, transfer of TP from the surface to the bottom layer is more effective under the current CES load composition than under the secondary treated composition, because more of the TP in secondary treated loads is present as DIP or desorbs to form DIP. This means that current CES loads produce largest TP increases in bottom waters, about 25% under median flow, and close to 100% under low flow.

Phosphate concentrations in surface waters are much higher under secondary treatment, and increase substantially downstream, due to desorption of PO_4 from the large adsorbed load (Fig. 6.3.9 a,b). The phosphate load is much lower for the current CES, and is almost exactly compensated in surface waters by increased bacterial uptake, so that predicted PO_4 concentrations in the wetlands under current and zero loads are almost identical. Secondary treatment almost doubles predicted PO_4 concentrations in the wetlands under both river flow scenarios, compared with current or zero loads. However, it should be noted that this prediction depends strongly on the modelling of adsorption-desorption, and calibration comparisons (section 5.3) suggested that the model may underestimate removal of PO4 through adsorption.

The increased efficiency of transfer of TP to bottom waters under current loads is also reflected in larger PO_4 concentrations in bottom waters upstream, as this organic P is remineralised.

Suspended particulate matter is calculated as the sum of inorganic sediments (TSS) and particulate organic matter. SPM in river water at New Norfolk (CS) and in bottom water at Bridgewater is assumed to be predominantly inorganic sediment (TSS: Table 5.3.1, 2). SPM in the CES discharge is assumed to be predominantly POM. In surface waters, the river TSS dominates, and the CES discharge increases SPM near the discharge by only about 10% under both low and high flow conditions (Fig. 6.3.10 a). Most of the POM from the CES sinks rapidly, and its contribution has almost disappeared by the time surface water reaches the wetlands. The much higher TSS concentrations at the Bridgewater boundary in bottom waters completely dominate other sources there, and there is no discernible effect of either CES load on bottom water SPM (Fig. 6.3.10 b). Under low flow, 95%ile surface SPM values are substantially higher in downstream boxes 13 and 14, and in the adjacent wetlands boxes 22 and 23. This is due to vertical mixing or upwelling of bottom waters with high SPM concentrations.

Phytoplankton biomass (as Chl a) is plotted in Fig. 6.3.11 a,b. Current CES loads reduce phytoplankton growth in surface waters under both median and low flow conditions. This is due to a combination of increased light limitation (due to CES colour) and increased nutrient limitation (due to bacterial uptake of DIN, PO_4 - see

above). Phytoplankton biomass in surface waters downstream increases under secondary treated CES loads, and again under zero loads. Nutrient concentrations are higher under secondary treated loads than current loads, while light availabiility increases under zero loads.

In bottom waters, phytoplankton growth is strongly light limited, and increases substantially under zero CES loads, due to the increase in light penetration associated with the removal of colour.

The predicted biomass of the three benthic plant groups, microphytobenthos (MPB), macroalgae and seagrass (Fig. 6.3.12 -14), is affected by an interplay among nutrient concentrations in the water column and sediment pore waters, and by shading. The model allows macroalgae to overgrow and shade seagrass, and both macroalgae and seagrass to shade MPB.

Macroalgae depend on nutrient concentrations in the water column. Predicted macroalgal biomass in the wetlands is lowest under current loads, higher under zero CES loads and highest under secondary treatment (Fig. 6.3.13 a,b). DIN concentrations in the wetlands are low under current loads, and similar under zero and secondary-treated loads. PO_4 concentrations in the wetlands are high under secondary treated loads, and similar and low under zero and current loads. It appears that, in the model, macroalgal biomass is N-limited under current CES loads, and P-limited under zero CES loads.

Seagrass and microphytobenthos in the wetlands depend on nutrient concentrations in sediment pore waters, and potentially on shading by macroalgae or, in the case of MPB, by seagrass. In the wetlands, MPB biomass is low and insensitive to CES loads in boxes 16, 18, and 20, at the back of the wetlands, and higher and more sensitive to CES loads, especially under low flow conditions, in boxes 17, 19, 21, 22 and 23 adjacent to the channel. MPB biomass in these boxes is lowest under zero CES loads, higher under current loads and highest under secondary treatment. This response contrasts with that of macroalgae, and may reflect the fact that pore water nutrient concentrations are more affected by delivery and sedimentation of particulate N and P at the wetlands.

Predicted seagrass biomass in the wetland boxes shows a variable response to CES loads (Fig. 6.3.14). Peak seagrass biomass is generally predicted to occur in box 17, possibly due to a tendency for higher sedimentation rates of TN and TP to occur in this box. In box 17, the smallest median biomass occurs under zero CES loads, but the relative effects of current and secondary treated loads vary with river flow. In other boxes, the response to CES loads changes with river flow, and varies from box to box. This may be due to interactions between nutrient supply, competition with MPB for pore water nutrients, and effects of shading by macroalgae. It can be concluded that the model does not predict an overwhelming or clear-cut impact of the modelled changes in CES loads on seagrass biomass.

In the channel, both MPB and macroalgae are strongly light-limited. Macroalgal biomass is close to zero in the channel under current and secondary CES loads, but under zero loads and median river flows increases in boxes 13 and 14, adjacent to Bridgewater, to levels comparable with those predicted for the wetlands (Fig. 6.3.13

a). Under median river flow (Fig. 6.3.12 a), the model predicts substantial MPB biomass in the downstream channel (boxes 13 and 14) under both current and secondary treated CES loads, and this biomass increases substantially, and occurs further upstream as far as box 7, under zero CES loads, when light attenuation due to CES colour is removed. Under low river flow, the model predicts low MPB biomass in the channel, and this increases substantially in downstream boxes 13 and 14 under zero CES loads (Fig. 6.3.12 b).

6.3.3 Discussion of Scenarios

The model shows a substantial and hardly surprising impact of CES organic carbon loads on respiration and oxygen consumption in bottom waters and sediments in the channel. The size of this impact depends on river flow, and oxygen concentrations in bottom waters at the downstream boundary. The model suggests that secondary treatment of the CES would increase oxygen concentrations from about 10 to 20% saturation in bottom waters, under low flow conditions. However, the river is also a substantial source of particulate organic carbon under median and high flow conditions, and the model predicts that accumulation and breakdown of this material in sediments could lead to substantial drawdown of bottom water oxygen even in the absence of CES loads. This is likely to be exaggerated in deep holes with low exchange rates with the overlying water column. Such an effect of river carbon is not unexpected - oxygen depletion is observed in bottom waters in the upper reaches of the Huon estuary, even though the Huon catchment is largely pristine (CSIRO Huon Study Team, 2000).

The current CES loads of DIN (NOx and NH_3) and DIP are relatively modest compared with other sources. The model predicts that the current CES load has a "negative" impact on DIN and DIP in surface waters and wetlands, through bacterial uptake of DIN and DIP in surface waters. The model also predicts that secondary-treated CES would have a relatively neutral impact on DIN, but would substantially increase DIP and TP in surface waters and wetlands.

There are some significant uncertainties attached to model predictions of DIN and DIP impacts. Although consistent with observed DIN distributions in surface waters, the hypothesized bacterial uptake of DIN is not directly confirmed by process studies. Perhaps more significantly, the model consistently overpredicts PO_4 in surface and bottom waters under current loads. In particular, there is no evidence in observations for the assumed New Norfolk STP load of PO_4. As discussed above, there is some uncertainty about the current size and composition of this load. However, it is possible that DIP removal mechanisms (probably P adsorption and sedimentation), are underestimated in the model. If this is the case, the model may also over-estimate the impact of the increased PO_4 and TP loads resulting from secondary treatment.

The changes in nutrient concentrations associated with different CES loads have relatively small effects on primary producers in the model. In the model, phytoplankton biomass in surface waters is already constrained by grazing and sinking losses, while phytoplankton growth in bottom waters is strongly light-limited. There are uncertainties about the model phytoplankton loss processes, and in principle species with low loss rates might be able to achieve higher biomasses in the lower estuary and wetlands than those presented here. However, the fact that the river

supplies a freshwater phytoplankton assemblage, and that salinity inevitably increases downstream, imposes severe restrictions on bloom development in the upper estuary.

The predicted nutrient concentrations in surface waters under any of these load scenarios are in any case not very high: < 0.5 μM for phosphate, and < 2 μM for nitrate and ammonia. Nutrient concentrations in bottom waters are substantially larger, and in theory, vertically migrating dinoflagellates might be able to achieve high biomass (cf CSIRO Huon Study Team, 2000). However, it seems likely that the salinity contrast between surface and bottom waters in the upper estuary is too large for dinoflagellates to tolerate. Task 2B_5B found little evidence of marine phytoplankton species in surface waters.

There are some predicted impacts of changes in nutrient supply on benthic plant communities in the wetlands. In particular, macroalgal biomass is strongly nutrient limited there, and responds to increases in water column nutrients under secondary treatment with a doubling of macroalgal biomass. Although the model allows for macroalgae to overgrow and shade seagrass, the model predicts that seagrass are predominantly nutrient limited, and seagrass biomass remains high under secondary treatment, despite increases in macroalgal shading, at least at the macroalgal biomass levels predicted. MPB biomass in wetlands is also predicted to increase under secondary treatment, despite increases in macroalgal biomass.

These predictions of interactions among benthic plants should be treated with some caution. The nutrient limitation of macroalgae, and its ability to shade seagrass and MPB, are reasonable predictions. However, as noted in section 5.3, the model does not resolve the fine scale horizontal spatial mosaic among seagrass and microphytobenthos. The one-layer sediment model used here cannot reproduce the vertical gradients in pore water nutrients, and may therefore not represent adequately competition among seagrass and MPB for pore water nutrients.

In the channel bottom layer, phytoplankton and benthic plants are strongly light limited, and the principal impact of the CES on plant growth there results from the contribution of "colour" to light attenuation. Removal of this effect under zero CES load results in substantial increases in phytoplankton, macroalgal and MPB biomass. This qualitative effect seems likely to be real, although again processes such as bottom stress, sediment stability and attachment sites for macroalgae, not represented in the model, may affect the quantitative predictions.

8 References

Baird, M.E. and S. M. Emsley (1999). Towards a mechanistic model of plankton population dynamics. *J. Plankton Res.* **21**: 85-126.

Baird, M.E., S.J.Walker, B.B. Wallace, I.T.Webster, J.S. Parslow. (2001) Towards a mechanistic model of estuarine eutrophication. MS In Prep.

Blumberg, A.F. and Herring, J., 1987. Circulation modelling using orthogonal curvilinear coordinates, **in** *Three-Dimensional Models of marine and Estuarine Dynamics*, eds. Nihoul, J.C.J and Jamart, B.M., Elsevier.

Coughanowr, C. (1997) State of the Derwent Estuary: a review of environmental quality data to 1997. Supervising Scientist Report 129, Supervising Scientist, Canberra.

CSIRO Huon Study Team, 2000. Huon Estuary Study - environmental research for integrated catchment management and aquaculture. Final report to Fisheries Research and Development Corporation. Project number 96/284, June 2000. CSIRO Division of Marine Research. Marine Laboratories, Hobart.

Davies , P.E. and Kalish, S.R., 1989. Water quality of the Upper Derwert Estuary. Tasmania, Inland Fisheries Commission, Tasmania, Occasional Report 89-03.

Grace, M. and A. Liang (2000a) Aspects of the fate of Boyer Mill resin acids in the Derwent River. Derwent River ERA Report, Task 8.

Grace, M. and A. Liang (2000b) Phosphorous Partitioning Studies. Derwent River ERA Report, Task 8.

Harris, G., Batley, G., Fox, D., Hall, D., Jernakoff, P., Molloy, R., Murray, A., Newell, B., Parslow, J., Skyring, G. and Walker, S. (1996*)* Port Phillip Bay Environmental Study Final Report, CSIRO, Canberra, Australia

Hunter, J.R. and Andrewartha, J.R., 1990. A modelling study of a proposed effluent discharge at Boyer, CSIRO Division of Oceanography, Report OMR-15/28.

Hunter, J.R. and Parslow, J., 1999. Mathematical modelling of the dispersal and fate of CES discharge from the Boyer mill in the Upper Derwent Estuary: Results of Part A, CSIRO Marine Research, report December, 1999.

Hunter, J.R., Walker, S.J. and Andrewartha, J.R., 1998. Modelling of the ANM Outfall in the Derwent Estuary, CSIRO Marine Research, Report OMR-115/119.

Kirk, J.T.O. (1983) Light and photosynthesis in aquatic ecosystems. Cambridge Univ. Press, Cambridge, UK. 401 pp.

Keulegan, G.H. (1957) An experimental study of the motion of saline water from locks into fresh water channels. U.S. Nat. Bur. Of Standards Report 5168.

Leonard, B.P. (1988) Universal limiter for transient interpolation modelling of the advective transport equations: the ULTIMATE conservative difference scheme. NASA Technical Memorandum 100916, ICOMP-88-11.

Mellor, G.L. and T. Yamada (1982) Development of a turbulence closure model for geophysical fluid problems, *Rev. Geophys*., 20, 851-875.

Mesinger, F., and Arakawa, A., 1976. Numerical methods used in atmospheric models, GARP Pub. Series No. 17, Global Atmospheric Research Programme, 64 pp.

Murray, A. G. and Parslow J. S. (1997) Port Phillip Bay Integrated model: Final Report. Port Phillip Bay Environment Study Technical Report no. 44, Melbourne

Nicholson, G.J. and A.R. Longmore (2000) Benthic Fluxes and Biogeochemical Processes in the Derwent River. Derwent River ERA Report, Task 8.

Roberts, S., G. Beattie, J. Beardall and A. Quigg (2001) Primary production, phytoplankton nutrient status and bacterial production in the Derwent River, Tasmania. Derwent River ERA Task 7, Final Report.

Royle, R.N. and Hart, B.T., 1984. Euphotic depth in the Derwent River. Report by Water Studies Centre, Monash University, for Australian Newsprint Mills. July.

Walker, S.J. (1997) A transport model of Port Phillip Bay. Port Phillip Bay Environment Study Technical Report no. 39, Melbourne

Walker, S.J. and Fandry, C.B., 1994. Modelling effluent dispersion in Australian coastal waters – Devonport 1991-1992, hydrodynamic modelling, CSIRO Division of Oceanography, Report OMR-59/40.

Walker, S.J. and Hunter, J.R., 1994. Numerical modelling of the ANM Outfall in the Derwent Estuary, CSIRO Division of Oceanography, Report OMR-62/64.

Walker, S.J. and Waring, J.R., 1998. A multiple grid, 3-dimensional, non-linear, variable-density hydrodynamic model with curvilinear horizontal coordinates and level (z) vertical coordinates, CSIRO Marine Research, Report OMR-118/120.

List of Figures

Figure 6.2.24 (a) Maximum mixing zone CES section (% CES), spring 45 wind 240 ^{o}T, TOTAL
Figure 6.2.24 (b) Maximum mixing zone CES:U18 section (% CES), spring 45 wind 240 ^{o}T, TOTAL
Figure 6.2.24 (c) Maximum mixing zone U18 section (% CES), spring 45 wind 240 ^{o}T, TOTAL
Figure 6.2.24 (d) Maximum mixing zone U18:U16/17 (% CES), spring 45 wind 240 ^{o}T, TOTAL

Figure 6.2.25 (a) 5 percentile mixing zone surface (% CES), combined scenarios, TOTAL_A
Figure 6.2.25 (a) 50 percentile mixing zone surface (% CES), combined scenarios, TOTAL_A
Figure 6.2.25 (a) 95 percentile mixing zone surface (% CES), combined scenarios, TOTAL_A

Figure 6.2.26 (a) 5 percentile mixing zone CES section (% CES), combined scenarios, TOTAL_A
Figure 6.2.26 (b) 5 percentile mixing zone CES:U18 section (% CES), combined scenarios, TOTAL_A
Figure 6.2.26 (c) 5 percentile mixing zone U18 section (% CES), combined scenarios, TOTAL_A
Figure 6.2.26 (d) 5 percentile mixing zone U18:U16/17 (% CES), combined scenarios, TOTAL_A

Figure 6.2.27 (a) 50 percentile mixing zone CES section (% CES), combined scenarios, TOTAL_A
Figure 6.2.27 (b) 50 percentile mixing zone CES:U18 (% CES), combined scenarios, TOTAL_A
Figure 6.2.27 (c) 50 percentile mixing zone U18 section (% CES), combined scenarios, TOTAL_A
Figure 6.2.27 (d) 50 percentile mixing zone U18:U16/17 (% CES), combined scenarios, TOTAL_A

Figure 6.2.28 (a) 95 percentile mixing zone CES section (% CES), combined scenarios, TOTAL_A
Figure 6.2.28 (b) 95 percentile mixing zone CES:U18 (% CES), combined scenarios, TOTAL_A
Figure 6.2.28 (c) 95 percentile mixing zone U18 section (% CES), combined scenarios, TOTAL_A
Figure 6.2.28 (d) 95 percentile mixing zone U18:U16/17 (% CES), combined scenarios, TOTAL_A

Figure 6.2.29 (a) Maximum mixing zone CES section (% CES), combined scenarios, TOTAL_A
Figure 6.2.29 (b) Maximum mixing zone CES:U18 section (% CES), combined scenarios, TOTAL_A
Figure 6.2.29 (c) Maximum mixing zone U18 section (% CES), combined scenarios, TOTAL_A
Figure 6.2.29 (d) Maximum mixing zone U18:U16/17 (% CES), combined scenarios, TOTAL_A

Figure 6.2.30 (a) –(l) RDRA surface plot (μgL^{-1}) for spring, 45 m^3s^{-1}, wind 5ms^{-1} 60^{o}T at 1hr intervals

Figure 6.2.31 (a) RPRA sedimentation rate (mgm^2day^{-1}), neap tide, 45 m^3s^{-1}, wind 5ms^{-1} 60^{o}T
Figure 6.2.31 (b) RPRA sedimentation rate (mgm^2day^{-1}), neap tide, 45 m^3s^{-1}, wind 5ms^{-1} 240^{o}T
Figure 6.2.31 (c) RPRA sedimentation rate (mgm^2day^{-1}), neap tide, 45 m^3s^{-1}, wind 5ms^{-1} 330^{o}T
Figure 6.2.31 (d) RPRA sedimentation rate (mgm^2day^{-1}), neap tide, 90 m^3s^{-1}, wind 5ms^{-1} 60^{o}T
Figure 6.2.31 (e) RPRA sedimentation rate (mgm^2day^{-1}), neap tide, 90 m^3s^{-1}, wind 5ms^{-1} 240^{o}T
Figure 6.2.31 (f) RPRA sedimentation rate (mgm^2day^{-1}), neap tide, 90 m^3s^{-1}, wind 5ms^{-1} 330^{o}T
Figure 6.2.31 (g) RPRA sedimentation rate (mgm^2day^{-1}), spring tide, 45 m^3s^{-1}, wind 5ms^{-1} 60^{o}T
Figure 6.2.31 (h) RPRA sedimentation rate (mgm^2day^{-1}), spring tide, 45 m^3s^{-1}, wind 5ms^{-1} 240^{o}T
Figure 6.2.31 (i) RPRA sedimentation rate (mgm^2day^{-1}), spring tide, 45 m^3s^{-1}, wind 5ms^{-1} 330^{o}T
Figure 6.2.31 (j) RPRA sedimentation rate (mgm^2day^{-1}), spring tide, 90 m^3s^{-1}, wind 5ms^{-1} 60^{o}T
Figure 6.2.31 (k) RPRA sedimentation rate (mgm^2day^{-1}), spring tide, 90 m^3s^{-1}, wind 5ms^{-1} 240^{o}T
Figure 6.2.31 (l) RPRA sedimentation rate (mgm^2day^{-1}), spring tide, 90 m^3s^{-1}, wind 5ms^{-1} 330^{o}T

Figure 6.2.32 (a) LPRA_A sedimentation rate (mgm^2day^{-1}), neap tide, 45 m^3s^{-1}, wind 5ms^{-1} 60^{o}T
Figure 6.2.32 (b) LPRA_A sedimentation rate (mgm^2day^{-1}), neap tide, 45 m^3s^{-1}, wind 5ms^{-1} 240^{o}T
Figure 6.2.32 (c) LPRA_A sedimentation rate (mgm^2day^{-1}), neap tide, 45 m^3s^{-1}, wind 5ms^{-1} 330^{o}T
Figure 6.2.32 (d) LPRA_A sedimentation rate (mgm^2day^{-1}), neap tide, 90 m^3s^{-1}, wind 5ms^{-1} 60^{o}T
Figure 6.2.32 (e) LPRA_A sedimentation rate (mgm^2day^{-1}), neap tide, 90 m^3s^{-1}, wind 5ms^{-1} 240^{o}T
Figure 6.2.32 (f) LPRA_A sedimentation rate (mgm^2day^{-1}), neap tide, 90 m^3s^{-1}, wind 5ms^{-1} 330^{o}T
Figure 6.2.32 (g) LPRA_A sedimentation rate (mgm^2day^{-1}), spring tide, 45 m^3s^{-1}, wind 5ms^{-1} 60^{o}T
Figure 6.2.32 (h) LPRA_A sedimentation rate (mgm^2day^{-1}), spring tide, 45 m^3s^{-1}, wind 5ms^{-1} 240^{o}T
Figure 6.2.32 (i) LPRA_A sedimentation rate (mgm^2day^{-1}), spring tide, 45 m^3s^{-1}, wind 5ms^{-1} 330^{o}T
Figure 6.2.32 (j) LPRA_A sedimentation rate (mgm^2day^{-1}), spring tide, 90 m^3s^{-1}, wind 5ms^{-1} 60^{o}T
Figure 6.2.32 (k) LPRA_A sedimentation rate (mgm^2day^{-1}), spring tide, 90 m^3s^{-1}, wind 5ms^{-1} 240^{o}T
Figure 6.2.32 (l) LPRA_A sedimentation rate (mgm^2day^{-1}), spring tide, 90 m^3s^{-1}, wind 5ms^{-1} 330^{o}T

Figure 6.2.33 (a) LPRA sedimentation rate (mgm^2day^{-1}), neap tide, 45 m^3s^{-1}, wind 5ms^{-1} 60^{o}T
Figure 6.2.33 (b) LPRA sedimentation rate (mgm^2day^{-1}), neap tide, 45 m^3s^{-1}, wind 5ms^{-1} 240^{o}T
Figure 6.2.33 (c) LPRA sedimentation rate (mgm^2day^{-1}), neap tide, 45 m^3s^{-1}, wind 5ms^{-1} 330^{o}T

Figure 2.2.1 : Model bathymetry and hydrographic sections

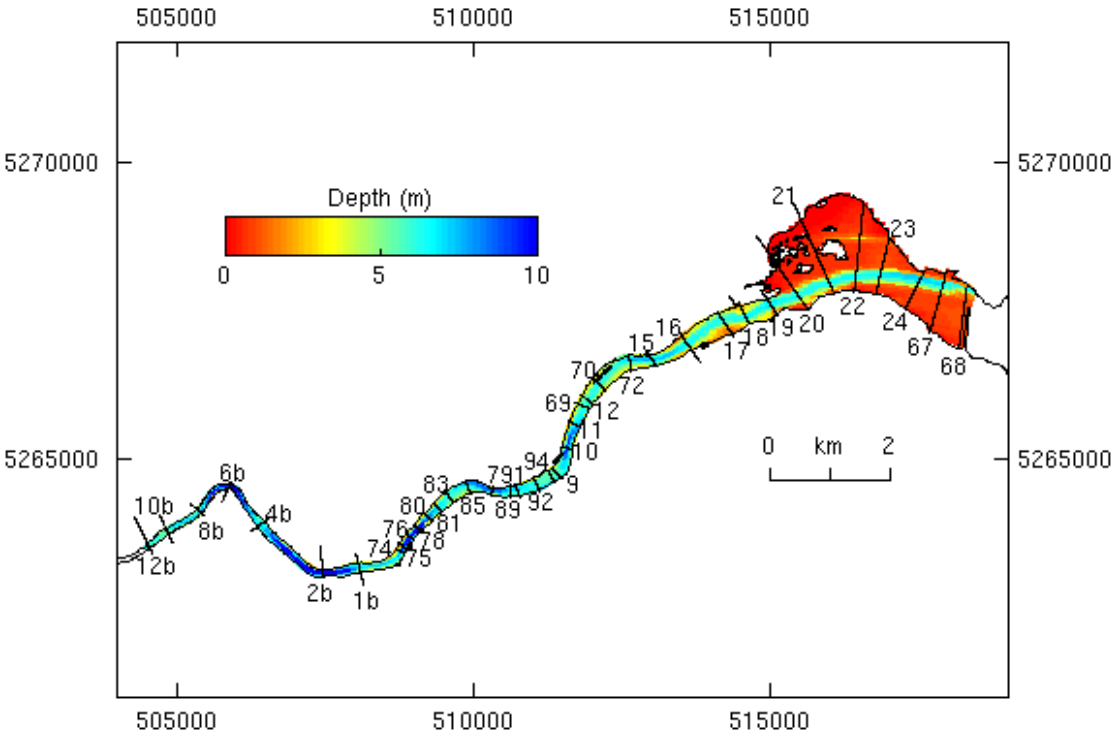

Figure 2.2.2 : Wetland bathymetry and hydrographic sections

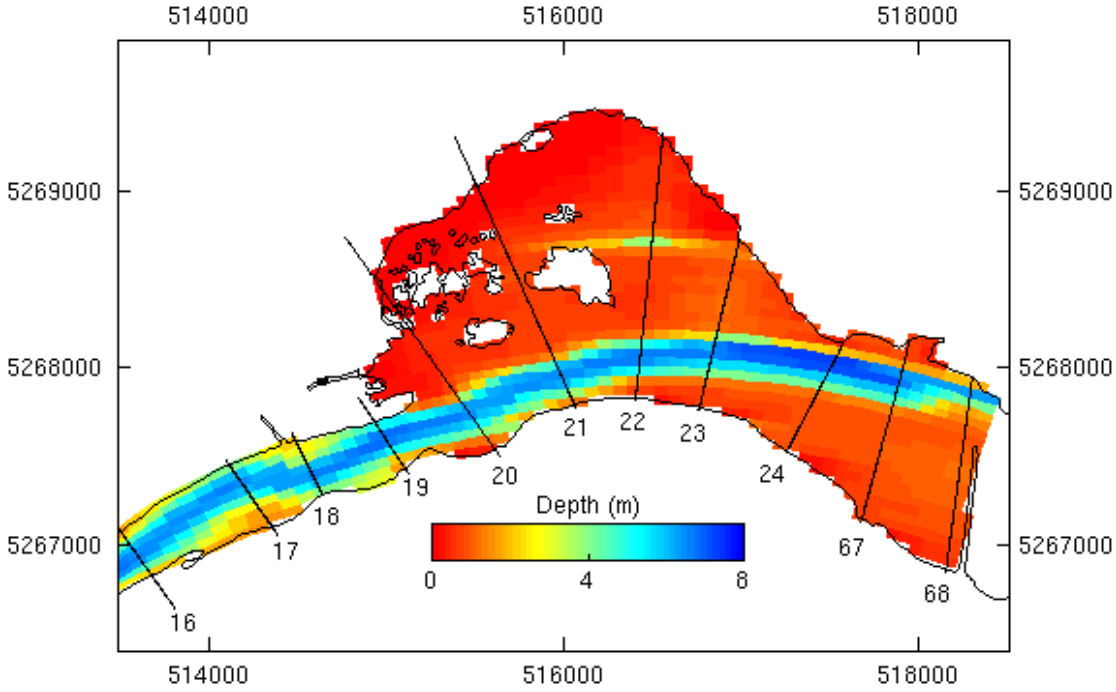

Figure 2.2.3 : Model bathymetry section 2B

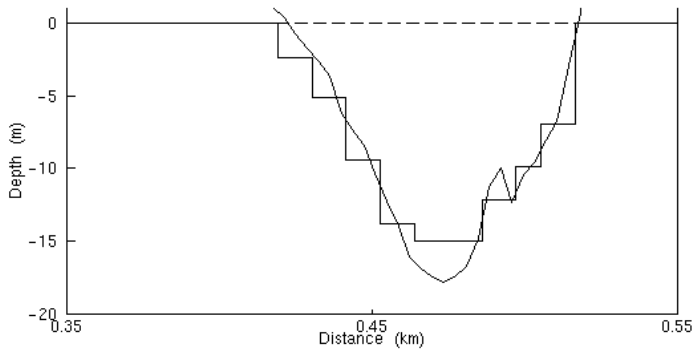

Figure 2.2.4 : : Model bathymetry section 17

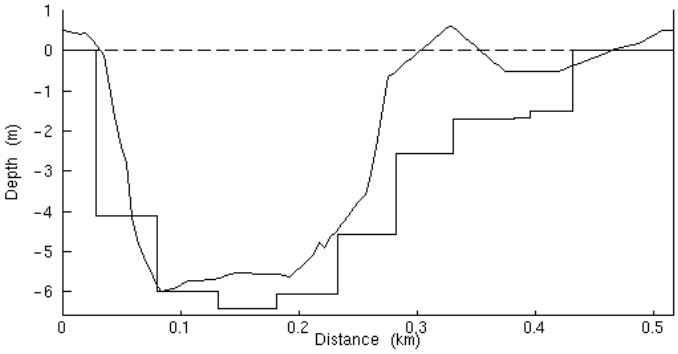

Figure 2.2.5 : Model bathymetry section 19

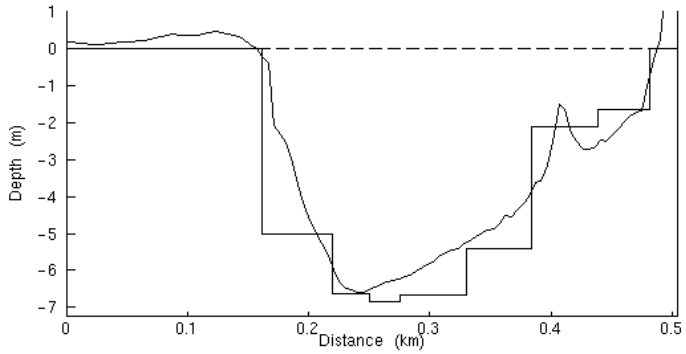

Figure 2.2.6 : Model bathymetry section 22

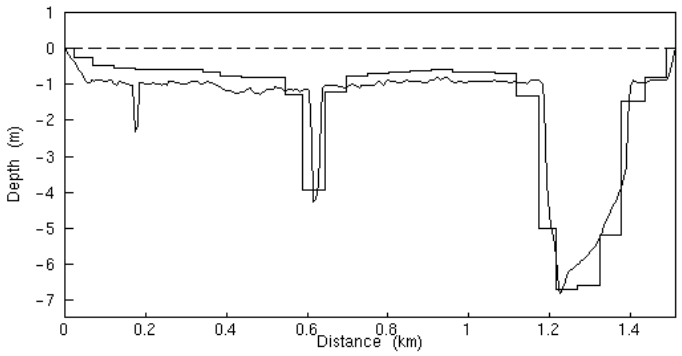

Figure 2.2.7 : Model bathymetry section 68

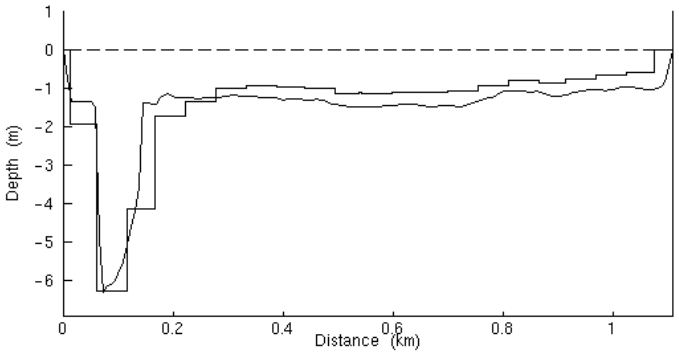

Figure 2.2.8 : Model bathymetry section 70

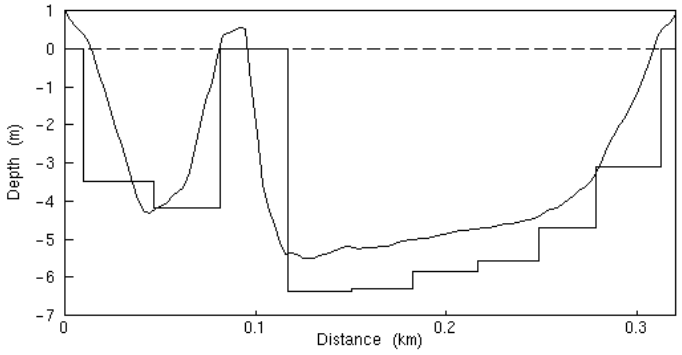

Figure 2.2.9 : Model bathymetry section 76

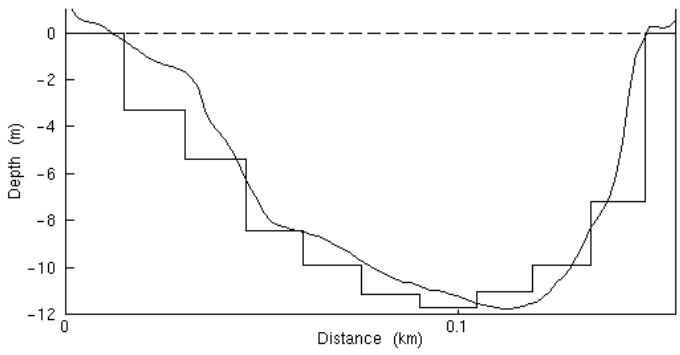

Figure 2.2.10 : Model bathymetry section 92

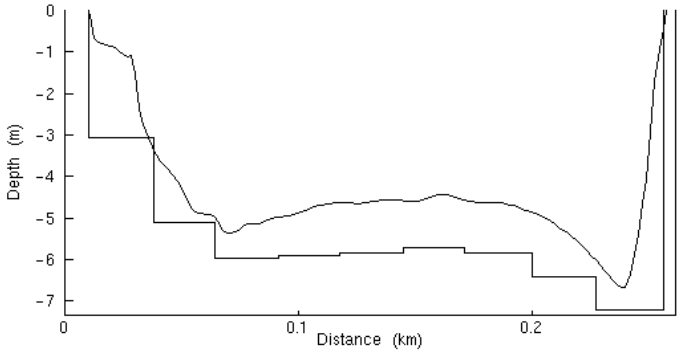

Figure 2.3.1 : Neap and spring tides over 24 hours

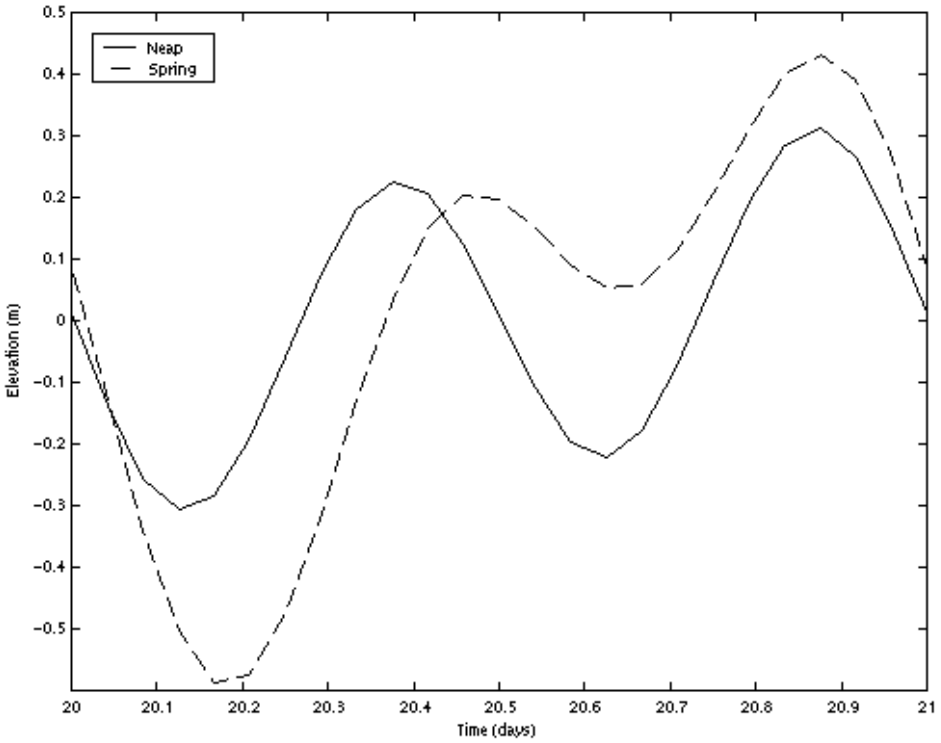

Figure 4.3.1 : The Box Model Geometry.

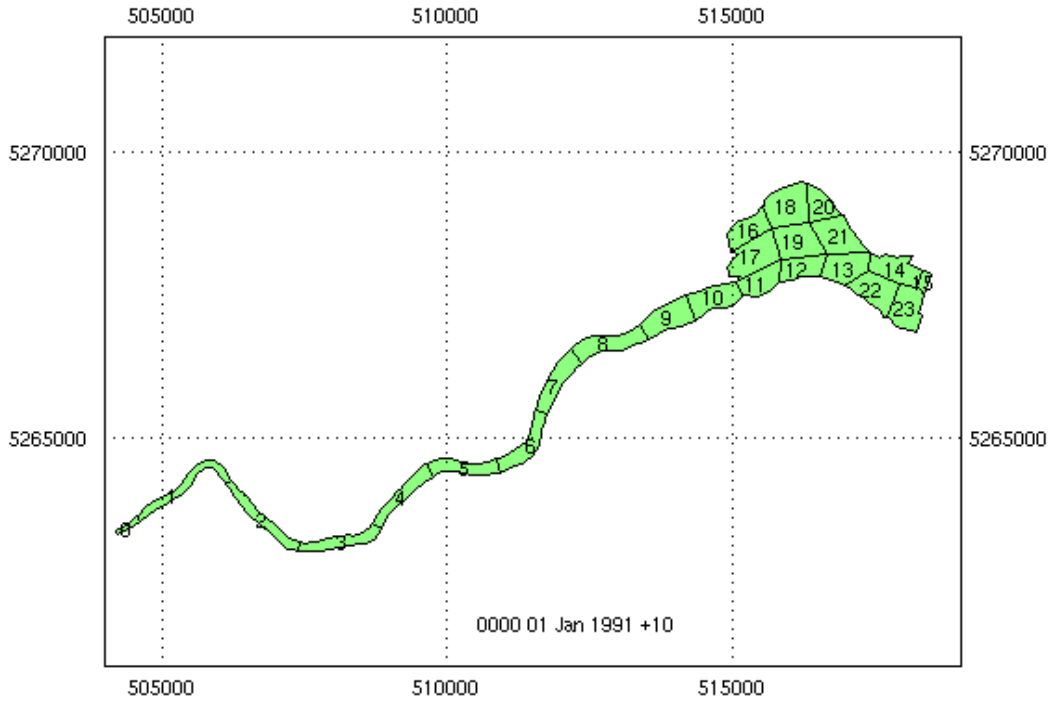

Figure 4.4.1. A schematic picture of nitrogen cycling in the model through pelagic, benthic and epibenthic components.

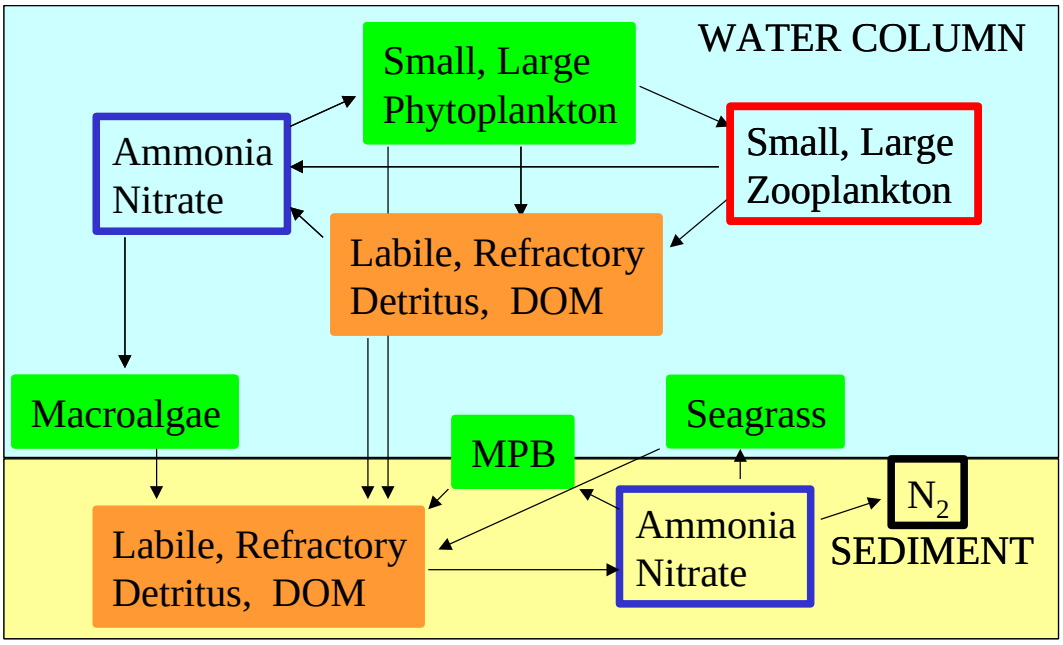

Figure 5.1.1 : Along-river salinity section (% CES) from CZP survey, 5 March 1993

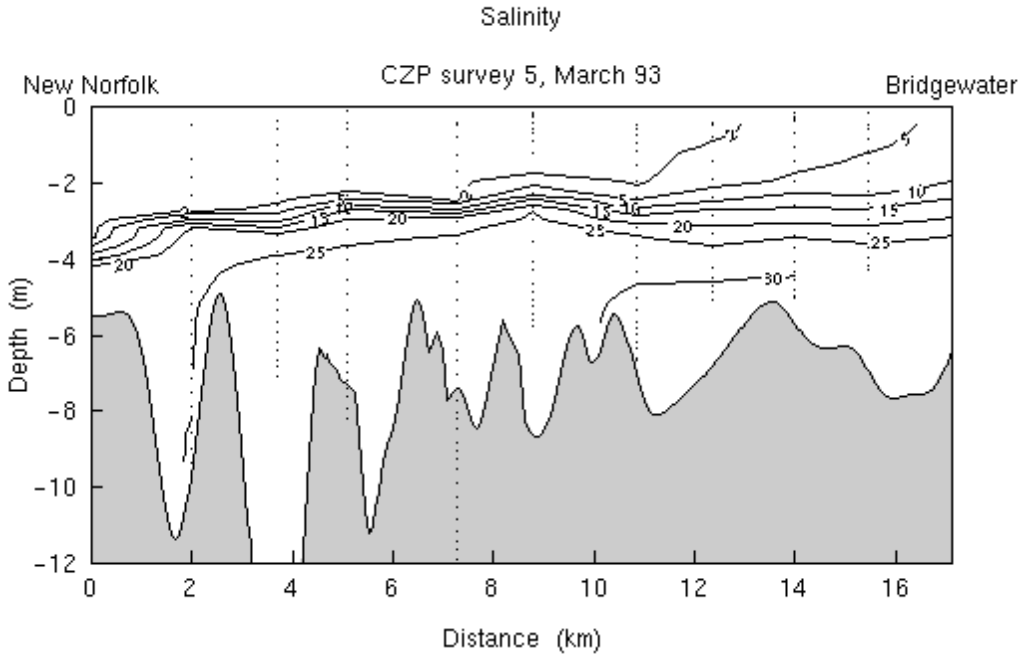

Figure 5.1.2 : Along-river salinity section (% CES) from CZP survey, 7 October 1993

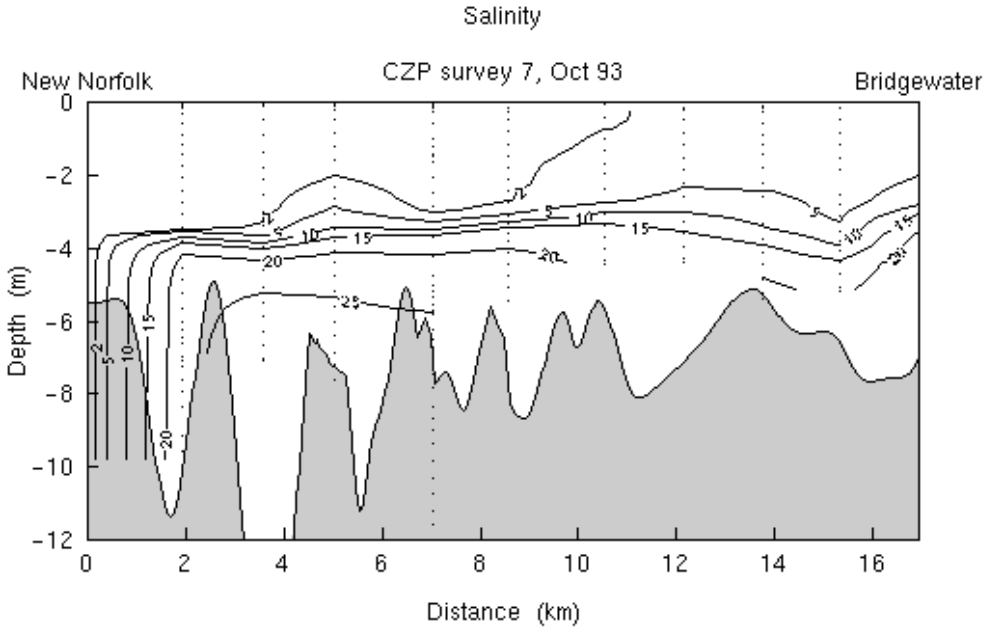

Figure 5.1.3 : Modelled along-river salinity section (% CES)
Neap tide, 45m^3s^{-1}, wind 5ms^{-1} 60^oT

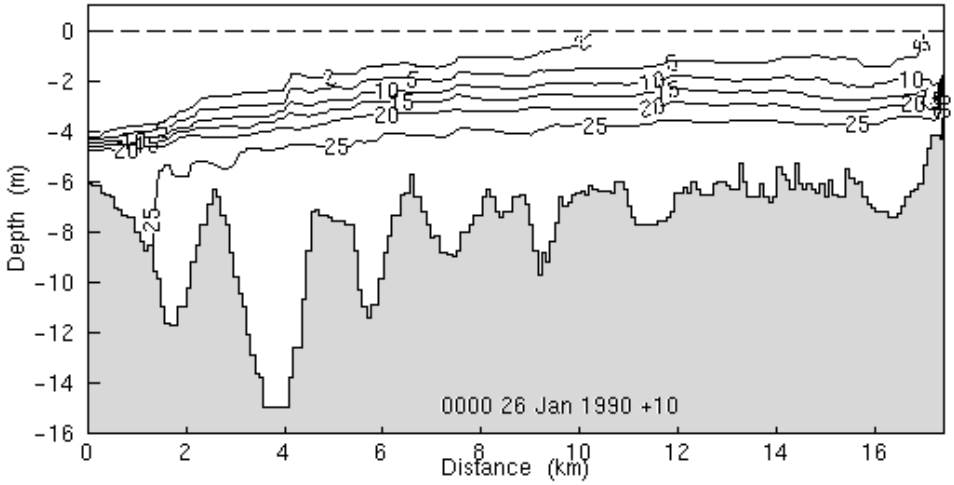

Figure 5.1.4 : Modelled along-river salinity section (% CES)
Neap tide, 90 m^3s^{-1}, wind 5ms^{-1} 60^oT

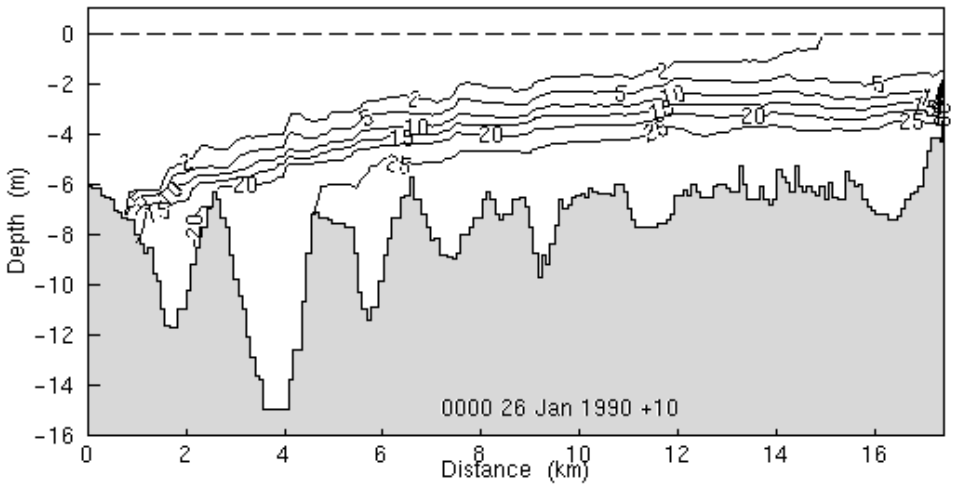

Figure 5.1.5 : Modelled along-river salinity section (% CES)
Spring tide, 90 m^3s^{-1}, wind $5ms^{-1}$ 60^oT

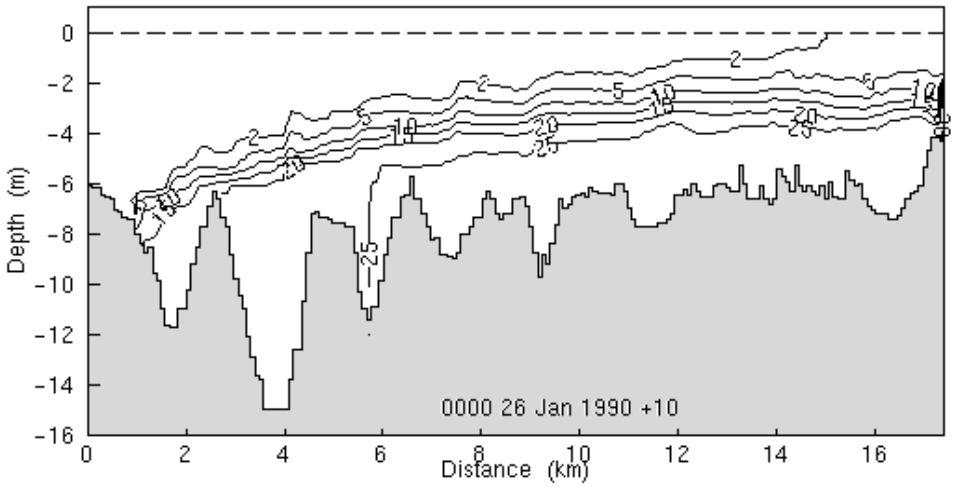

Figure 5.2.1 : Resin acid calibration, Station U16/17, surface layer

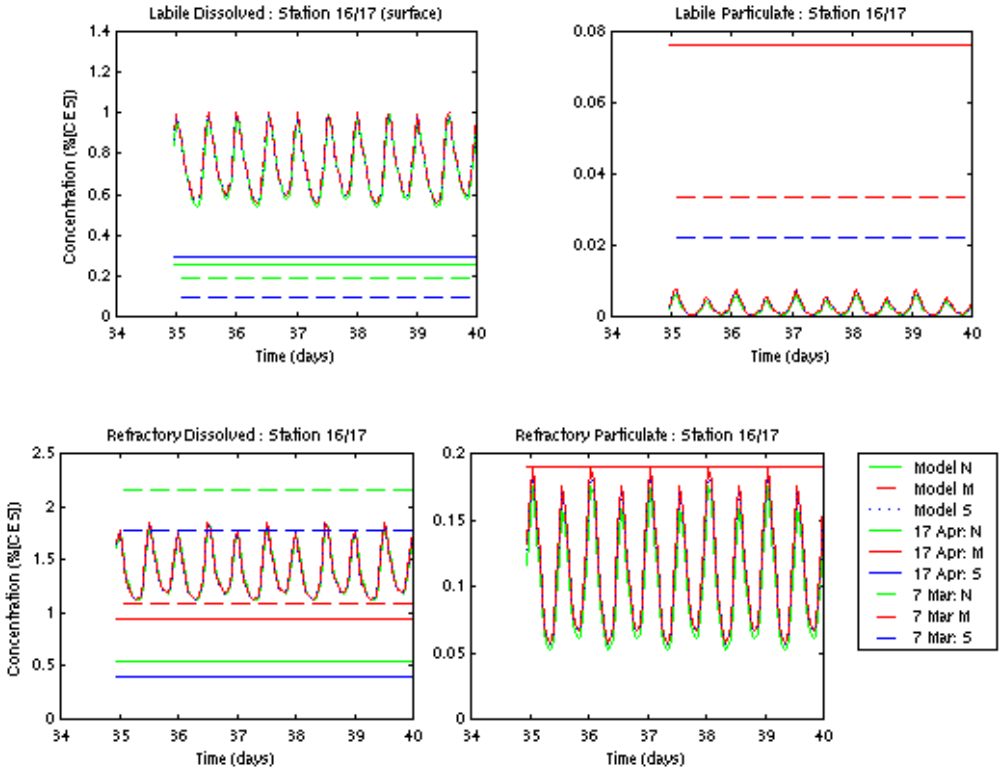

Figure 5.2.2 : Resin acid calibration, Station U16/17, bottom layer

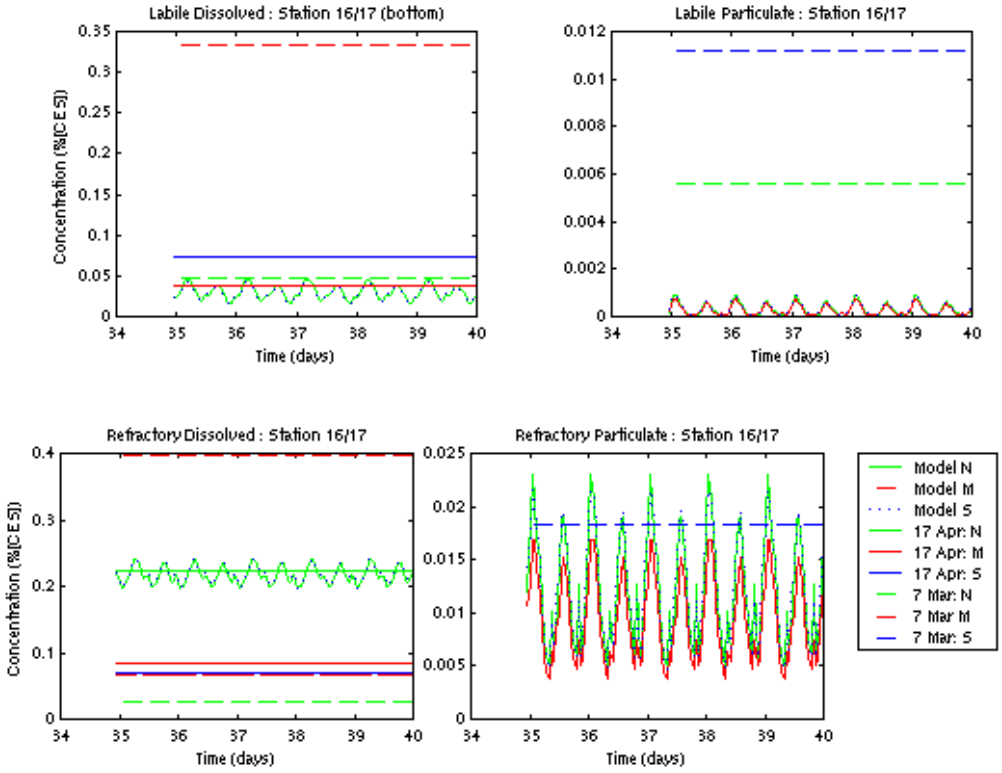

Figure 5.2.3 : Resin acid calibration, Station U18, surface layer

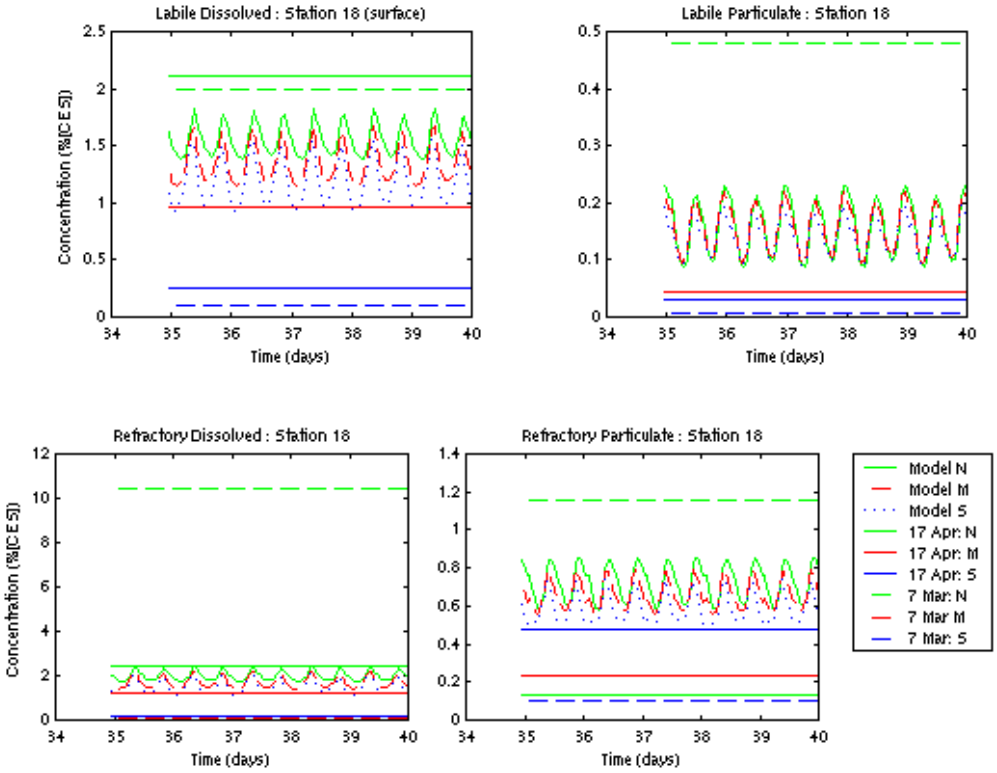

Figure 5.2.4 : Resin acid calibration, Station U18, bottom layer

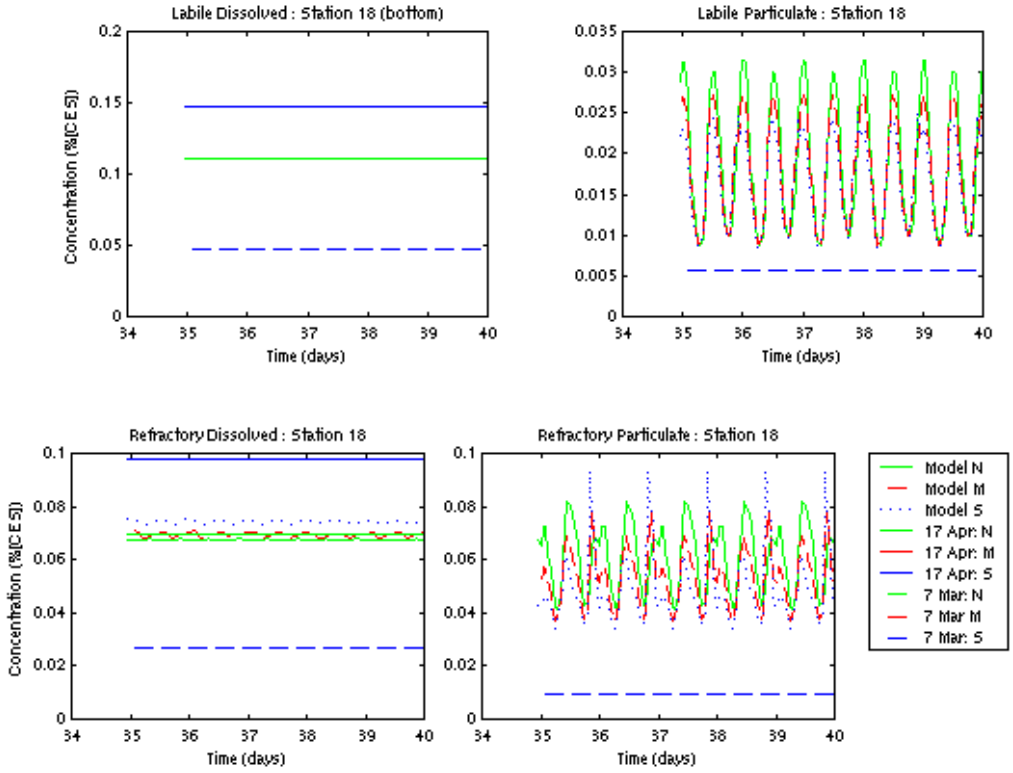

Figure 5.2.5 : Resin acid calibration, Station U12, surface and bottom layers

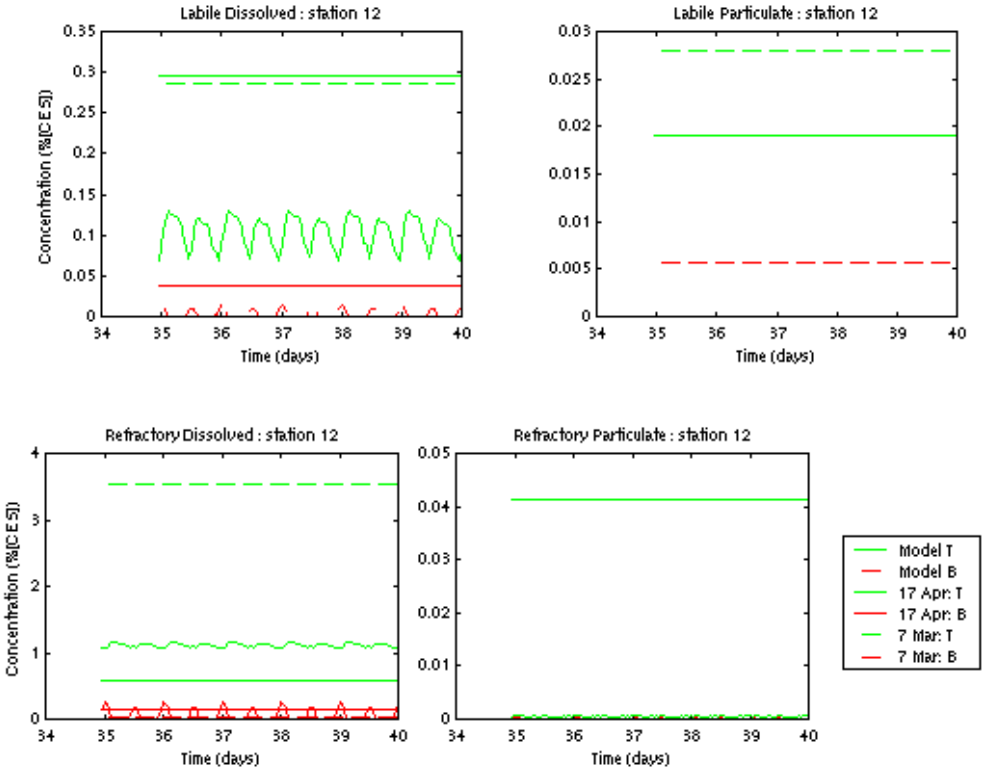

Figure 5.2.6 : Labile particulate acid with adsorption, all stations

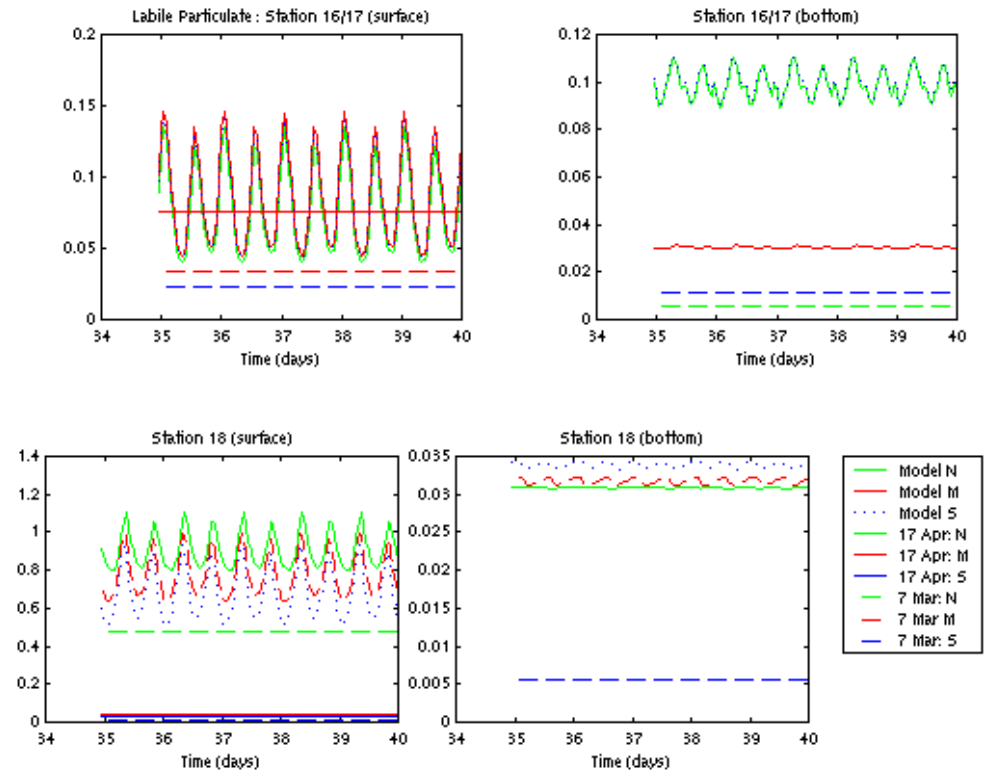

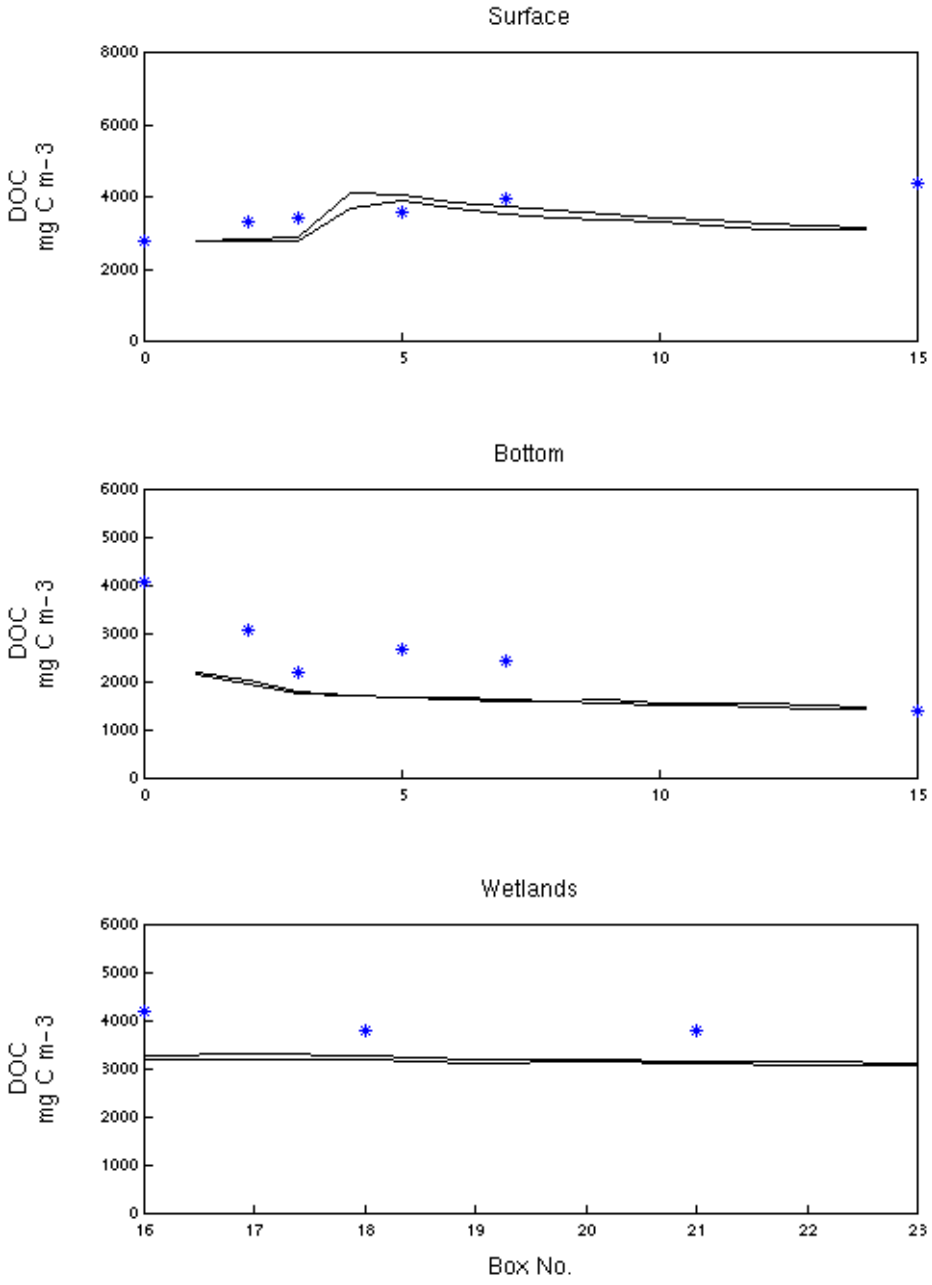

Fig. 5.3.1 a. Comparison of predicted (line) and observed (asterisk) DOC in model boxes in channel surface, channel bottom and wetlands, for survey November 23, 1999.

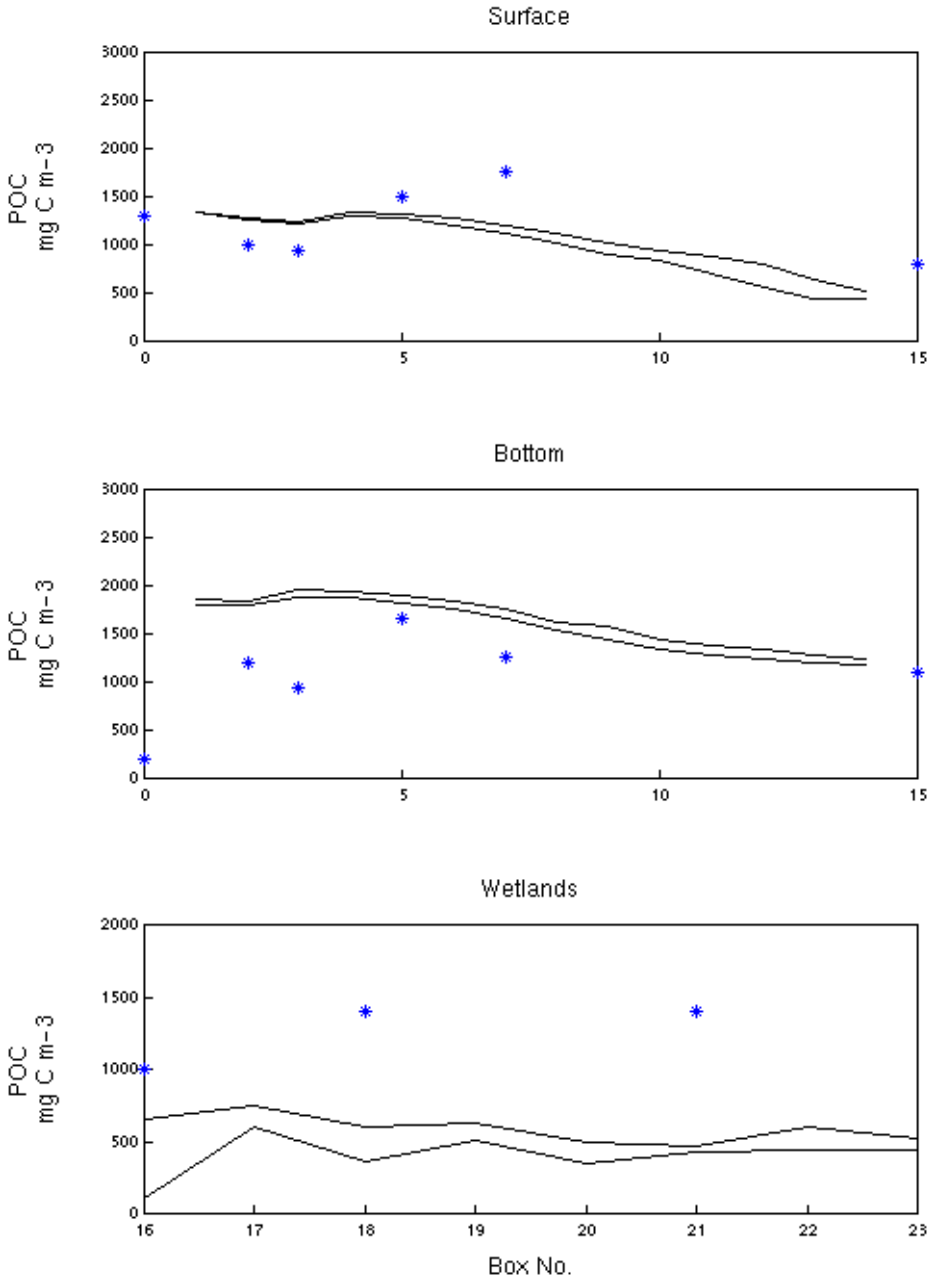

Fig. 5.3.1 b. Comparison of predicted (line) and observed (asterisk) POC in model boxes in channel surface, channel bottom and wetlands, for survey November 23, 1999.

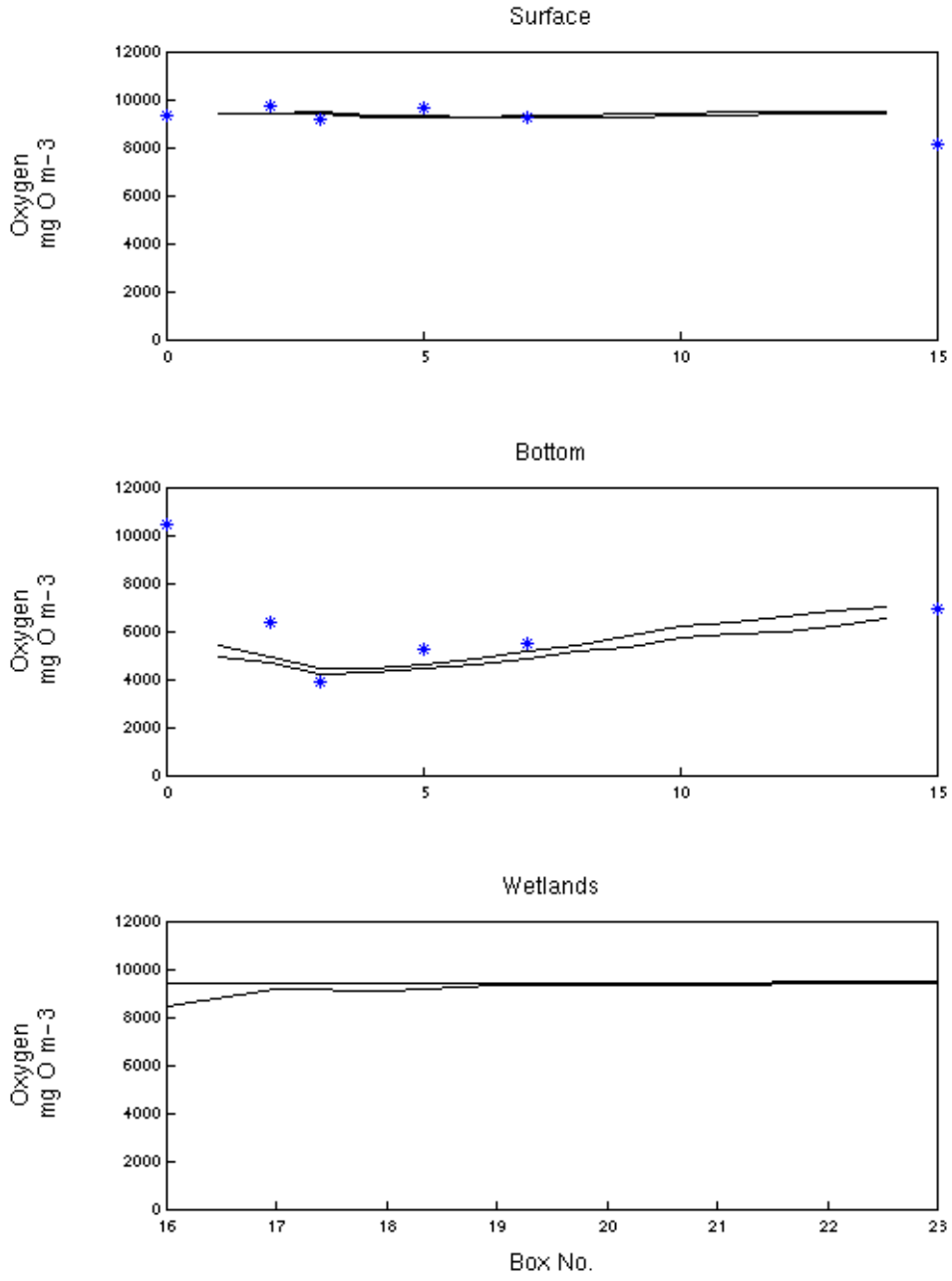

Fig. 5.3.1 c. Comparison of predicted (line) and observed (asterisk) Oxygen in model boxes in channel surface, channel bottom and wetlands, for survey November 23, 1999.

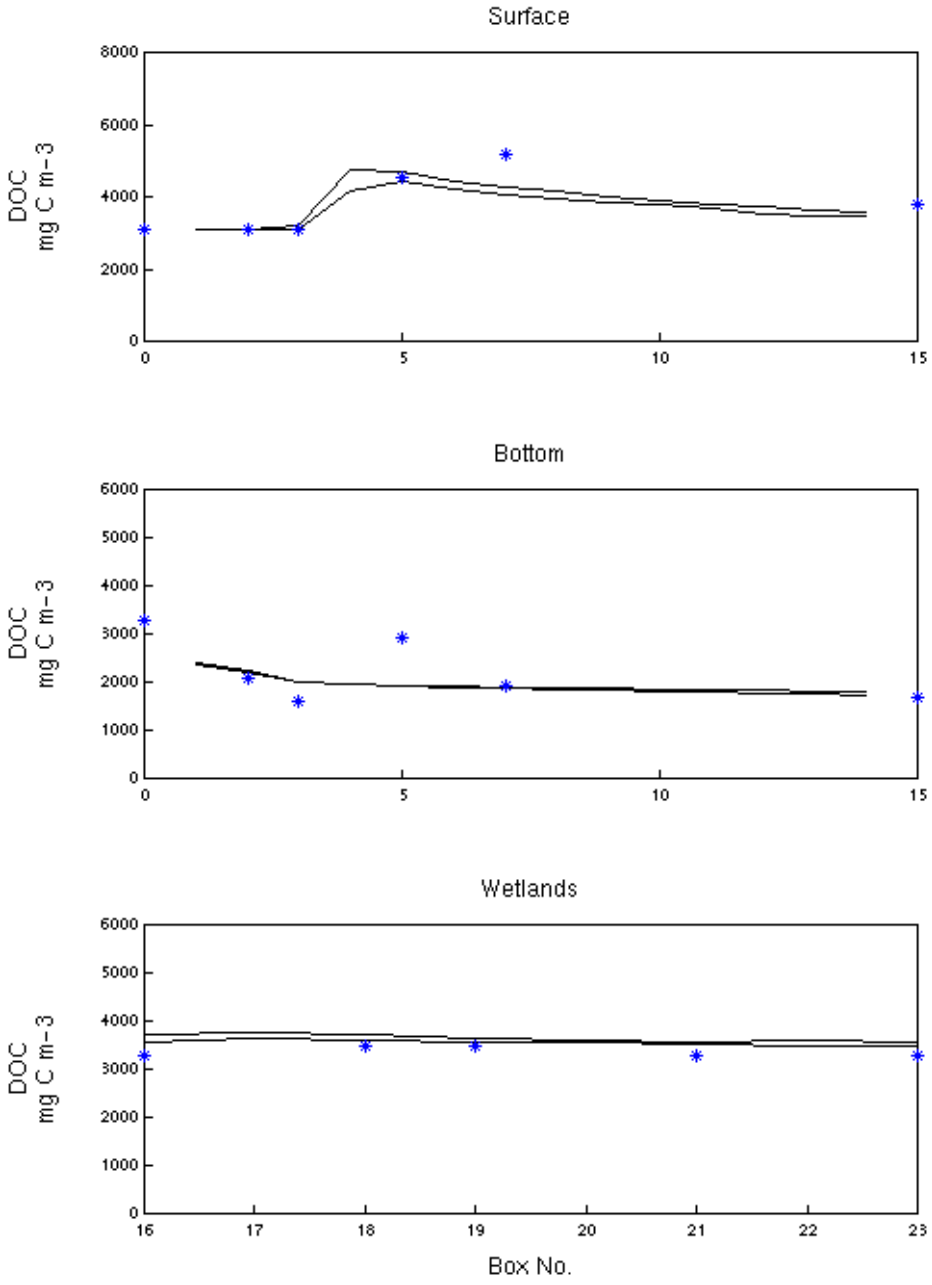

Fig. 5.3.2 a. Comparison of predicted (line) and observed (asterisk) DOC in model boxes in channel surface, channel bottom and wetlands, for survey December 14, 1999.

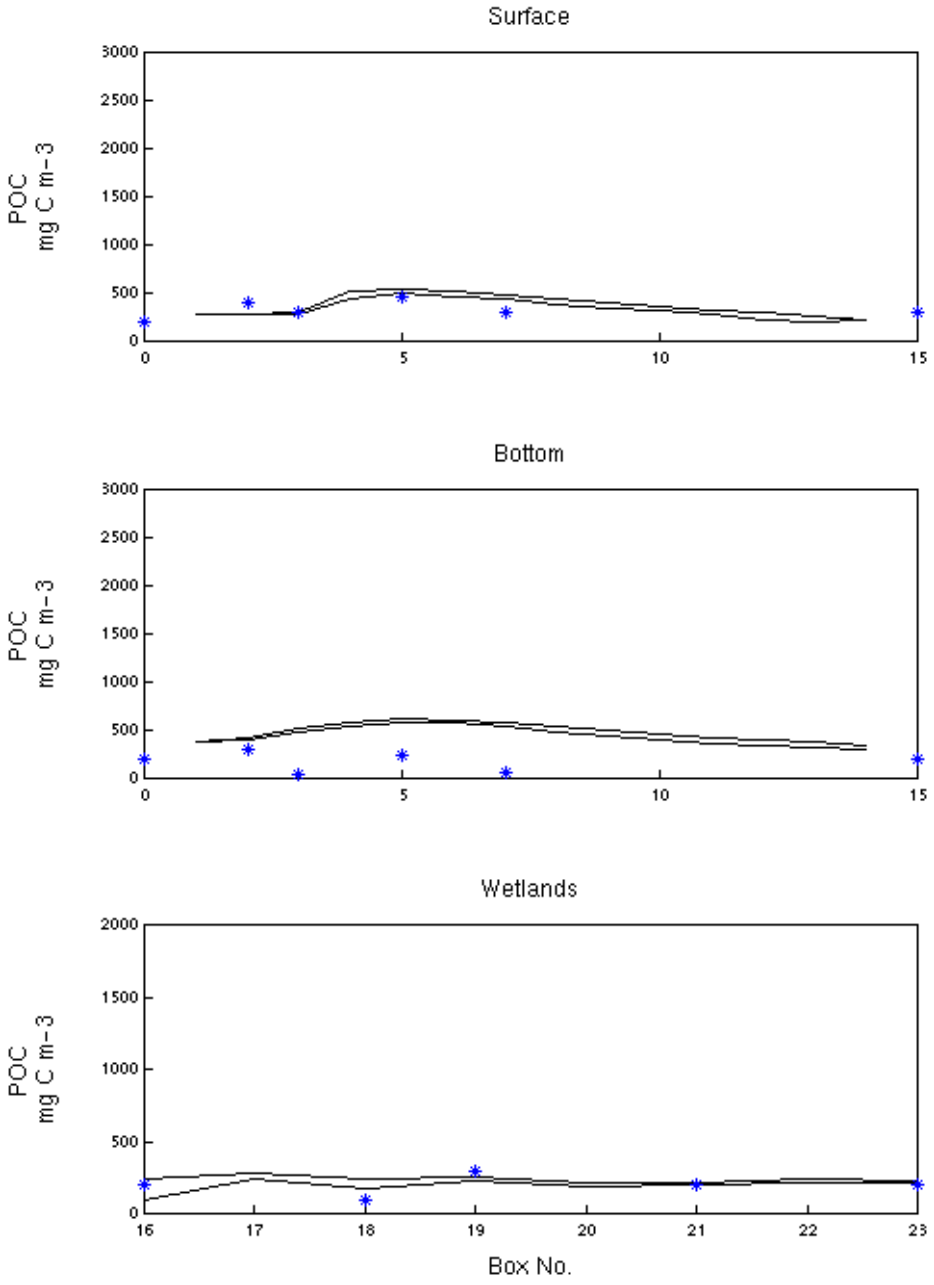

Fig. 5.3.2 b. Comparison of predicted (line) and observed (asterisk) POC in model boxes in channel surface, channel bottom and wetlands, for survey December 14, 1999.

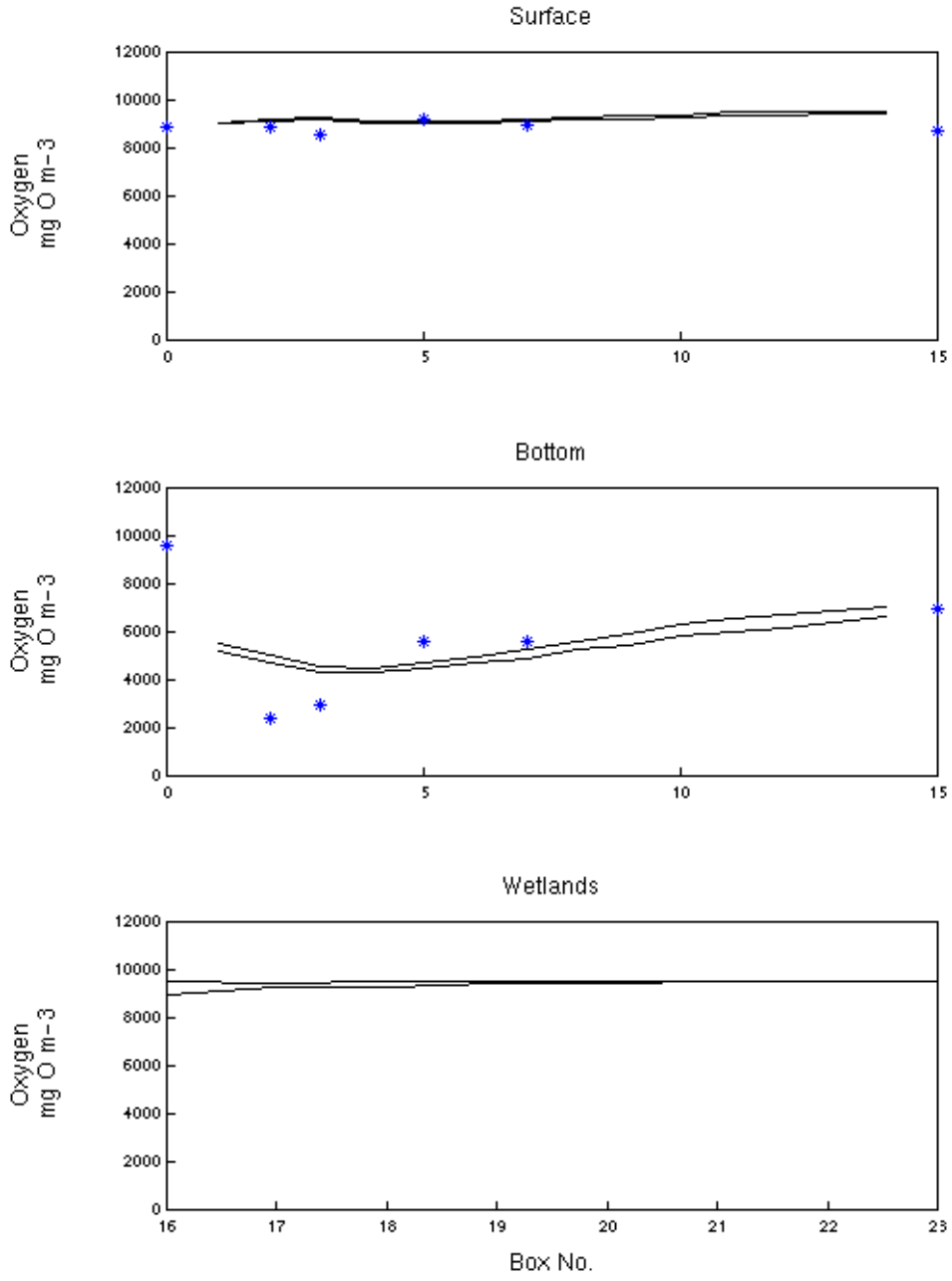

Fig. 5.3.2 c. Comparison of predicted (line) and observed (asterisk) Oxygen in model boxes in channel surface, channel bottom and wetlands, for survey December 14, 1999.

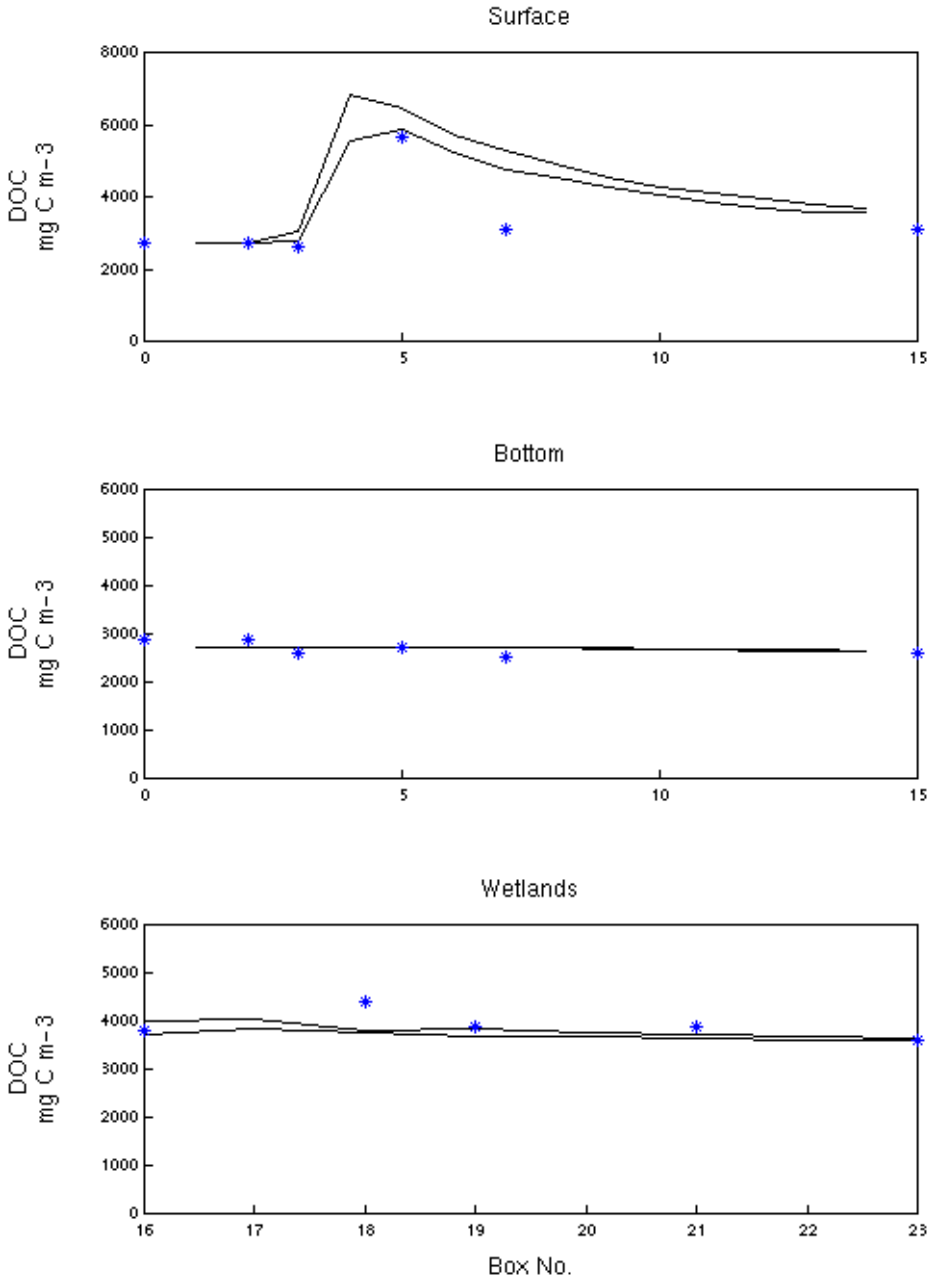

Fig. 5.3.3 a. Comparison of predicted (line) and observed (asterisk) DOC in model boxes in channel surface, channel bottom and wetlands, for survey March 7, 2000.

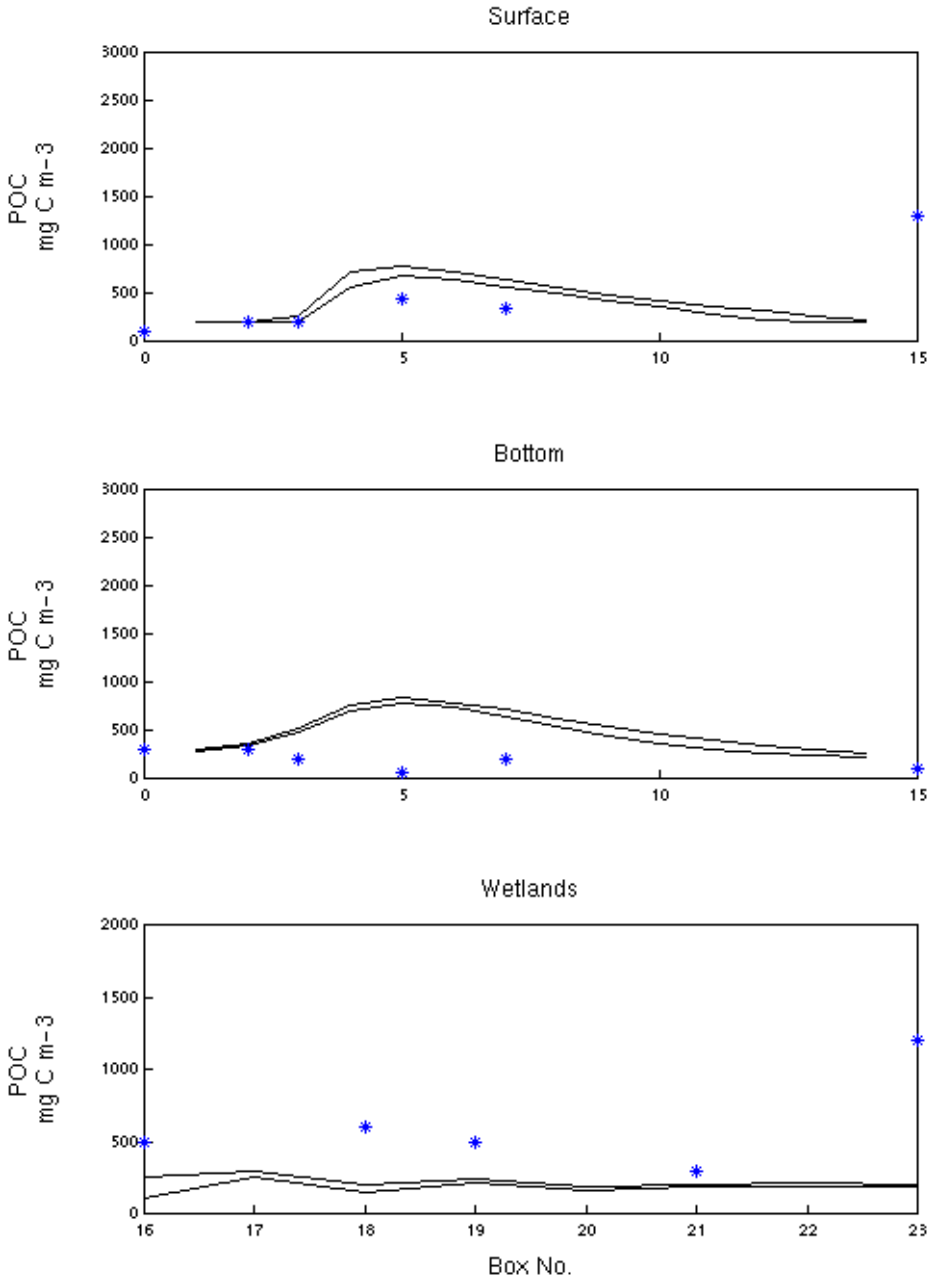

Fig. 5.3.3 b. Comparison of predicted (line) and observed (asterisk) POC in model boxes in channel surface, channel bottom and wetlands, for survey March 7, 2000.

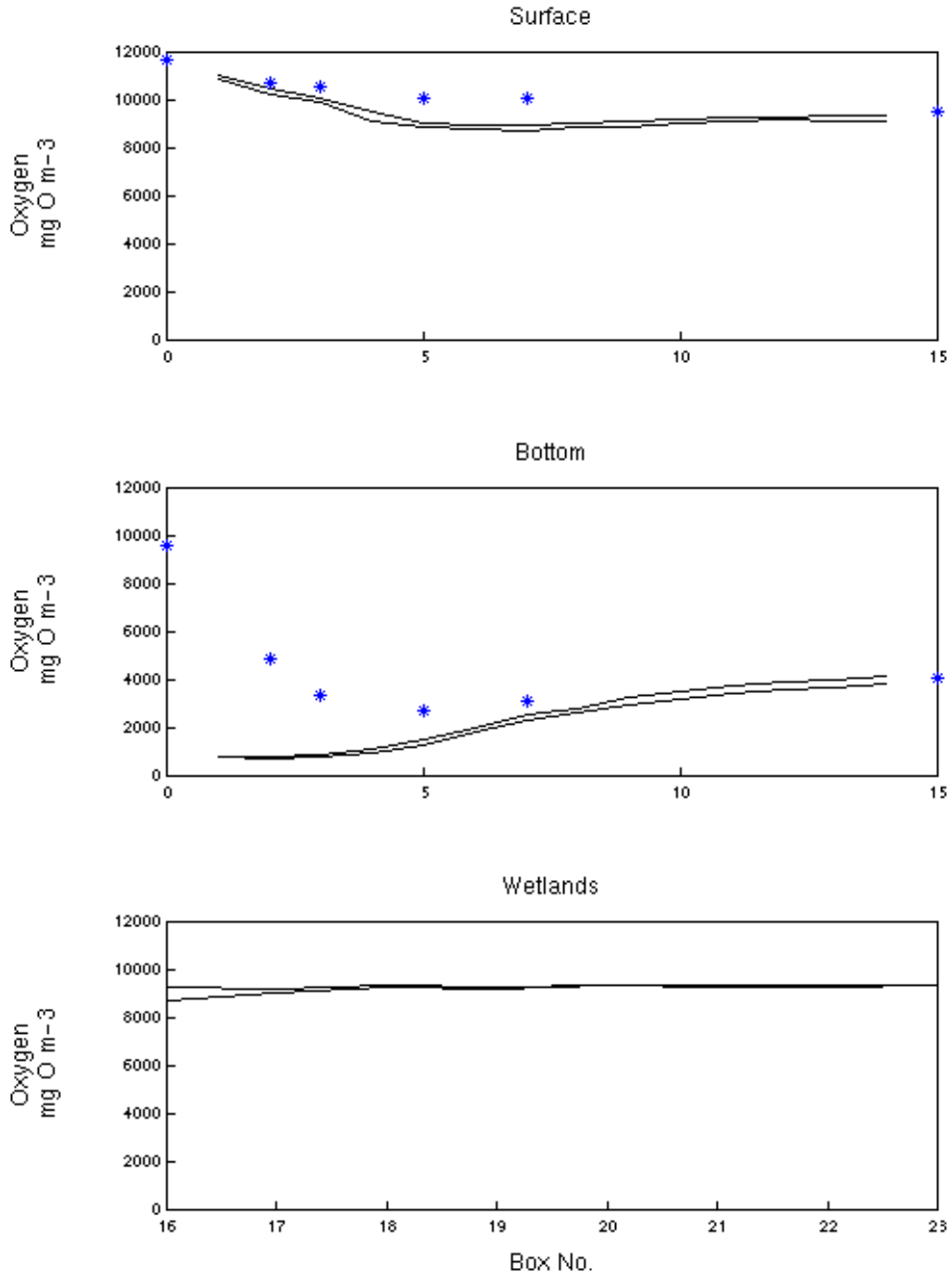

Fig. 5.3.3 c. Comparison of predicted (line) and observed (asterisk) Oxygen in model boxes in channel surface, channel bottom and wetlands, for survey March 7, 2000.

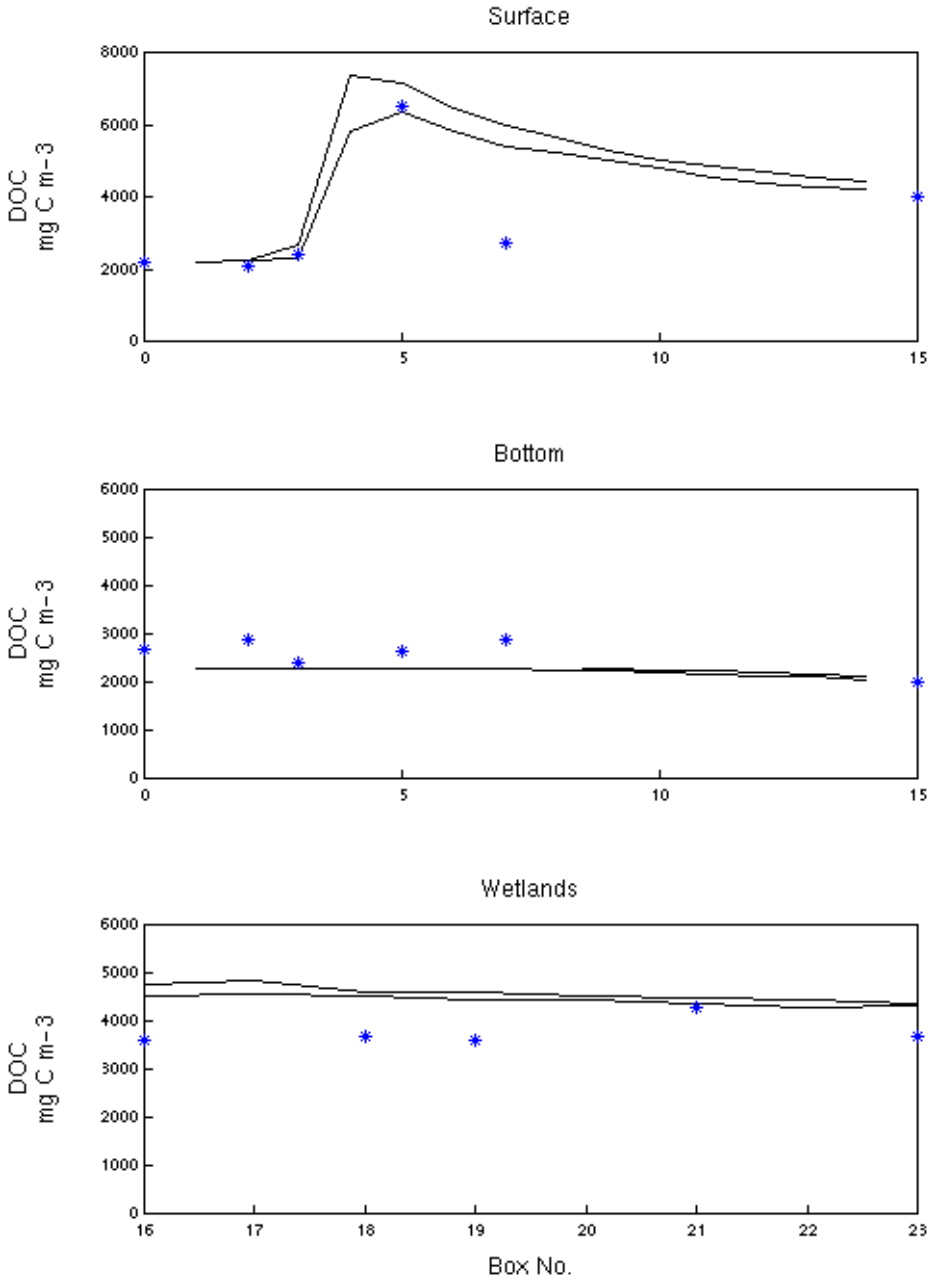

Fig. 5.3.4 a. Comparison of predicted (line) and observed (asterisk) DOC in model boxes in channel surface, channel bottom and wetlands, for survey April 17, 2000.

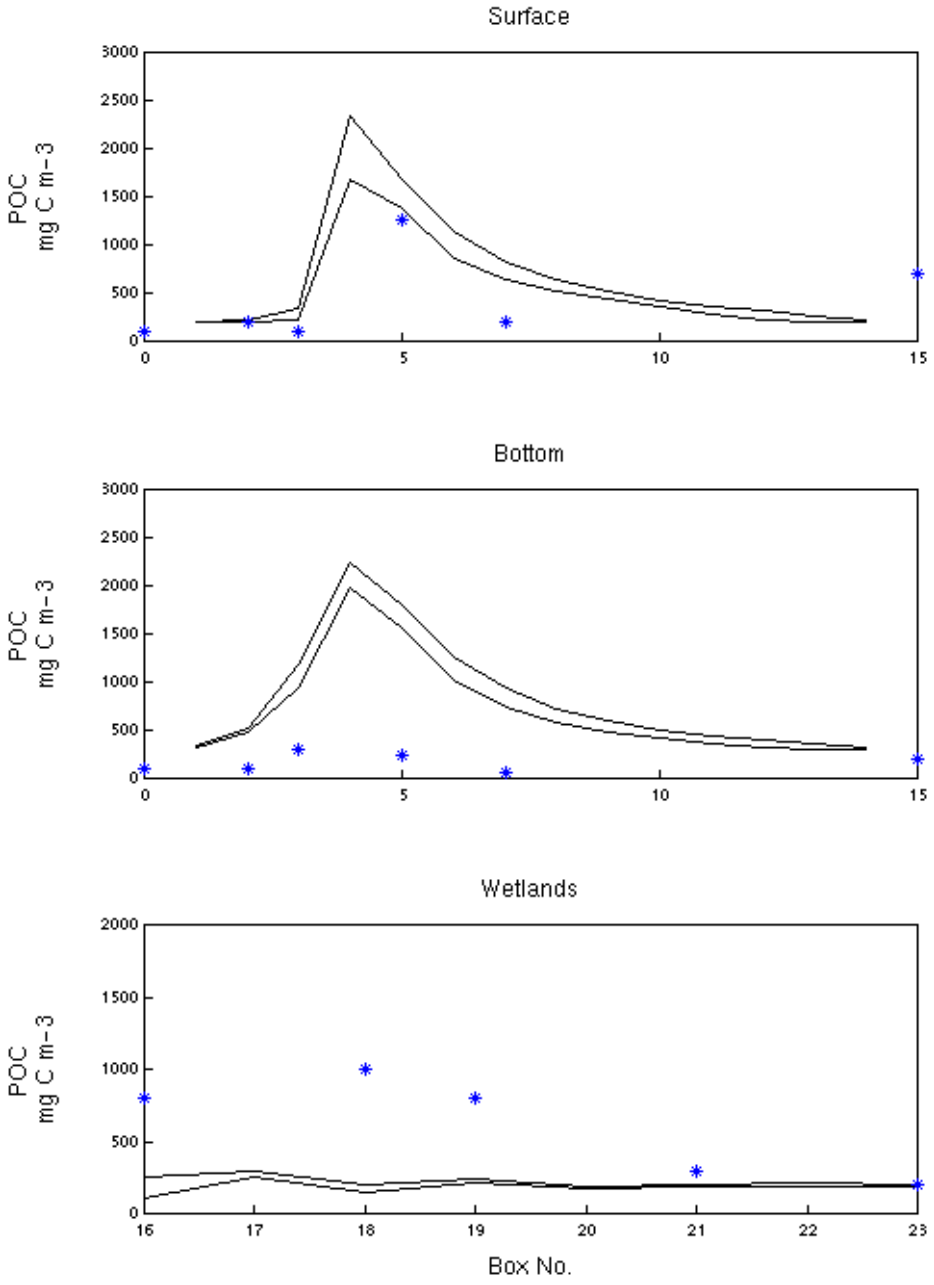

Fig. 5.3.4 b. Comparison of predicted (line) and observed (asterisk) POC in model boxes in channel surface, channel bottom and wetlands, for survey April 17, 2000.

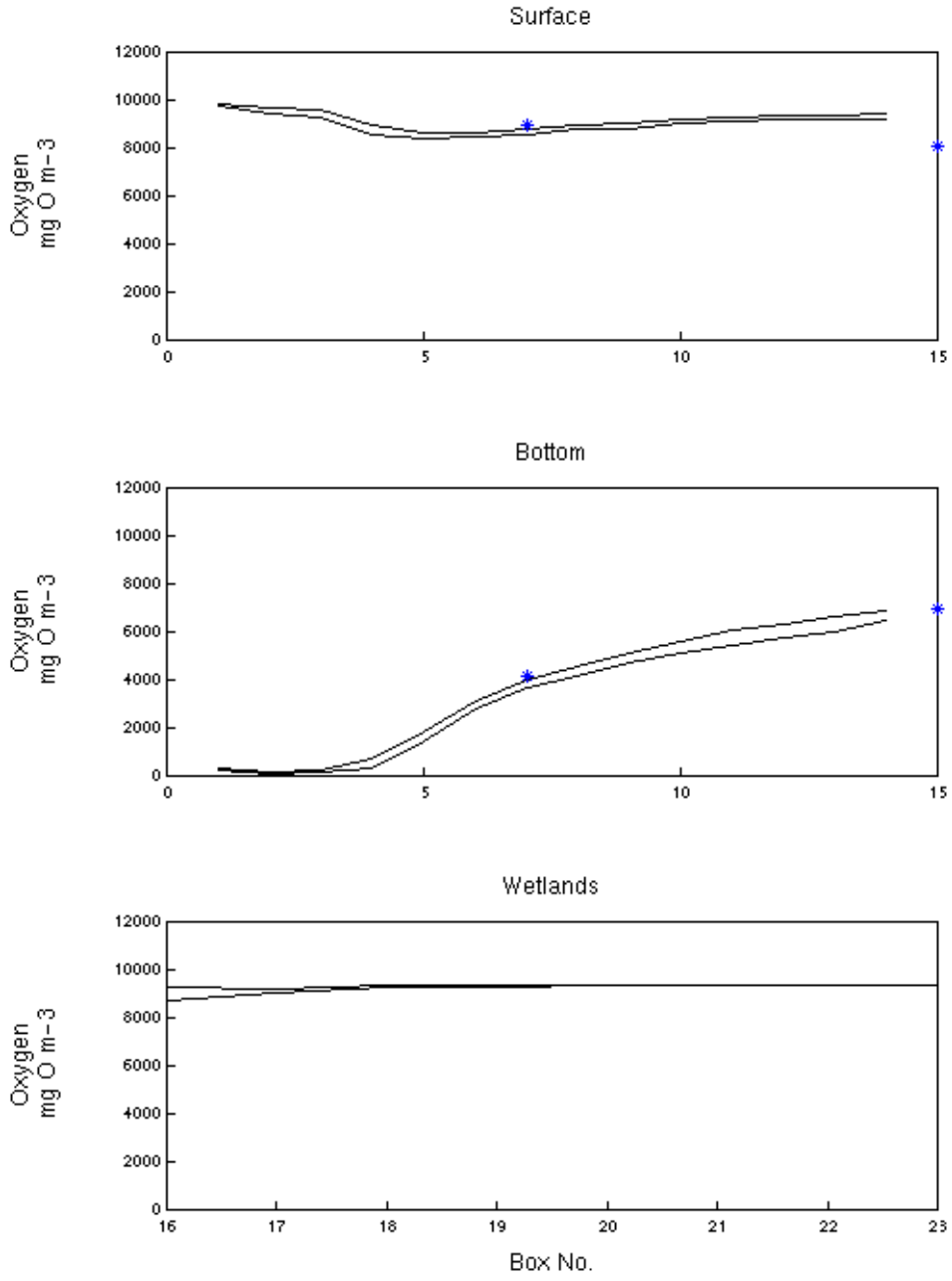

Fig. 5.3.4 c. Comparison of predicted (line) and observed (asterisk) Oxygen in model boxes in channel surface, channel bottom and wetlands, for survey April 17, 2000.

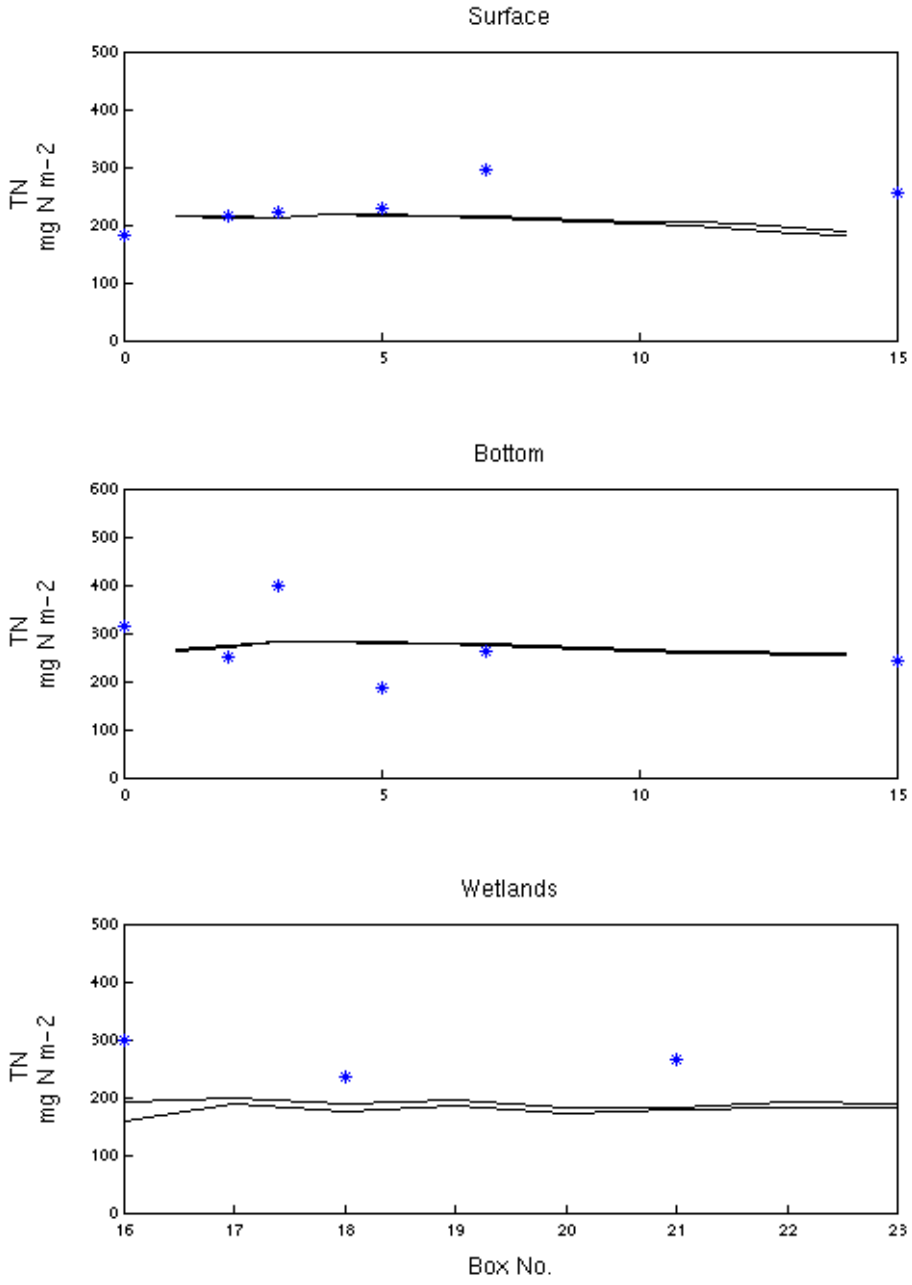

Fig. 5.3.5 a. Comparison of predicted (line) and observed (asterisk) TN in model boxes in channel surface, channel bottom and wetlands, for survey November 23, 1999.

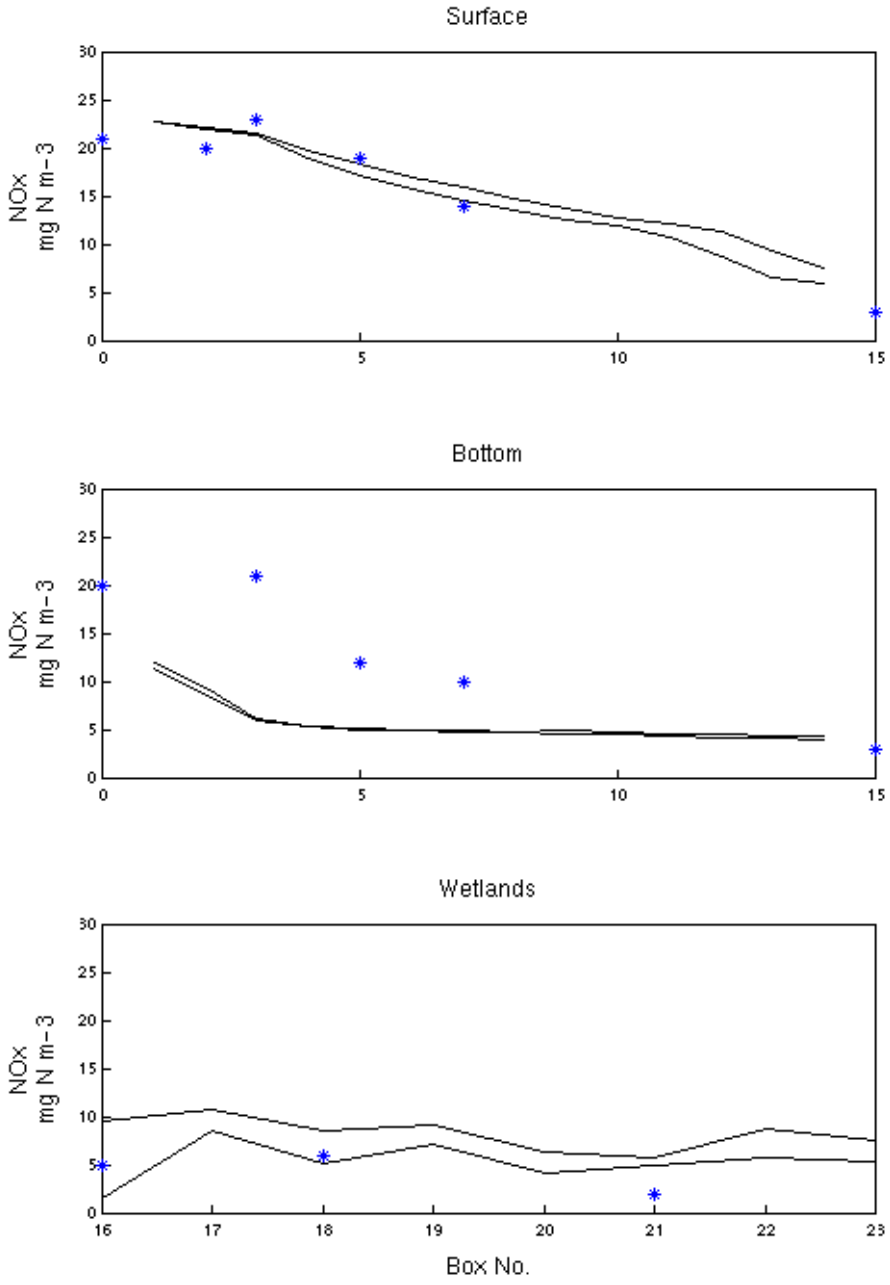

Fig. 5.3.5 b. Comparison of predicted (line) and observed (asterisk) NOx in model boxes in channel surface, channel bottom and wetlands, for survey November 23, 1999.

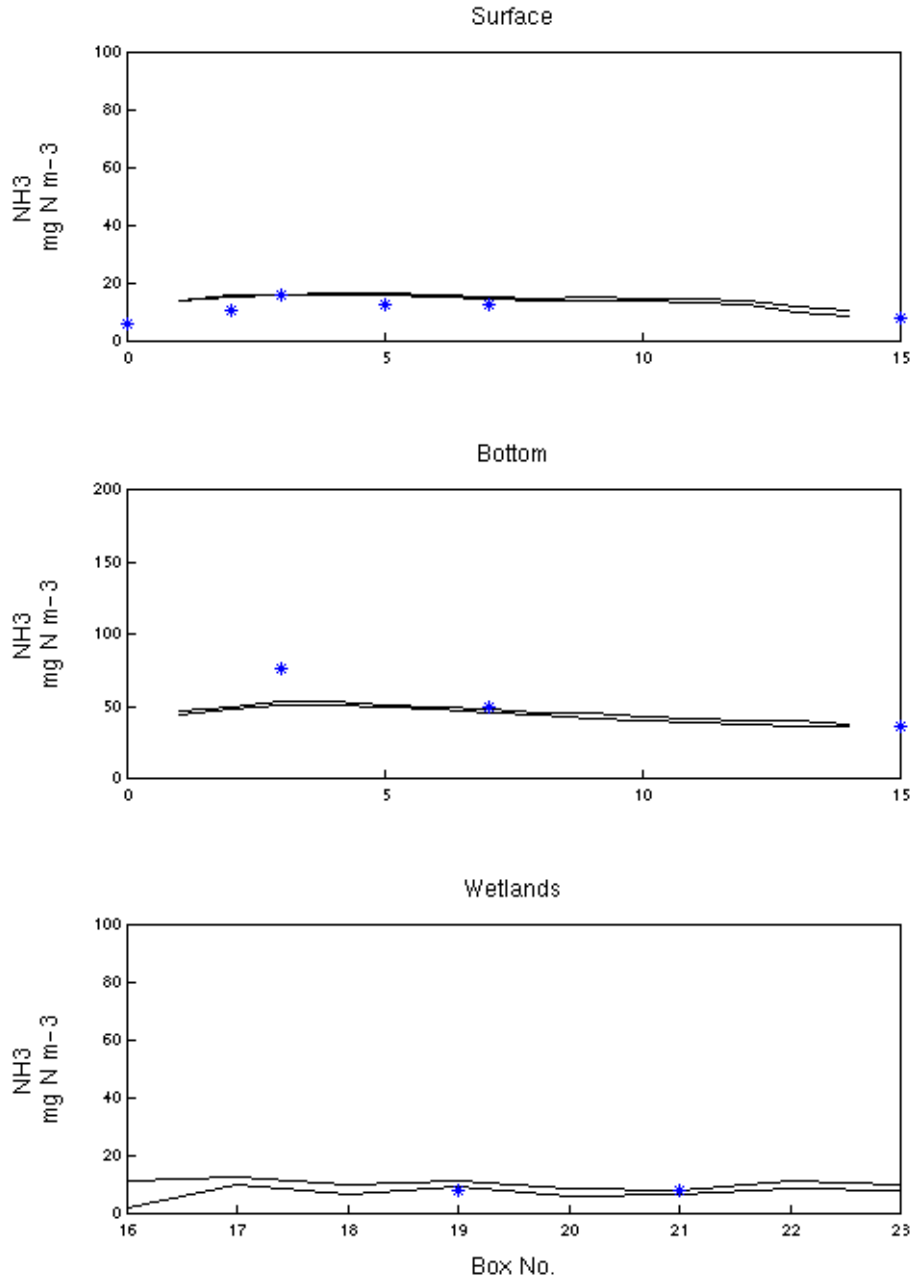

Fig. 5.3.5 c. Comparison of predicted (line) and observed (asterisk) NH_3 in model boxes in channel surface, channel bottom and wetlands, for survey November 23, 1999.

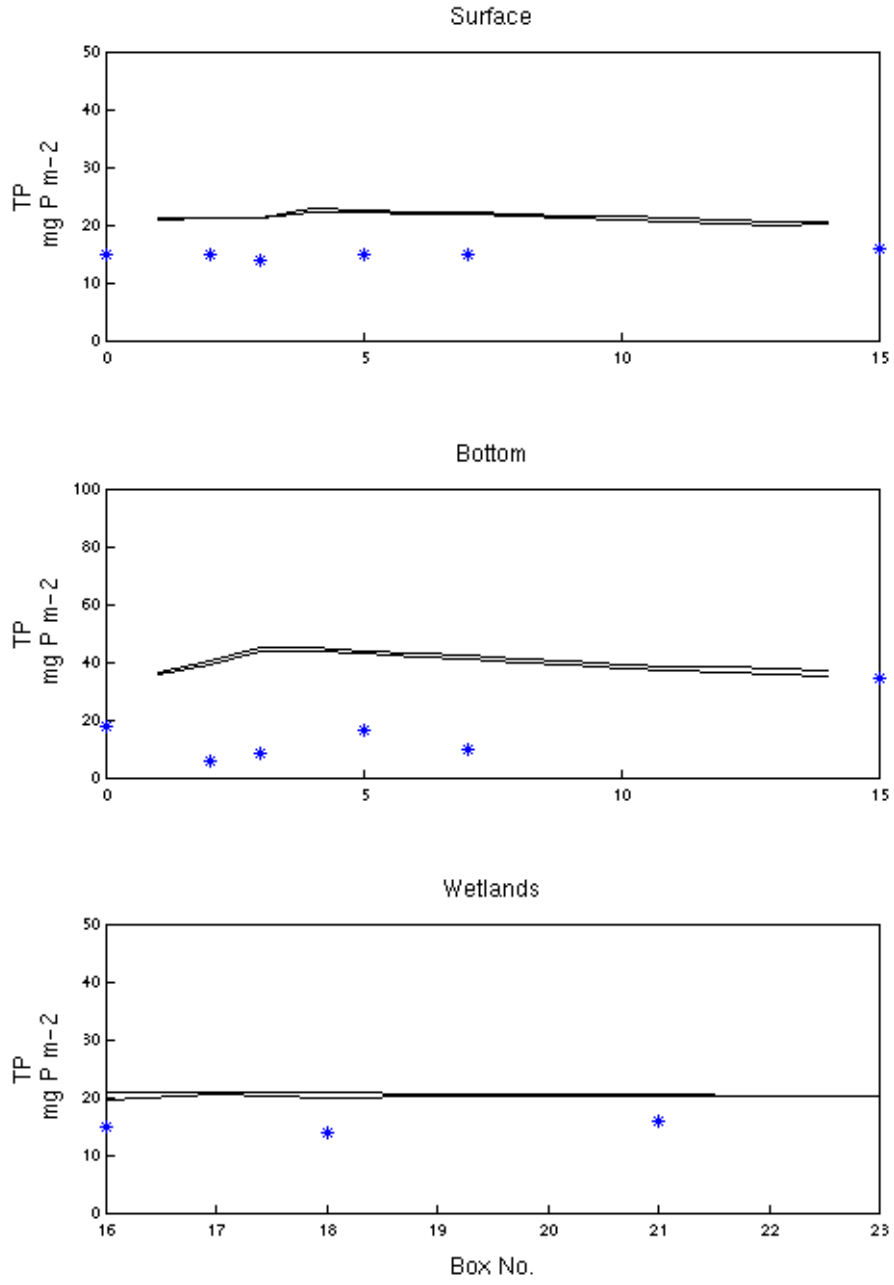

Fig. 5.3.5 d. Comparison of predicted (line) and observed (asterisk) TP in model boxes in channel surface, channel bottom and wetlands, for survey November 23, 1999.

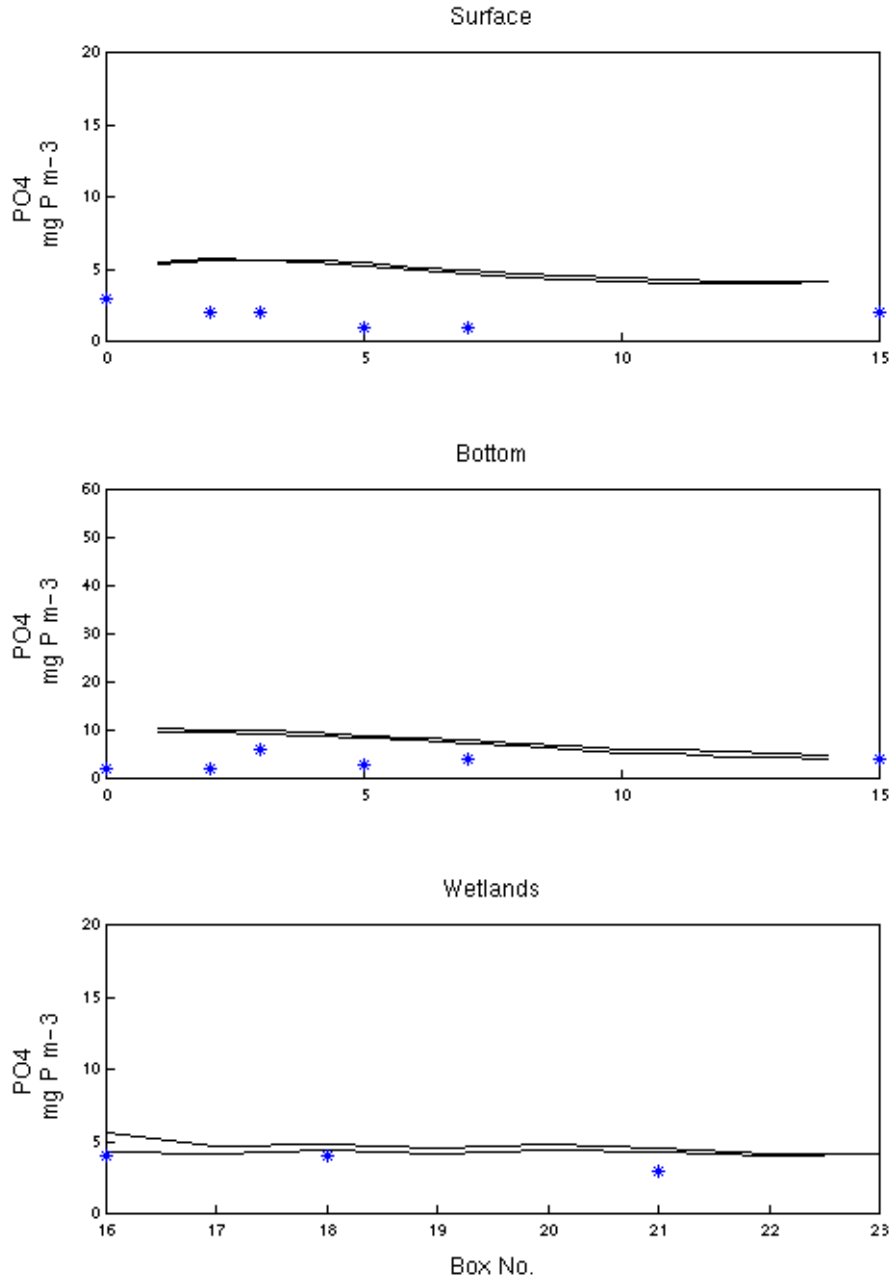

Fig. 5.3.5 e. Comparison of predicted (line) and observed (asterisk) PO_4 in model boxes in channel surface, channel bottom and wetlands, for survey November 23, 1999.

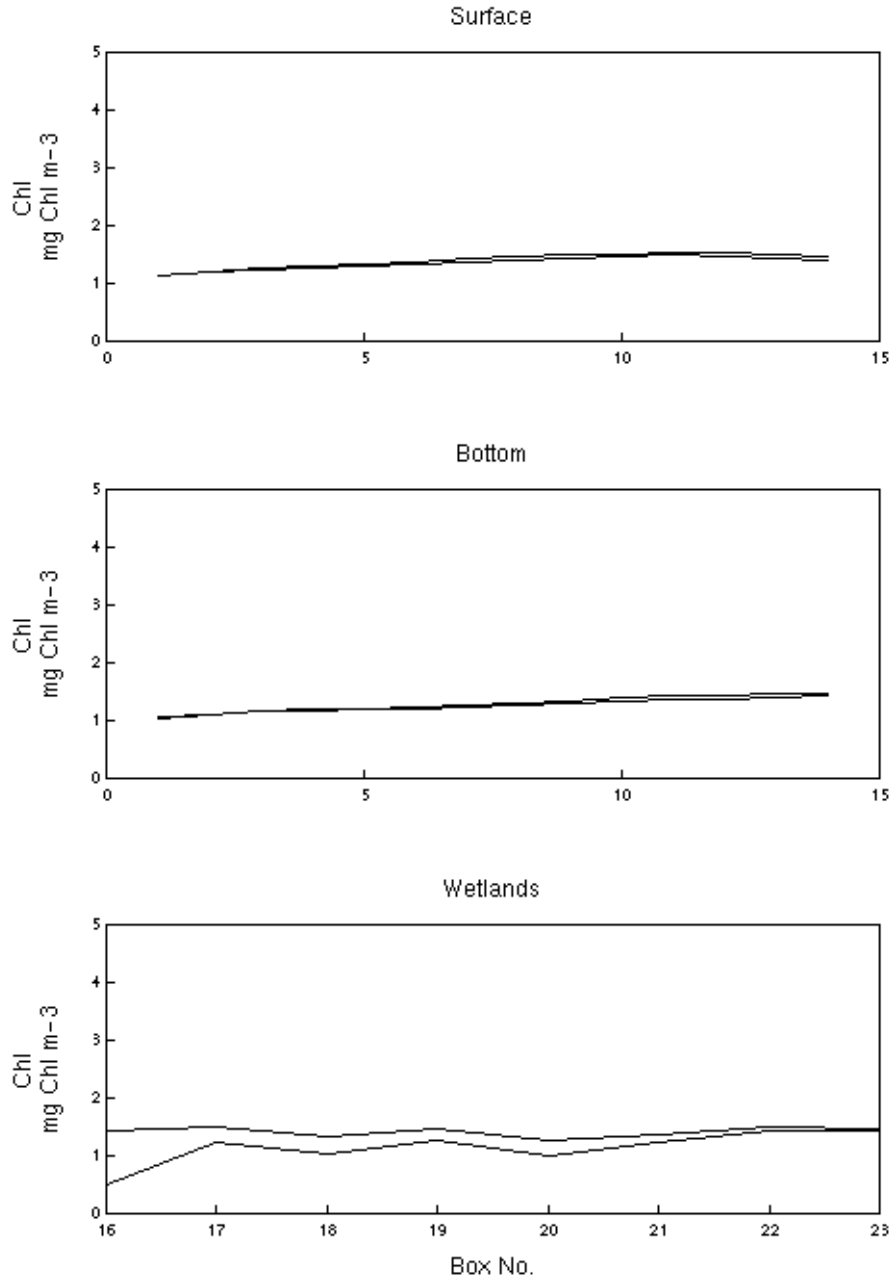

Fig. 5.3.5 f. Comparison of predicted (line) and observed (asterisk) Chl a in model boxes in channel surface, channel bottom and wetlands, for survey November 23, 1999.

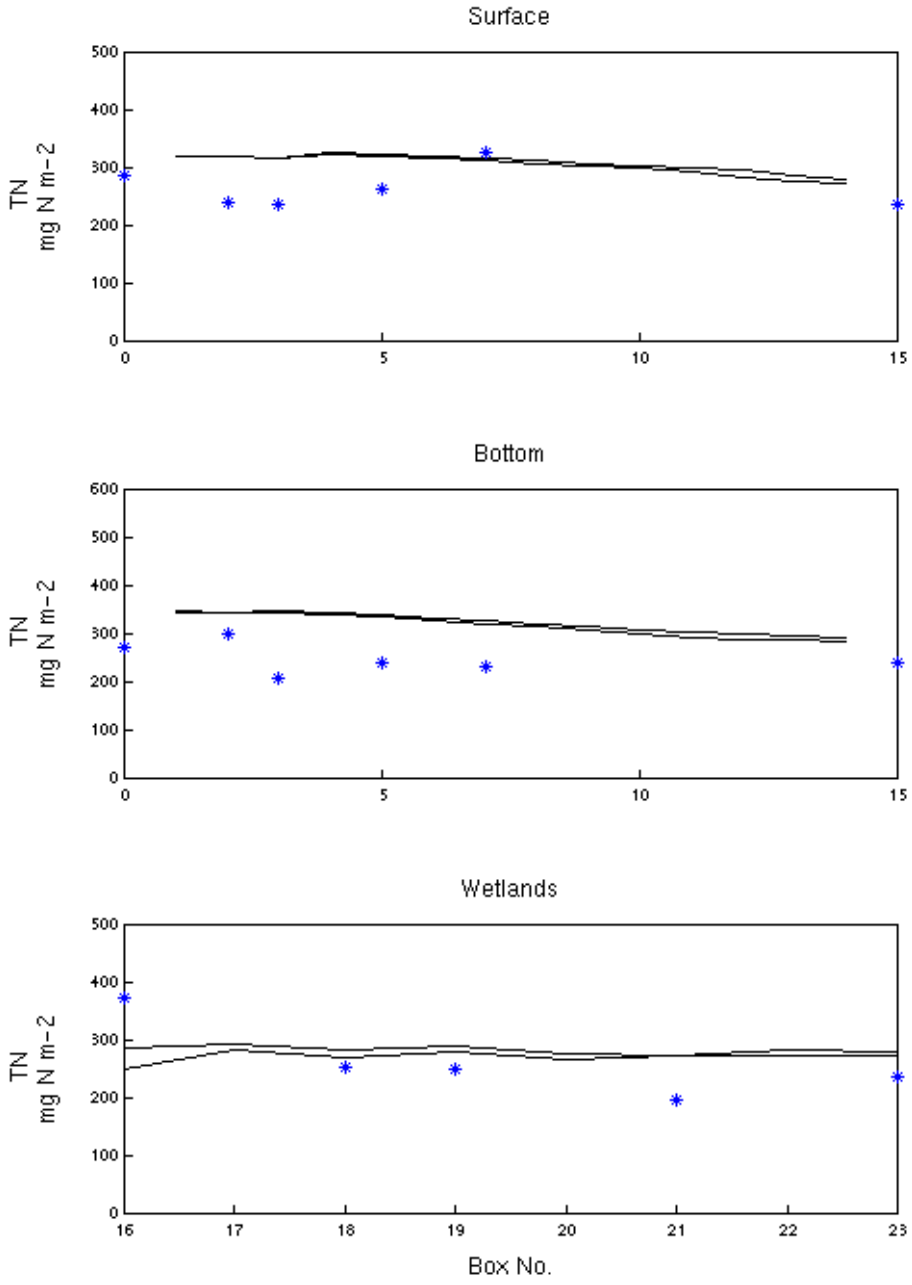

Fig. 5.3.6 a. Comparison of predicted (line) and observed (asterisk) TN in model boxes in channel surface, channel bottom and wetlands, for survey December 14, 1999.

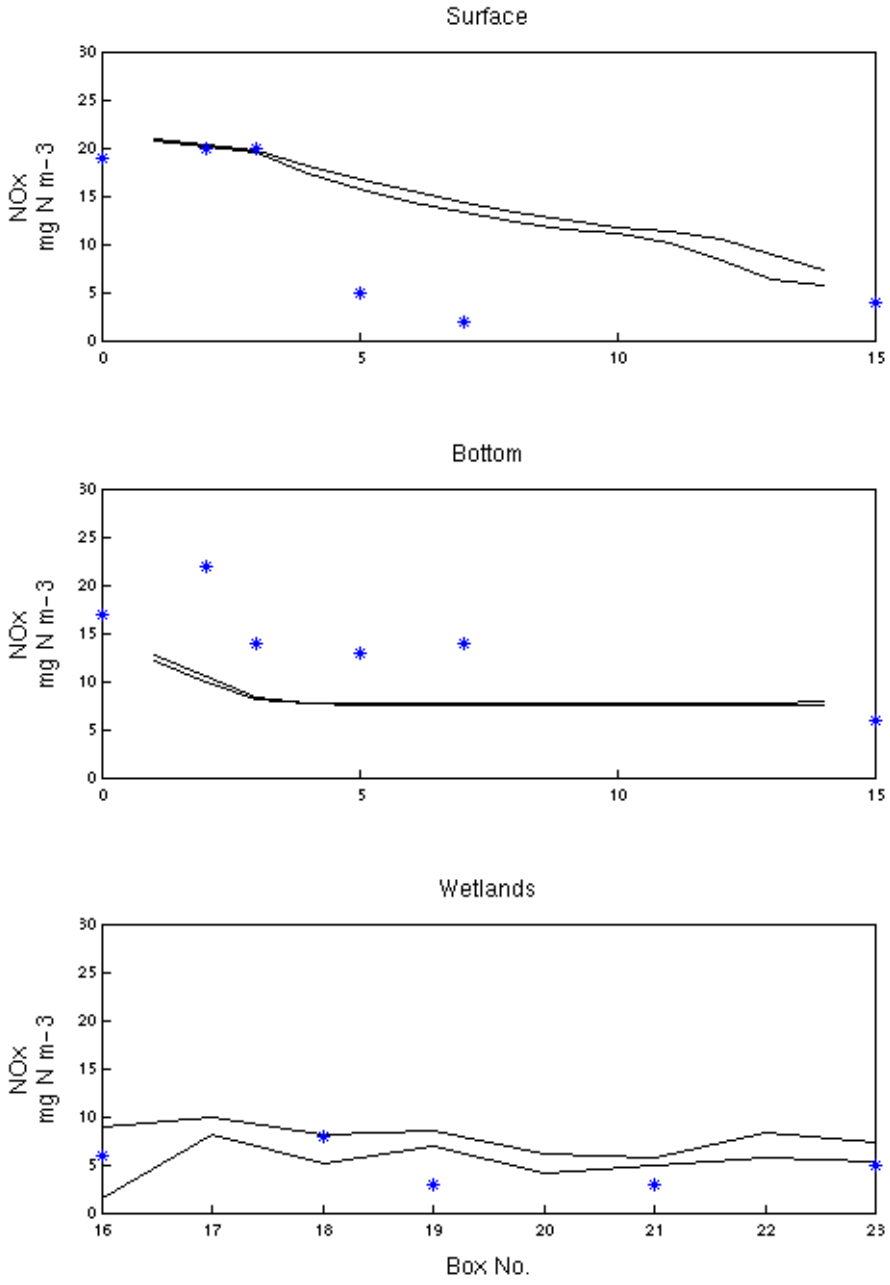

Fig. 5.3.6 b. Comparison of predicted (line) and observed (asterisk) NOx in model boxes in channel surface, channel bottom and wetlands, for survey December 14, 1999.

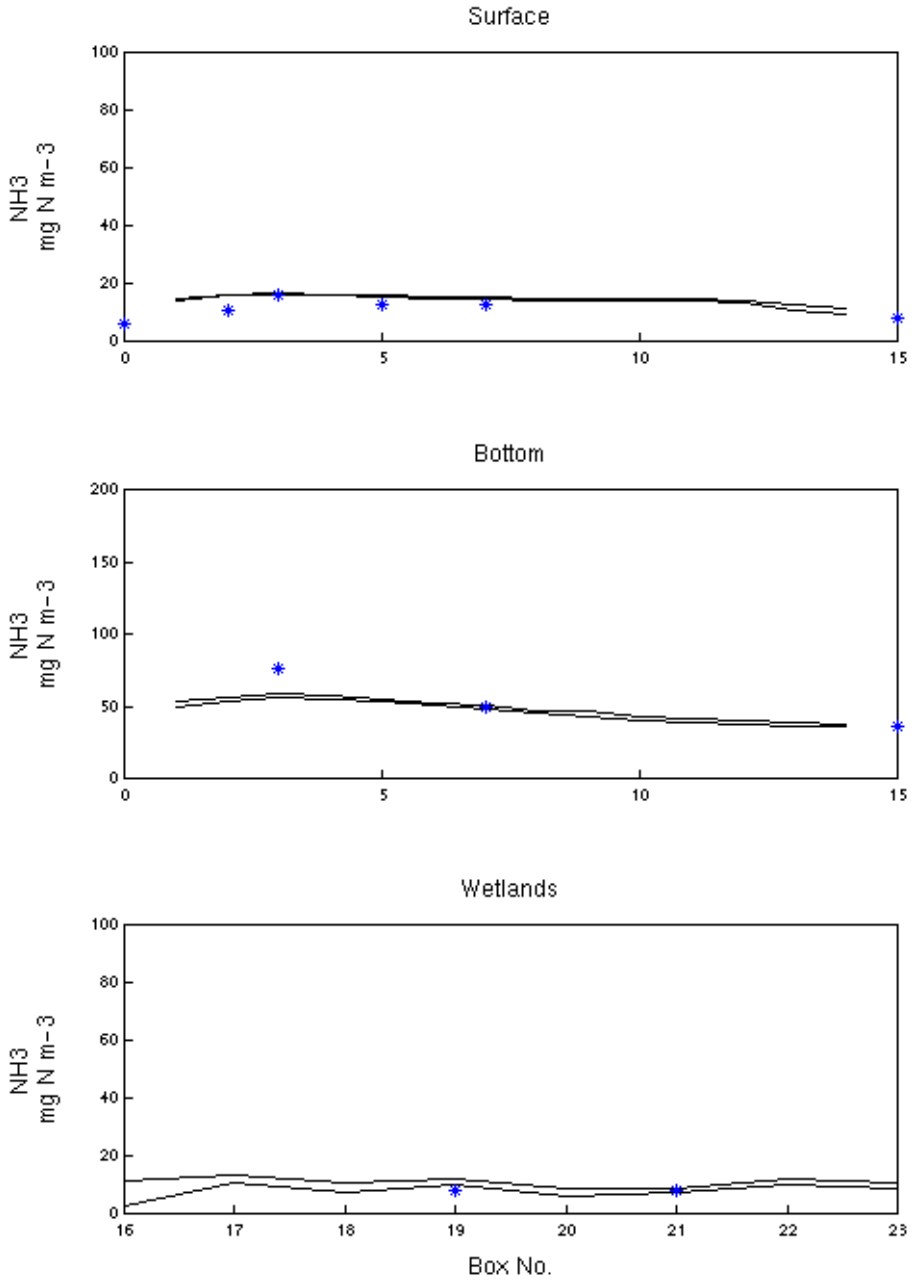

Fig. 5.3.6 c. Comparison of predicted (line) and observed (asterisk) NH_3 in model boxes in channel surface, channel bottom and wetlands, for survey December 14, 1999.

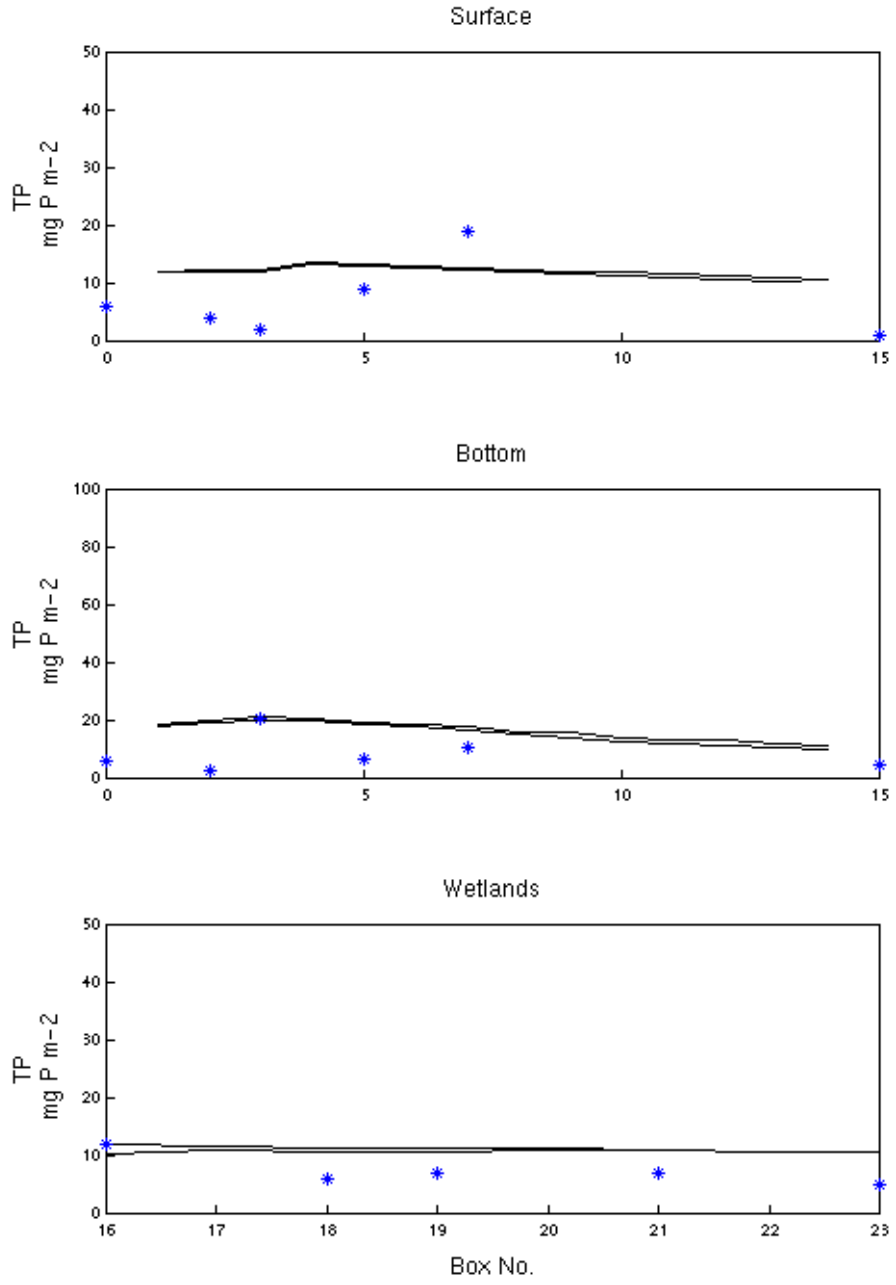

Fig. 5.3.6 d. Comparison of predicted (line) and observed (asterisk) TP in model boxes in channel surface, channel bottom and wetlands, for survey December 14, 1999.

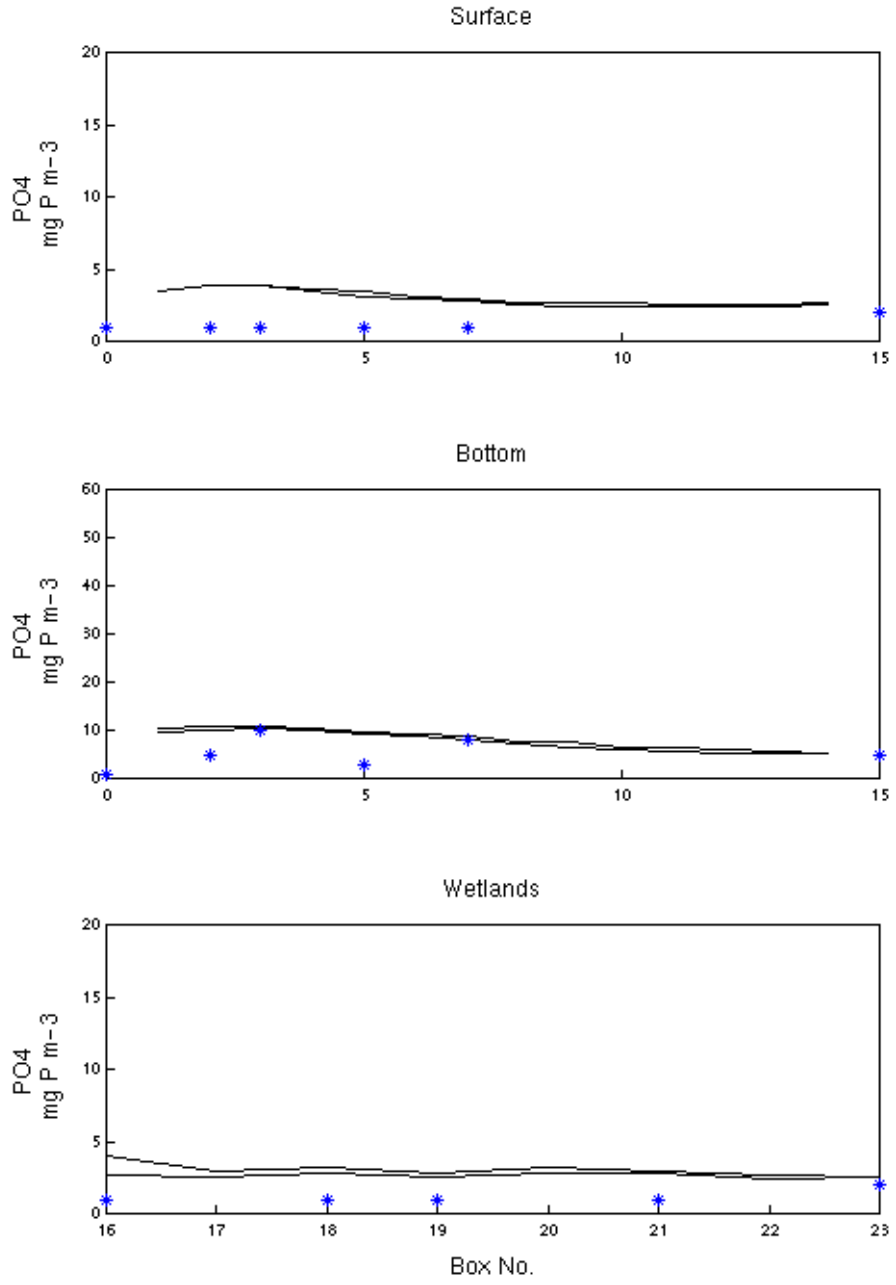

Fig. 5.3.6 e. Comparison of predicted (line) and observed (asterisk) PO_4 in model boxes in channel surface, channel bottom and wetlands, for survey December 14, 1999.

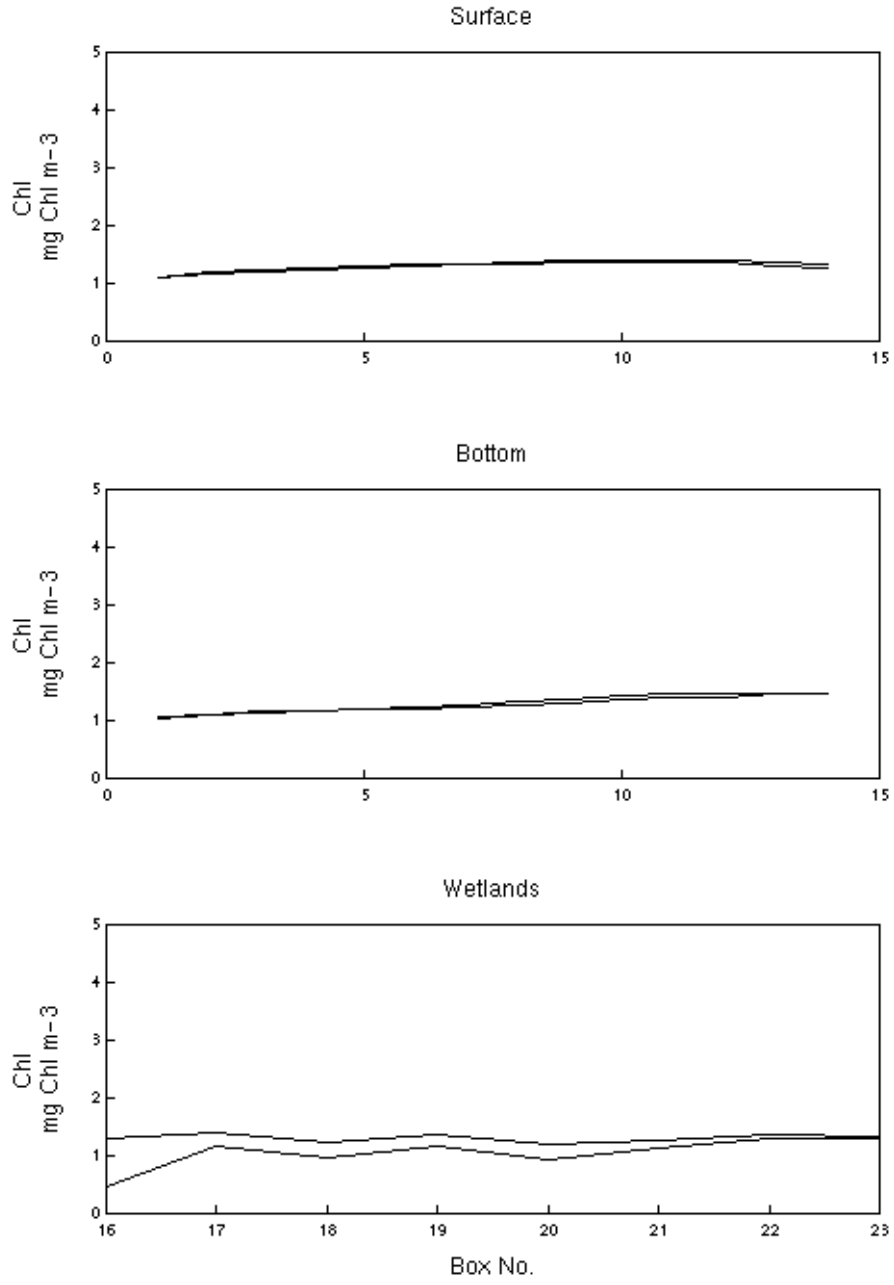

Fig. 5.3.6 f. Comparison of predicted (line) and observed (asterisk) Chl a in model boxes in channel surface, channel bottom and wetlands, for survey December 14, 1999.

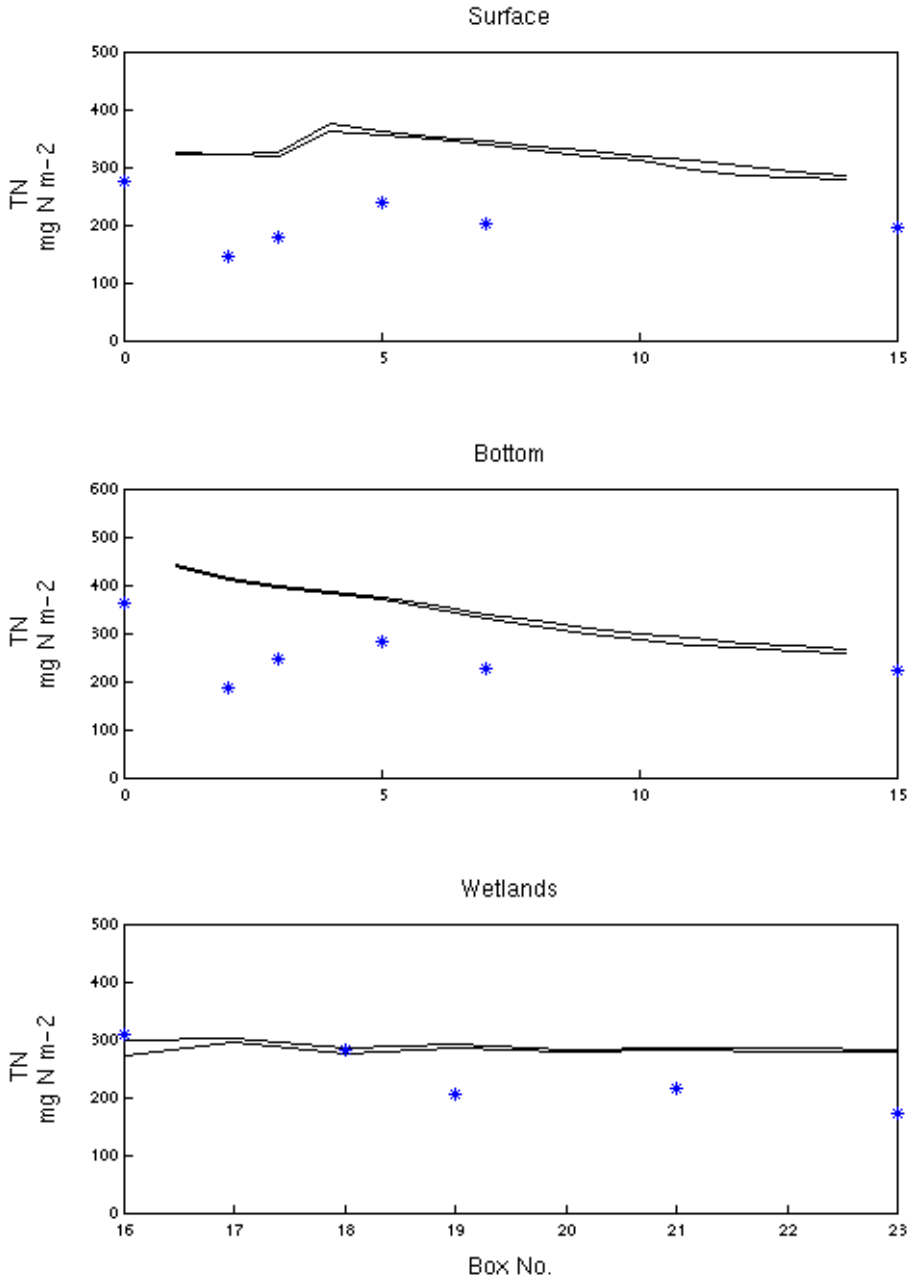

Fig. 5.3.7 a. Comparison of predicted (line) and observed (asterisk) TN in model boxes in channel surface, channel bottom and wetlands, for survey March 7, 2000.

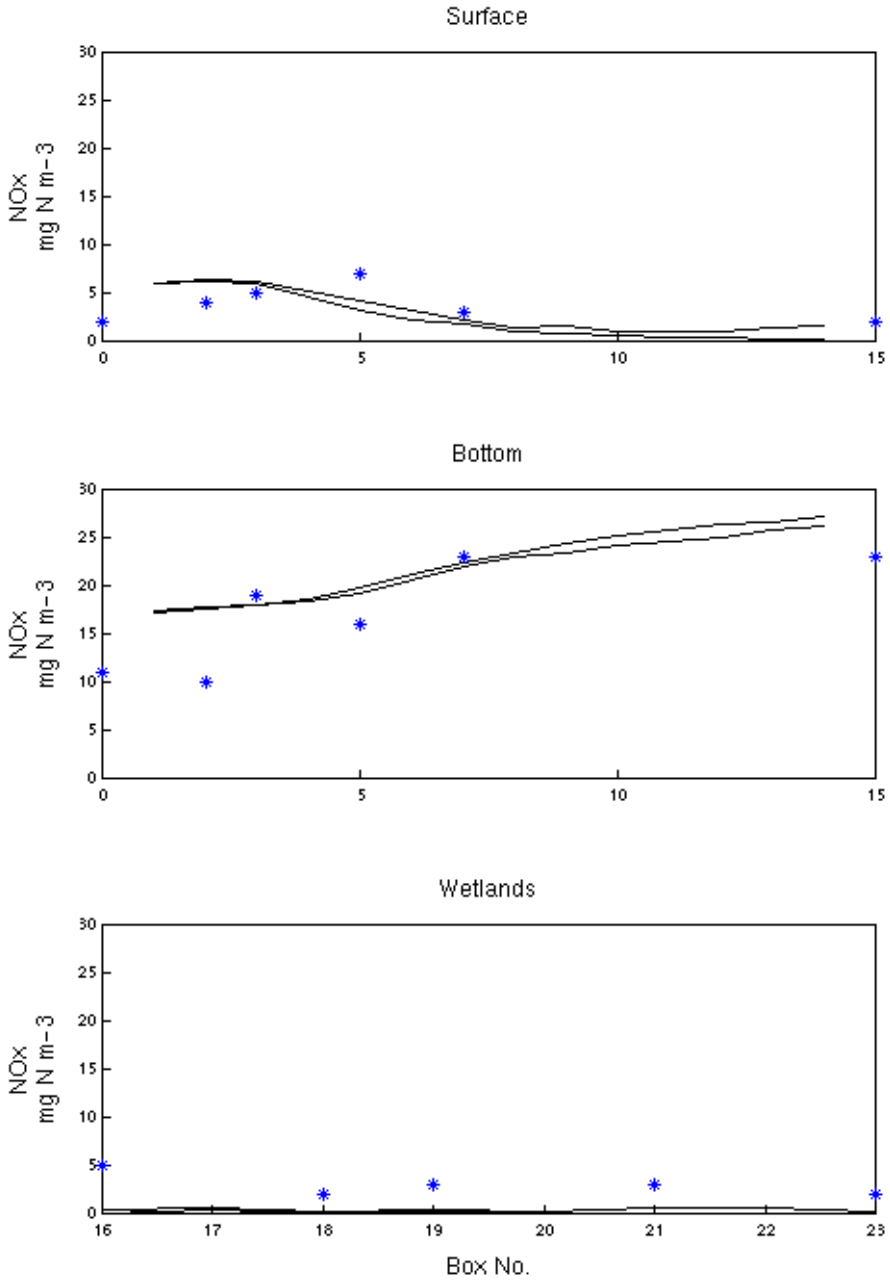

Fig. 5.3.7 b. Comparison of predicted (line) and observed (asterisk) NOx in model boxes in channel surface, channel bottom and wetlands, for survey March 7, 2000.

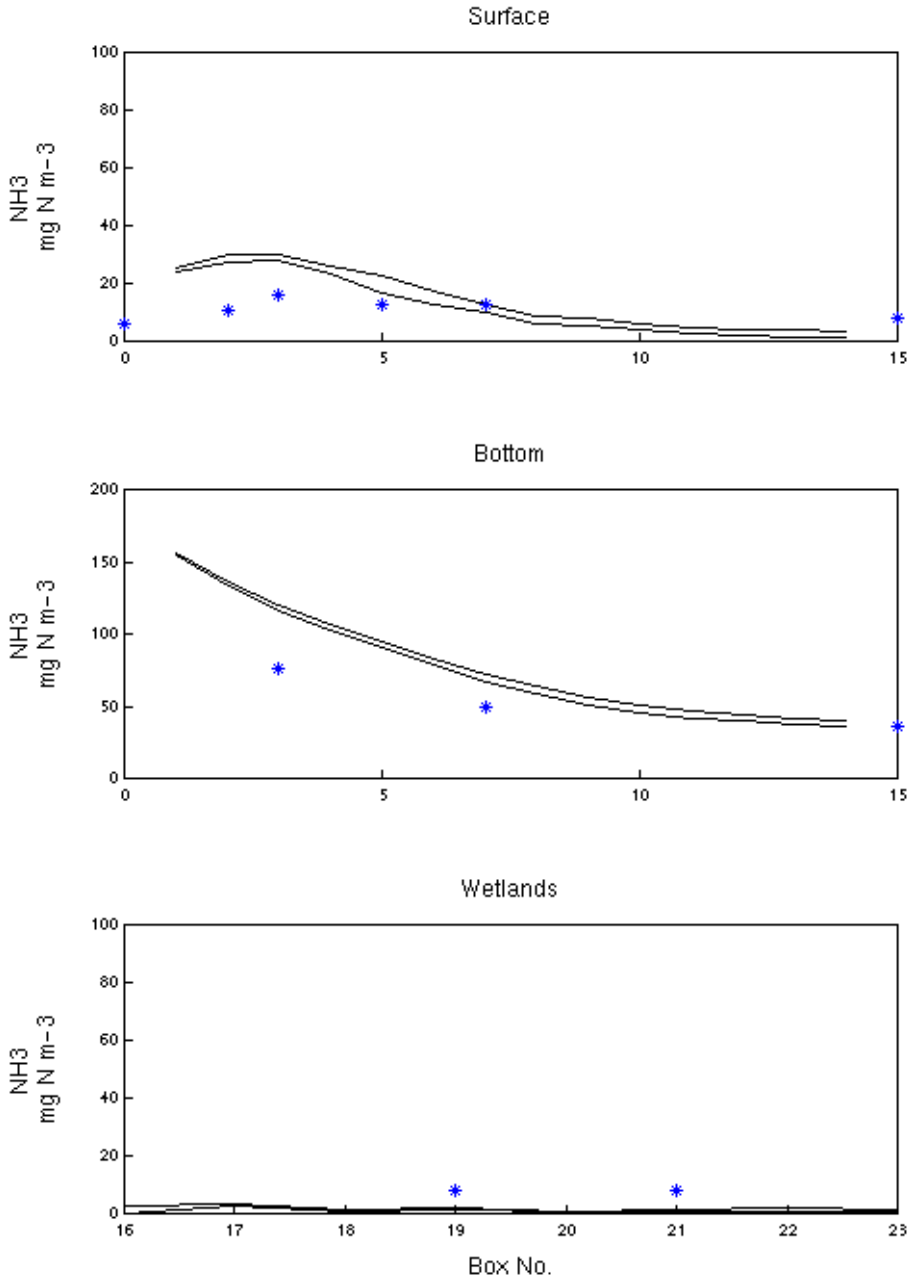

Fig. 5.3.7 c. Comparison of predicted (line) and observed (asterisk) NH_3 in model boxes in channel surface, channel bottom and wetlands, for survey March 7, 2000.

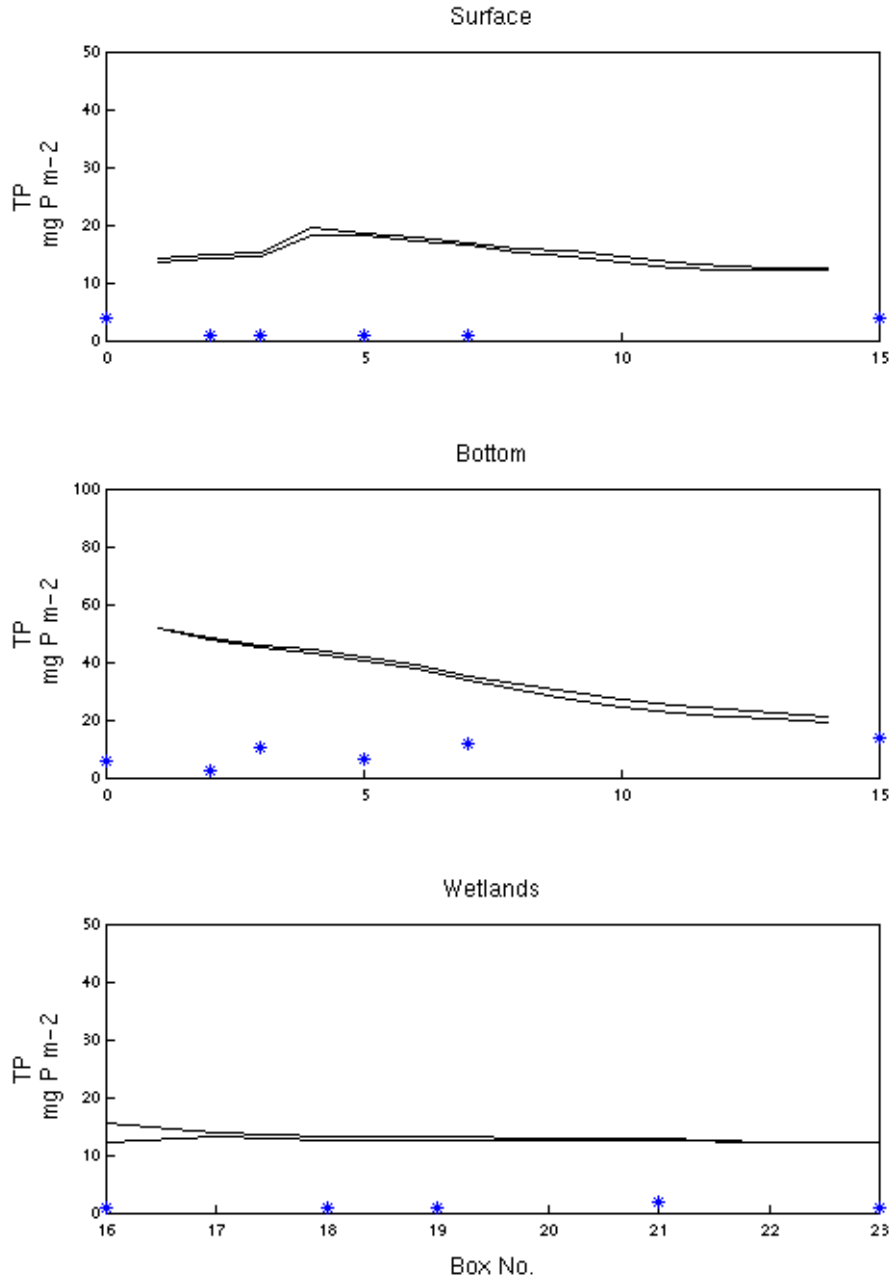

Fig. 5.3.7 d. Comparison of predicted (line) and observed (asterisk) TP in model boxes in channel surface, channel bottom and wetlands, for survey March 7, 2000.

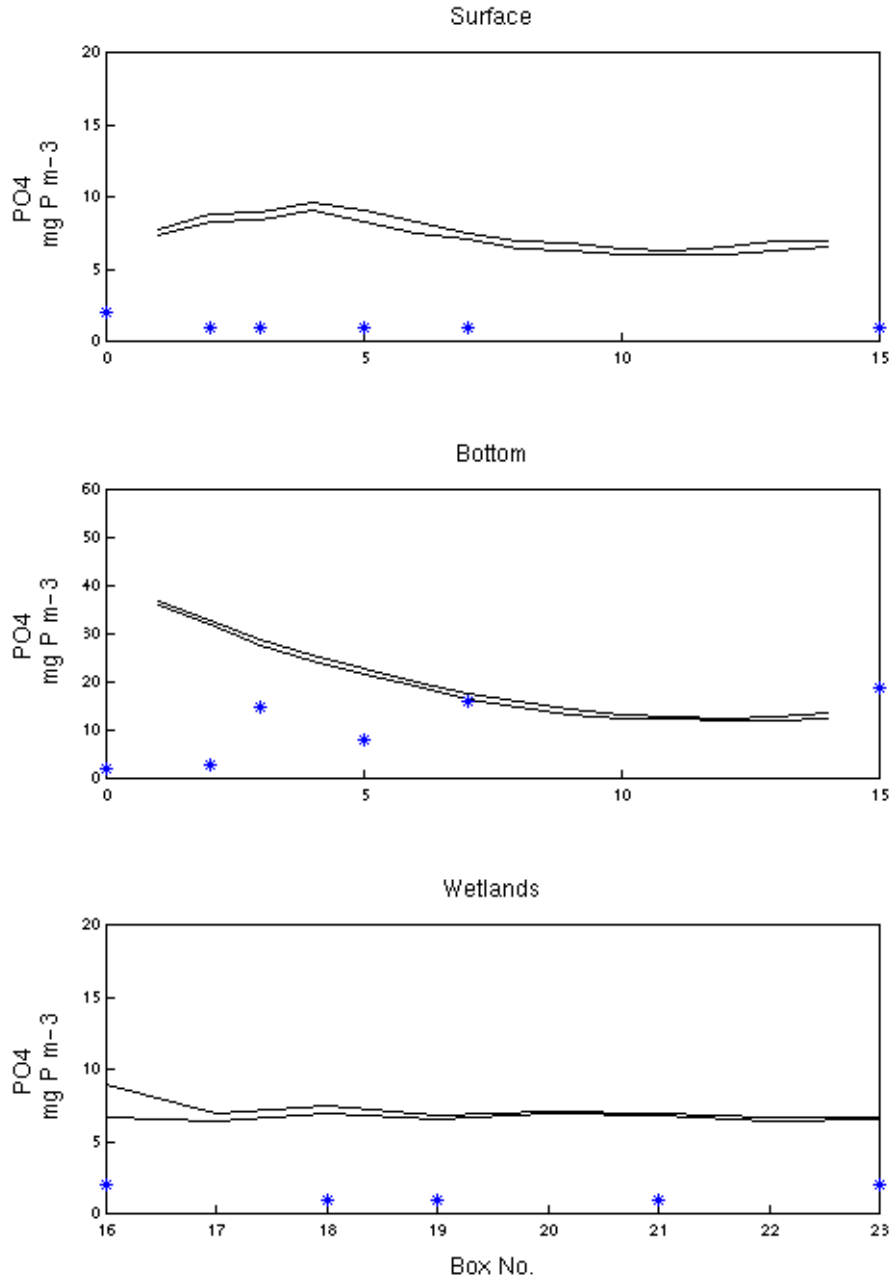

Fig. 5.3.7 e. Comparison of predicted (line) and observed (asterisk) PO_4 in model boxes in channel surface, channel bottom and wetlands, for survey March 7, 2000.

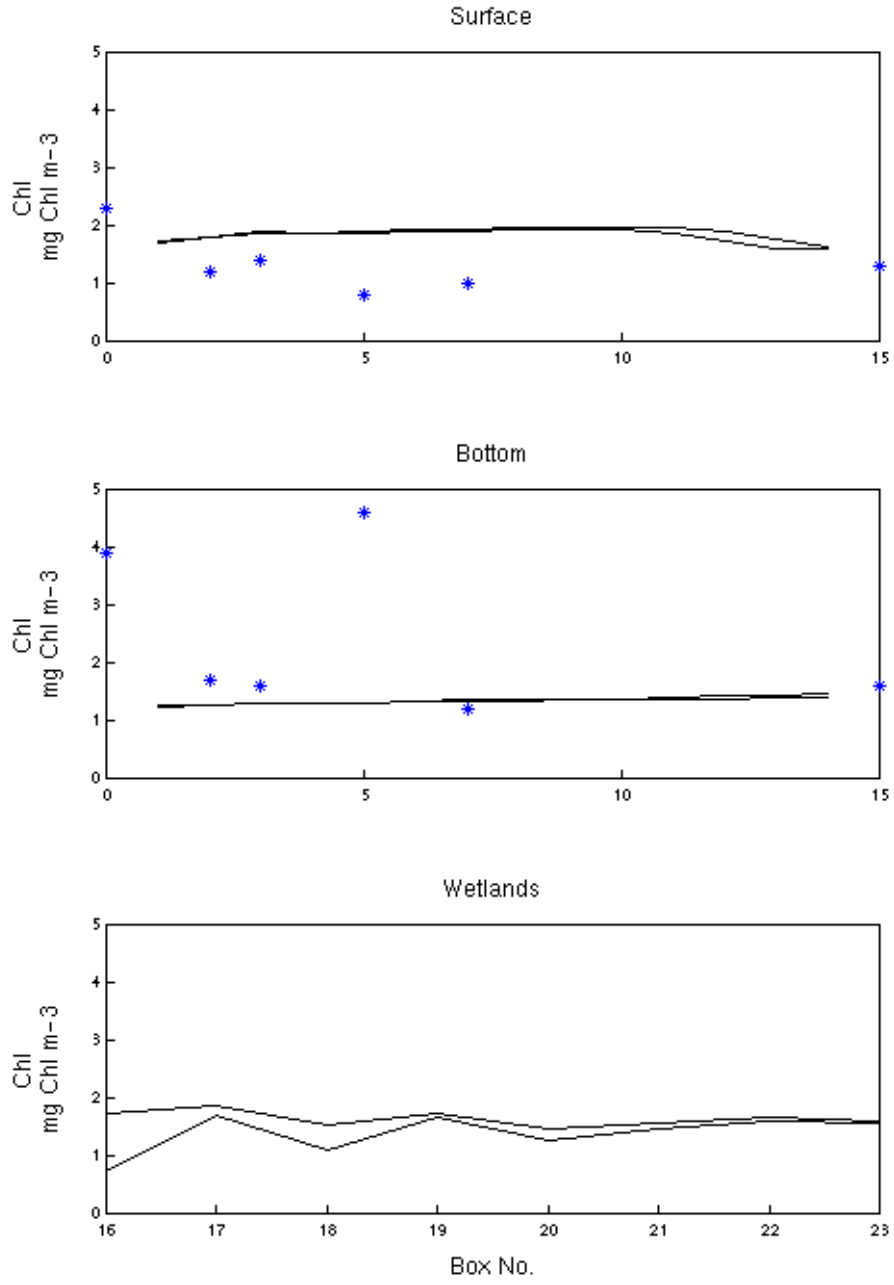

Fig. 5.3.7 f. Comparison of predicted (line) and observed (asterisk) Chl a in model boxes in channel surface, channel bottom and wetlands, for survey March 7, 2000.

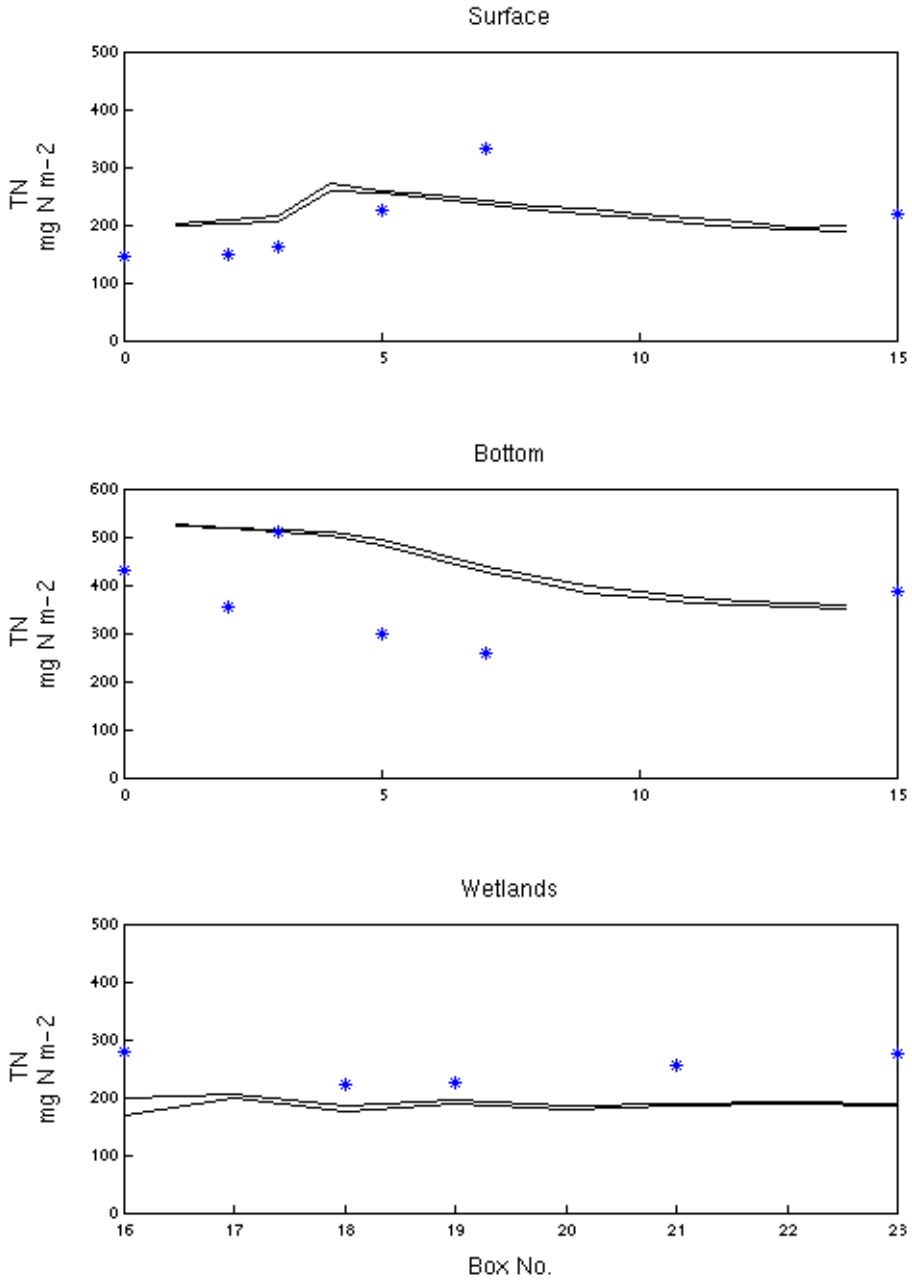

Fig. 5.3.8 a. Comparison of predicted (line) and observed (asterisk) TN in model boxes in channel surface, channel bottom and wetlands, for survey April 17, 2000.

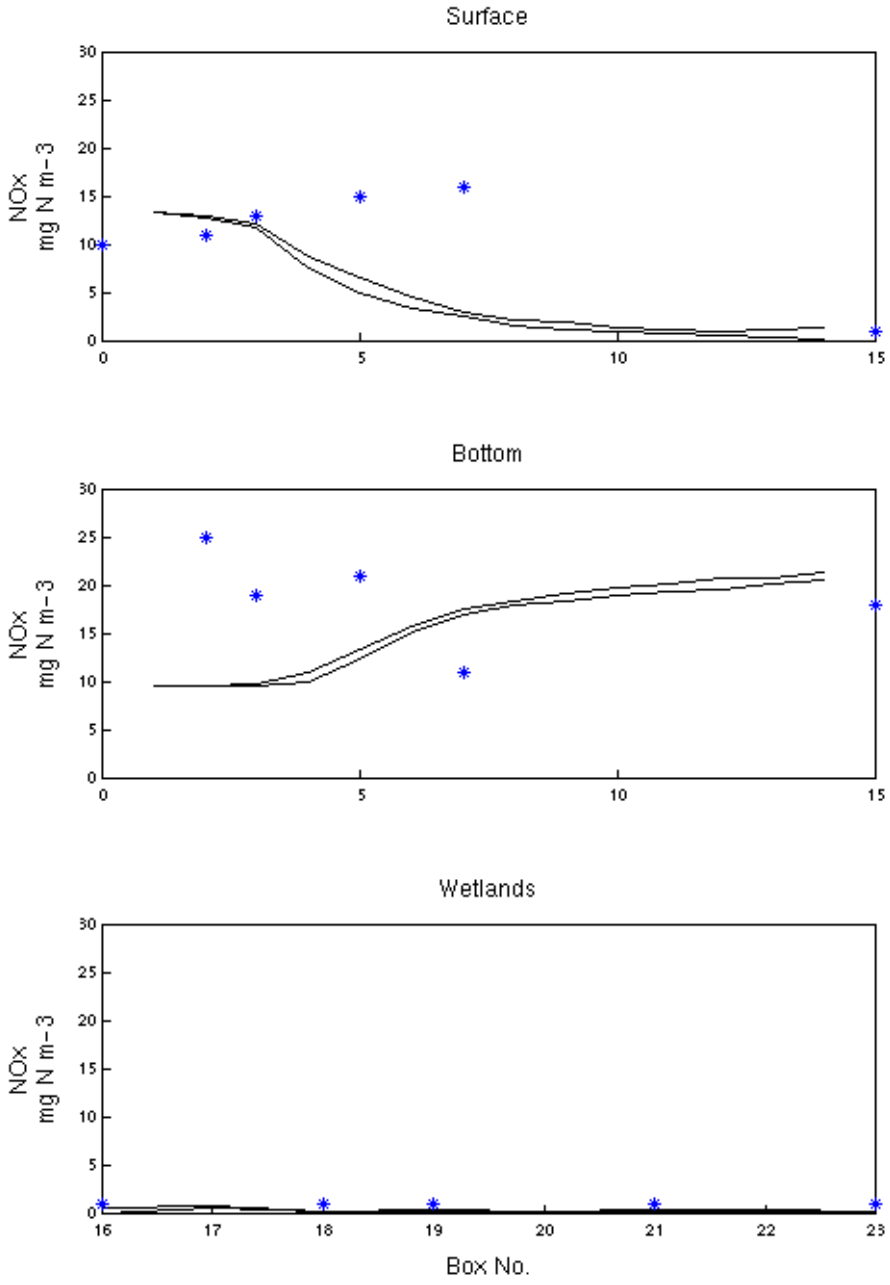

Fig. 5.3.8 b. Comparison of predicted (line) and observed (asterisk) NOx in model boxes in channel surface, channel bottom and wetlands, for survey April 17, 2000.

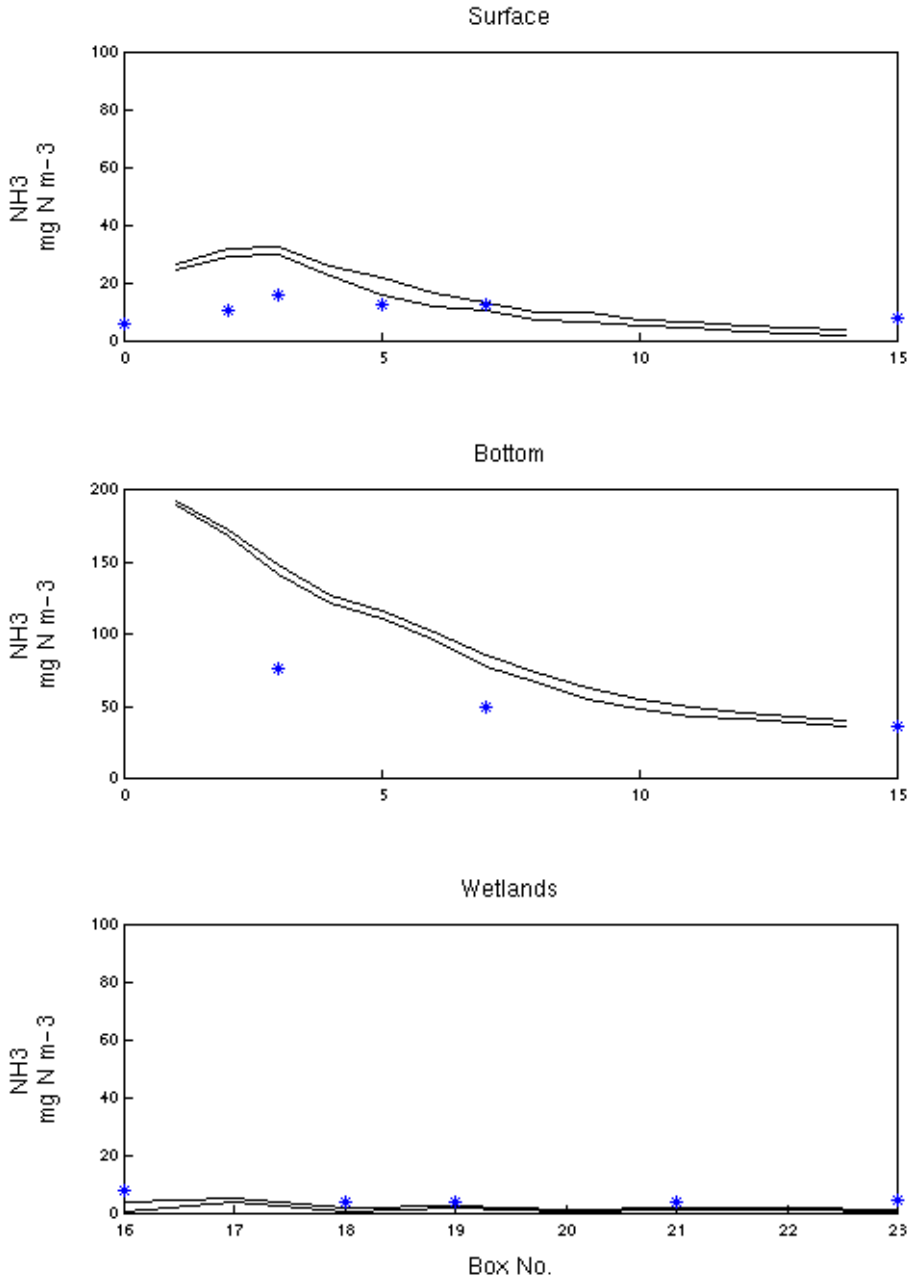

Fig. 5.3.8 c. Comparison of predicted (line) and observed (asterisk) NH_3 in model boxes in channel surface, channel bottom and wetlands, for survey April 17, 2000.

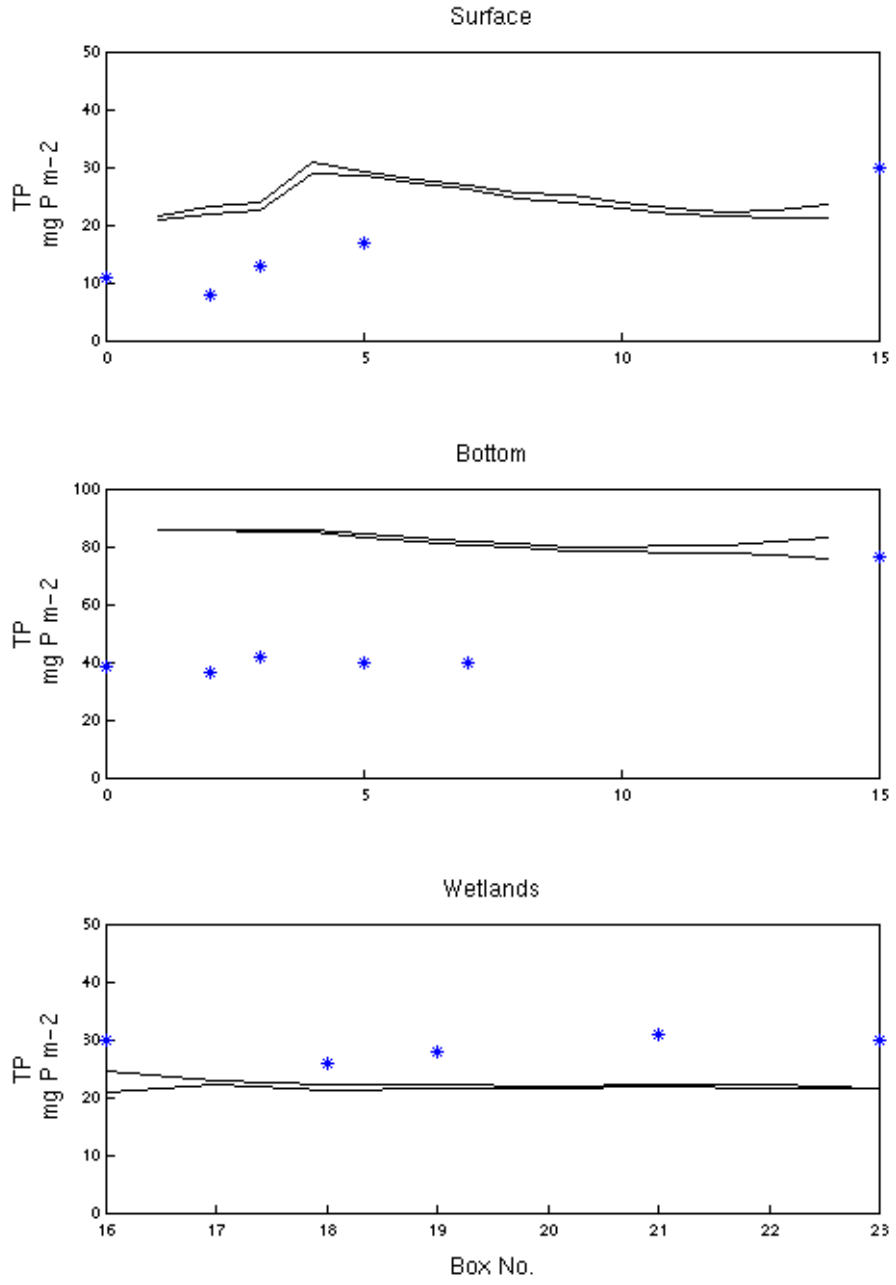

Fig. 5.3.8 d. Comparison of predicted (line) and observed (asterisk) TP in model boxes in channel surface, channel bottom and wetlands, for survey April 17, 2000.

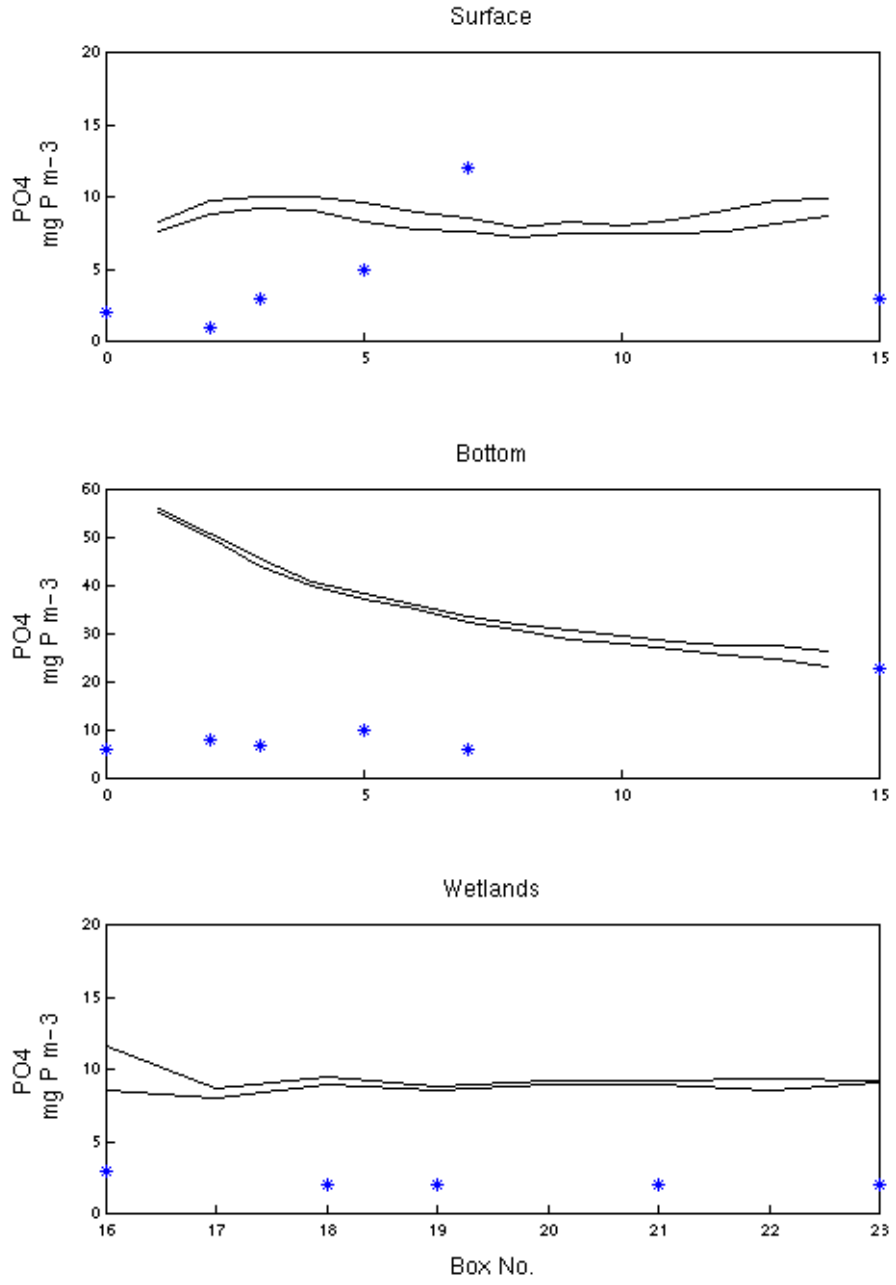

Fig. 5.3.8 e. Comparison of predicted (line) and observed (asterisk) PO_4 in model boxes in channel surface, channel bottom and wetlands, for survey April 17, 2000.

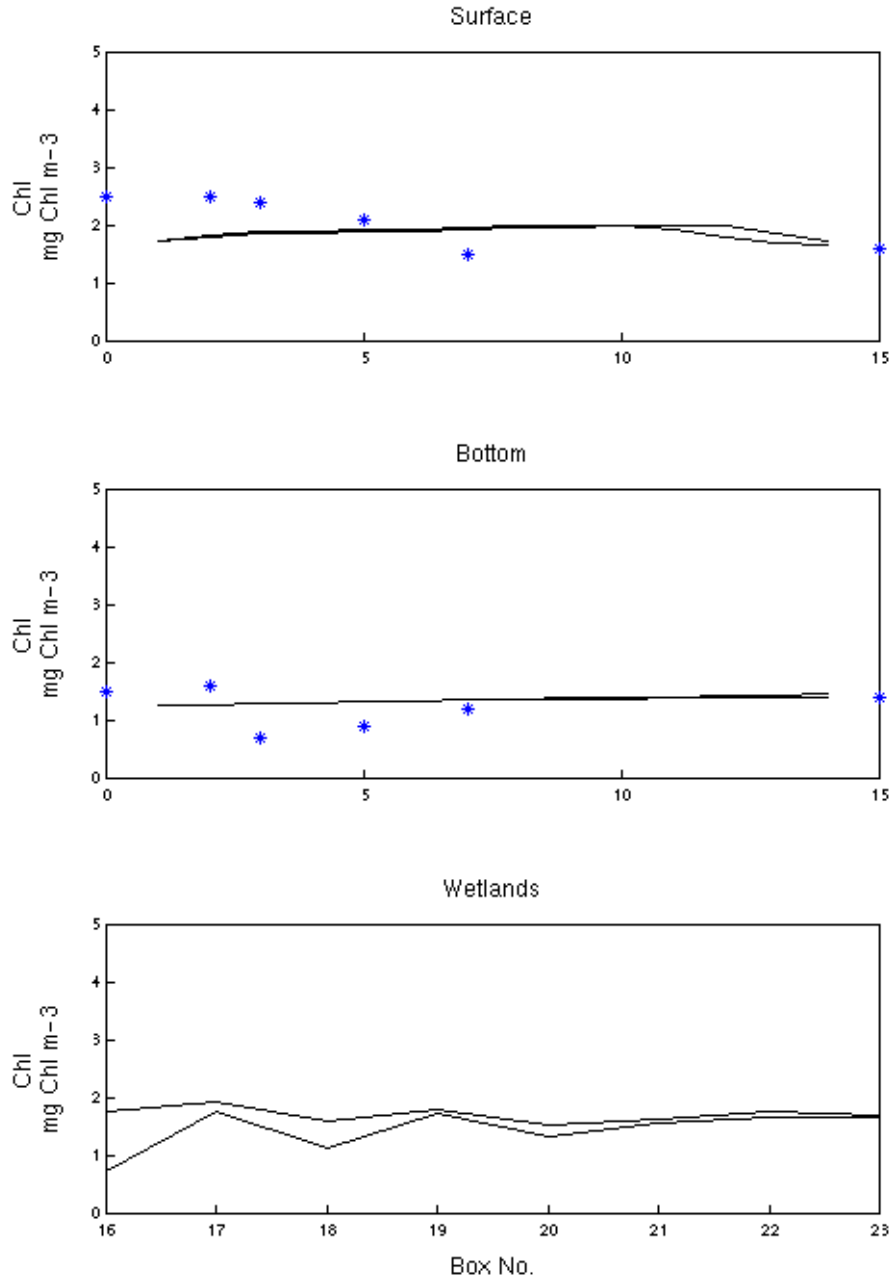

Fig. 5.3.8 f. Comparison of predicted (line) and observed (asterisk) Chl a in model boxes in channel surface, channel bottom and wetlands, for survey April 17, 2000.

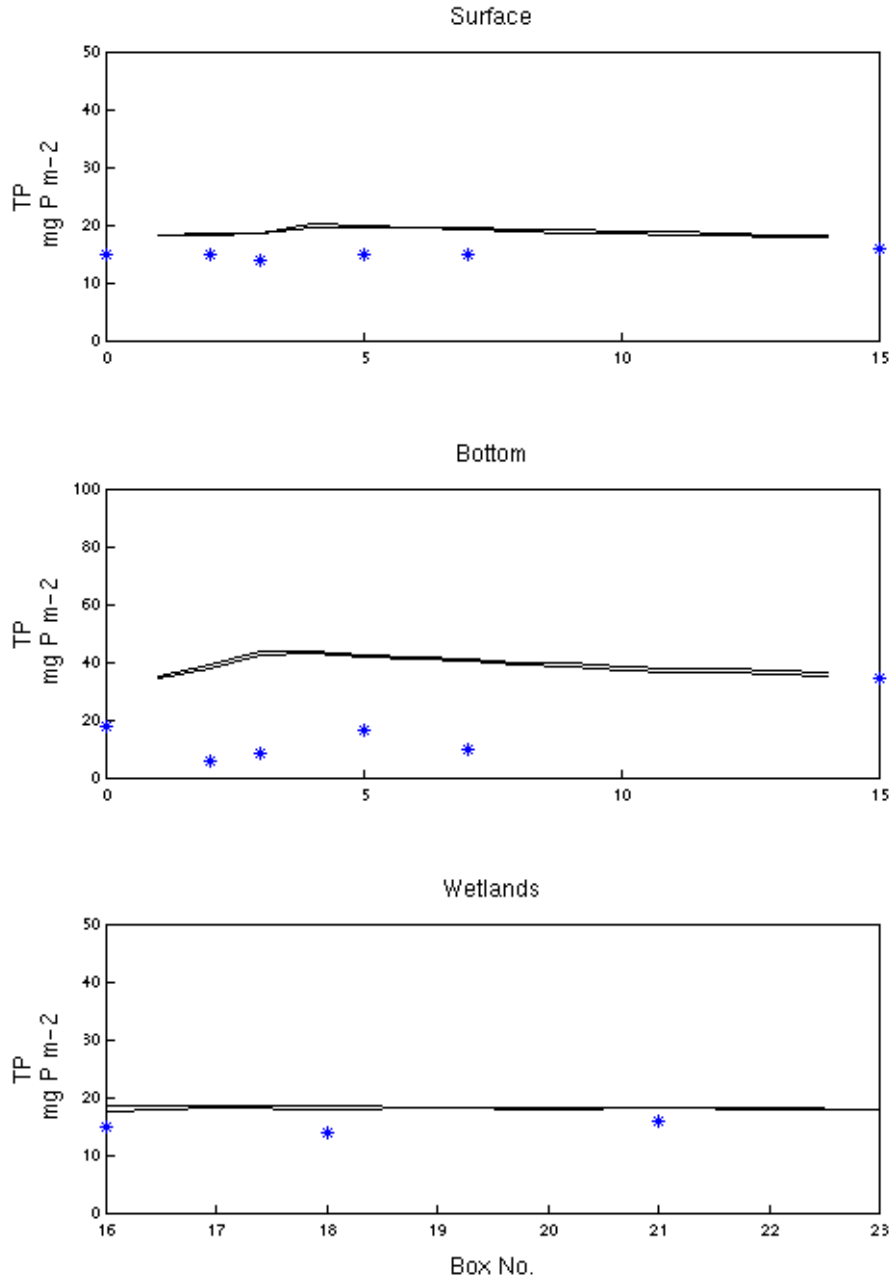

Fig. 5.3.9 a. Comparison of predicted (line) and observed (asterisk) TP in model boxes in channel surface, channel bottom and wetlands, for survey November 23, 1999, with zero PO_4 load from New Norfolk STP.

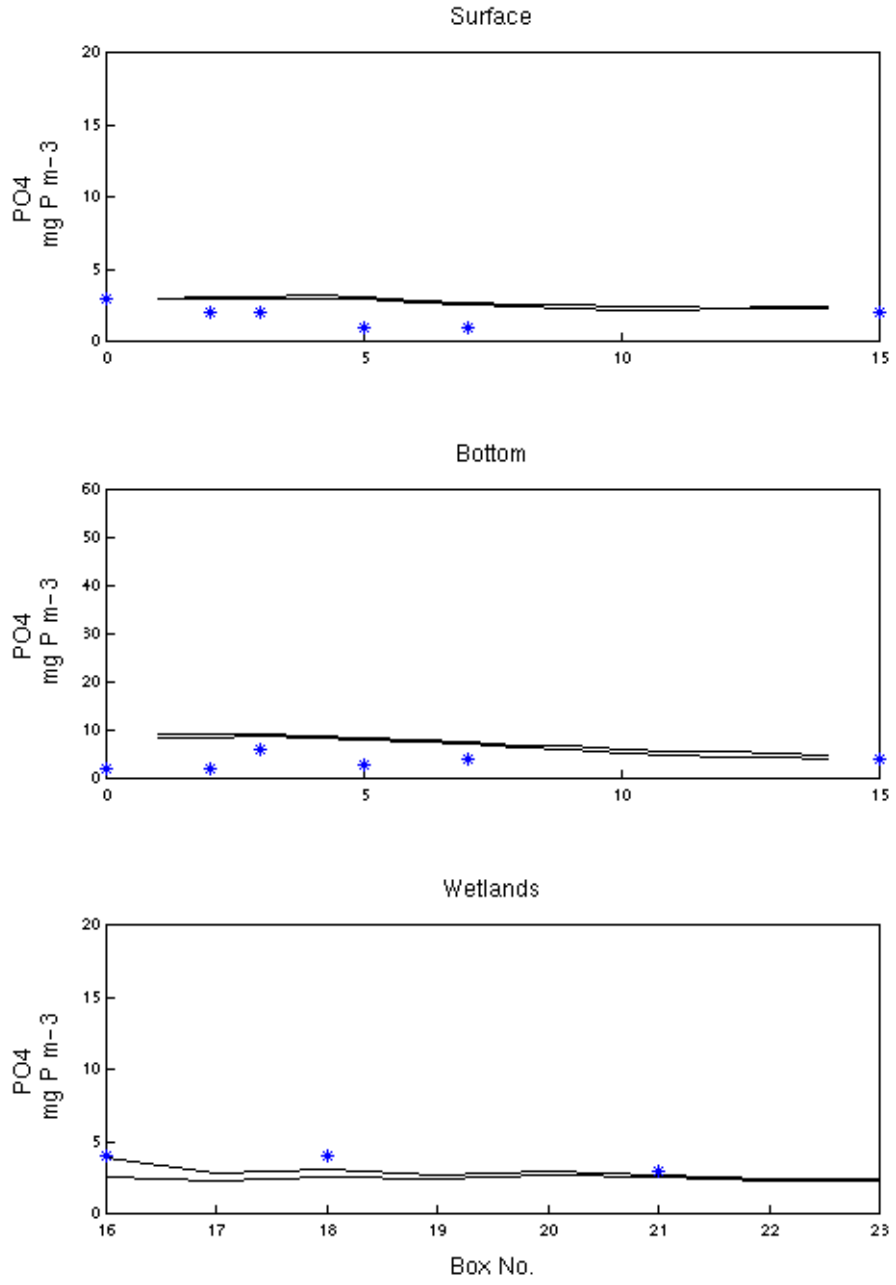

Fig. 5.3.9 b. Comparison of predicted (line) and observed (asterisk) PO_4 in model boxes in channel surface, channel bottom and wetlands, for survey November 23, 1999, with zero PO_4 load from New Norfolk STP.

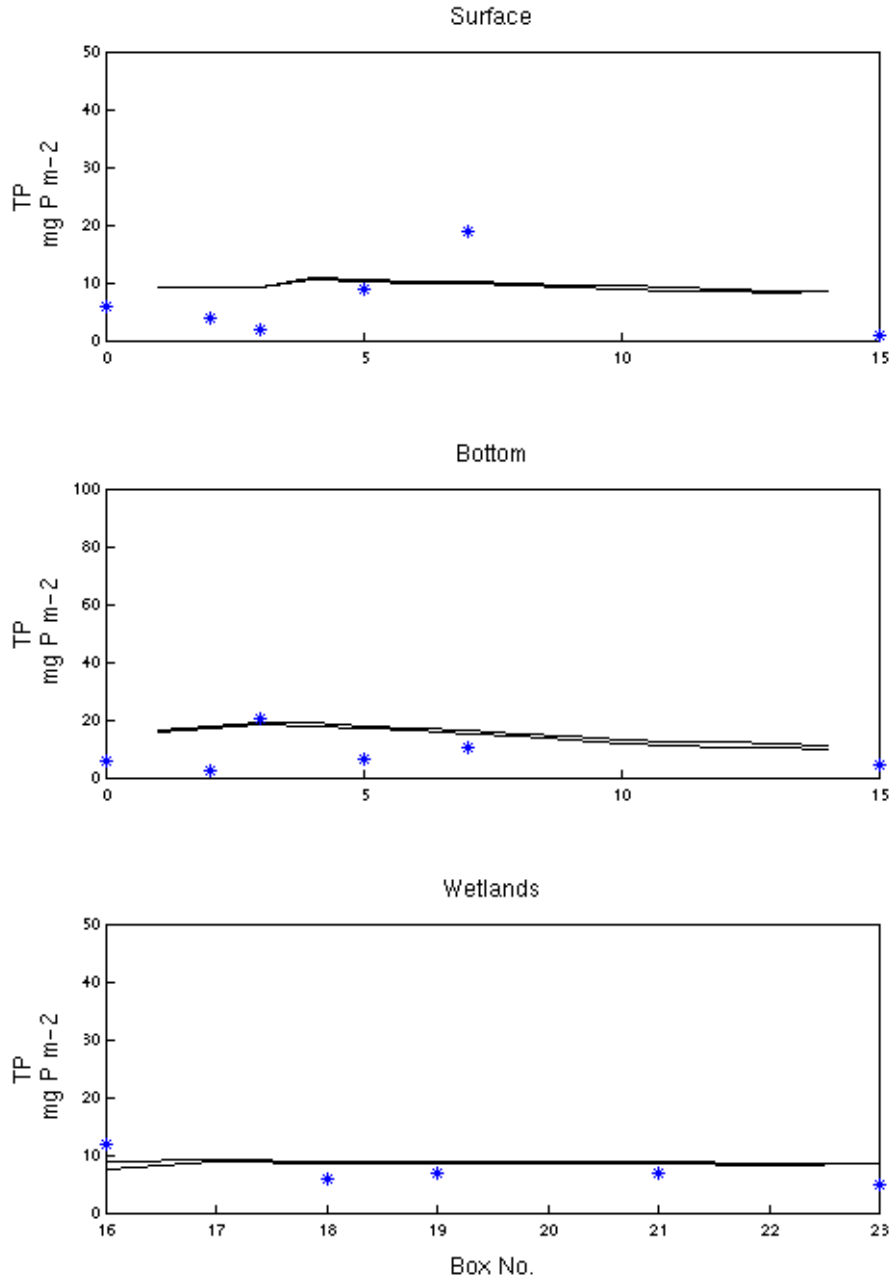

Fig. 5.3.9 c. Comparison of predicted (line) and observed (asterisk) TP in model boxes in channel surface, channel bottom and wetlands, for survey December 14, 1999, with zero PO_4 load from New Norfolk STP.

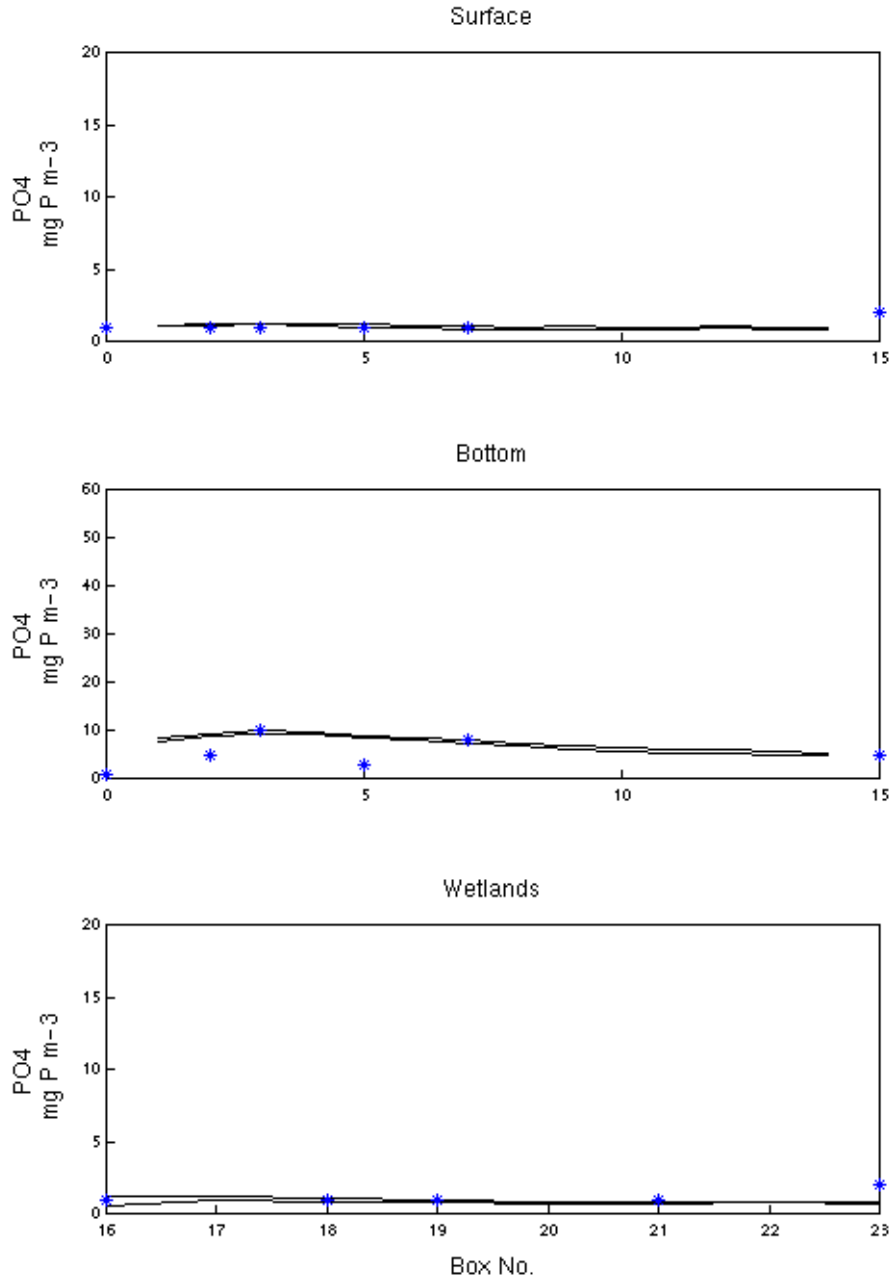

Fig. 5.3.9 d. Comparison of predicted (line) and observed (asterisk) PO_4 in model boxes in channel surface, channel bottom and wetlands, for survey December 14, 1999, with zero PO_4 load from New Norfolk STP.

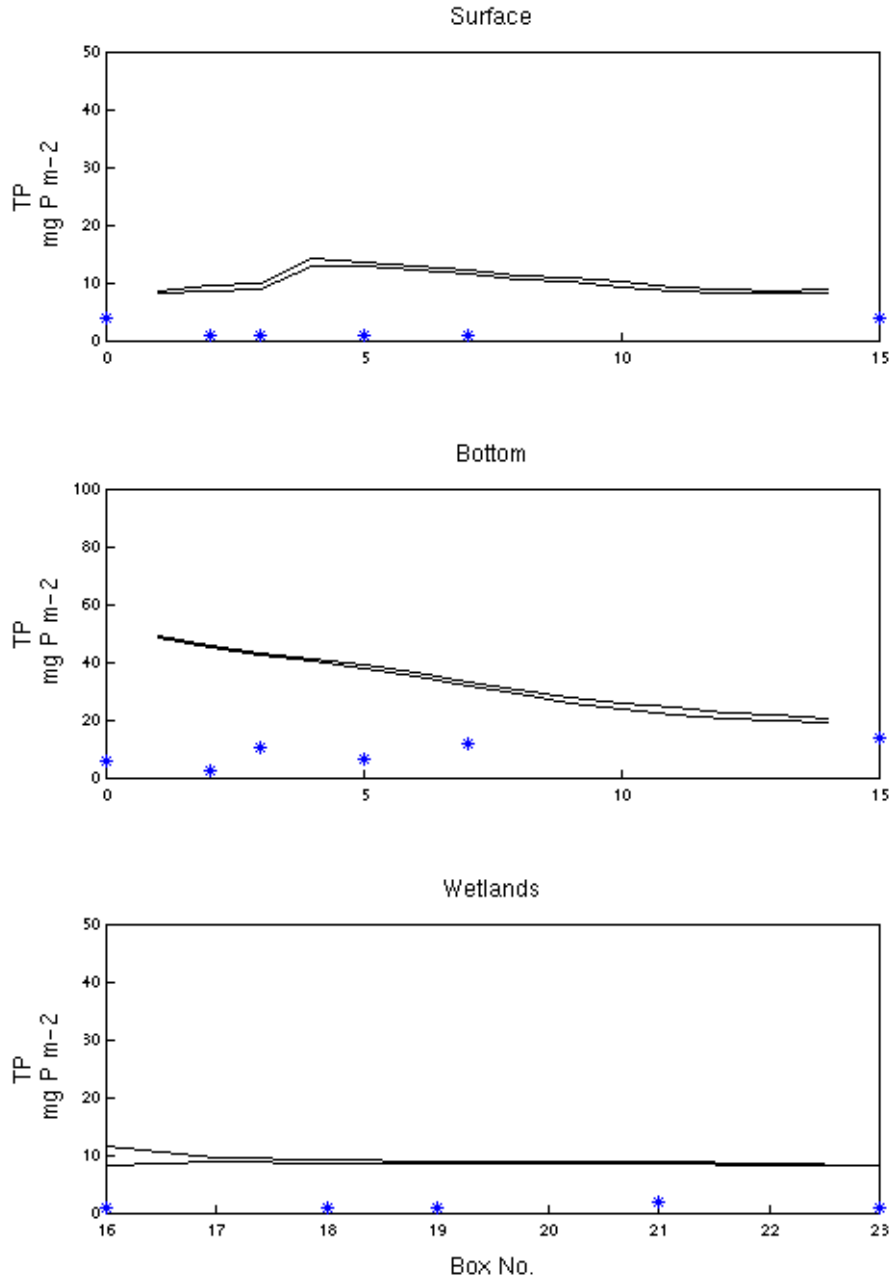

Fig. 5.3.9 e. Comparison of predicted (line) and observed (asterisk) TP in model boxes in channel surface, channel bottom and wetlands, for survey March 7, 2000, with zero PO_4 load from New Norfolk STP.

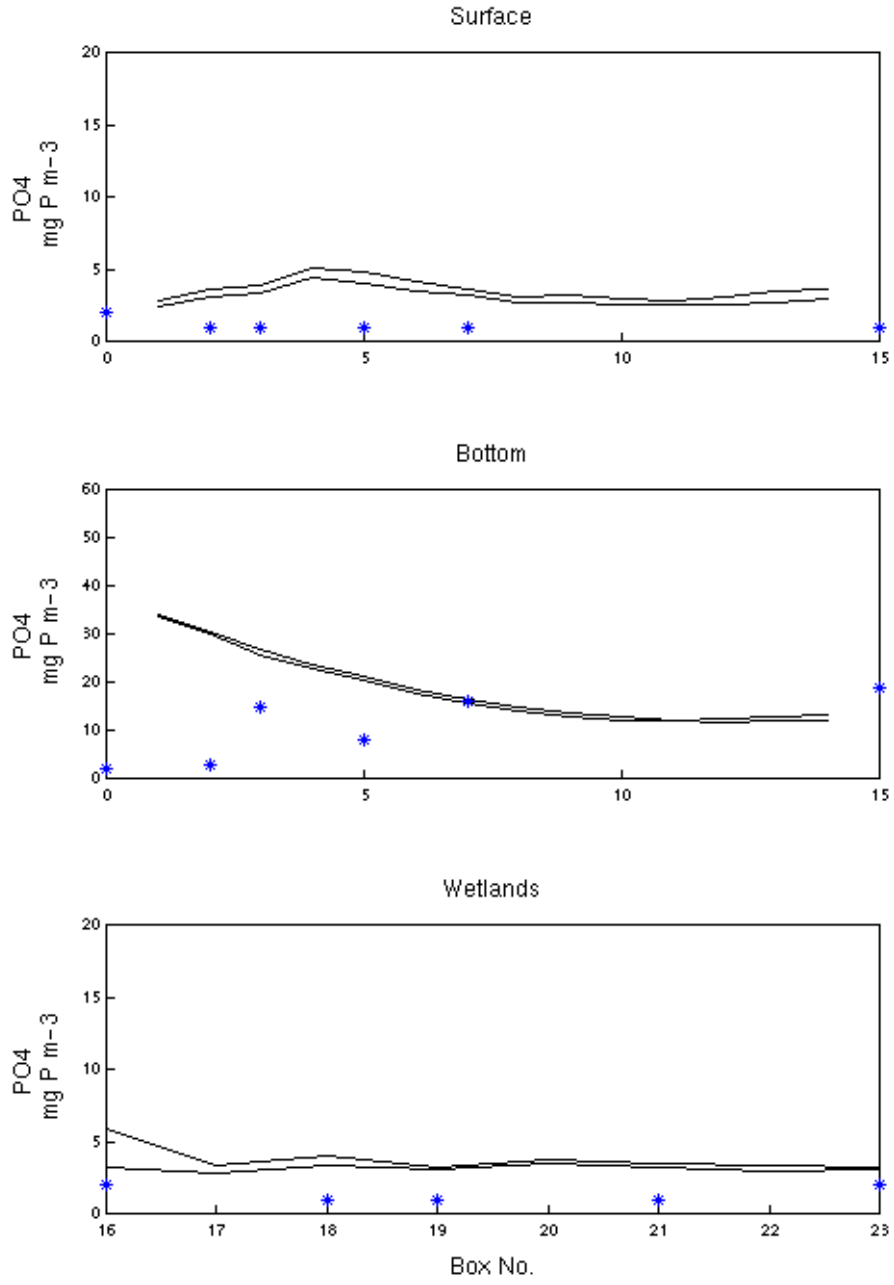

Fig. 5.3.9 f. Comparison of predicted (line) and observed (asterisk) PO_4 in model boxes in channel surface, channel bottom and wetlands, for survey March 7, 2000, with zero PO_4 load from New Norfolk STP.

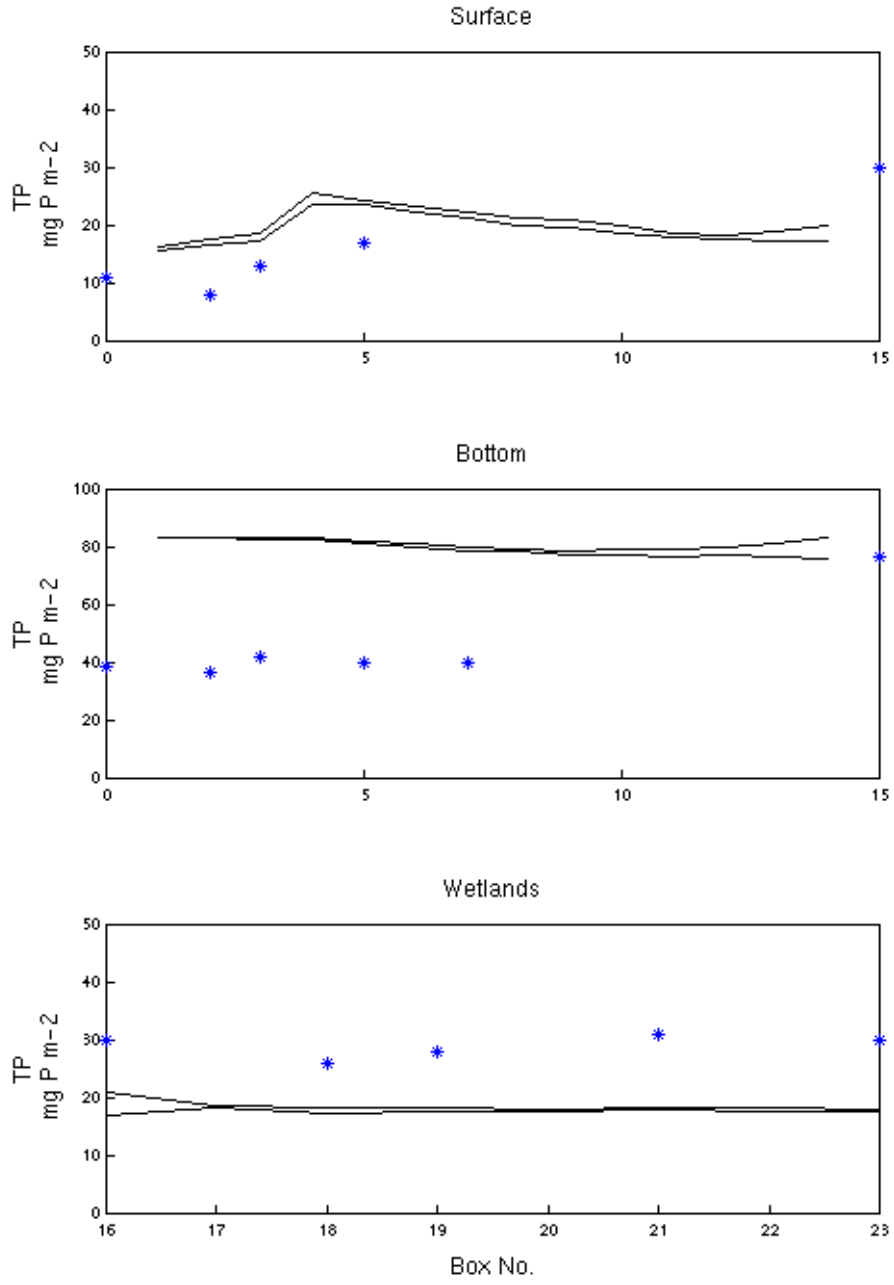

Fig. 5.3.9 g. Comparison of predicted (line) and observed (asterisk) TP in model boxes in channel surface, channel bottom and wetlands, for survey April 17, 2000, with zero PO_4 load from New Norfolk STP.

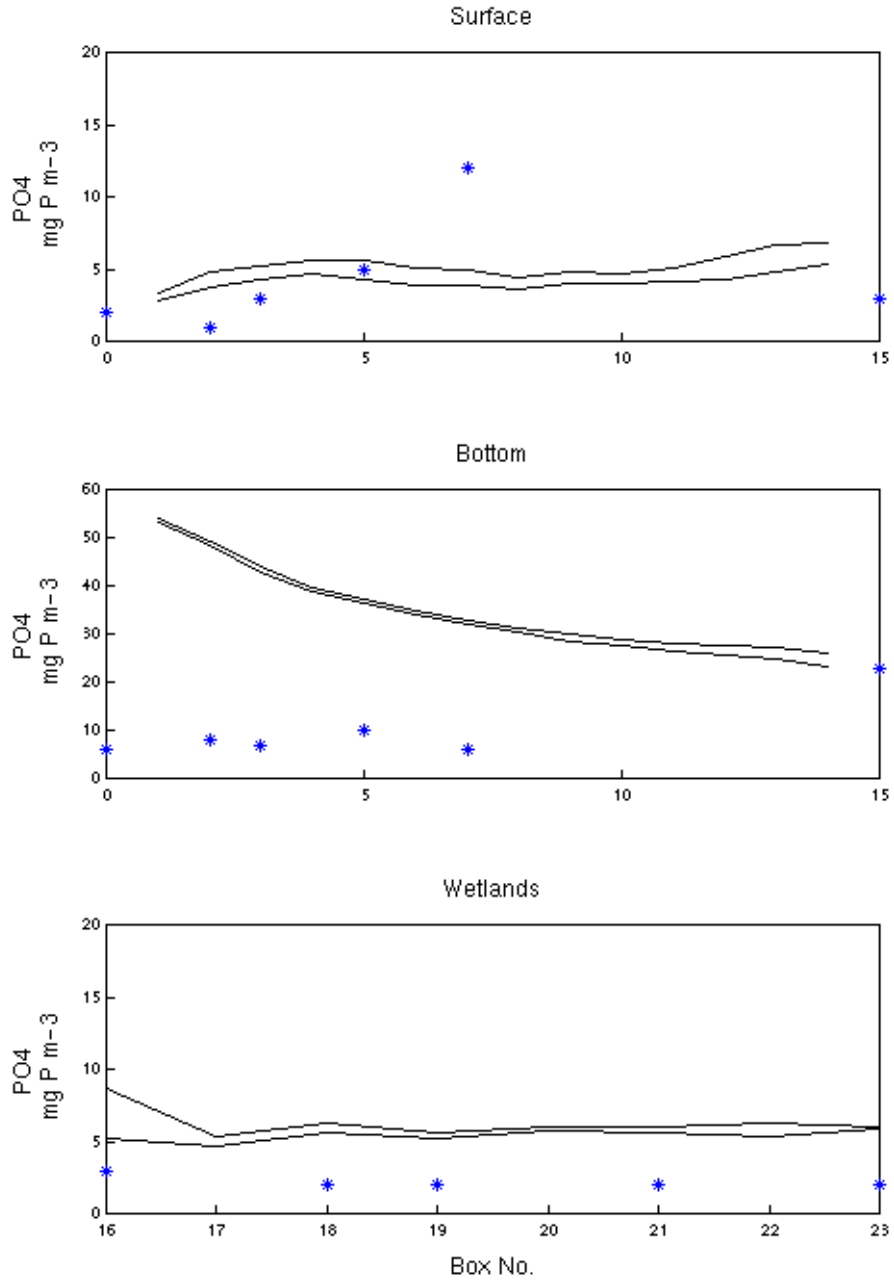

Fig. 5.3.9 h. Comparison of predicted (line) and observed (asterisk) PO_4 in model boxes in channel surface, channel bottom and wetlands, for survey April 17, 2000, with zero PO_4 load from New Norfolk STP.

Figure 6.1.1 : Ebb tide wetland salinity distribution (psu)
Neap tide, 45m^{3}s^{-1}, wind 5ms^{-1} 60^{o}T

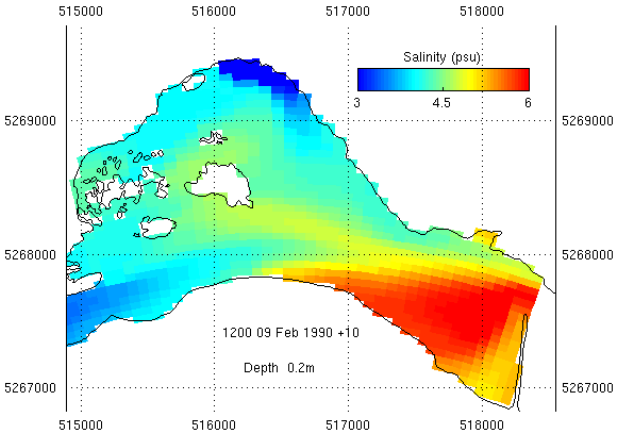

Figure 6.1.2 : Flood tide wetland salinity distribution (psu)
Neap tide, 45m^{3}s^{-1}, wind 5ms^{-1} 60^{o}T

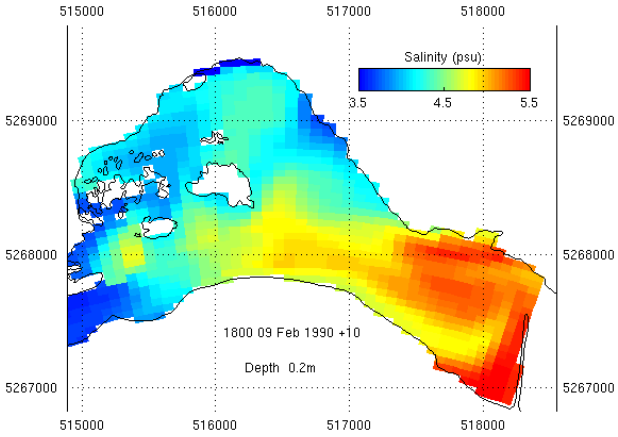

Figure 6.1.3 : Ebb tide wetland salinity distribution (psu)
Spring tide, 90m^{3}s^{-1}, wind 5ms^{-1} 60^{o}T

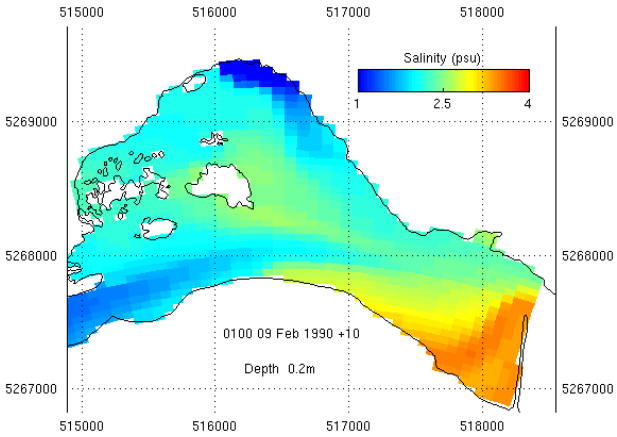

Figure 6.1.4 : Flood tide wetland salinity distribution (psu)
Spring tide, 90m^{3}s^{-1}, wind 5ms^{-1} 60^{o}T

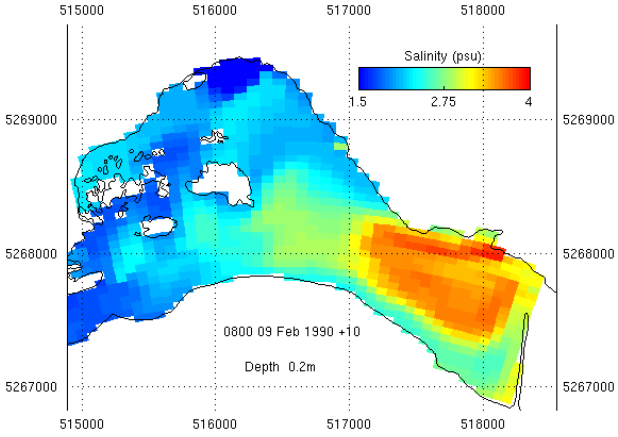

Figure 6.1.5 : Along-river salinity section (psu), neap tide, 45 m^3s^{-1}, wind $5ms^{-1}$ 240^oT

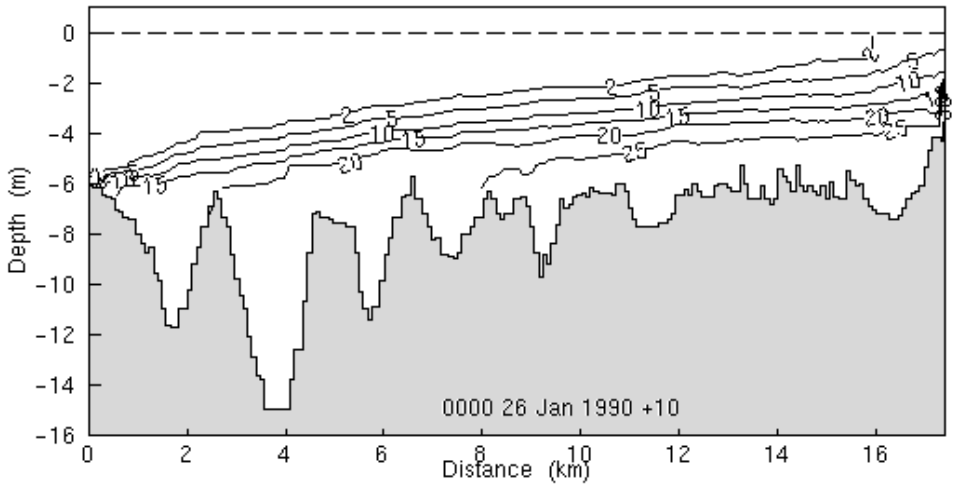

Figure 6.1.6 : Ebb tide wetland salinity distribution (psu)
Neap tide, $45m^3s^{-1}$, wind $5ms^{-1}$ 240^oT

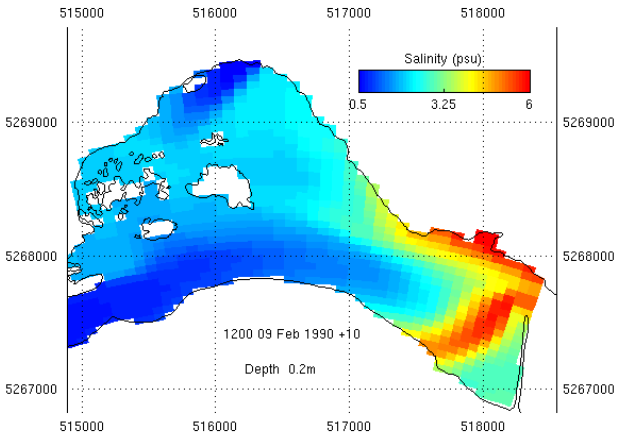

Figure 6.1.7 : Flood tide wetland salinity distribution (psu)
Neap tide, $45m^3s^{-1}$, wind $5ms^{-1}$ 240^oT

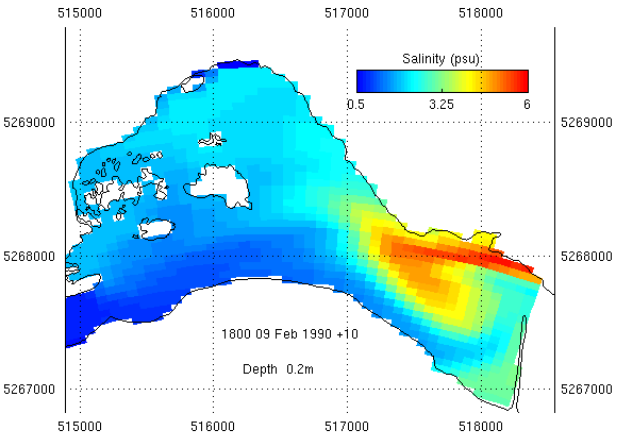

Figure 6.1.8 : Along-river salinity section (psu), spring tide, 90 m^3s^{-1}, wind $5ms^{-1}$ 240°T

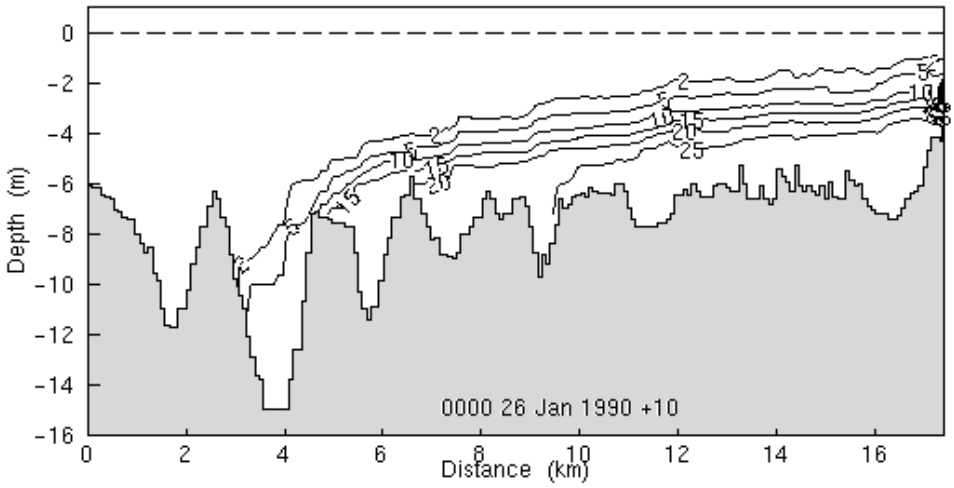

Figure 6.1.9 : Ebb tide wetland salinity distribution (psu)
Spring tide, 90m^3s^{-1}, wind $5ms^{-1}$ 240°T

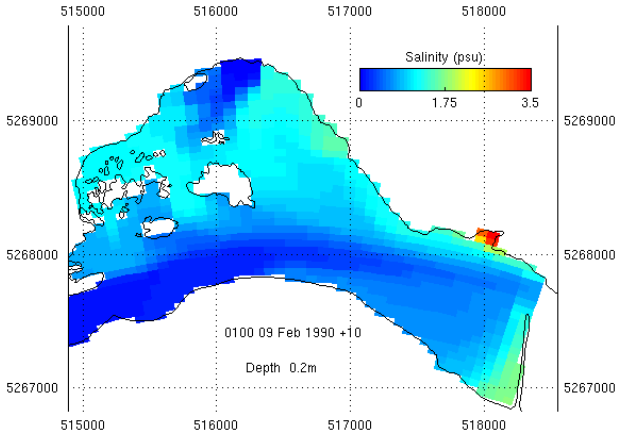

Figure 6.1.10 : Flood tide wetland salinity distribution (psu)
Spring tide, 90m^3s^{-1}, wind $5ms^{-1}$ 240°T

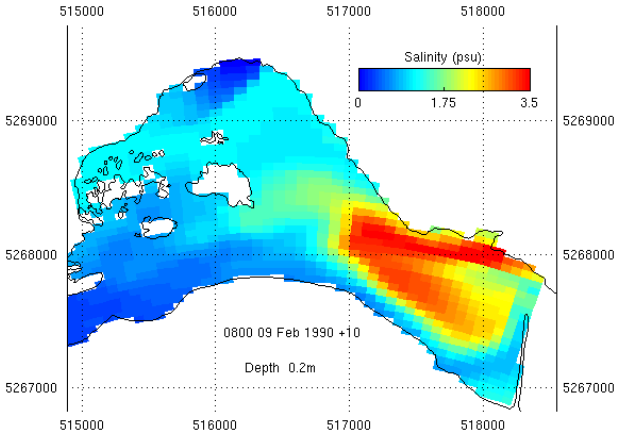

Figure 6.1.11 : Along-river salinity section (psu), neap tide, 45 m^3s^{-1}, wind 5ms^{-1} 330^oT

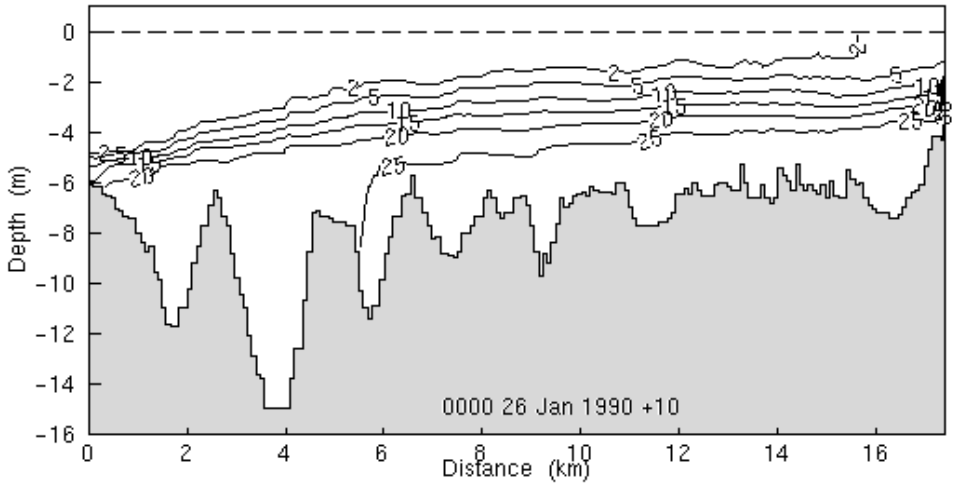

Figure 6.1.12 : Ebb tide wetland salinity distribution (psu)
Neap tide, 45m^3s^{-1}, wind 5ms^{-1} 330^oT

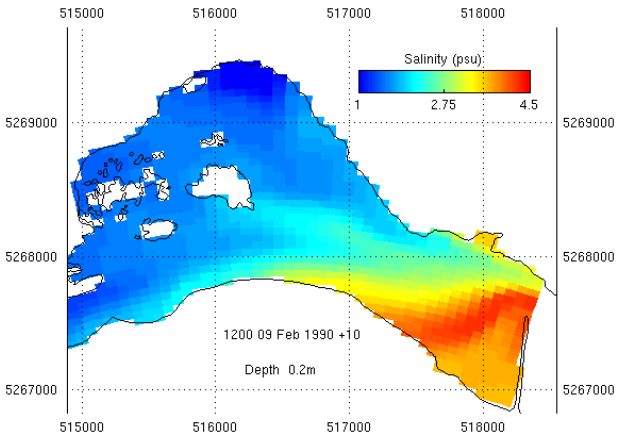

Figure 6.1.13 : Flood tide wetland salinity distribution (psu)
Neap tide, 45m^3s^{-1}, wind 5ms^{-1} 330^oT

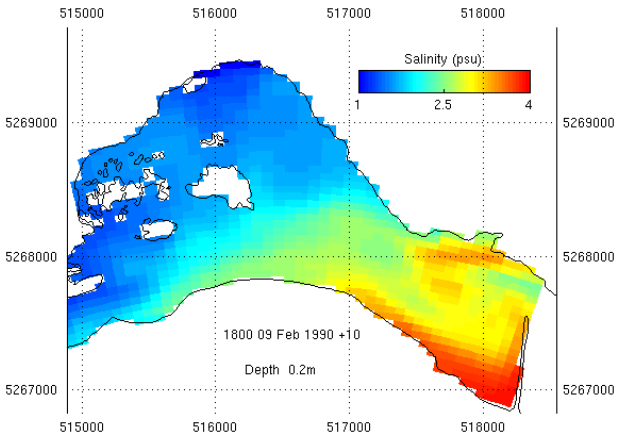

Figure 6.1.14 : Along-river salinity section (psu), spring tide, 90 m^3s^{-1}, wind $5ms^{-1}$ 330°T

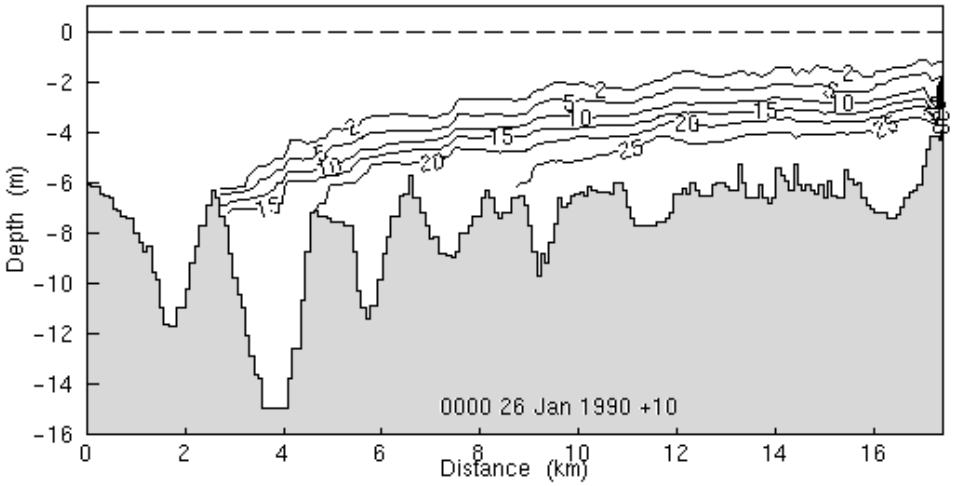

Figure 6.1.15 : Ebb tide wetland salinity distribution (psu)
Spring tide, 90m^3s^{-1}, wind $5ms^{-1}$ 330°T

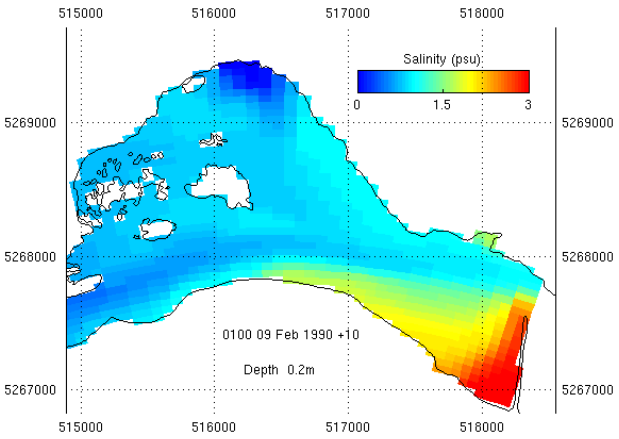

Figure 6.1.16 : Flood tide wetland salinity distribution (psu)
Spring tide, 90m^3s^{-1}, wind $5ms^{-1}$ 330°T

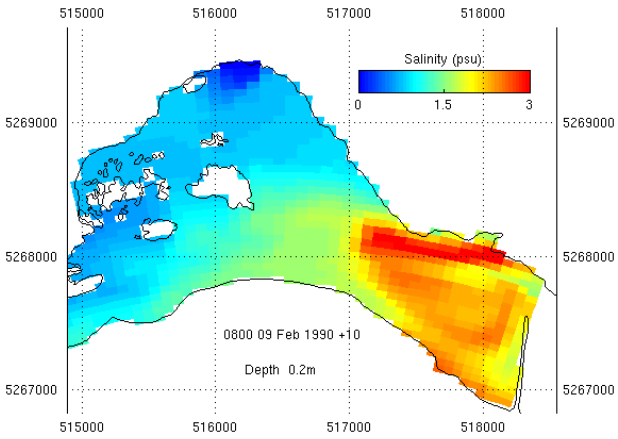

Fig 6.2.1 (a) : Box model percentiles (%CES), combined scenarios, RDRA

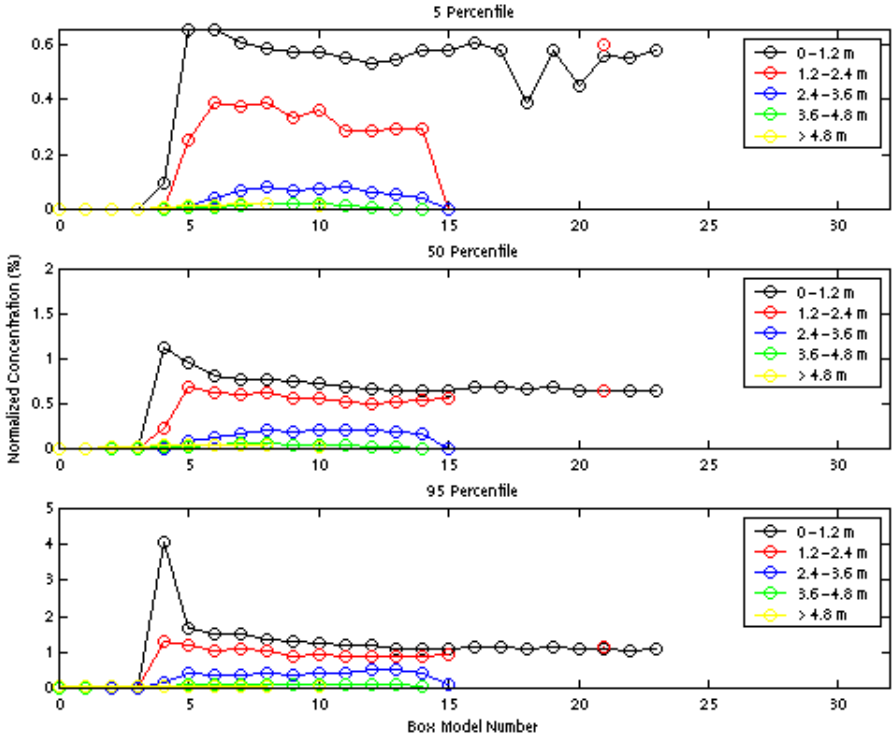

Fig 6.2.1 (b) : Box model minimum and maximum (%CES)
Combined scenarios, RDRA

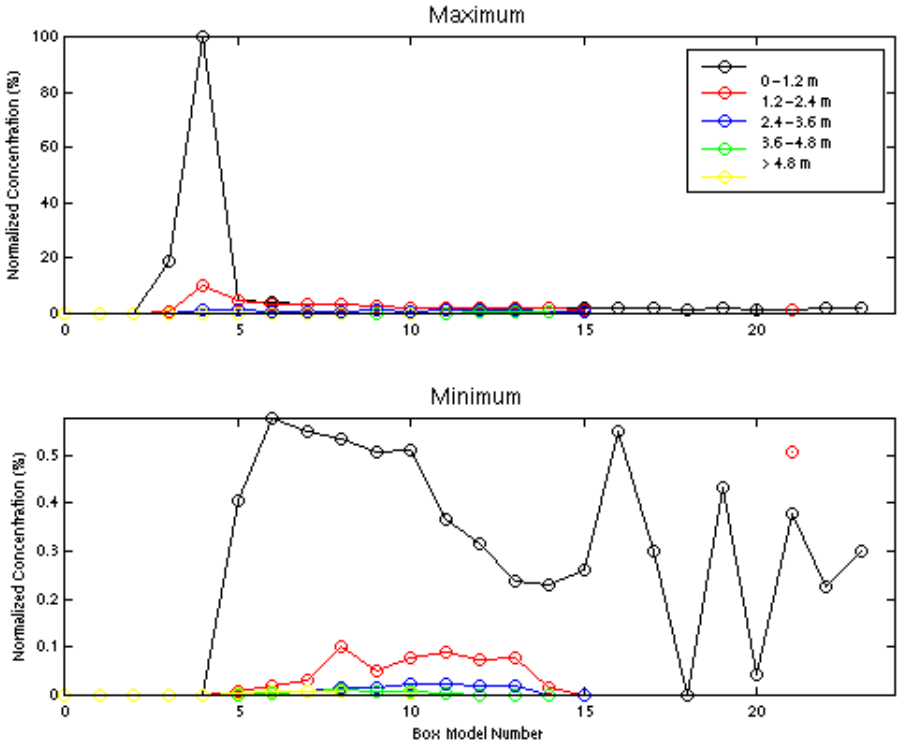

Fig 6.2.2 (a) : Box model percentiles (%CES), combined scenarios, RPRA

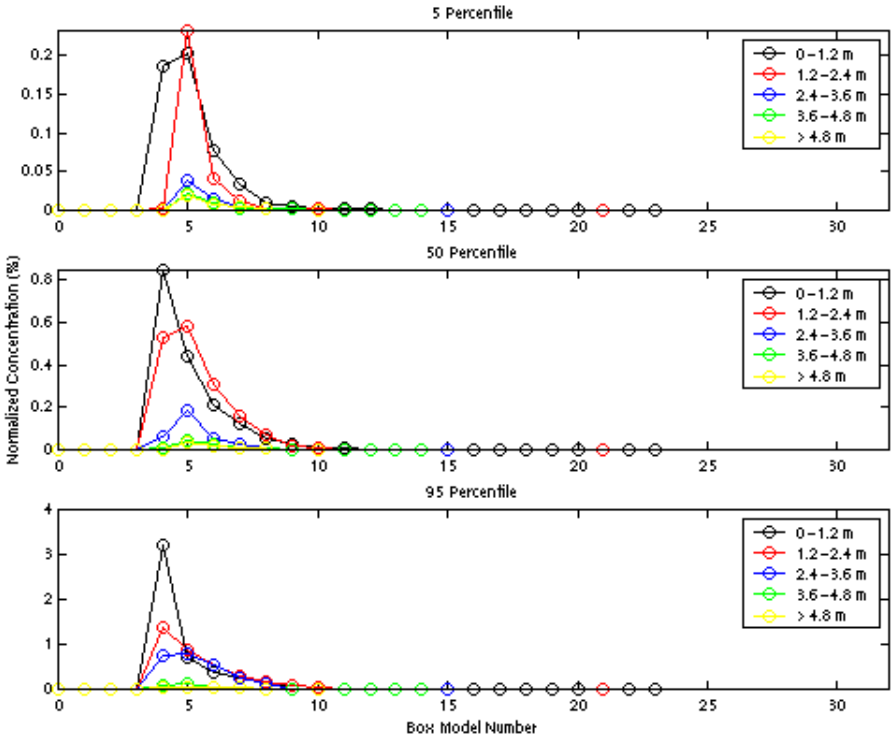

Fig 6.2.2 (b) : Box model minimum and maximum (%CES)
Combined scenarios, RPRA

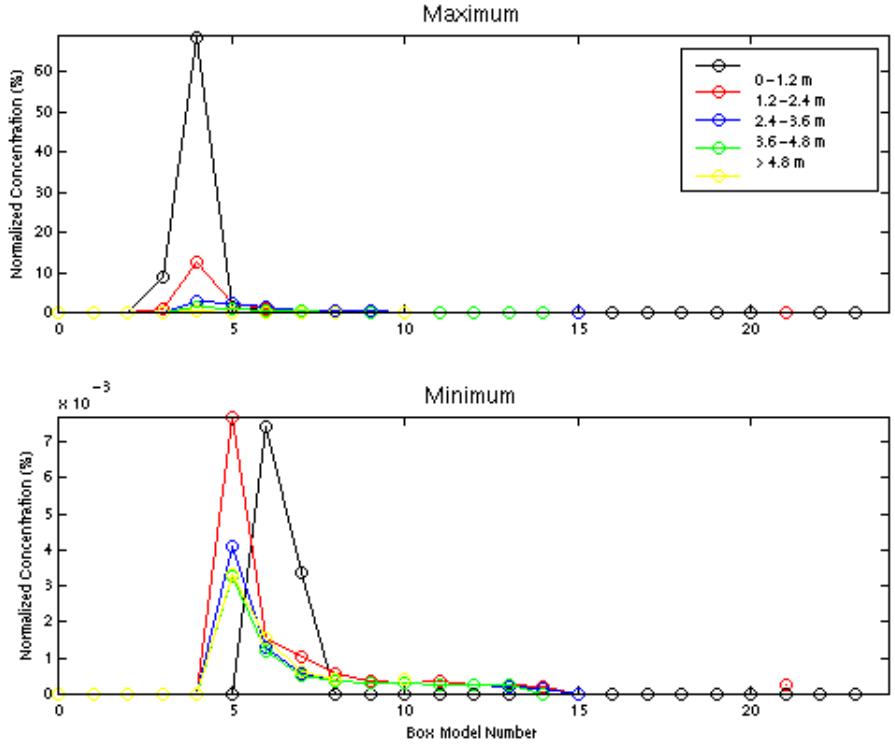

Fig 6.2.3 (a) : Box model percentiles (%CES), combined scenarios, LDRA

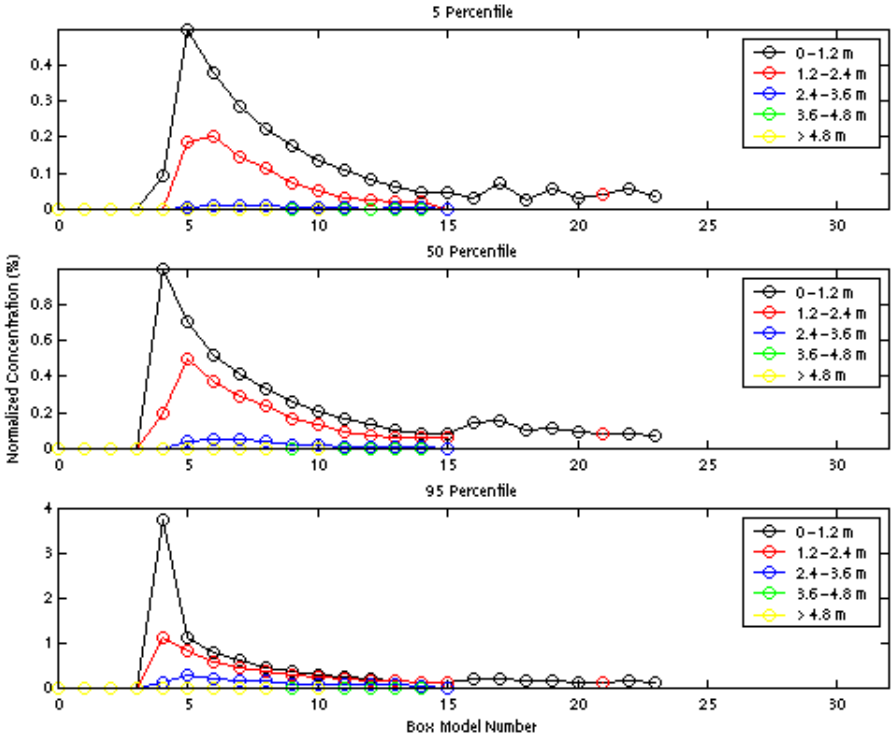

Fig 6.2.3 (b) : Box model minimum and maximum (%CES)
Combined scenarios, LDRA

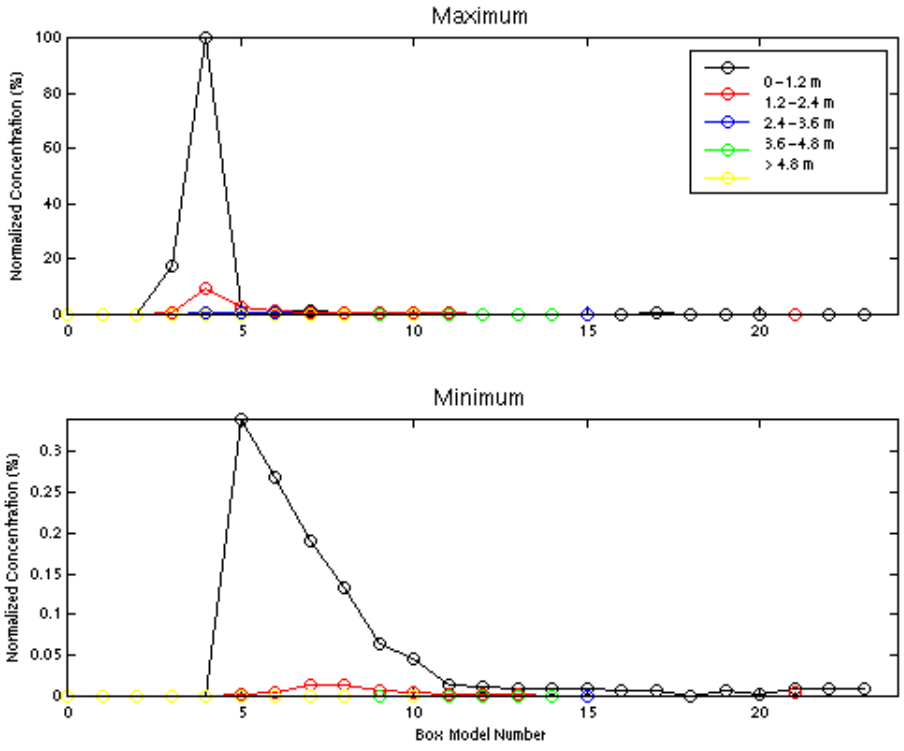

Fig 6.2.4(a) : Box model percentiles (%CES), combined scenarios, LPRA

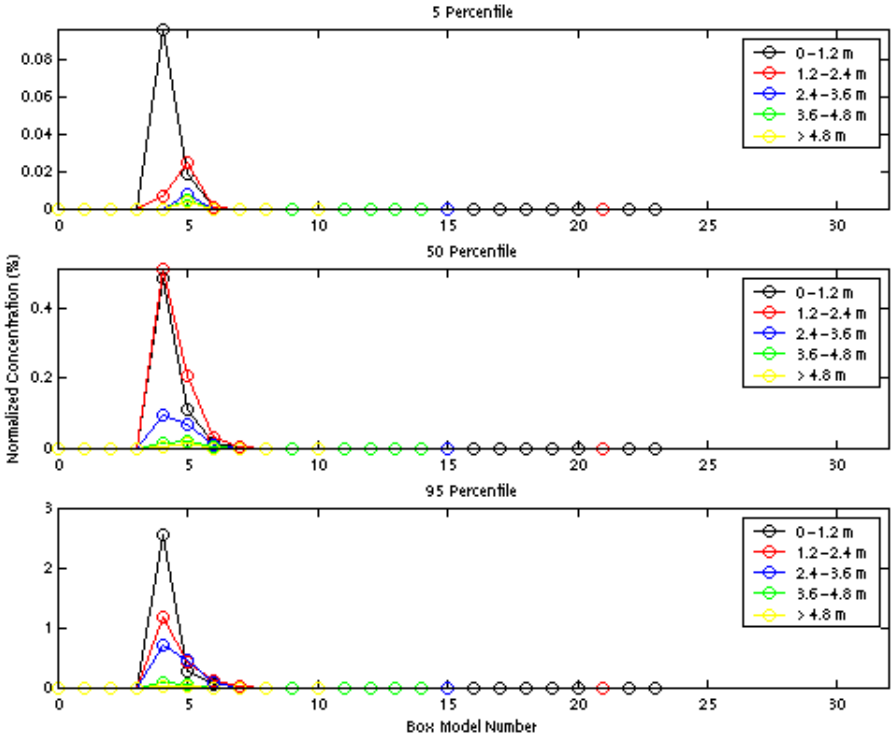

Fig 6.2.4(b) : Box model minimum and maximum (%CES)
Combined scenarios, LPRA

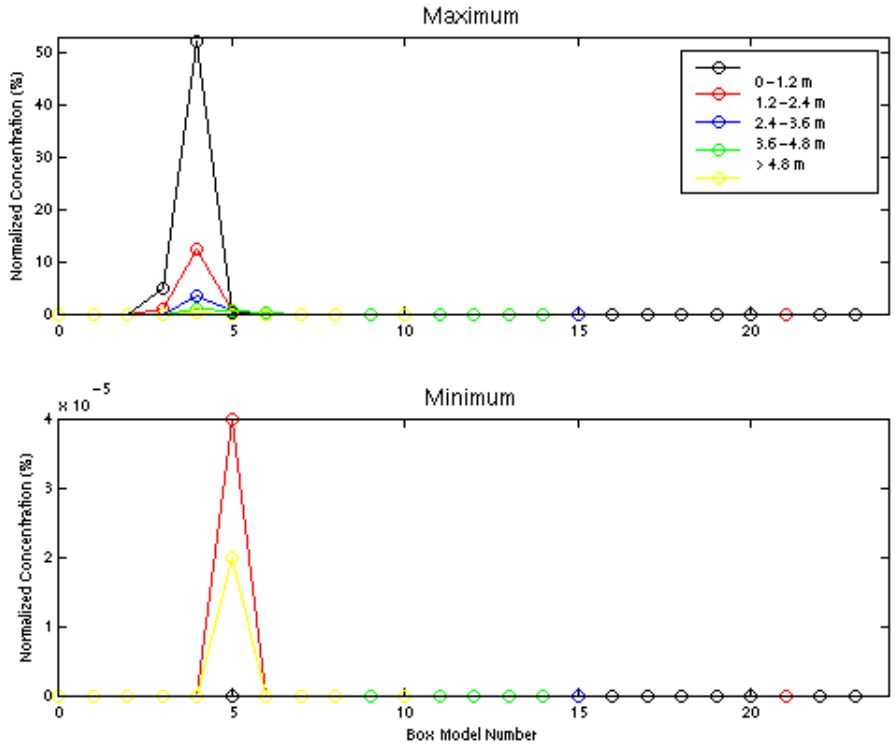

Fig 6.2.5(a) : Box model percentiles (%CES), combined scenarios, LPRA_A

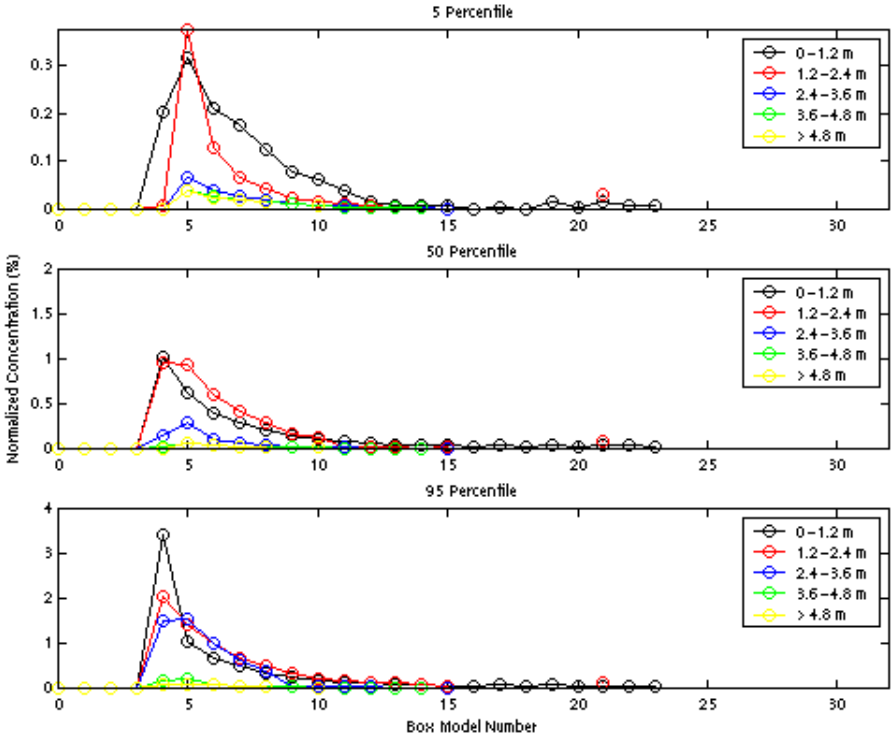

Fig 6.2.5(b) : Box model minimum and maximum (%CES)
Combined scenarios, LPRA_A

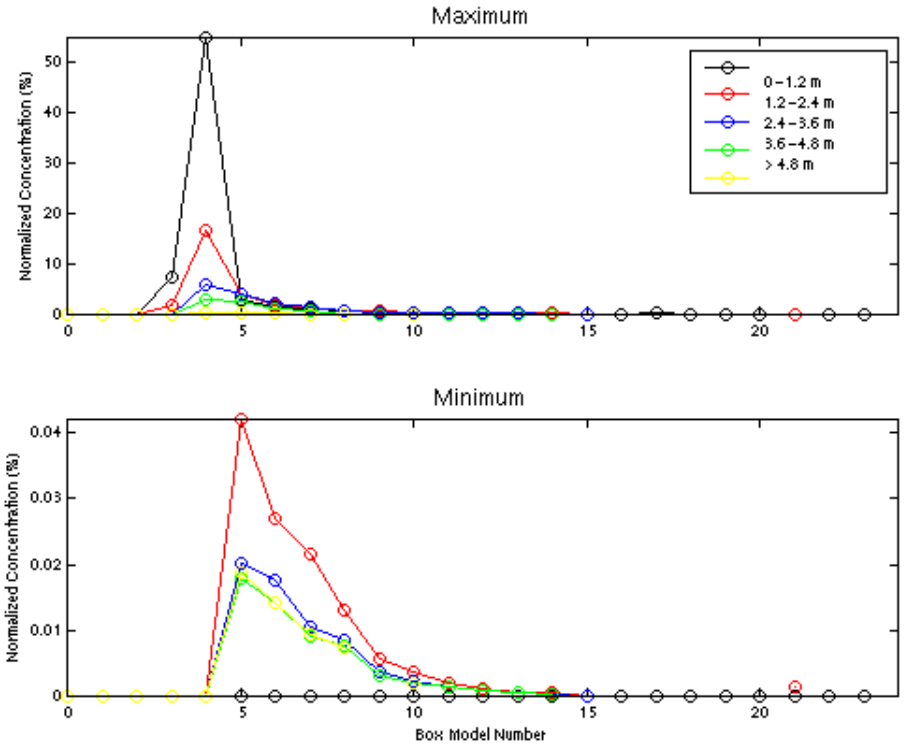

Fig 6.2.6(a) : Box model percentiles (%CES), combined scenarios, TOTAL

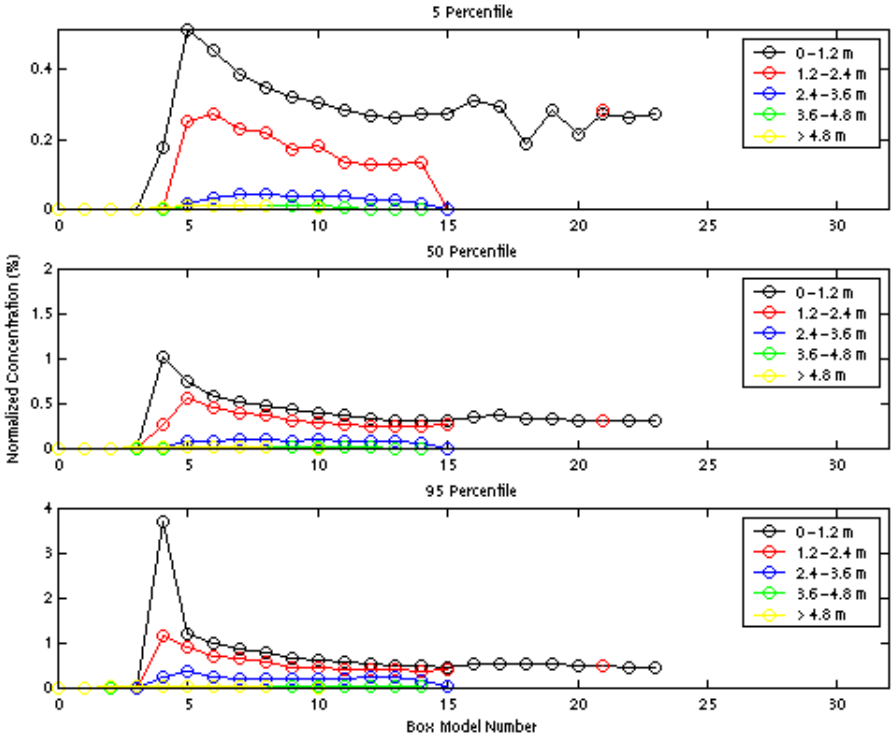

Fig 6.2.6(b) : Box model minimum and maximum (%CES)
Combined scenarios, TOTAL

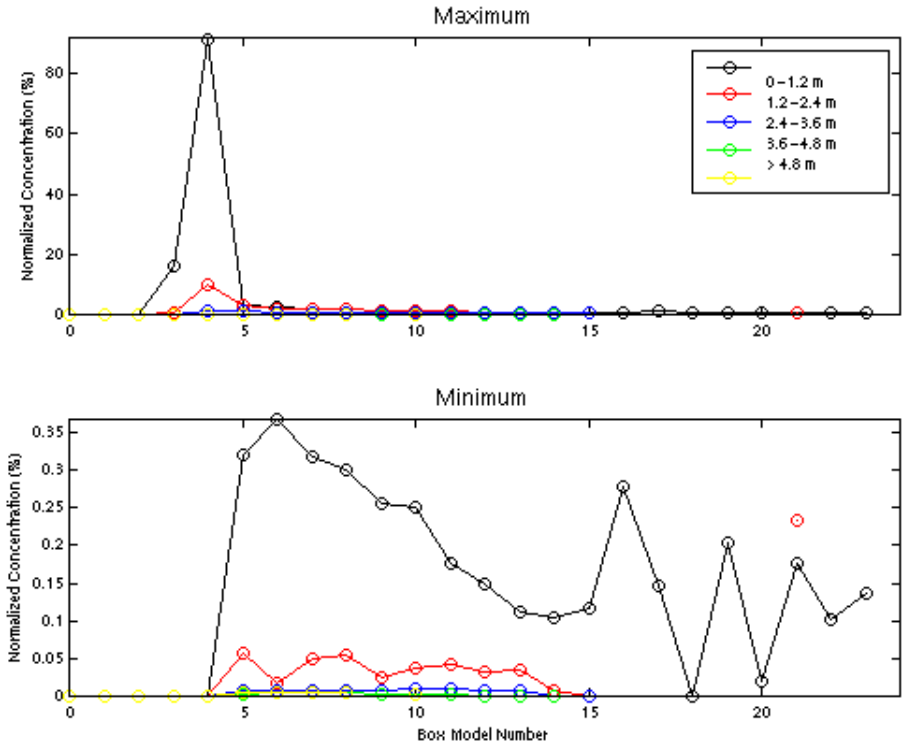

Fig 6.2.7(a) : Box model percentiles (%CES), combined scenarios, TOTAL_A

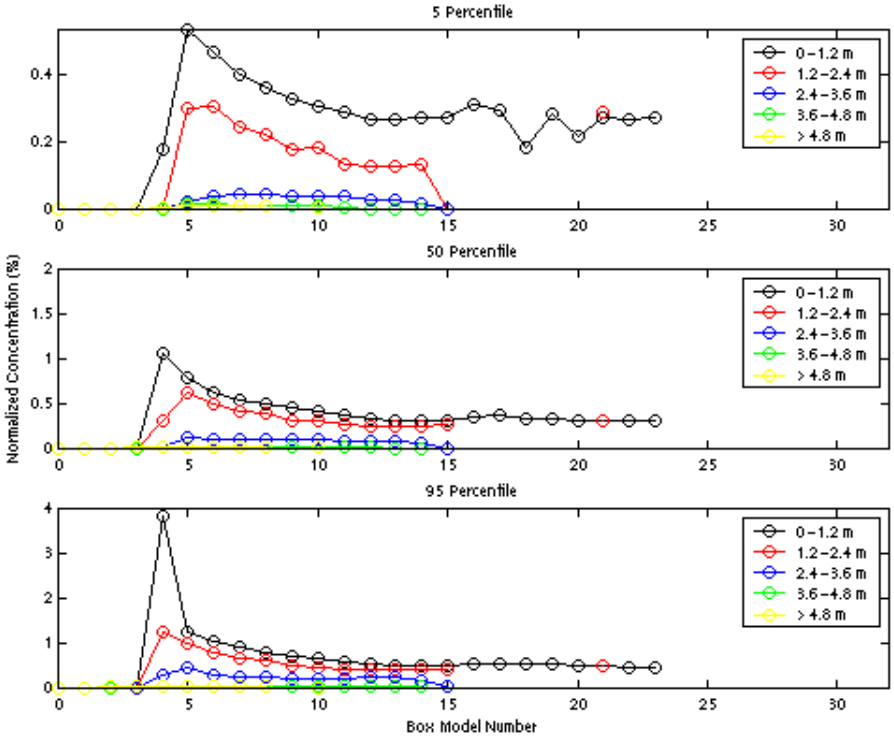

Fig 6.2.7(b) : Box model minimum and maximum (%CES)
Combined scenarios, TOTAL_A

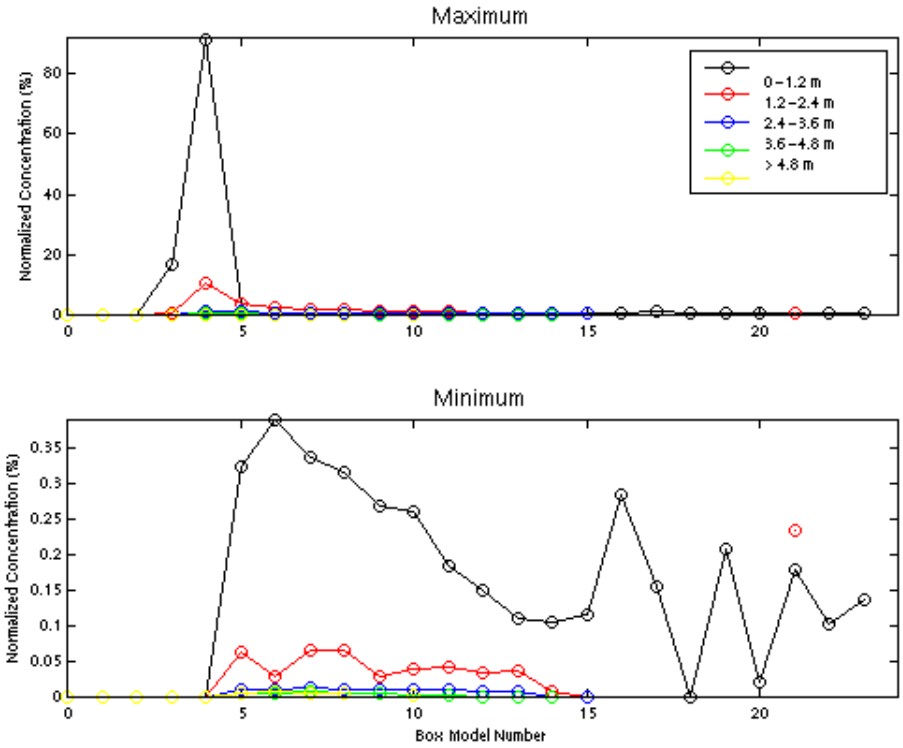

Fig 6.2.8(a) : Box model percentiles (%CES), combined scenarios, CES tracer

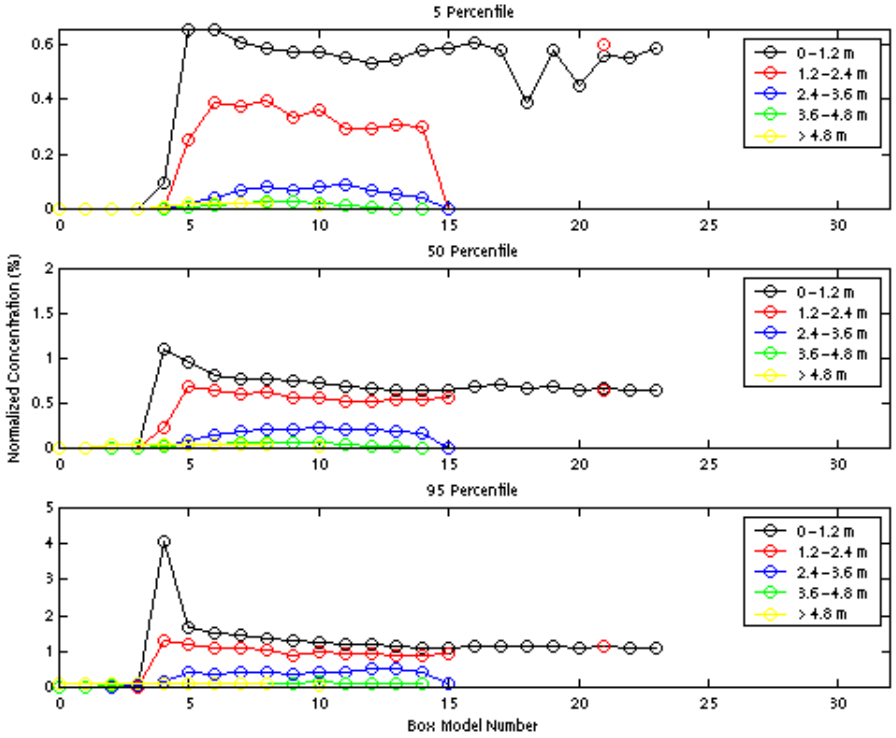

Fig 6.2.8(b) : Box model minimum and maximum (%CES)
Combined scenarios, CES tracer

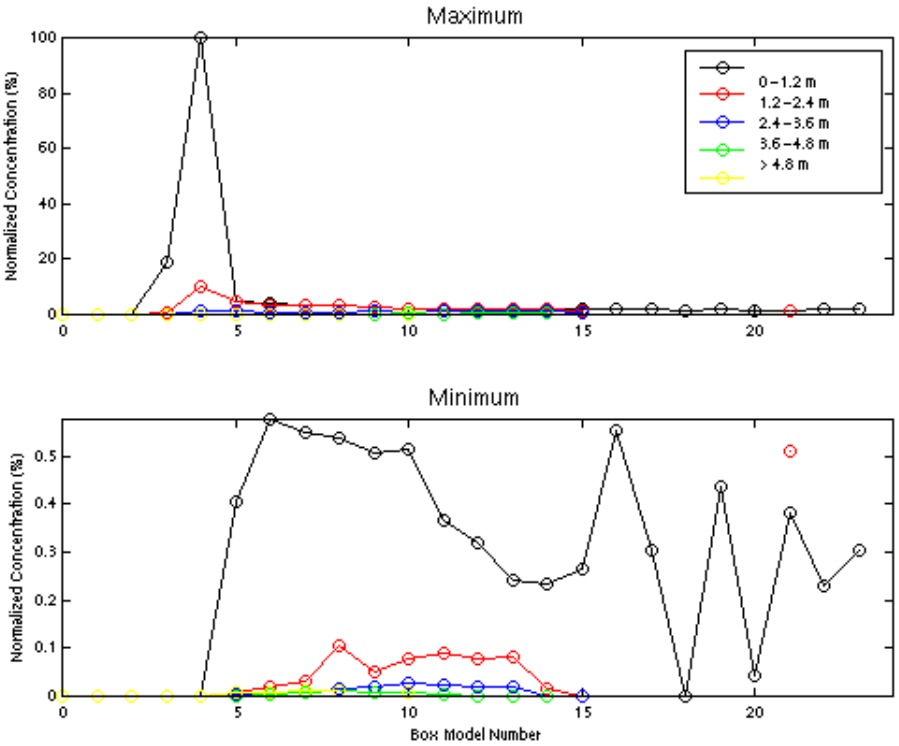

Figure 6.2.9 (a) : Combined Total Resin Acids (5%-ile CES)

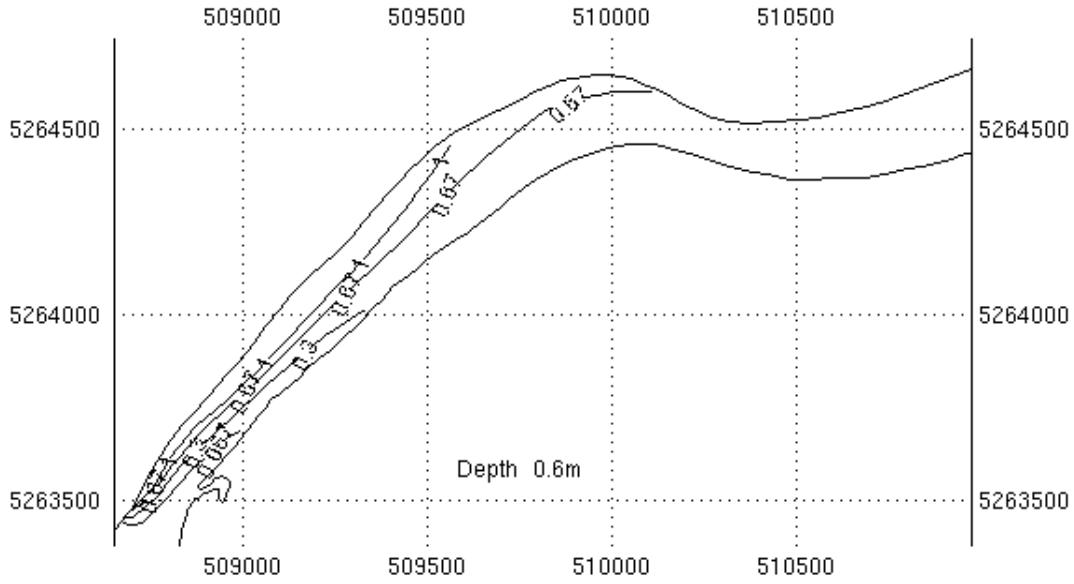

Figure 6.2.9 (b) : Combined Total Resin Acids (50%-ile CES)

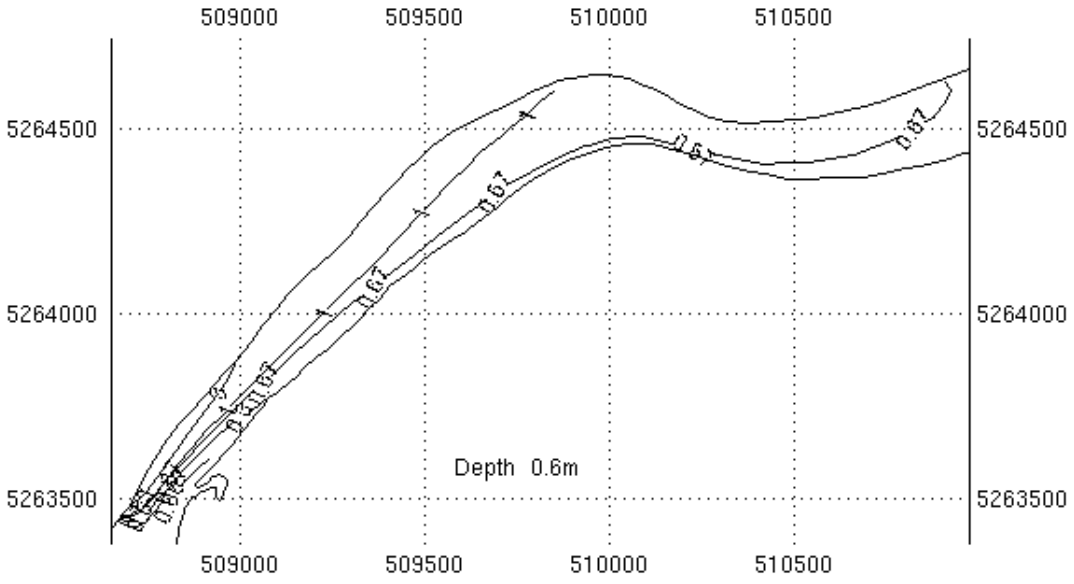

Figure 6.2.9 (c) : Combined Total Resin Acids (95%-ile)

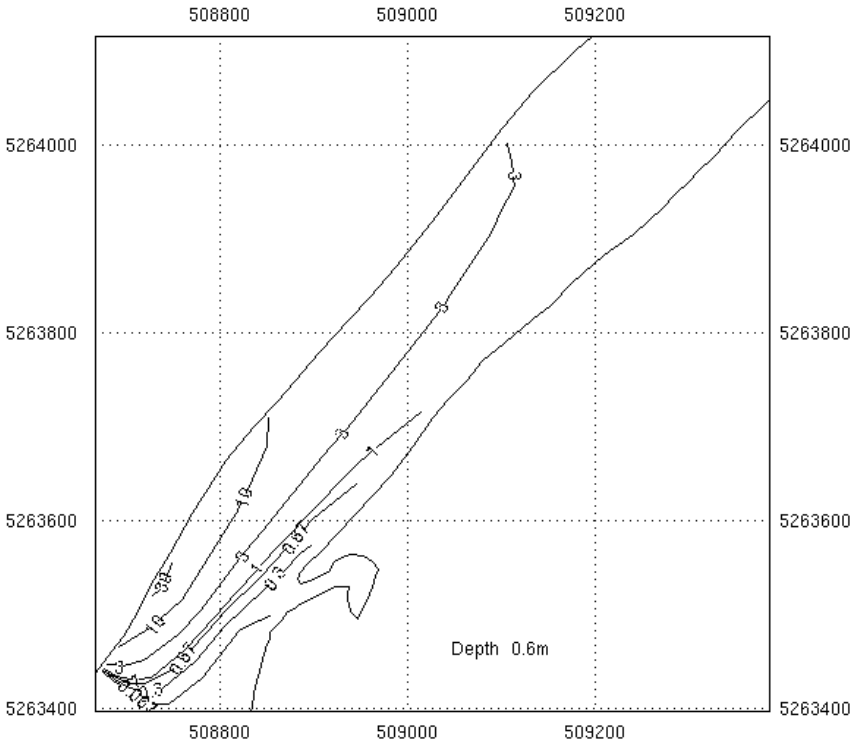

Figure 6.2.10 : Locations of vertical cross sections

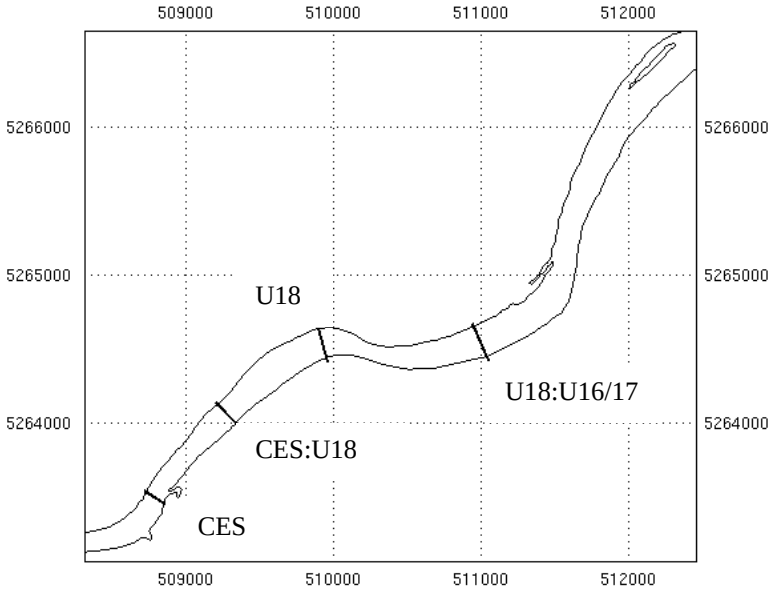

Figure 6.2.11 (a) : Combined Total Resin Acids (5%-ile CES)

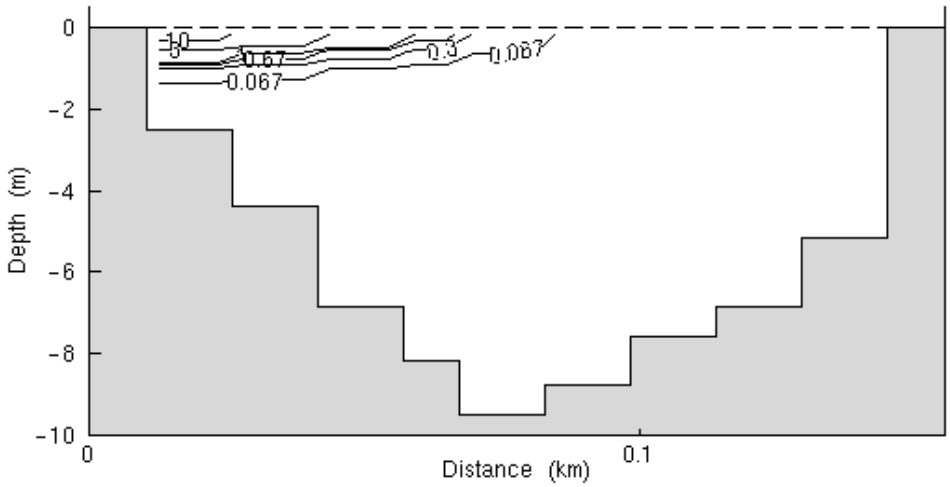

Figure 6.2.11 (b) : Combined Total Resin Acids (5%-ile between U18 and CES)

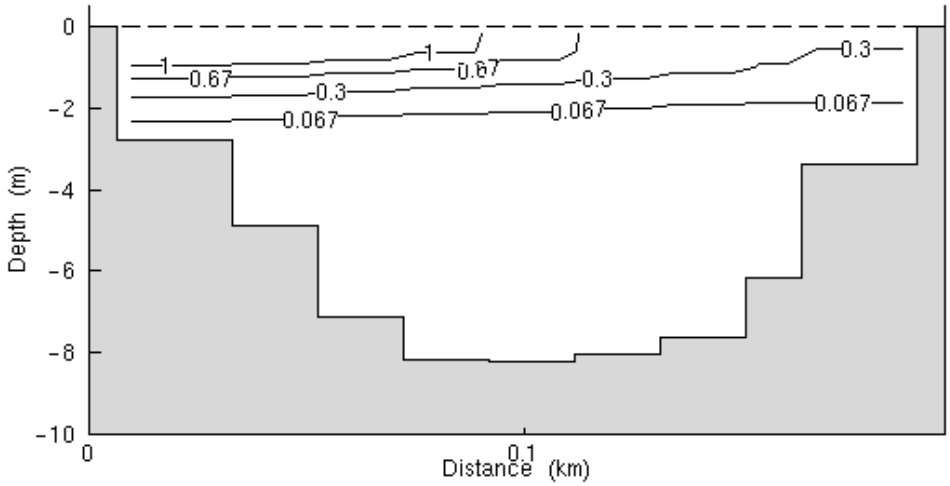

Figure 6.2.11 (c) : Combined Total Resin Acids (5%-ile U18)

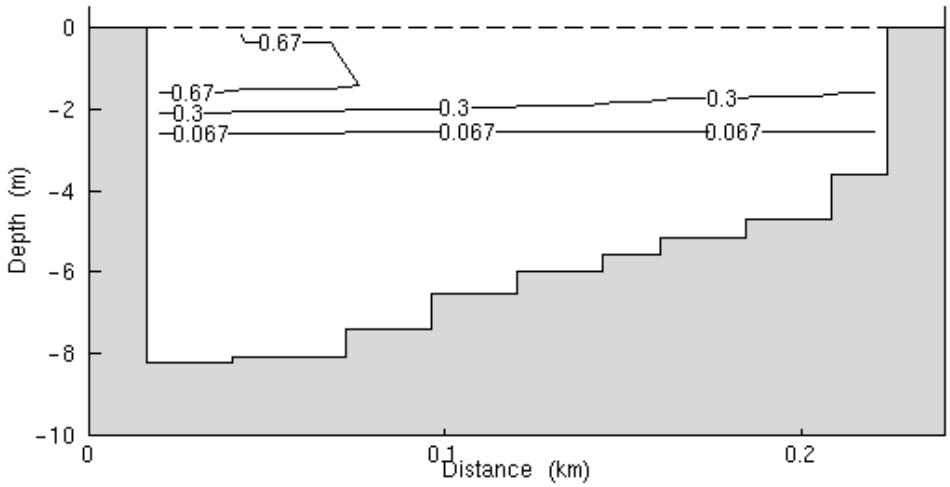

Figure 6.2.11 (d) : Combined Total Resin Acids (5%-ile between U18 and U16/17)

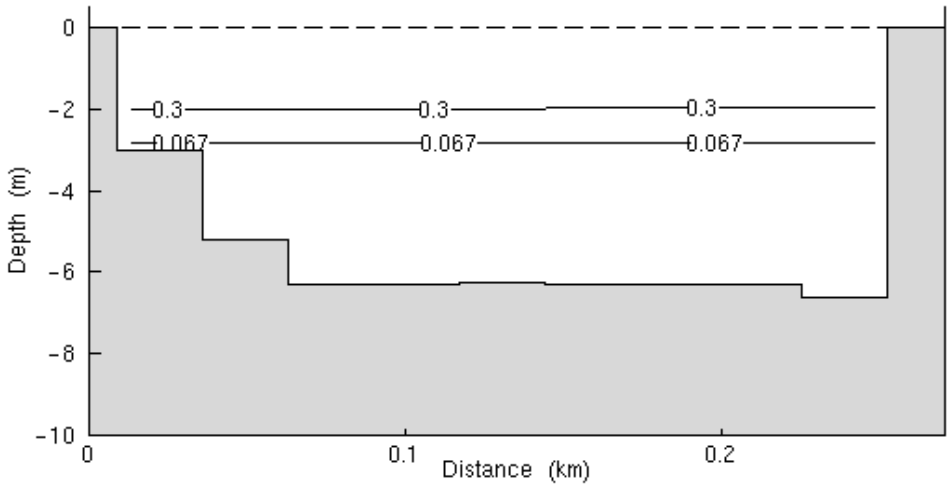

Figure 6.2.12 (a) : Total Resin Acids (50%-ile CES)

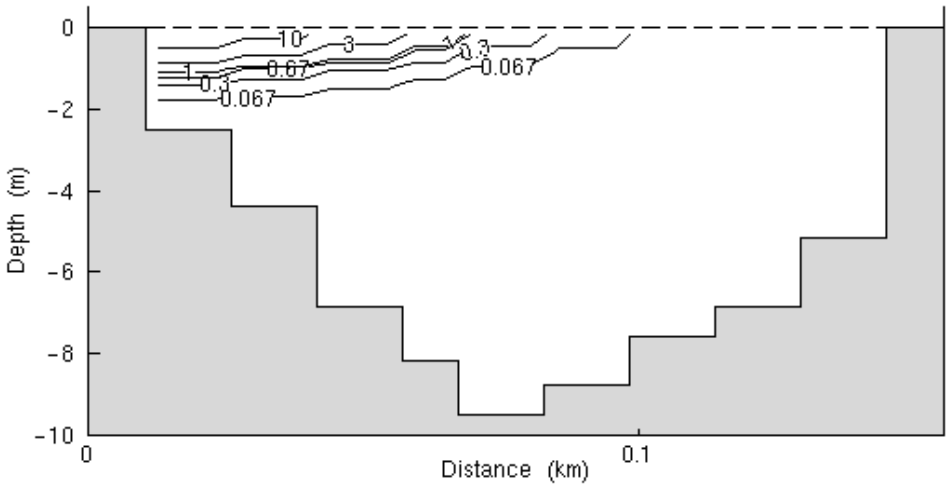

Figure 6.2.12 (b) : Total Resin Acids (50%-ile between U18 and CES)

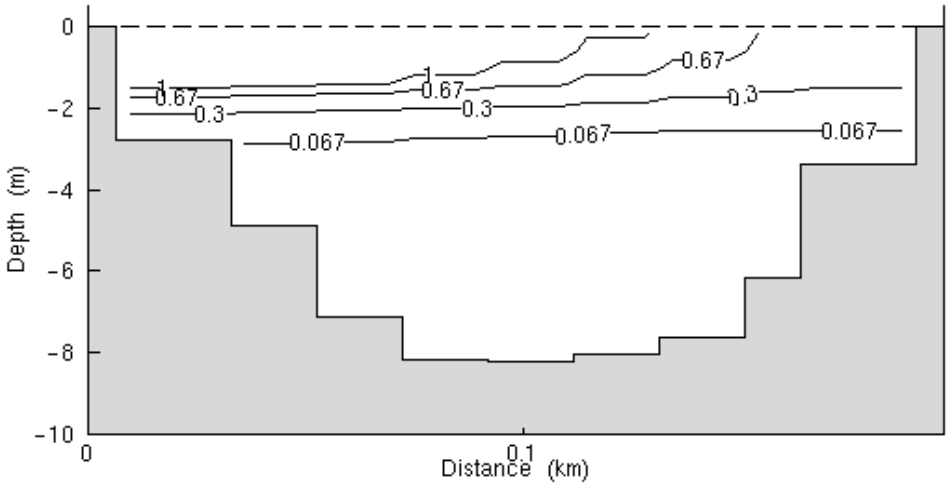

Figure 6.2.12 (c) : Total Resin Acids (50%-ile U18)

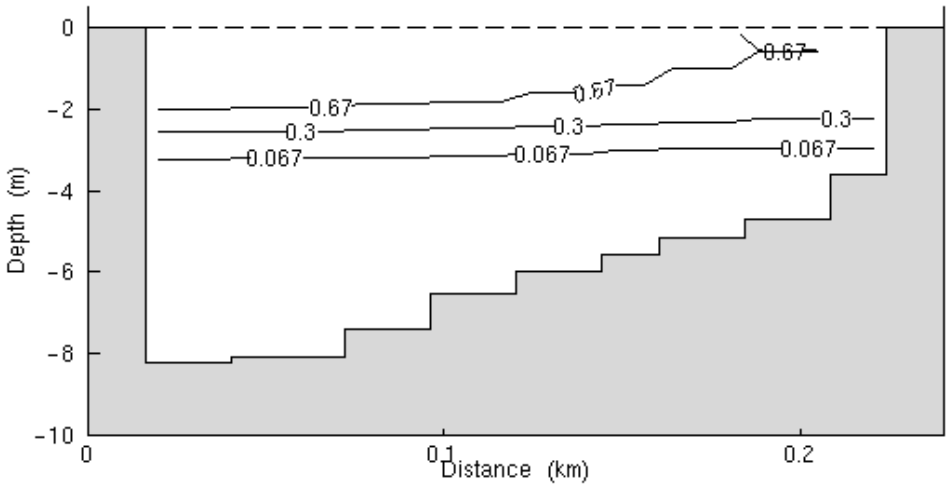

Figure 6.2.12 (d) : Total Resin Acids (50%-ile between U18 and U16/17)

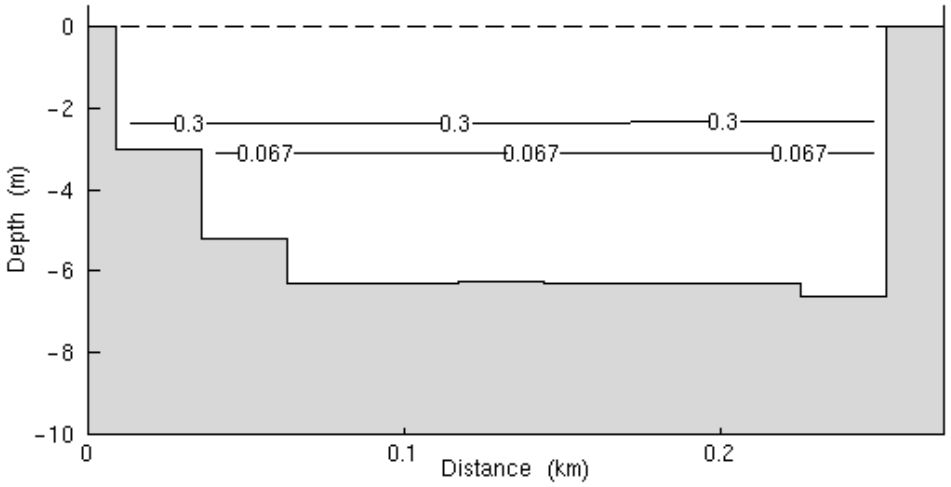

Figure 6.2.13 (a) : Total Resin Acids (95%-ile CES)

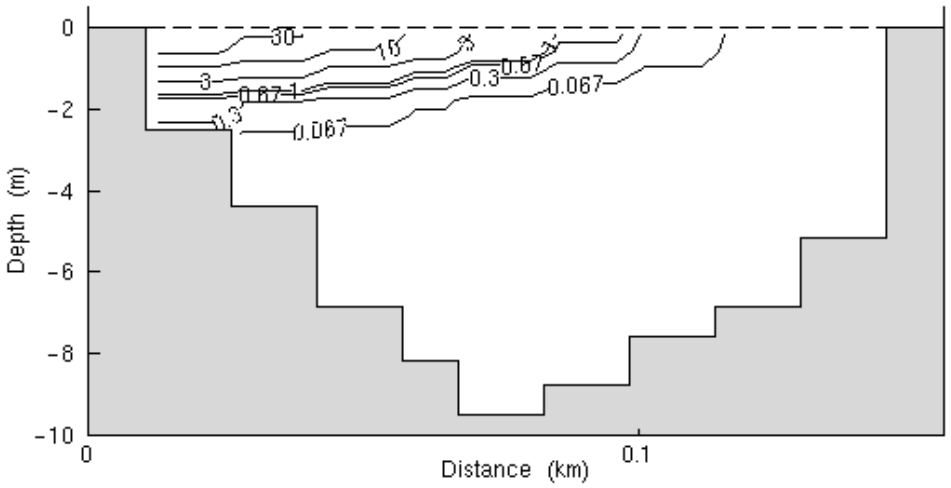

Figure 6.2.13 (b) : Total Resin Acids (95%-ile between U18 and CES)

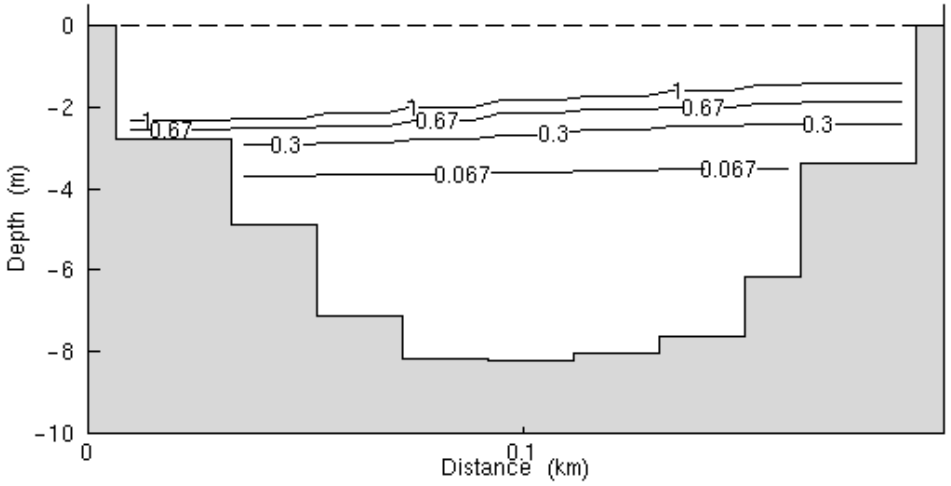

Figure 6.2.13 (c) : Total Resin Acids (95%-ile U18)

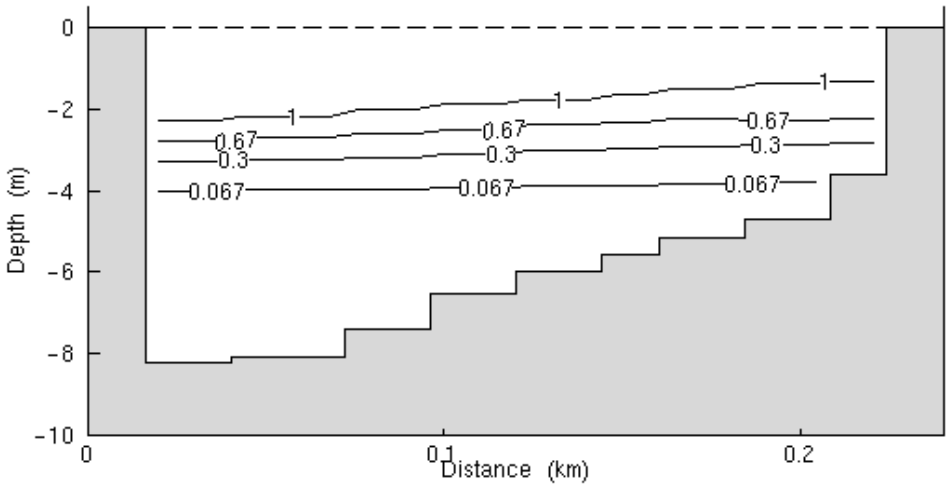

Figure 6.2.13 (d) : Total Resin Acids (95%-ile between U18 and U16/17)

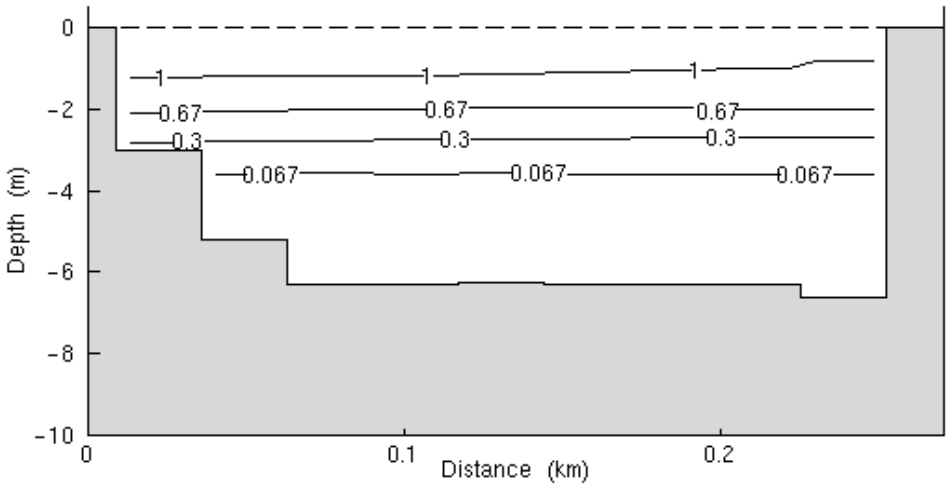

Figure 6.2.14 (a) : Combined Total Resin Acids (maximum CES)

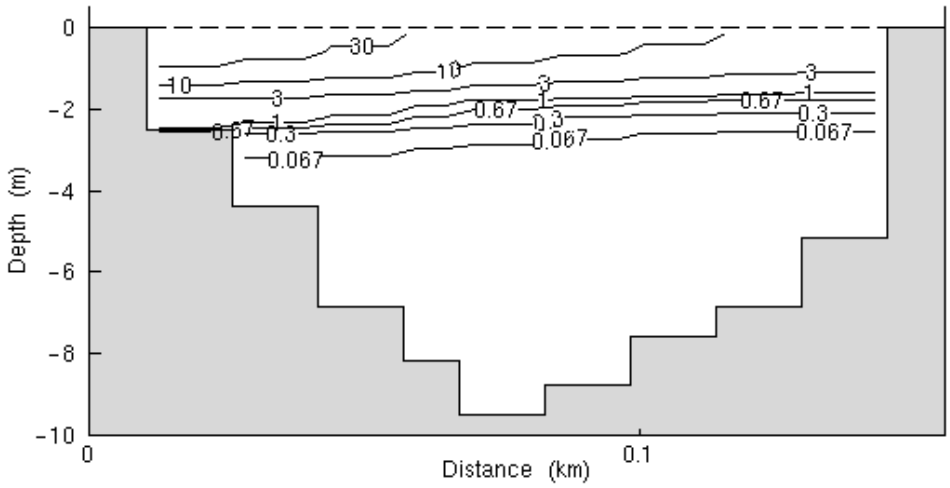

Figure 6.2.14 (b) : Combined Total Resin Acids (maximum between U18 and CES)

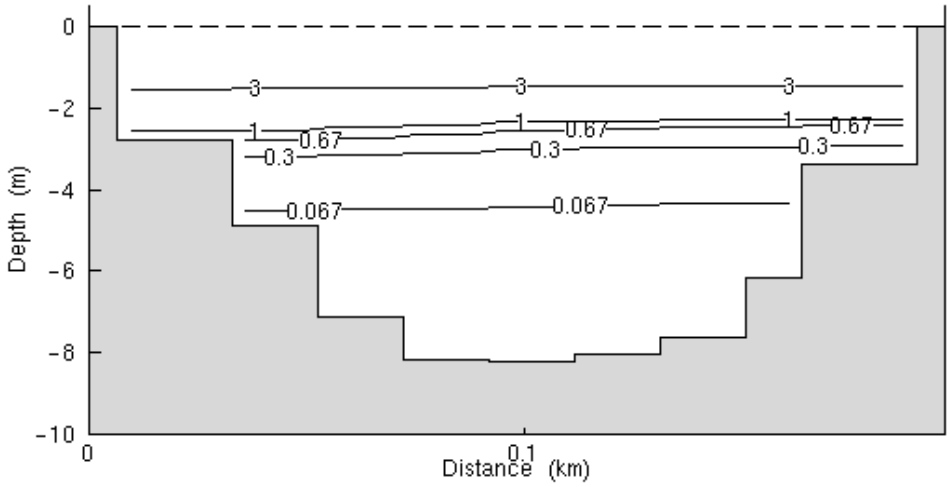

Figure 6.2.14 (c) : Combined Total Resin Acids (maximum U18)

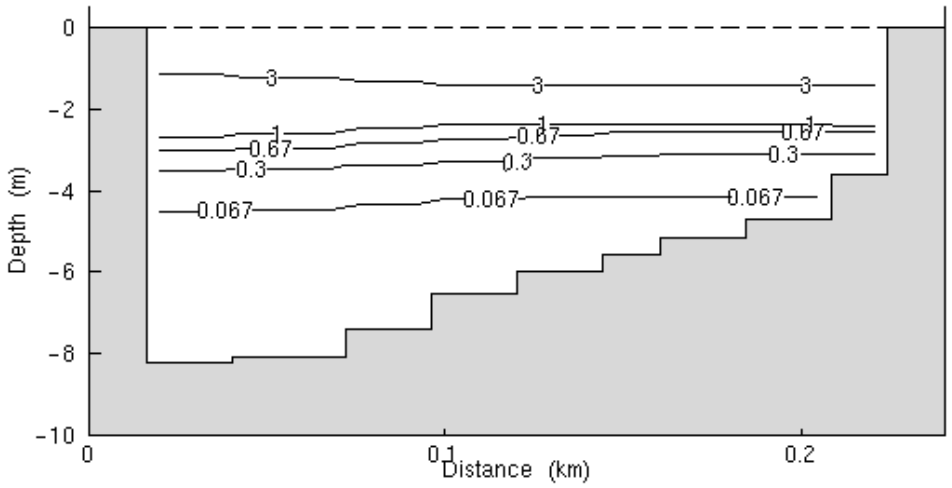

Figure 6.2.14 (d) : Combined Total Resin Acids (maximum between U18 and U16/17)

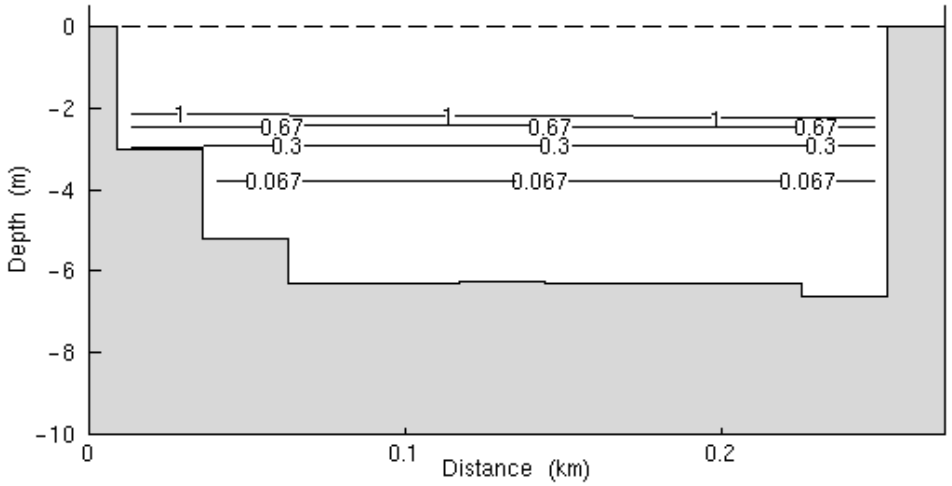

Figure 6.2.15 (a) : Neap 90 Wind 240 (typical scenario) Total Resin Acids (5%-ile CES)

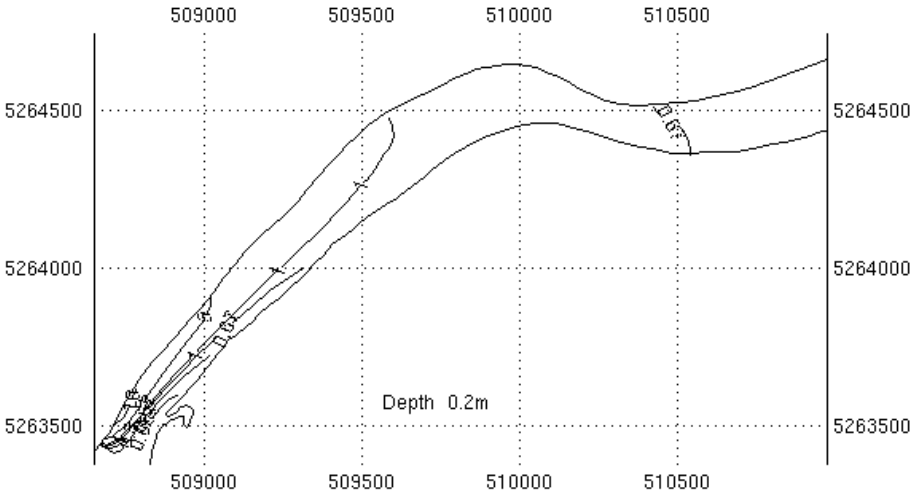

Figure 6.2.15 (b) : Neap 90 Wind 240 (typical scenario) Total Resin Acids (50%-ile)

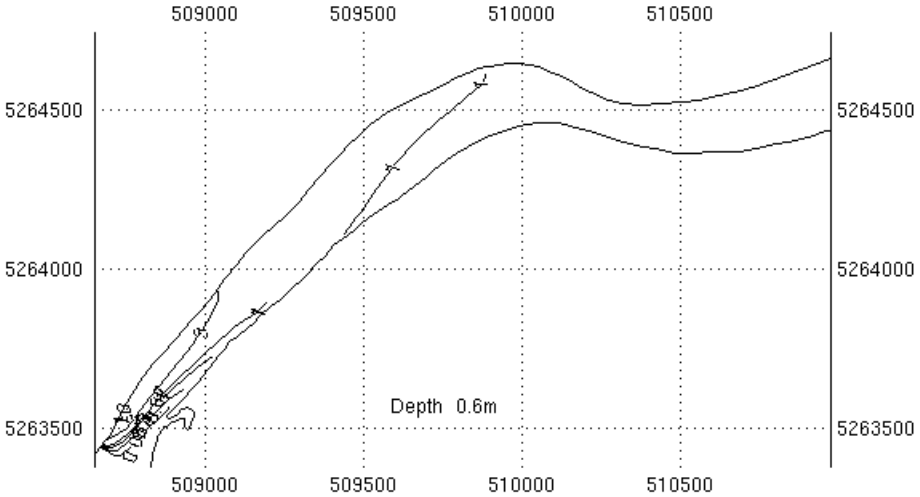

Figure 6.2.15 (c) : Neap 90 Wind 240 (typical scenario) Total Resin Acids (95%-ile)

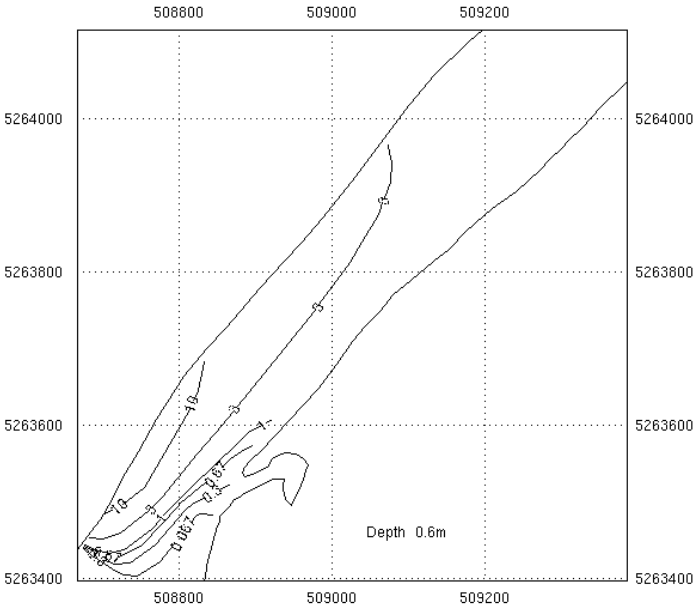

Figure 6.2.16 (a) : Spring 45 Wind 240 (extreme scenario) Total Resin Acids (5%-ile CES)

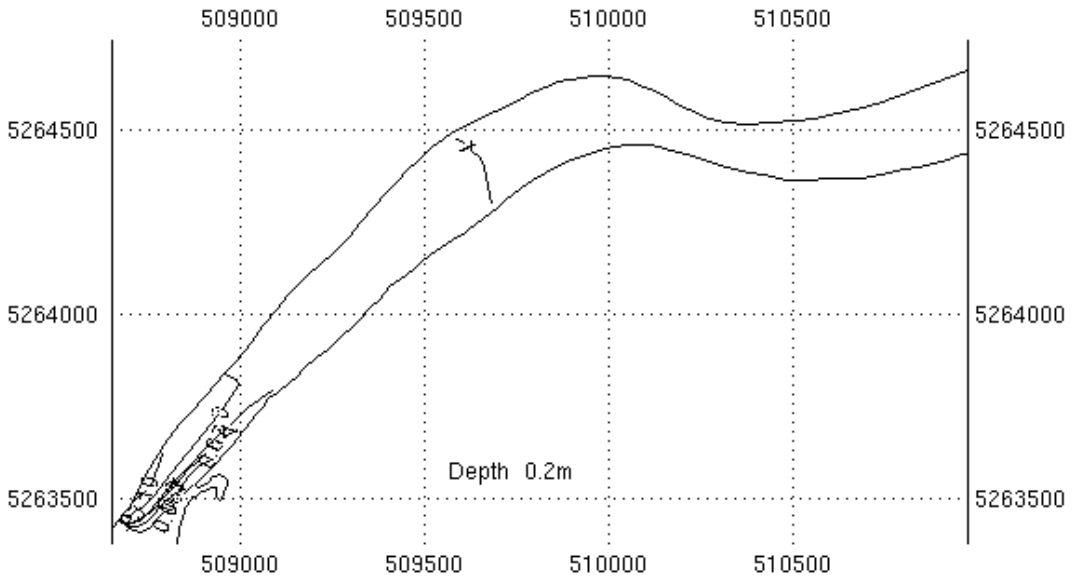

Figure 6.2.16 (b) : Spring 45 Wind 240 (extreme scenario) Total Resin Acids (50%-ile)

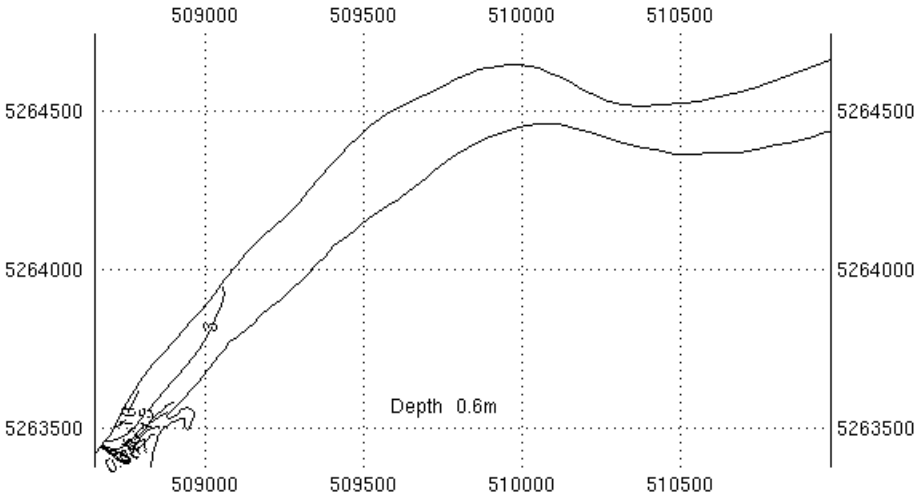

Figure 6.2.16 (c) : Spring 45 Wind 240 (extreme scenario) Total Resin Acids (95%-ile)

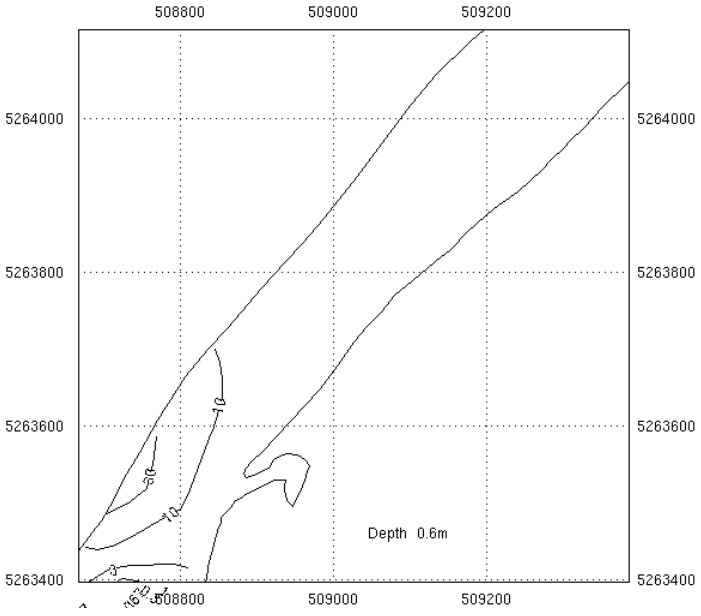

Figure 6.2.17 (a) : Neap 90 Wind 240 (typical scenario) Total Resin Acids (5%-ile CES)

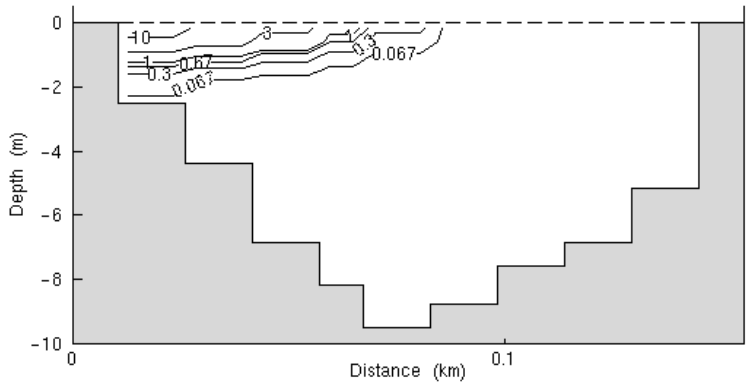

Figure 6.2.17 (b) : Neap 90 Wind 240 (typical scenario) Total Resin Acids (5%-ile between U18 and CES)

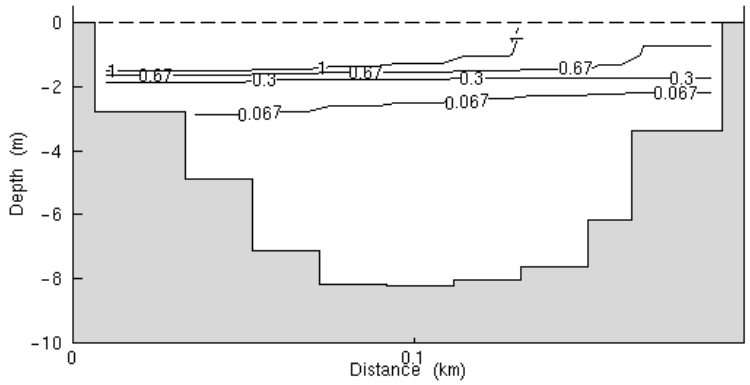

Figure 6.2.17 (c) : Neap 90 Wind 240 (typical scenario) Total Resin Acids (5%-ile U18)

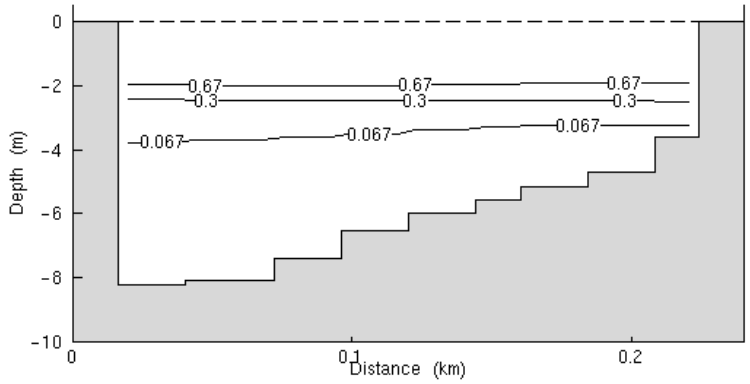

Figure 6.2.17 (d) : Neap 90 Wind 240 (typical scenario) Total Resin Acids (5%-ile between U18 and U16/17)

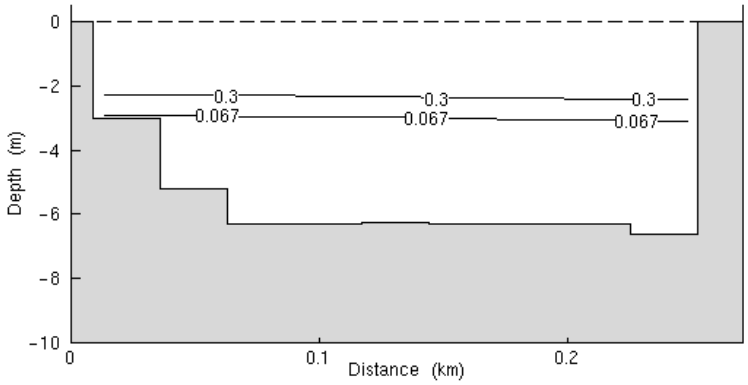

Figure 6.2.18 (a) : Neap 90 Wind 240 (typical scenario) Total Resin Acids (50%-ile CES)

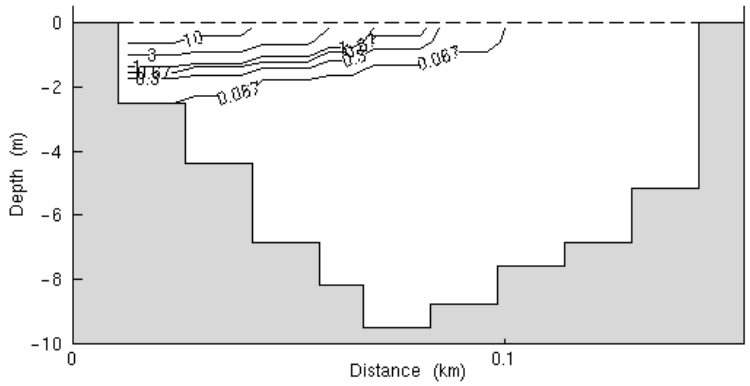

Figure 6.2.18 (b) : Neap 90 Wind 240 (typical scenario) Total Resin Acids (50%-ile between U18 and CES)

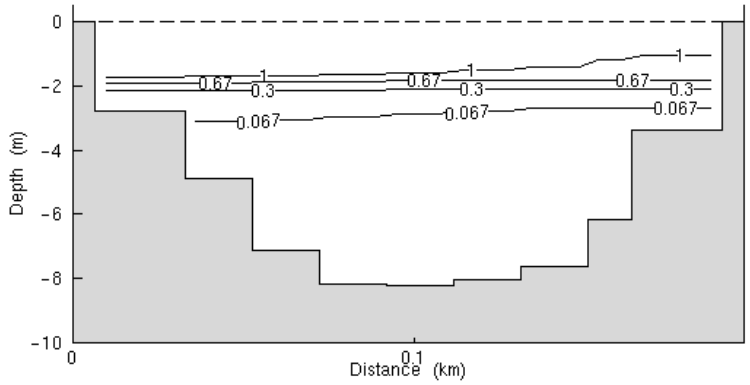

Figure 6.2.18 (c) : Neap 90 Wind 240 (typical scenario) Total Resin Acids (50%-ile U18)

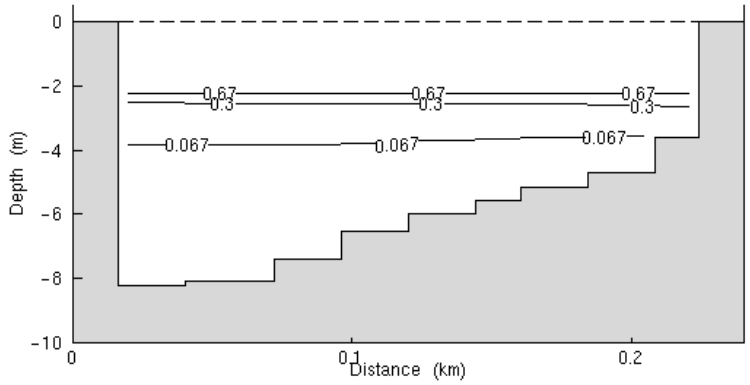

Figure 6.2.18 (d) : Neap 90 Wind 240 (typical) Total Resin Acids (50%-ile between U18 and U16/17)

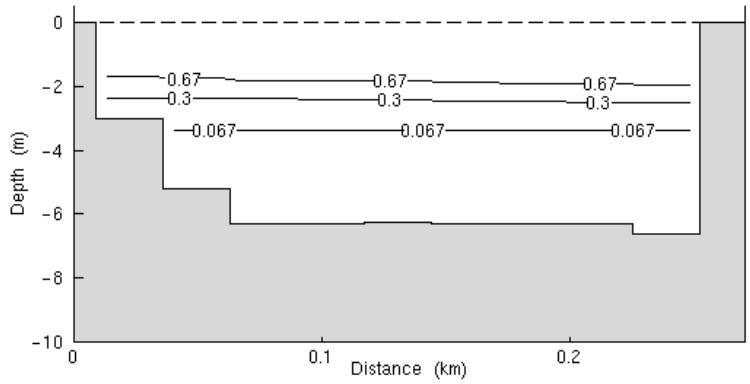

Figure 6.2.19 (a) : Neap 90 Wind 240 (typical scenario) Total Resin Acids (95%-ile CES)

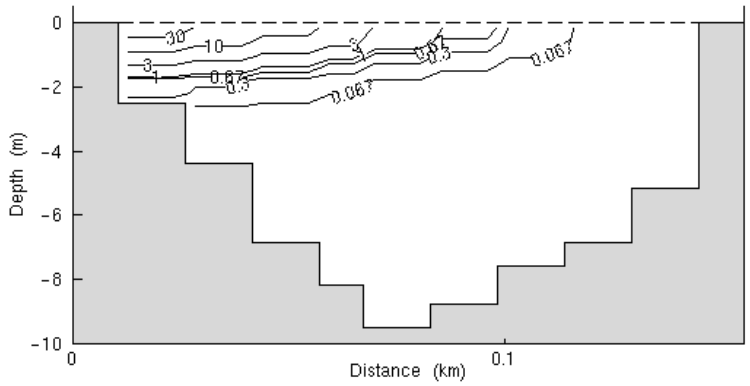

Figure 6.2.19 (b) : Neap 90 Wind 240 (typical) Total Resin Acids (95%-ile between U18 and CES)

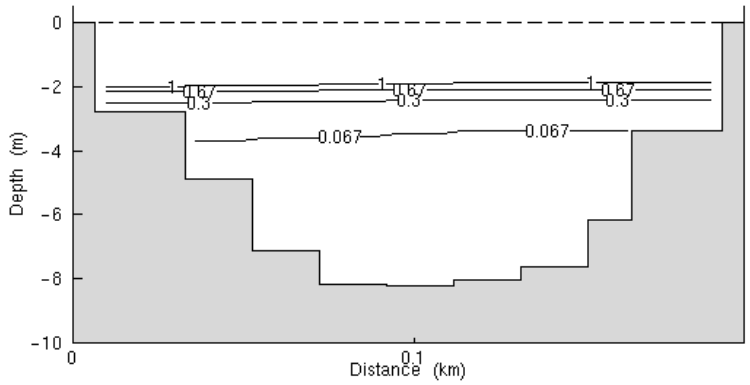

Figure 6.2.19 (c) : Neap 90 Wind 240 (typical scenario) Total Resin Acids (95%-ile U18)

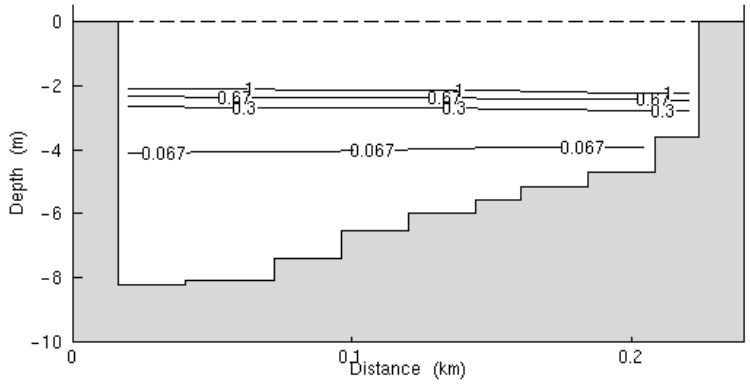

Figure 6.2.19 (d) : Neap 90 Wind 240 (typical) Total Resin Acids (95%-ile between U18 and U16/17)

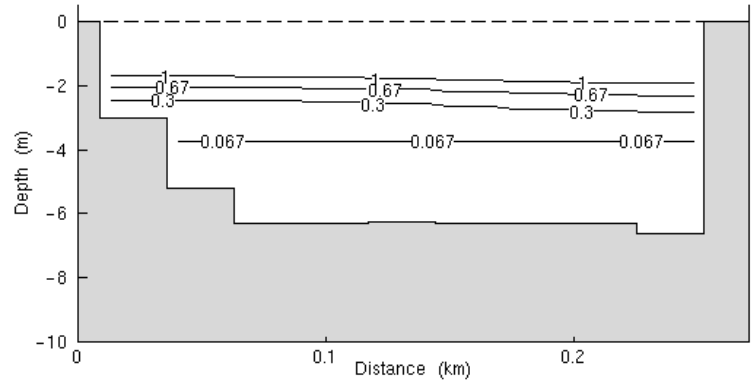

Figure 6.2.20 (a) : Neap 90 Wind 240 (typical scenario) Total Resin Acids (maximum CES)

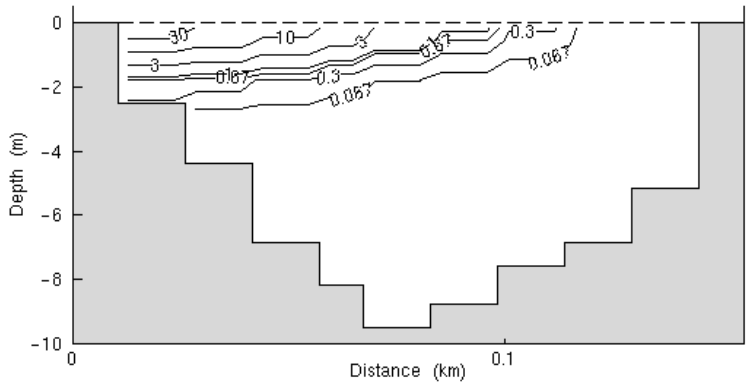

Figure 6.2.20 (b) : Neap 90 Wind 240 (typical) Total Resin Acids (maximum between U18 and CES)

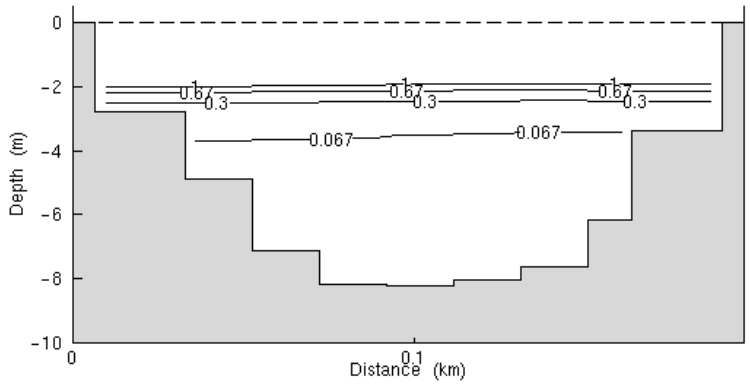

Figure 6.2.20 (c): Neap 90 Wind 240 (typical scenario) Total Resin Acids (maximum U18)

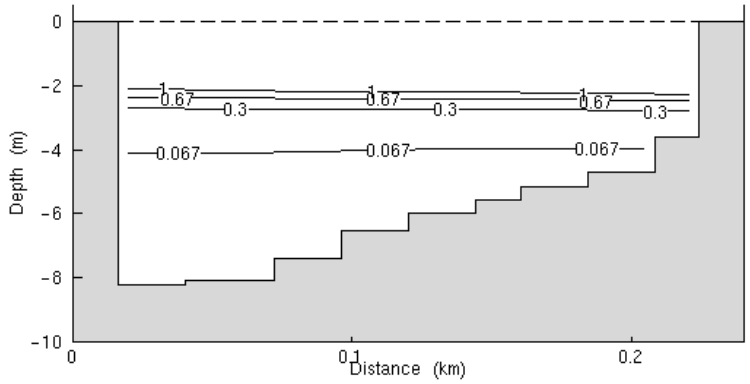

Figure 6.2.20(d) : Neap 90 Wind 240 (typical) Total Resin Acids (maximum between U18 and U16/17)

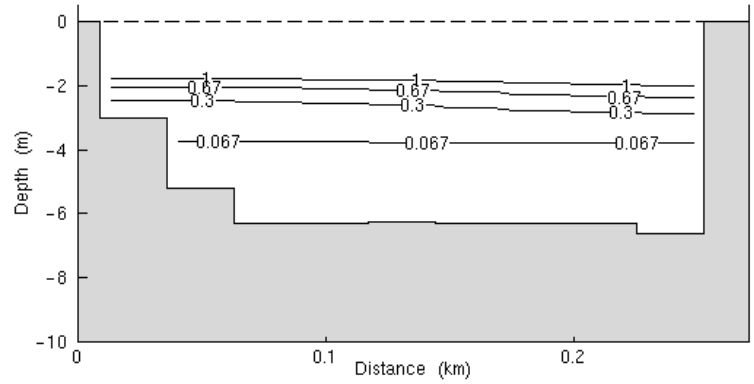

Figure 6.2.21 (a) : Spring 45 Wind 240 (extreme scenario) Total Resin Acids (5%-ile CES)

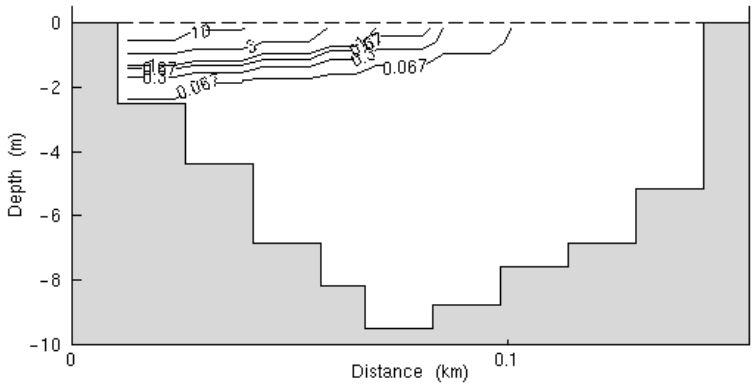

Figure 6.2.21 (b) : Spring 45 Wind 240 (extreme) Total Resin Acids (5%-ile between U18 and CES)

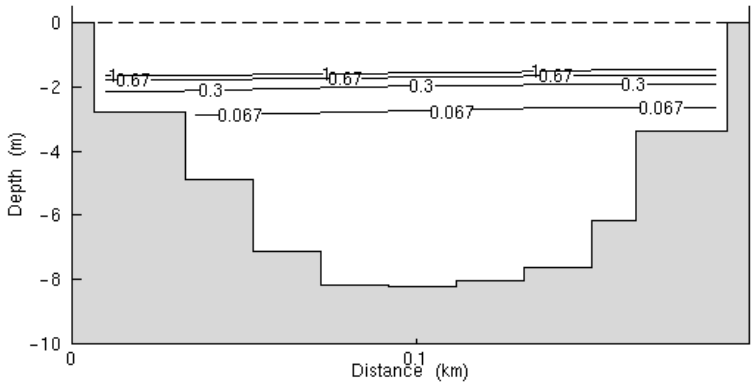

Figure 6.2.21 (c) : Spring 45 Wind 240 (extreme scenario) Total Resin Acids (5%-ile U18)

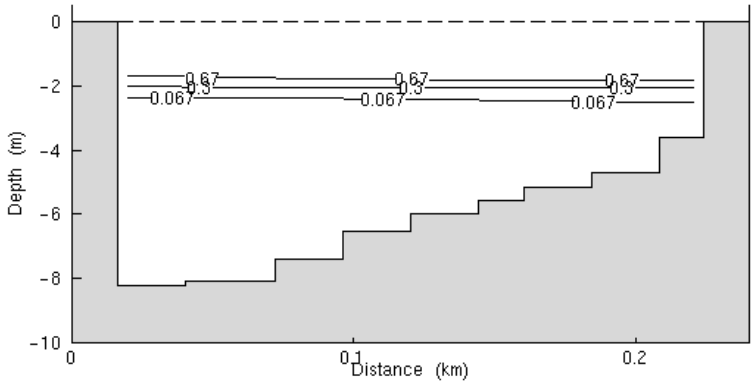

Figure 6.2.21 (d) : Spring 45 Wind 240 (extreme) Total Resin Acids (5%-ile between U18 and U16/17)

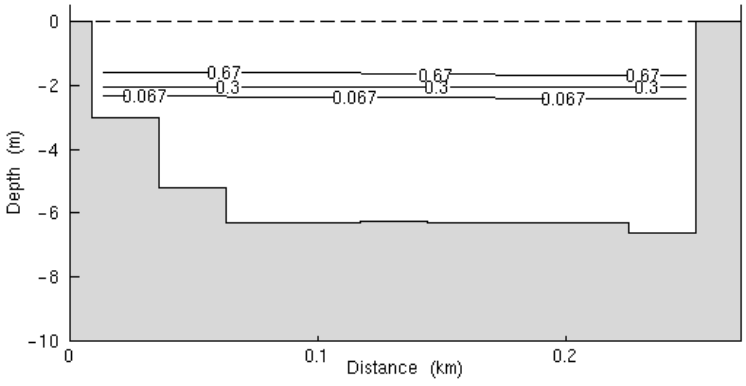

Figure 6.2.22 (a) : Spring 45 Wind 240 (extreme scenario) Total Resin Acids (50%-ile CES)

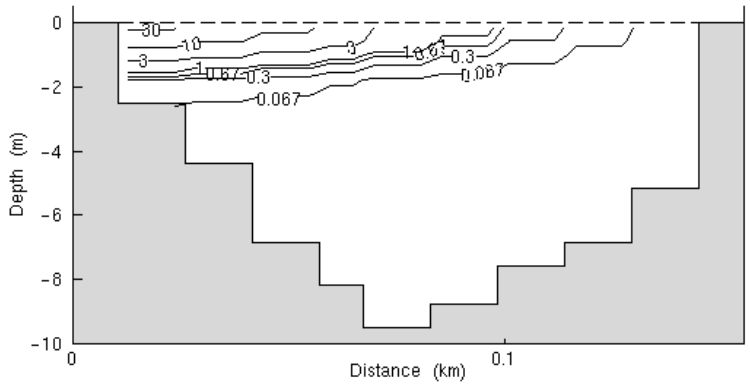

Figure 6.2.22 (b) : Spring 45 Wind 240 (extreme) Total Resin Acids (50%-ile between U18 and CES)

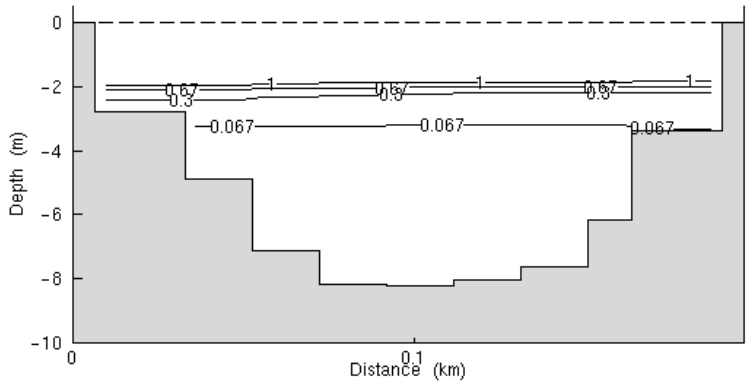

Figure 6.2.22 (c) : Spring 45 Wind 240 (extreme scenario) Total Resin Acids (50%-ile U18)

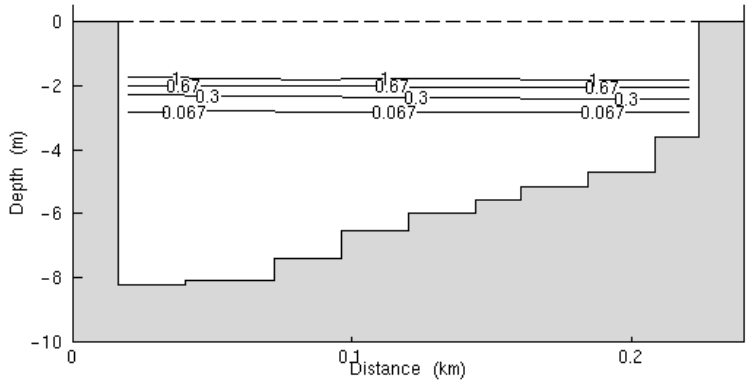

Figure 6.2.22 (d) : Spring 45 Wind 240 (extreme) Total Resin Acids (50%-ile between U18 and U16/17)

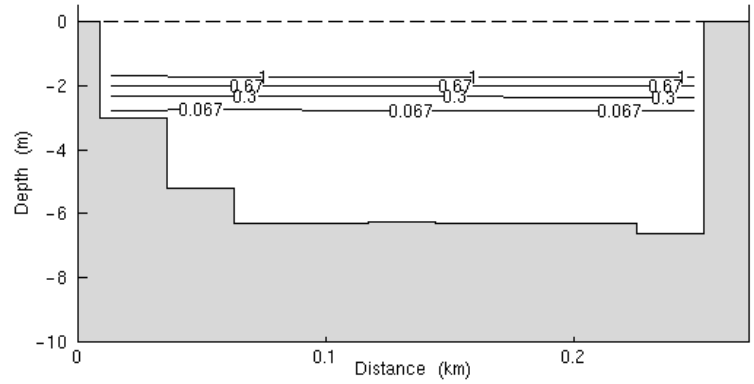

Figure 6.2.23 (a) : Spring 45 Wind 240 (extreme scenario) Total Resin Acids (95%-ile CES)

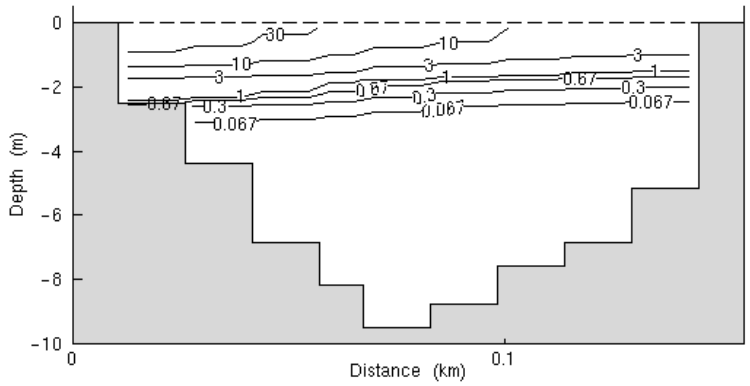

Figure 6.2.23 (b) : Spring 45 Wind 240 (extreme) Total Resin Acids (95%-ile between U18 and CES)

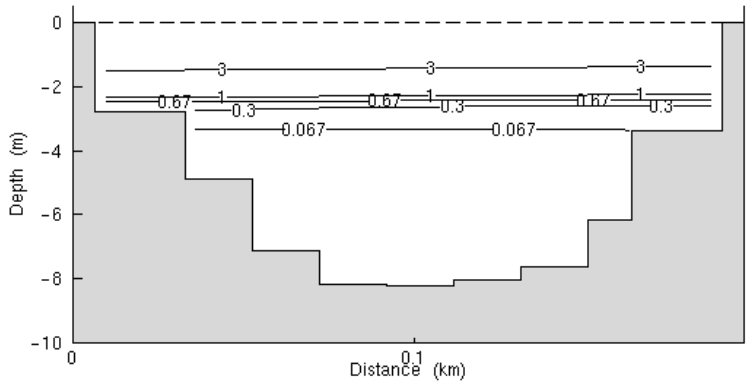

Figure 6.2.23 (c) : Spring 45 Wind 240 (extreme scenario) Total Resin Acids (95%-ile U18)

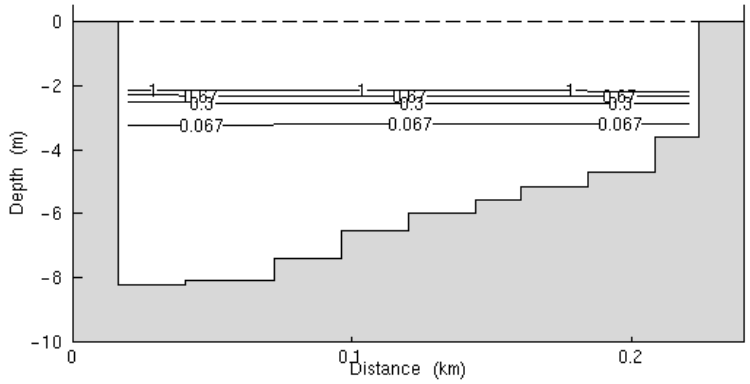

Figure 6.2.23 (d) : Spring 45 Wind 240 (extreme) Total Resin Acids (95%-ile between U18 and U16/17)

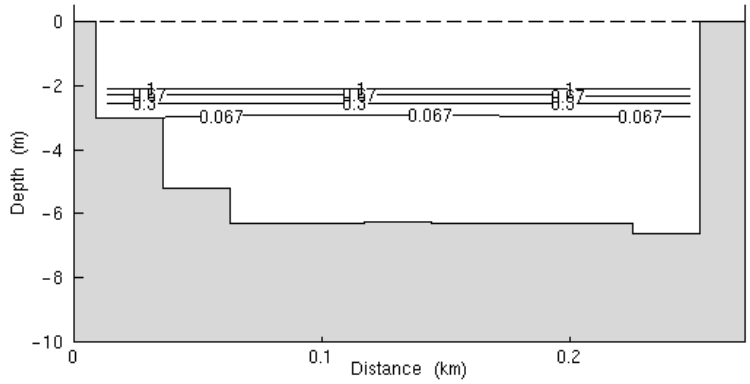

Figure 6.2.24 (a) : Spring 45 Wind 240 (extreme scenario) Total Resin Acids (maximum CES)

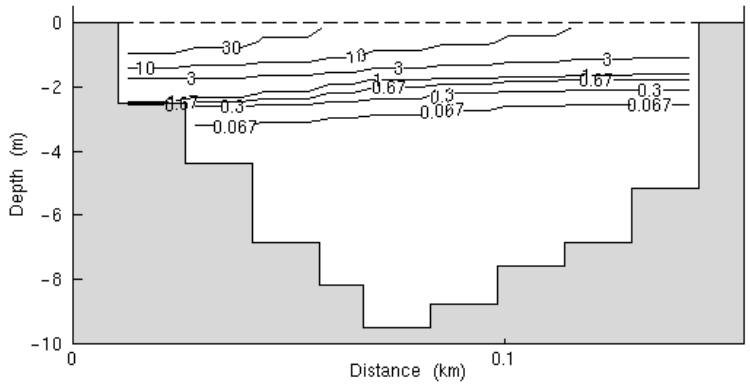

Figure 6.2.24 (b) : Spring 45 Wind 240 (extreme) Total Resin Acids (maximum between U18 and CES)

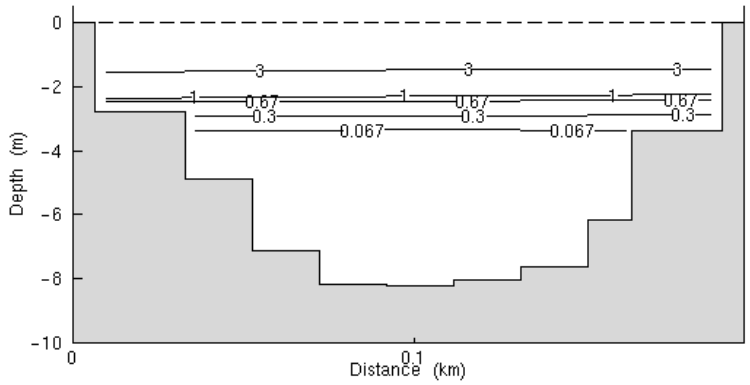

Figure 6.2.24 (c) : Spring 45 Wind 240 (extreme scenario) Total Resin Acids (maximum U18)

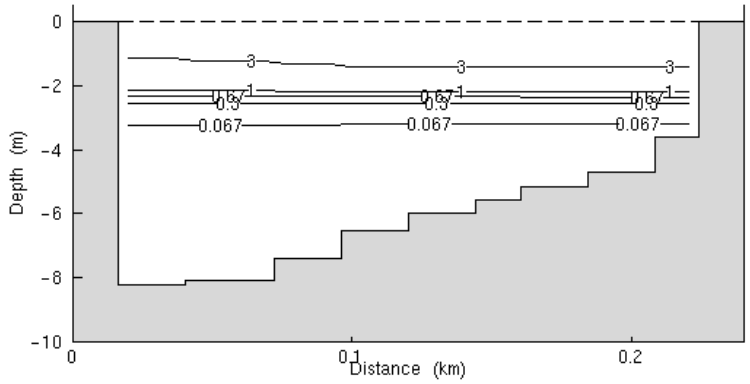

Figure 6.2.24 (d) : Spring 45 Wind 240 (extreme) Total Resin Acids (maximum between U18 and U16/17)

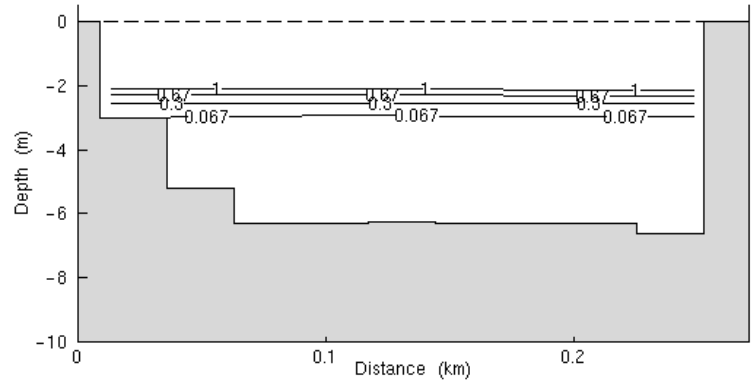

Figure 6.2.25 (a) : Combined Total_A Resin Acids (5%-ile CES)

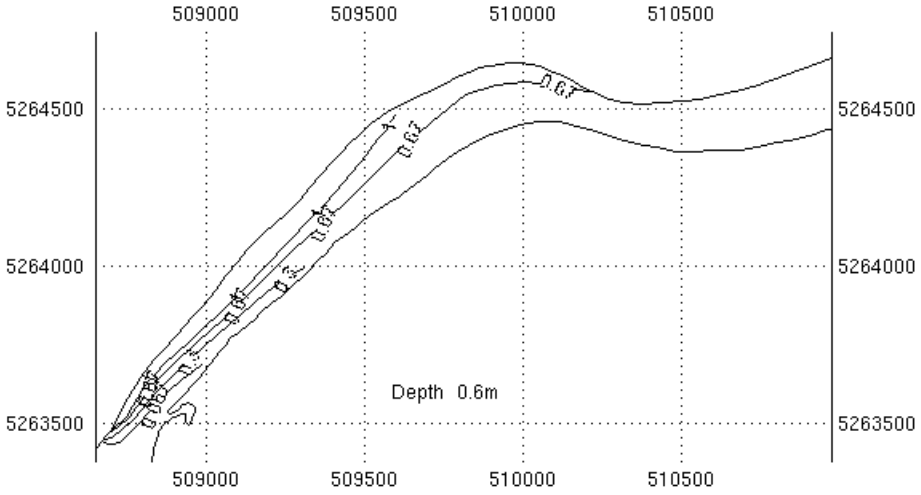

Figure 6.2.25 (b) : Combined Total_A Resin Acids (50%-ile)

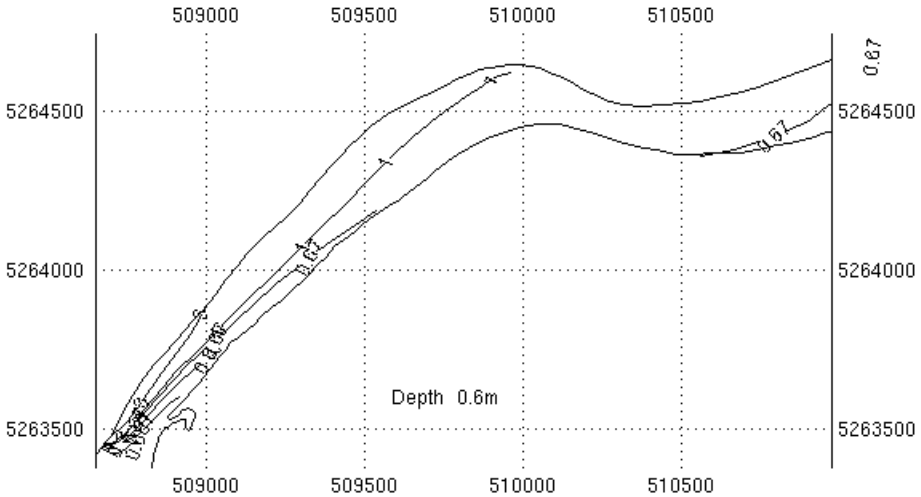

Figure 6.2.25 (c) : Combined Total_A Resin Acids (95%-ile)

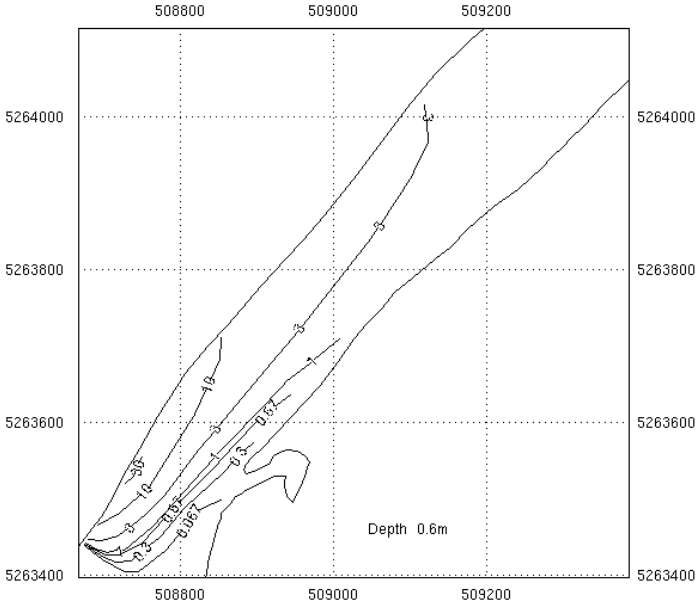

Figure 6.2.26 (a) : Combined Total_A Resin Acids (5%-ile CES)

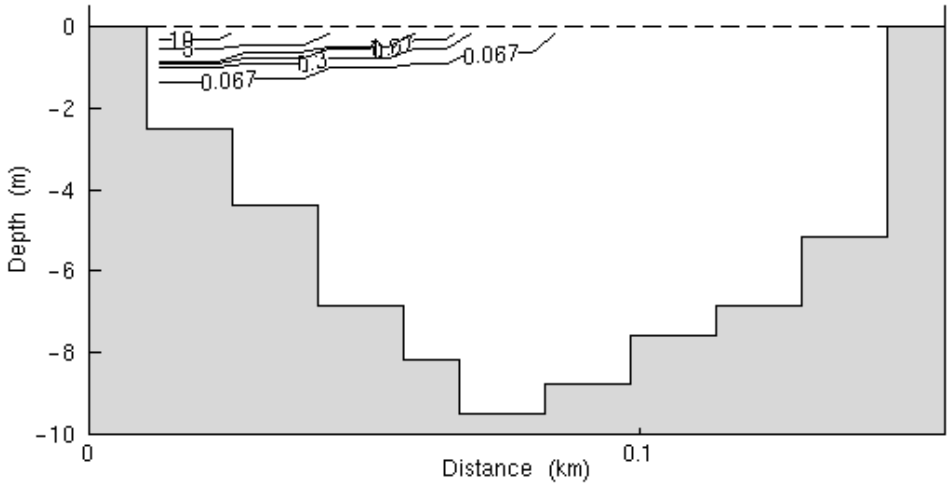

Figure 6.2.26 (b) : Combined Total_A Resin Acids (5%-ile between U18 and CES)

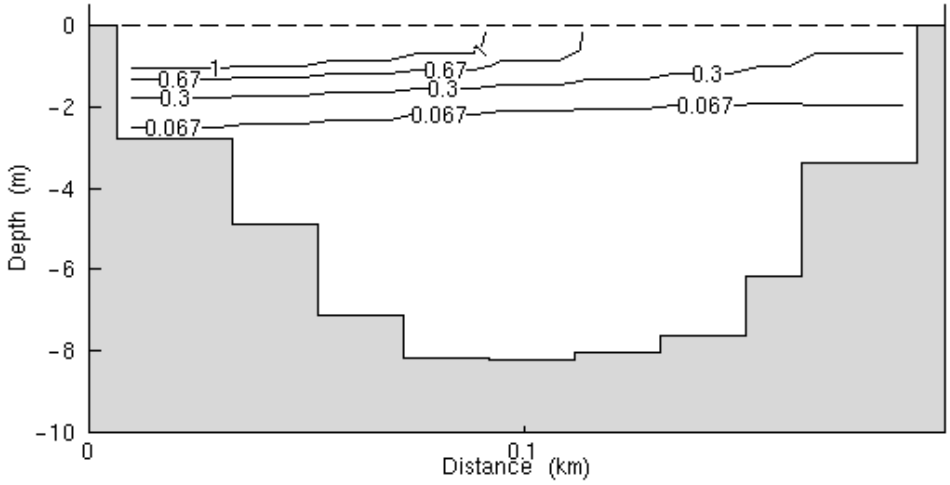

Figure 6.2.26 (c) : Combined Total_A Resin Acids (5%-ile U18)

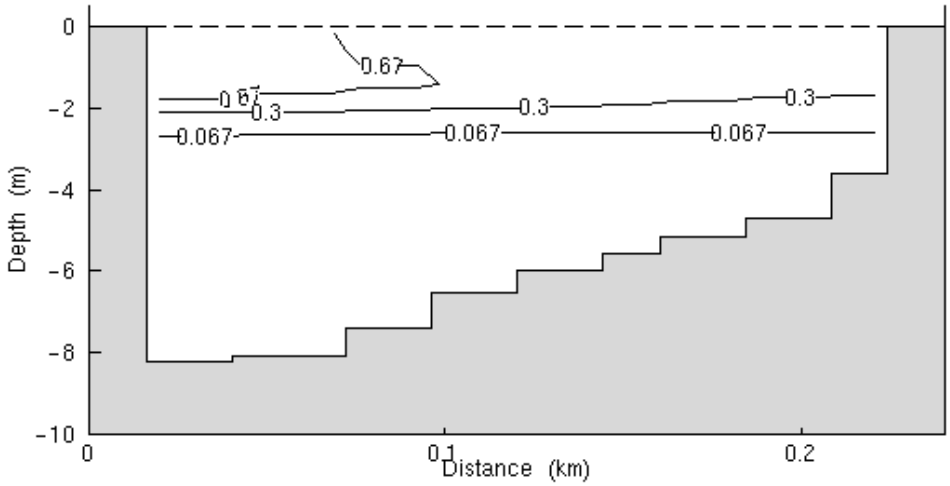

Figure 6.2.26 (d): Combined Total_A Resin Acids (5%-ile between U18 and U16/17)

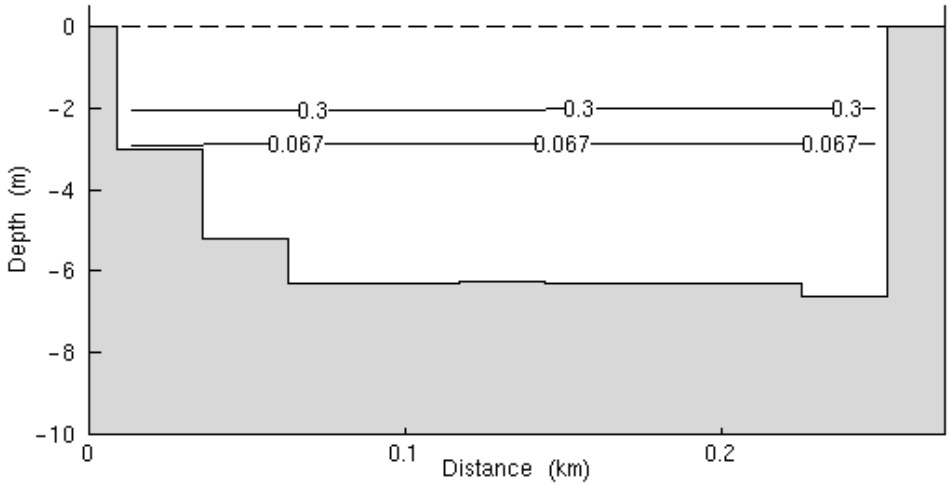

Figure 6.2.27 (a) : Combined Total_A Resin Acids (50%-ile CES)

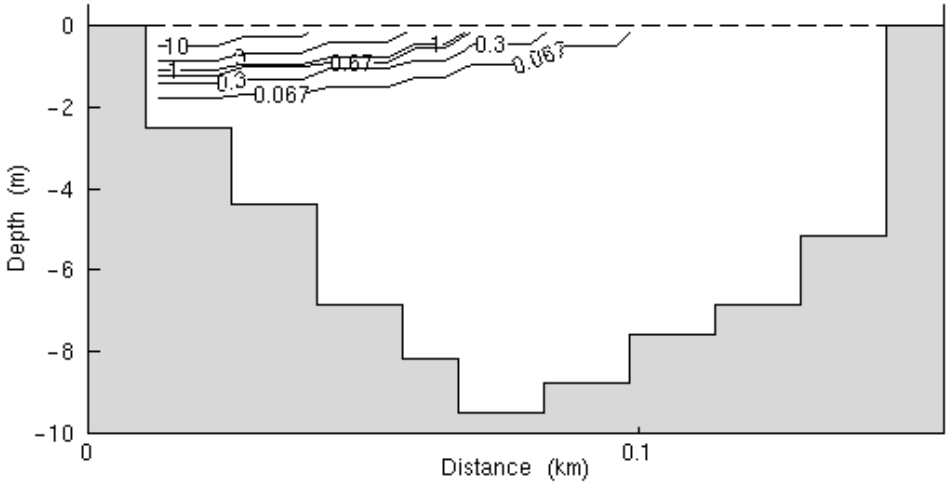

Figure 6.2.27 (b) : Combined Total_A Resin Acids (50%-ile between U18 and CES)

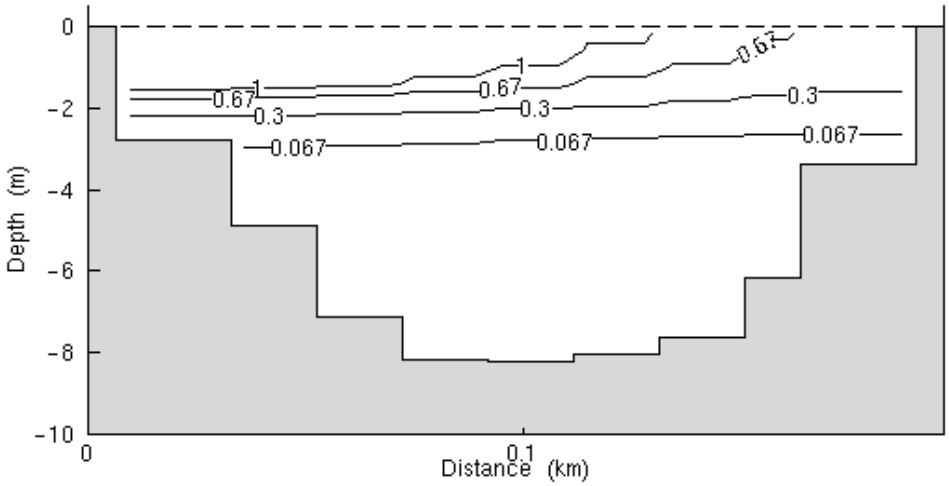

Figure 6.2.27 (c) : Combined Total_A Resin Acids (50%-ile U18)

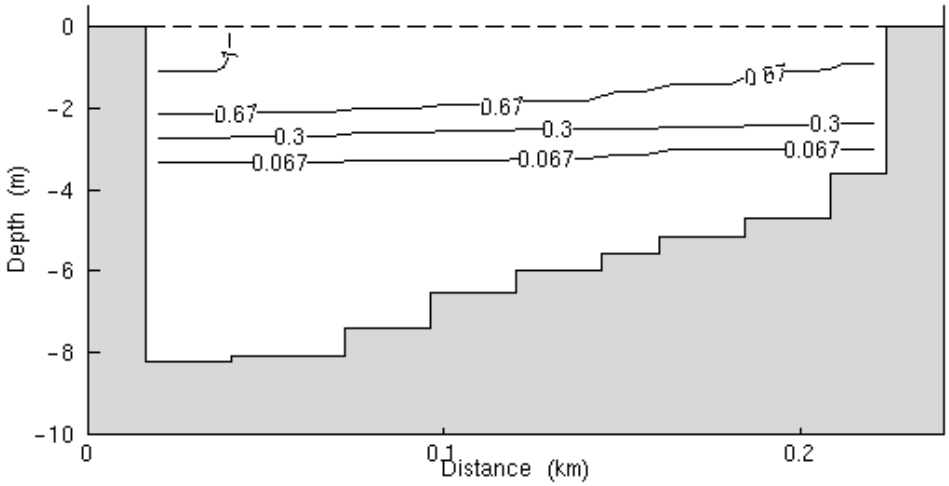

Figure 6.2.27 (d) : Combined Total_A Resin Acids (50%-ile between U18 and U16/17)

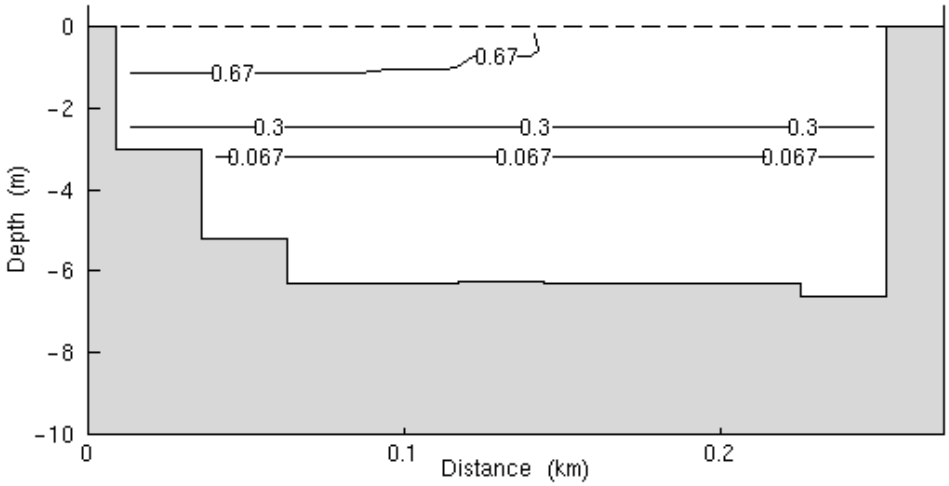

Figure 6.2.28 (a) : Combined Total_A Resin Acids (95%-ile CES)

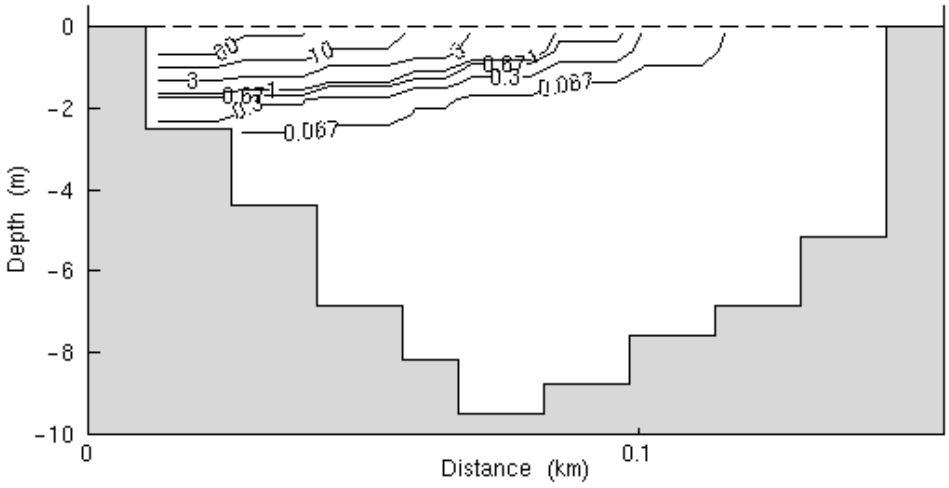

Figure 6.2.28 (b) : Combined Total_A Resin Acids (95%-ile between U18 and CES)

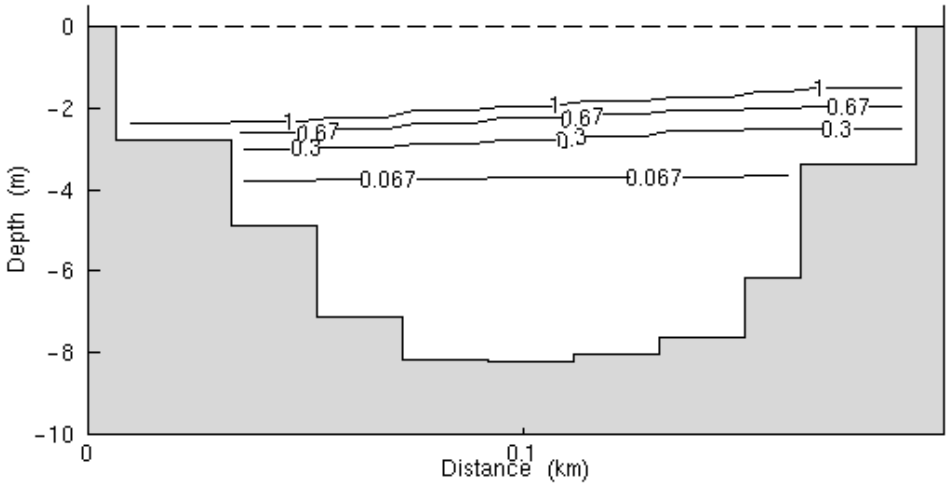

Figure 6.2.28 (c) : Combined Total_A Resin Acids (95%-ile U18)

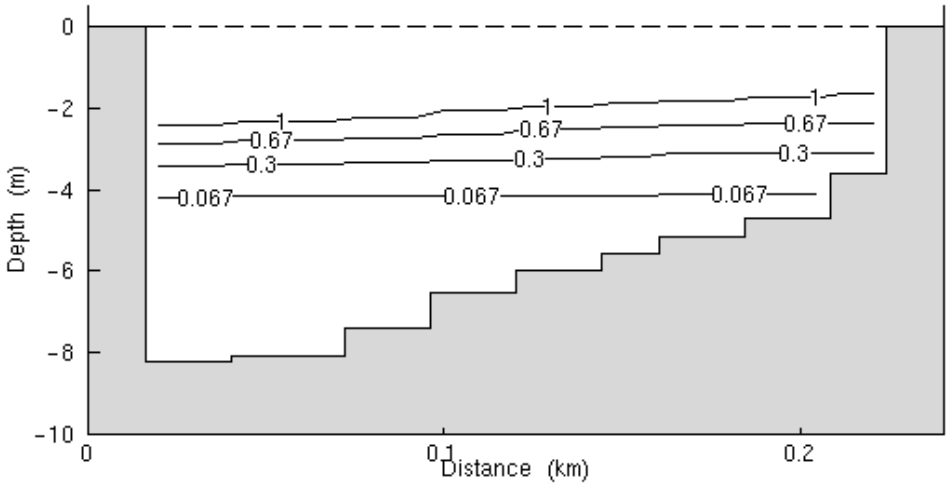

Figure 6.2.28 (d) : Combined Total_A Resin Acids (95%-ile between U18 and U16/17)

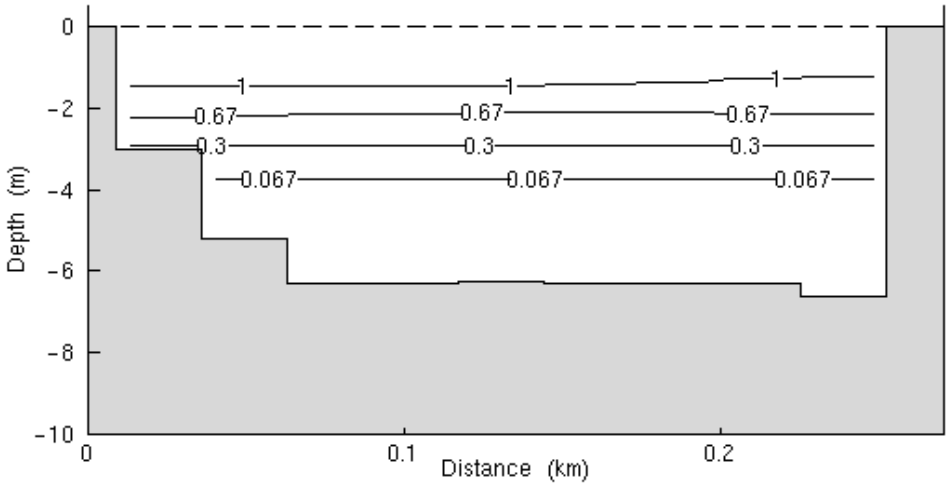

Figure 6.2.29 (a) : Combined Total_A Resin Acids (maximum CES)

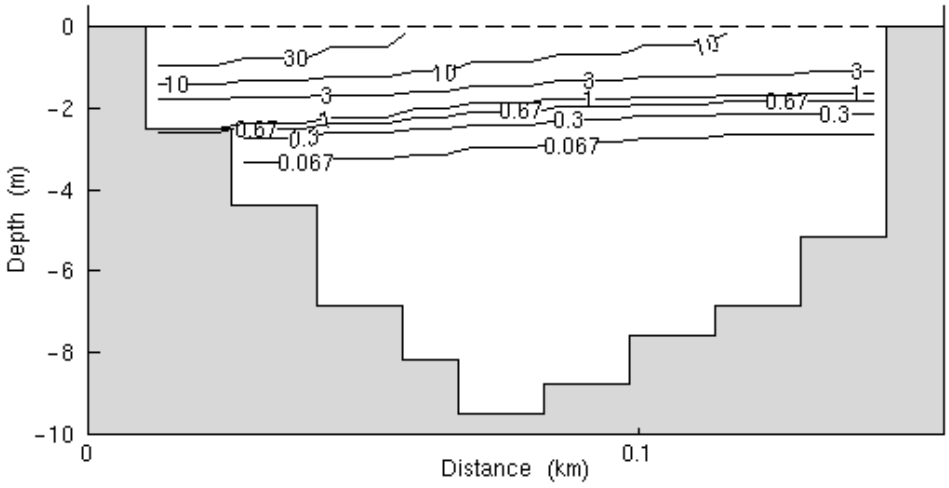

Figure 6.2.29 (b) : Combined Total_A Resin Acids (maximum between U18 and CES)

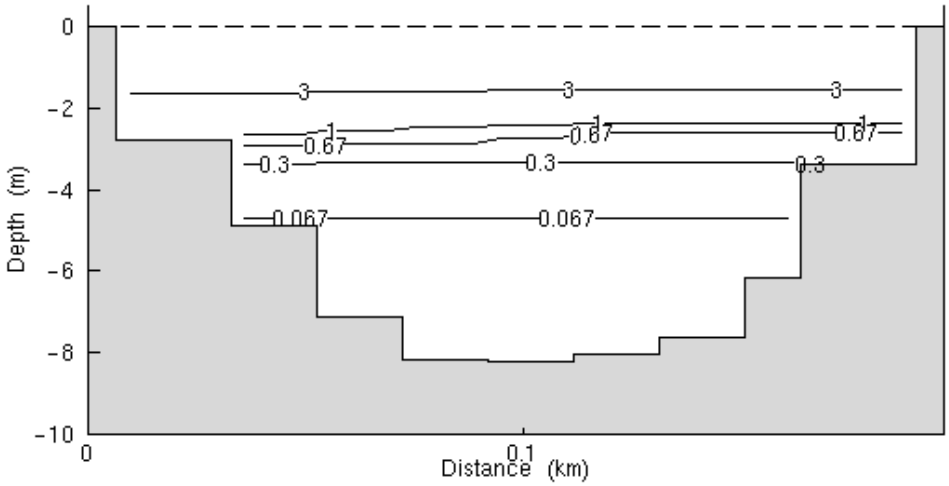

Figure 6.2.29 (c) : Combined Total_A Resin Acids (maximum U18)

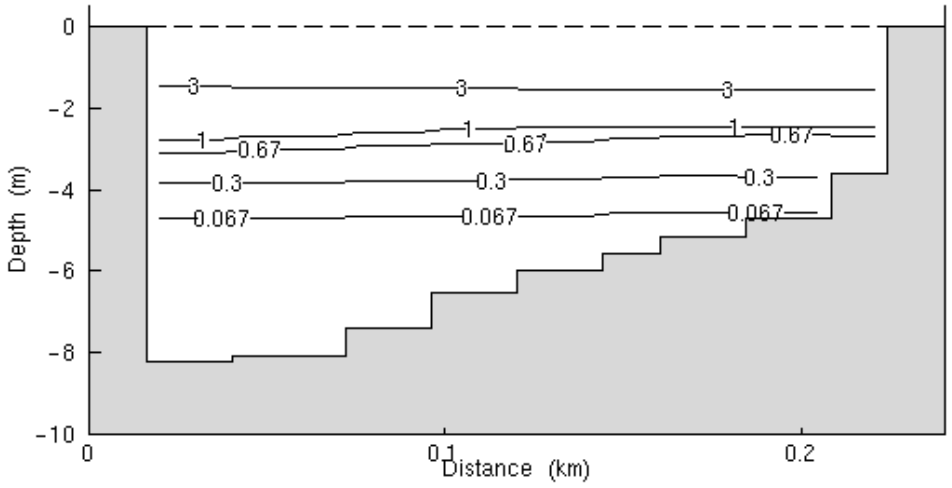

Figure 6.2.29 (d) : Combined Total_A Resin Acids (maximum between U18 and U16/17)

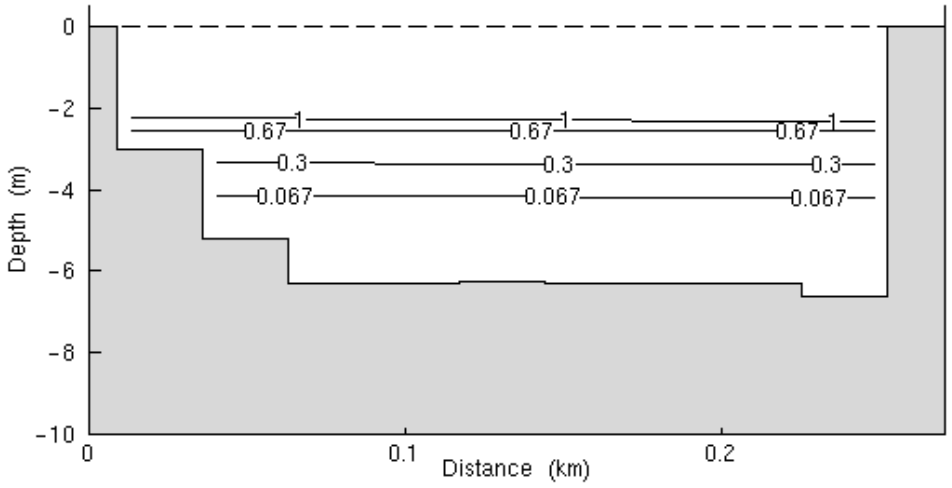

Figure 6.2.30 (a) –(l) RDRA surface plot (μgL^{-1}) for spring, 45 m^3s^{-1}, wind 5ms^{-1} 60^oT at 1hr intervals

Figure 6.2.30 (a)

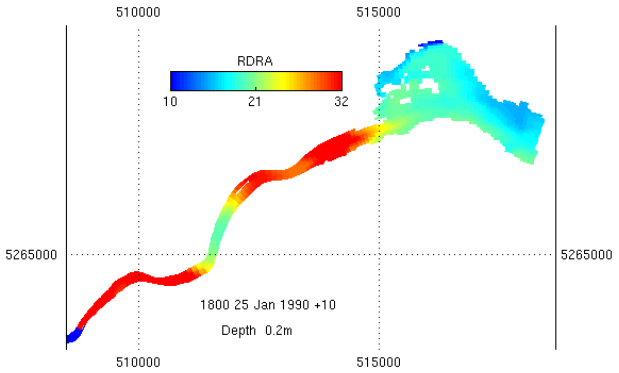

Figure 6.2.30 (b)

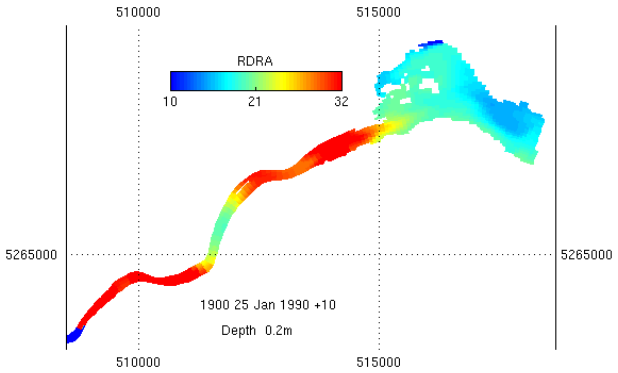

Figure 6.2.30 (c)

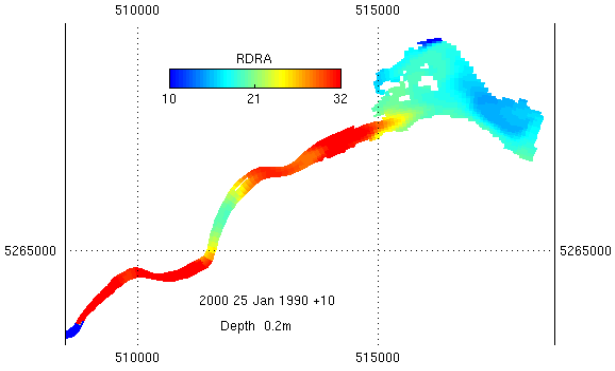

Figure 6.2.30 (d)

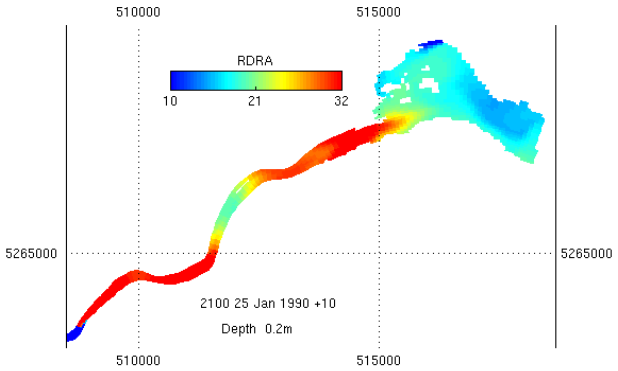

Figure 6.2.30 (e)

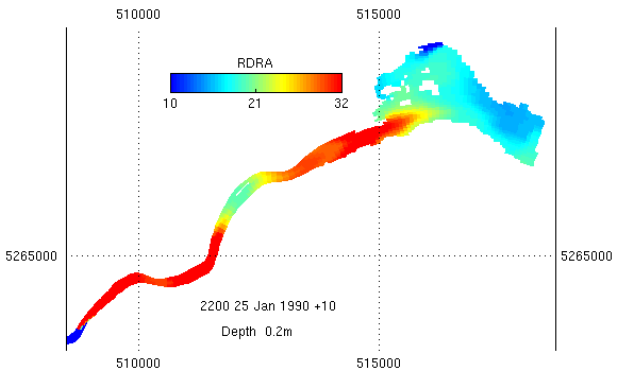

Figure 6.2.30 (f)

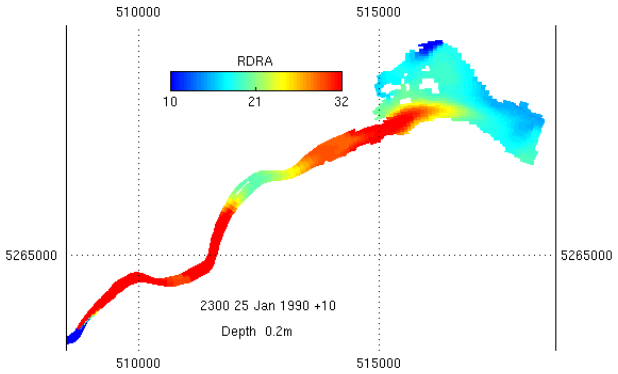

Figure 6.2.30 (g)

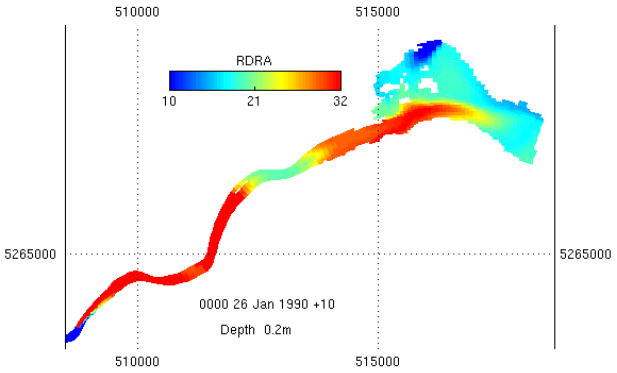

Figure 6.2.30 (h)

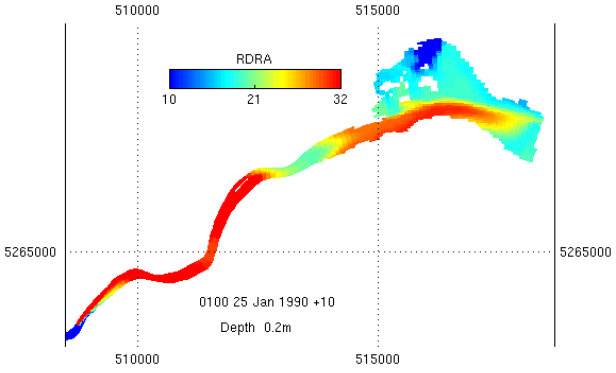

Figure 6.2.30 (i)

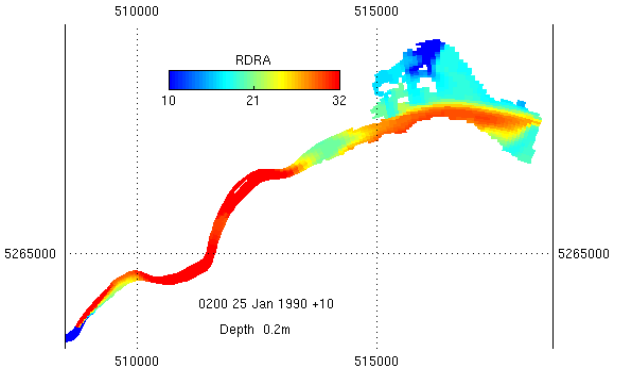

Figure 6.2.30 (j)

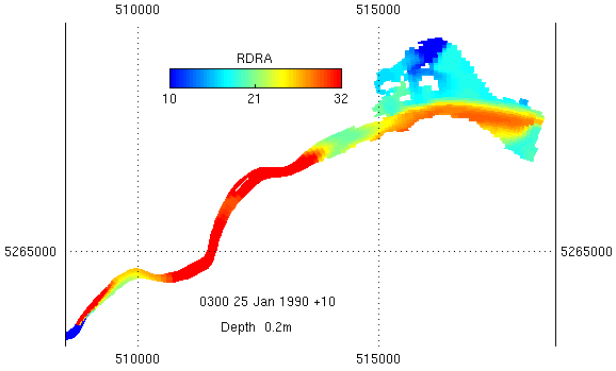

Figure 6.2.30 (k)

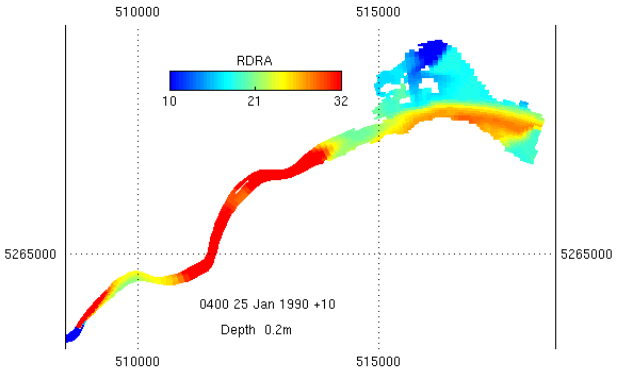

Figure 6.2.30 (l)

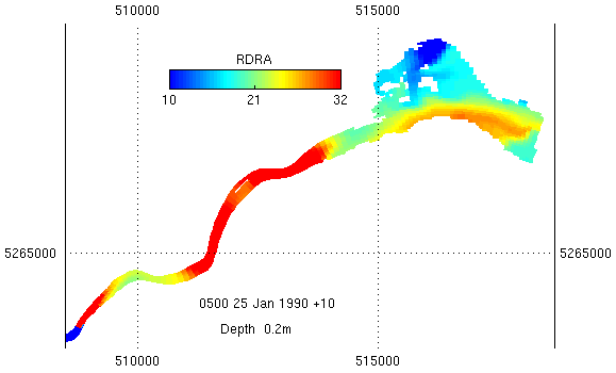

Figure 6.2.31 (a) –(l) : RPRA sedimentation rate (mgm^2day^{-1})

Figure 6.2.31 (a)

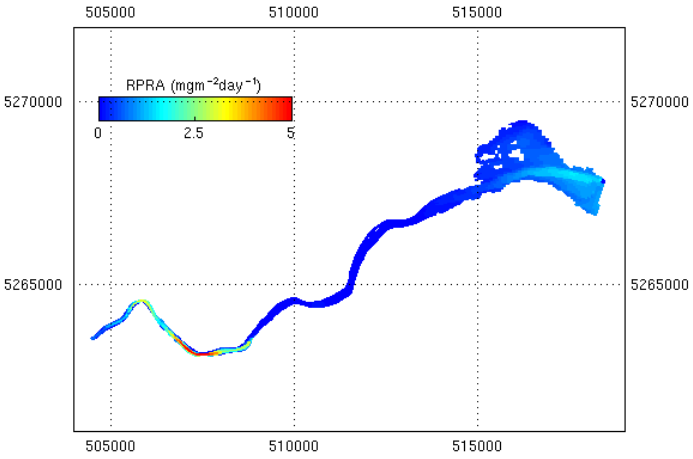

Figure 6.2.31 (b)

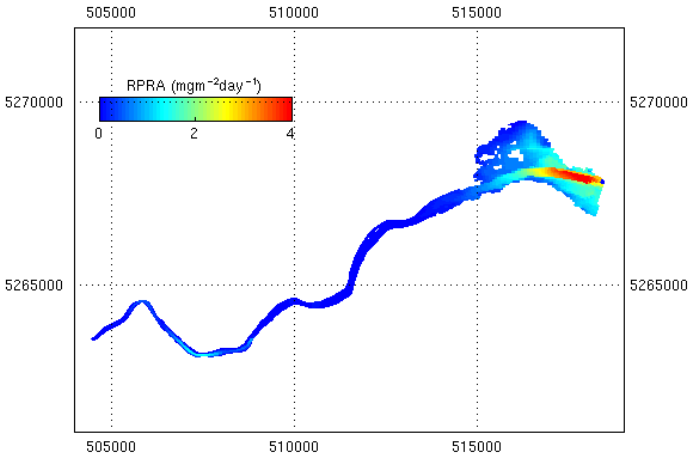

Figure 6.2.31 (c)

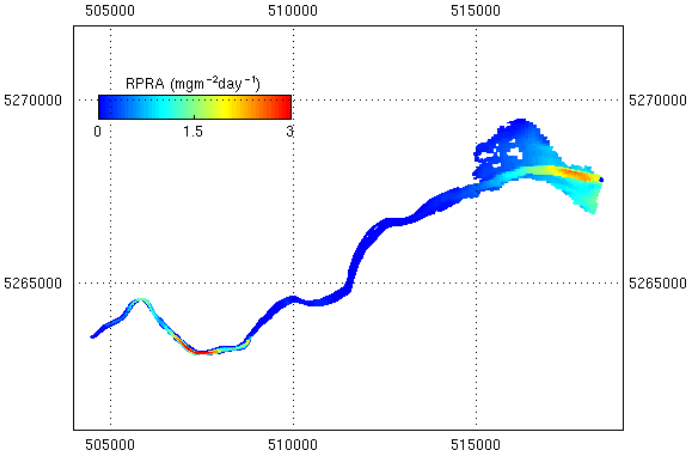

Figure 6.2.31 (d)

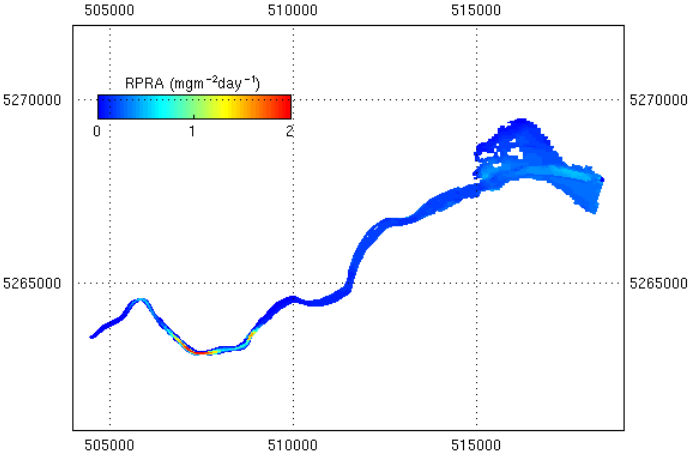

Figure 6.2.31 (e)

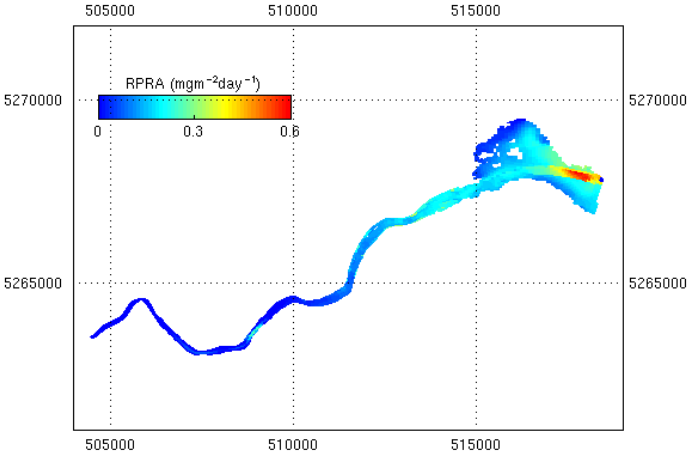

Figure 6.2.31 (f)

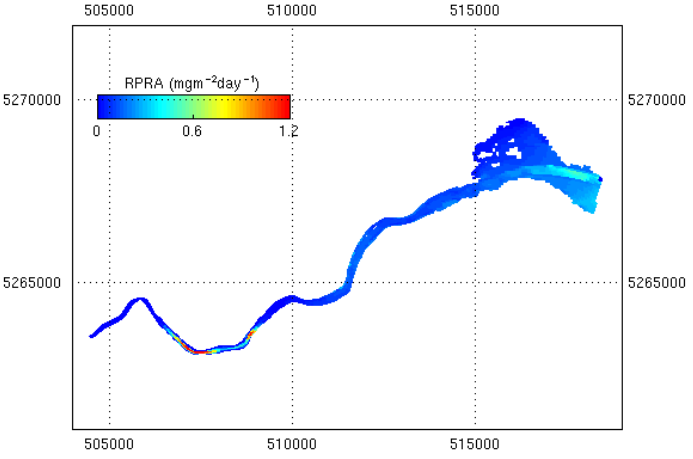

Figure 6.2.31 (g)

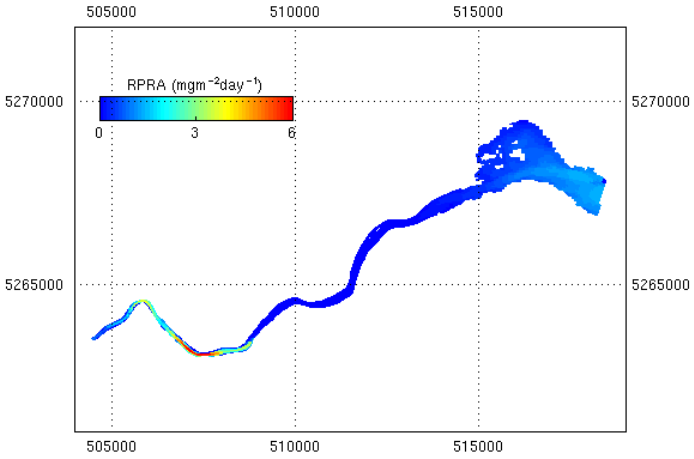

Figure 6.2.31 (h)

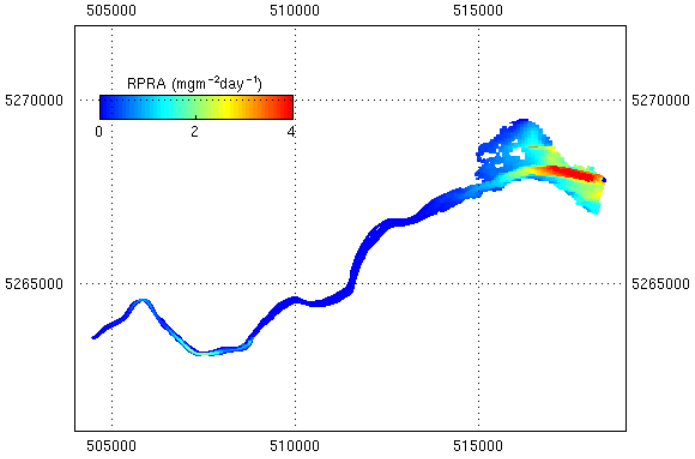

Figure 6.2.31 (i)

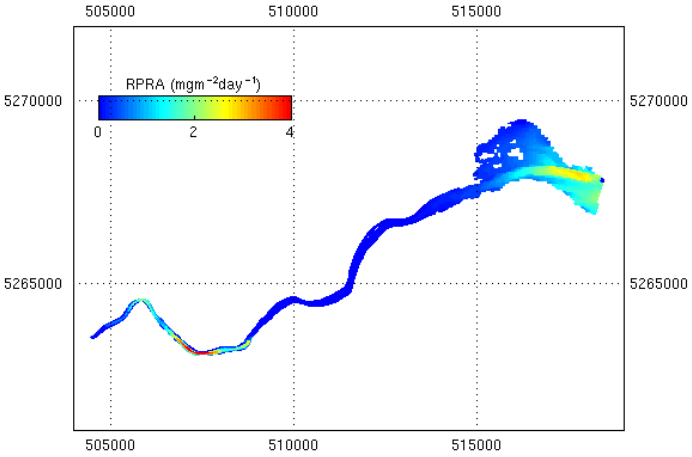

Figure 6.2.31 (j)

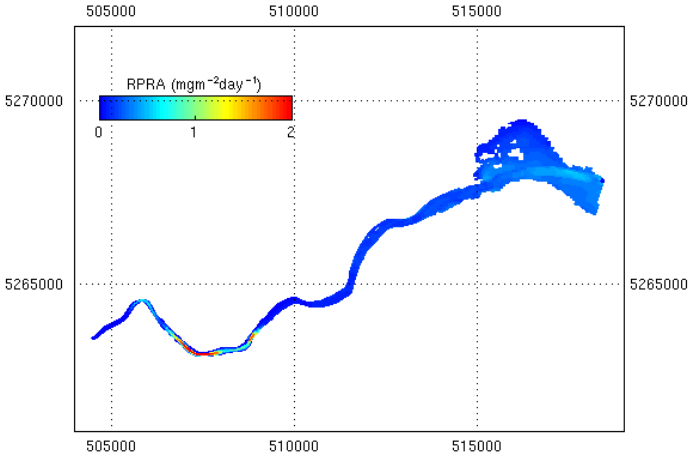

Figure 6.2.31 (k)

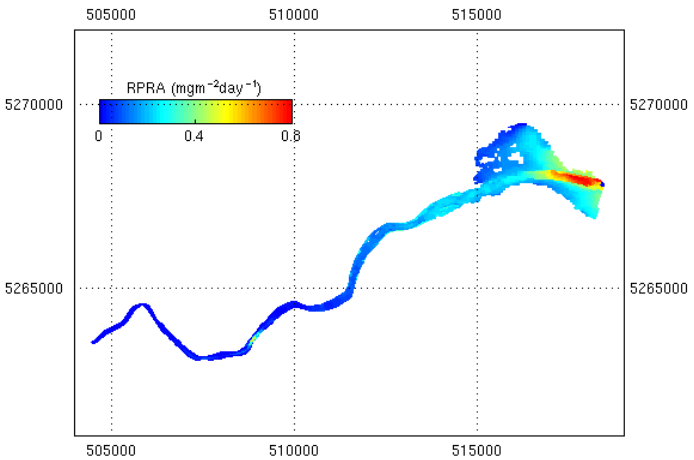

Figure 6.2.31 (l)

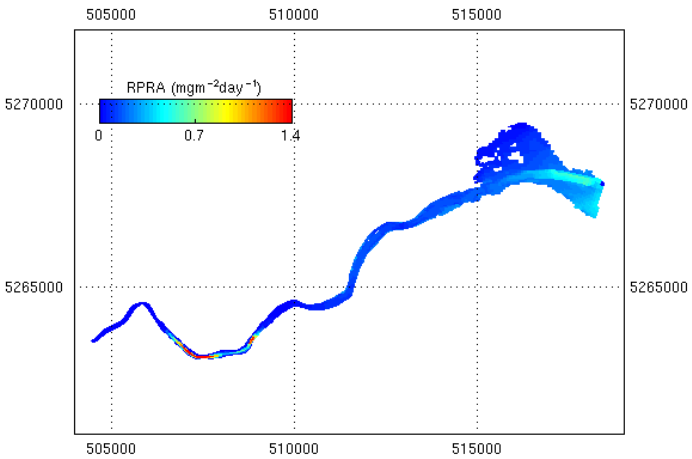

Figure 6.2.32 (a)-(l) : LPRA_A sedimentation rate (mgm^2day^{-1})

Figure 6.2.32 (a)

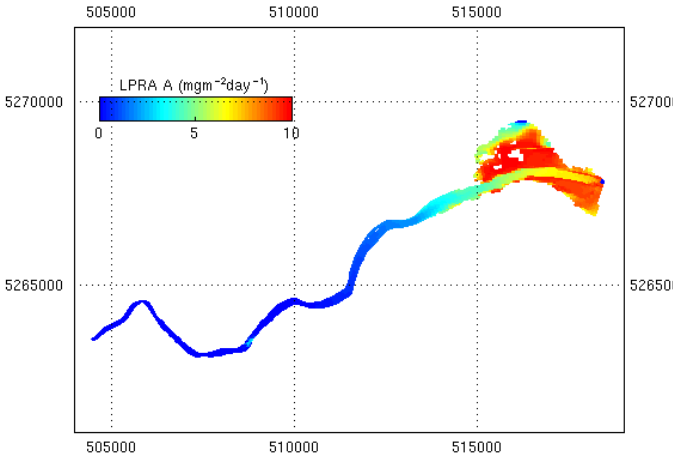

Figure 6.2.32 (b)

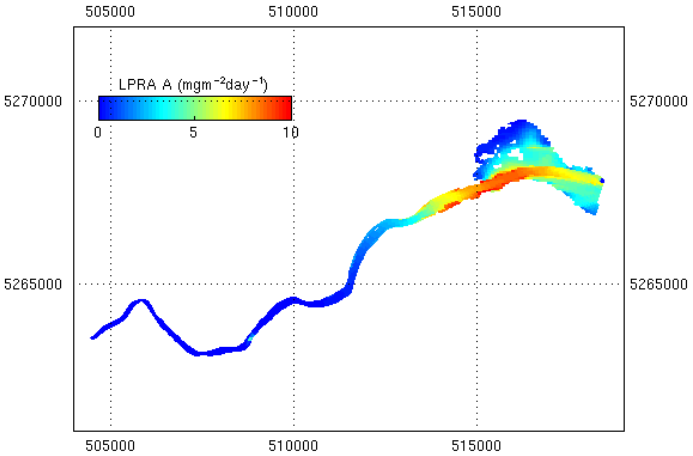

Figure 6.2.32 (c)

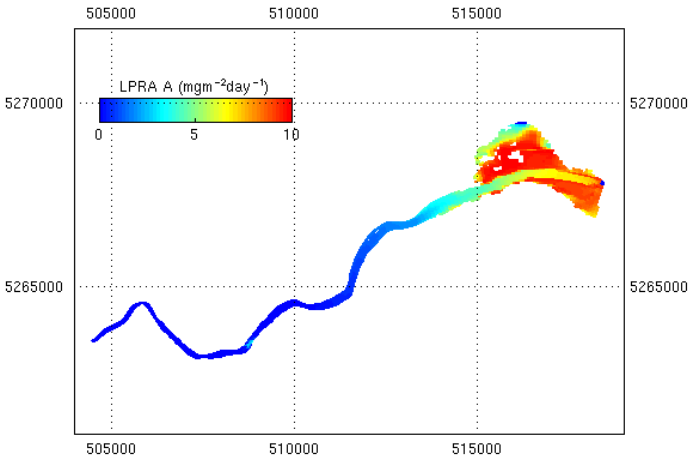

Figure 6.2.32 (d)

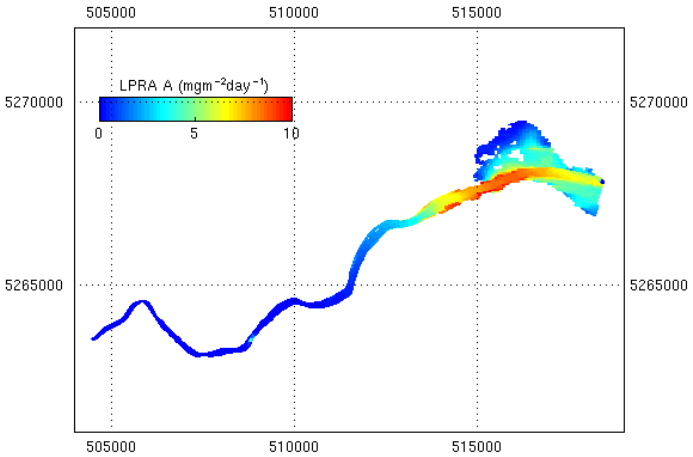

Figure 6.2.32 (e)

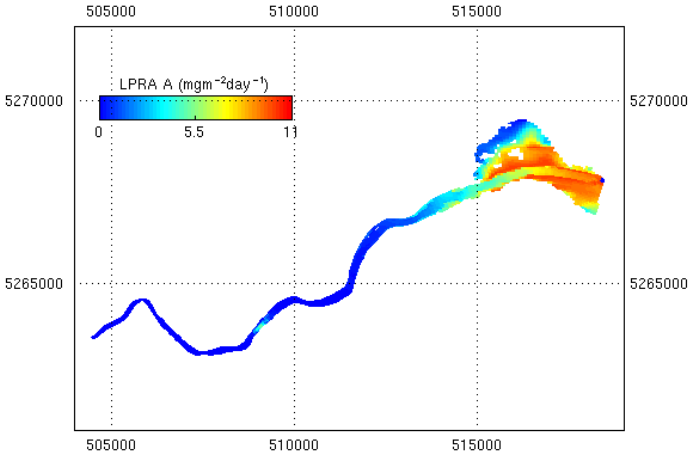

Figure 6.2.32 (f)

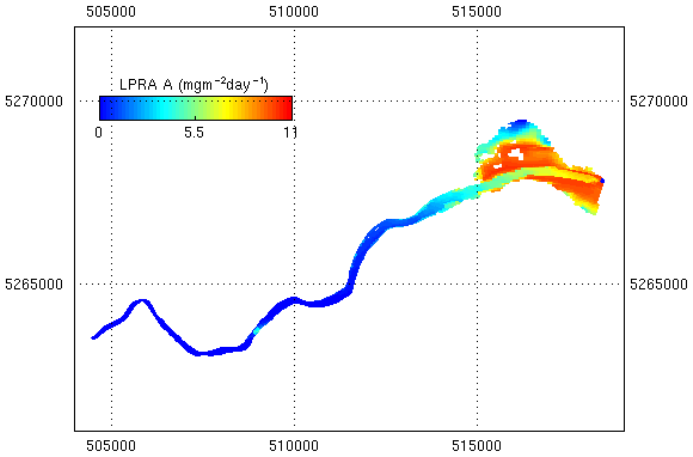

Figure 6.2.32 (g)

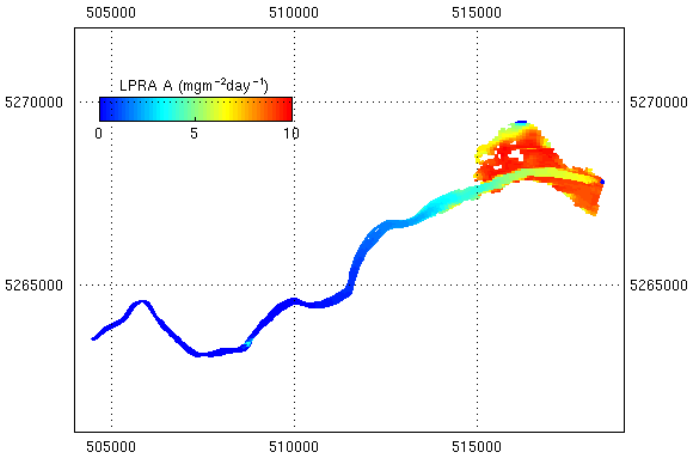

Figure 6.2.32 (h)

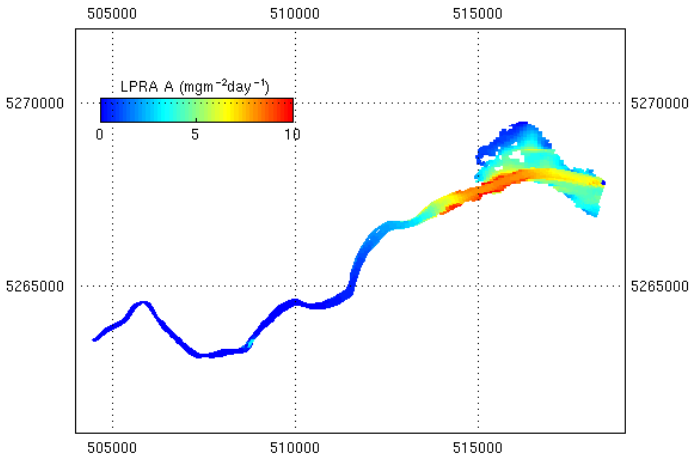

Figure 6.2.32 (i)

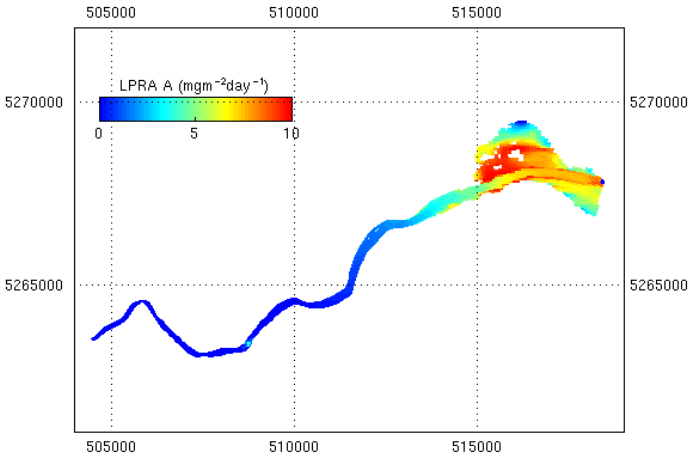

Figure 6.2.32 (j)

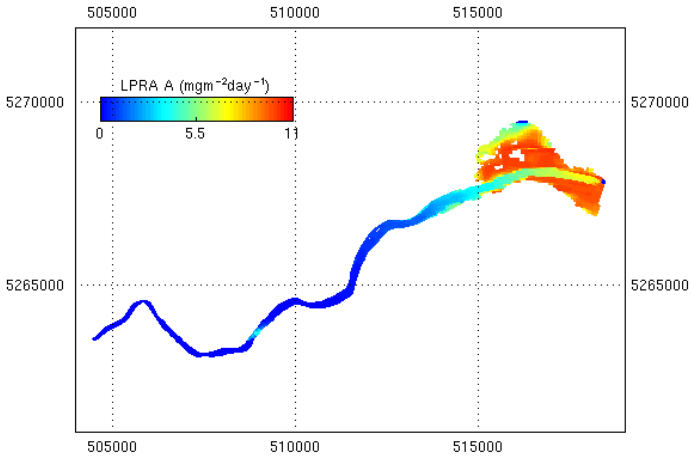

Figure 6.2.32 (k)

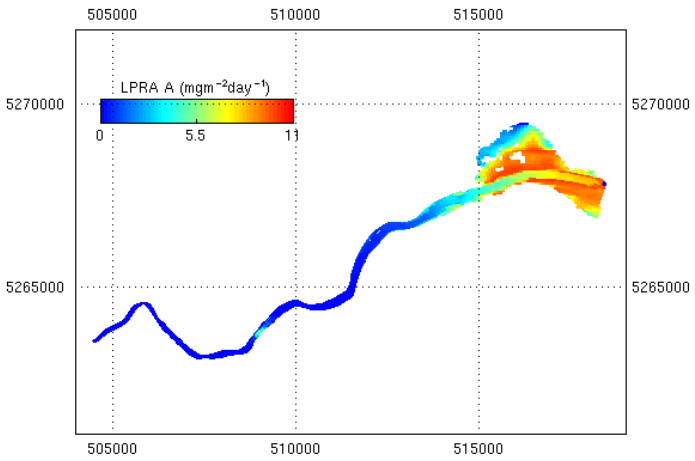

Figure 6.2.32 (l)

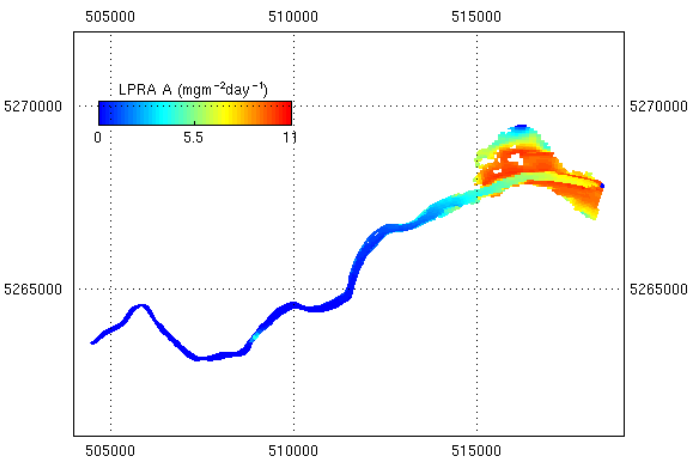

Figure 6.2.33 (a)-(l) : LPRA sedimentation rate ($mgm^{2}day^{-1}$)

Figure 6.2.33 (a)

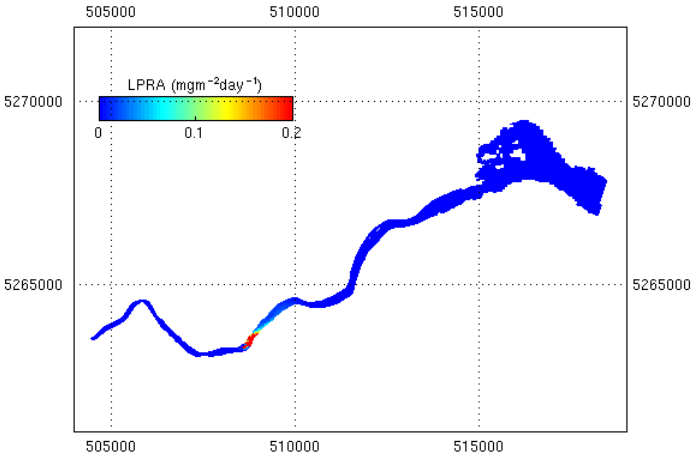

Figure 6.2.33 (b)

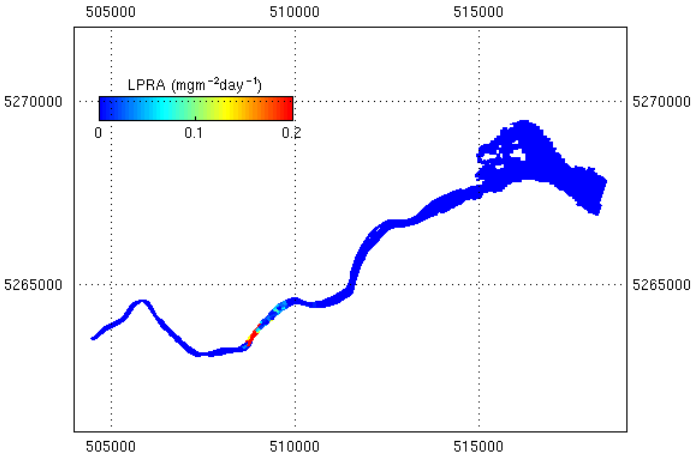

Figure 6.2.33 (c)

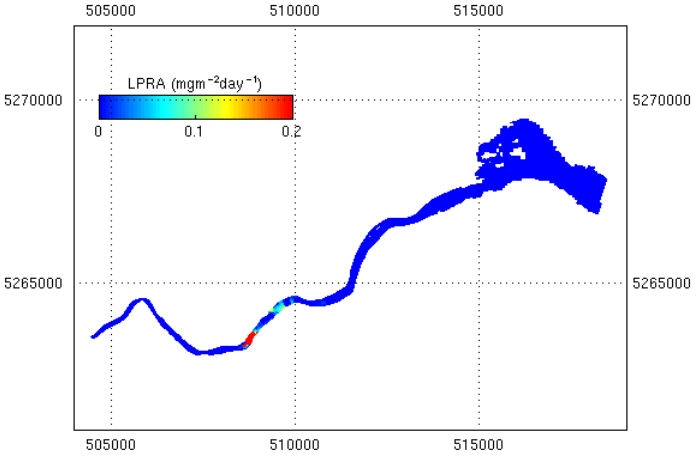

Figure 6.2.33 (d)

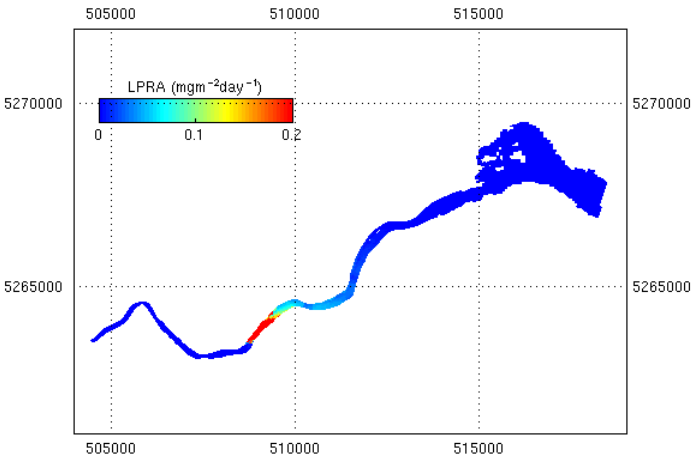

Figure 6.2.33 (e)

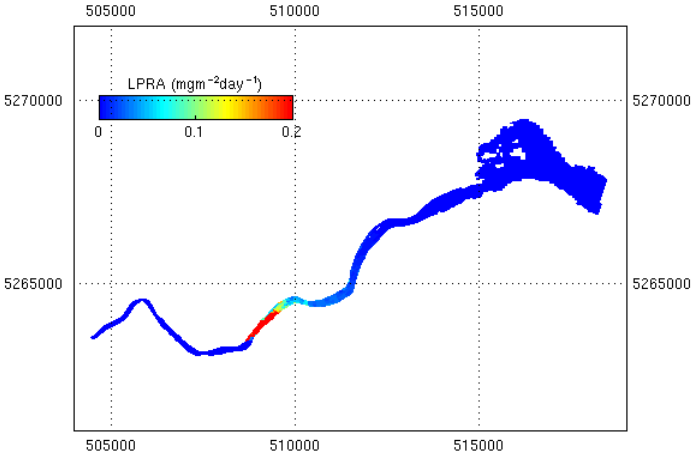

Figure 6.2.33 (f)

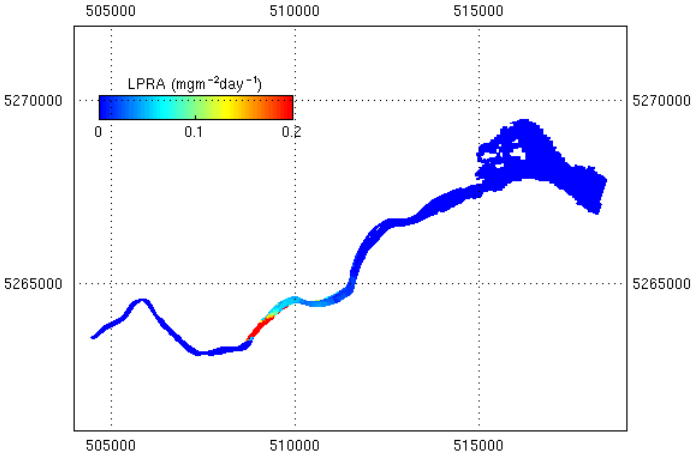

Figure 6.2.33 (g)

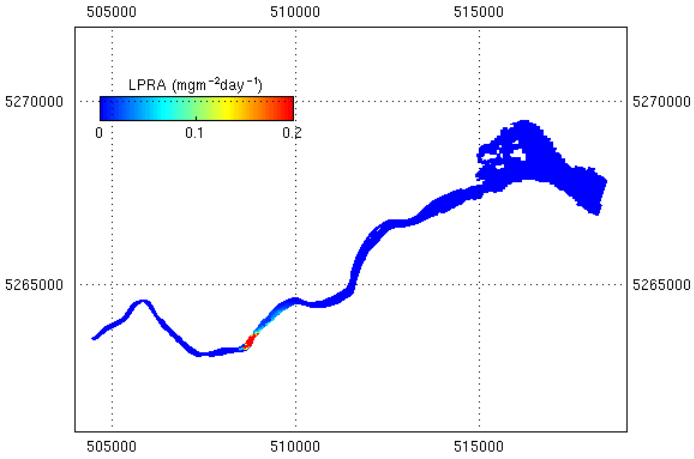

Figure 6.2.33 (h)

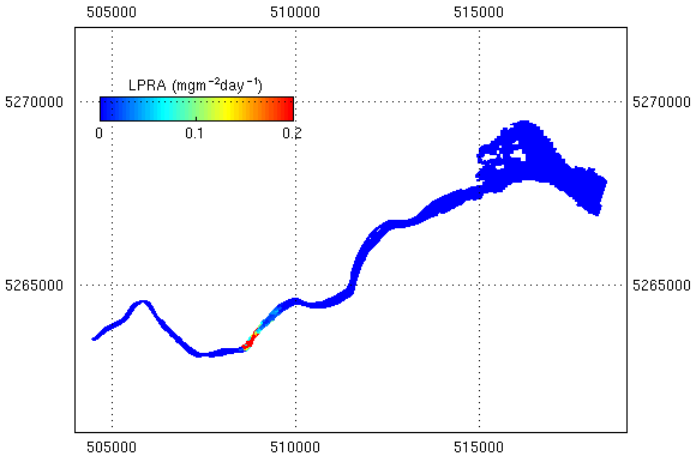

Figure 6.2.33 (i)

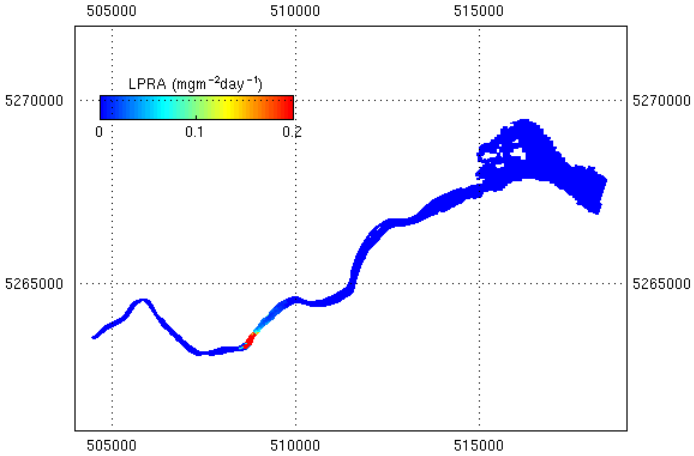

Figure 6.2.33 (j)

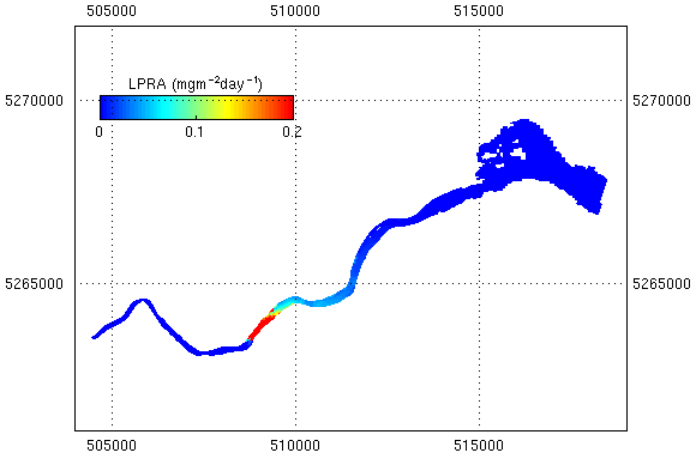

Figure 6.2.33 (k)

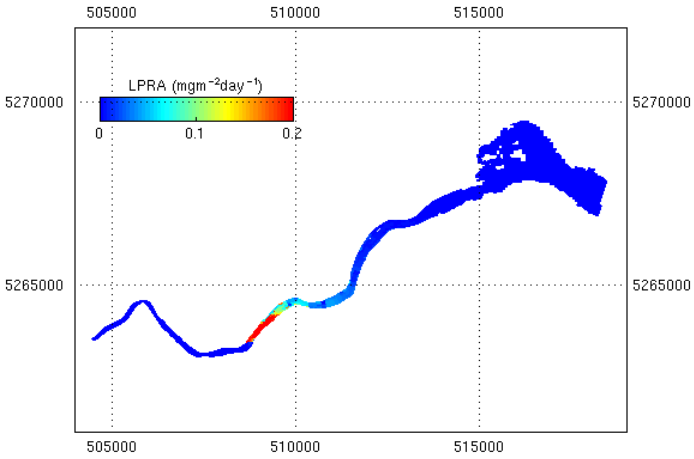

Figure 6.2.33 (l)

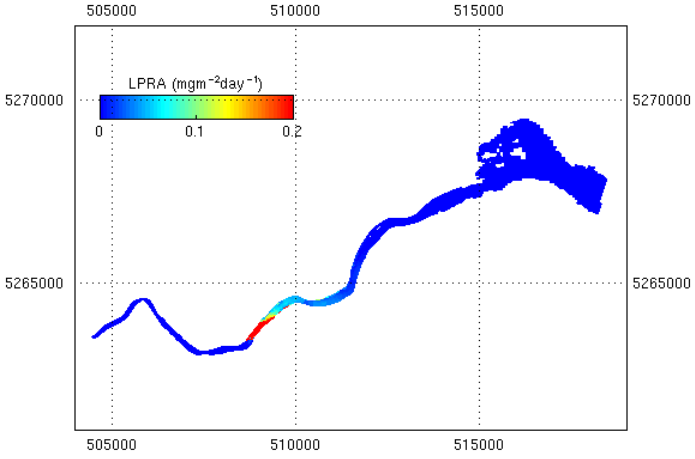

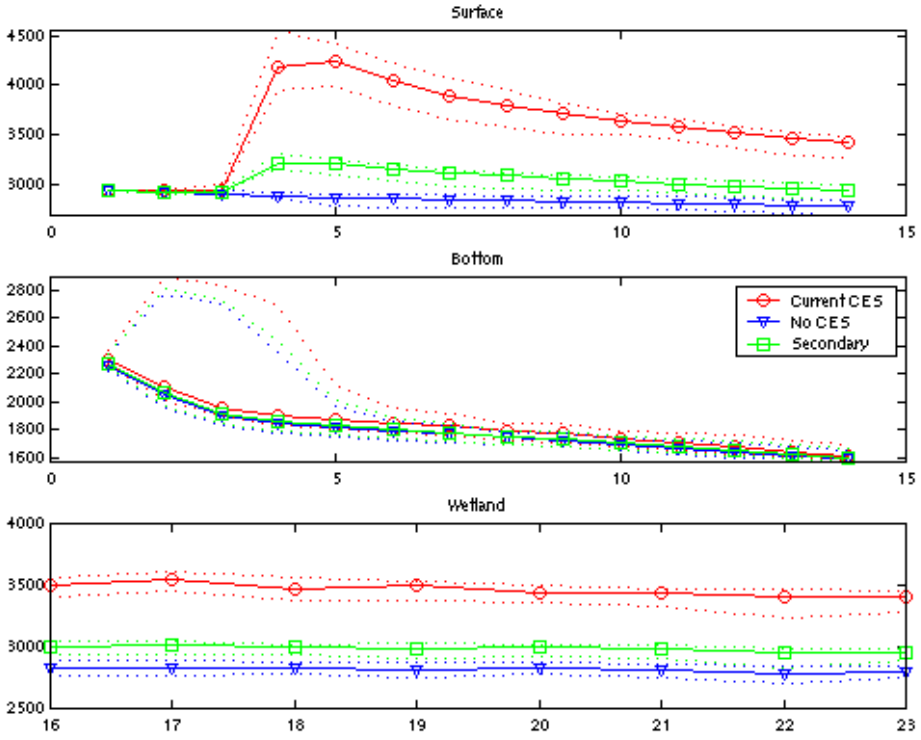

Fig. 6.3.1 a. Median flow (Nov-Dec) scenarios, DOC (mg C m^{-3}) vs box #. Dashed lines indicate 5, 95%iles.

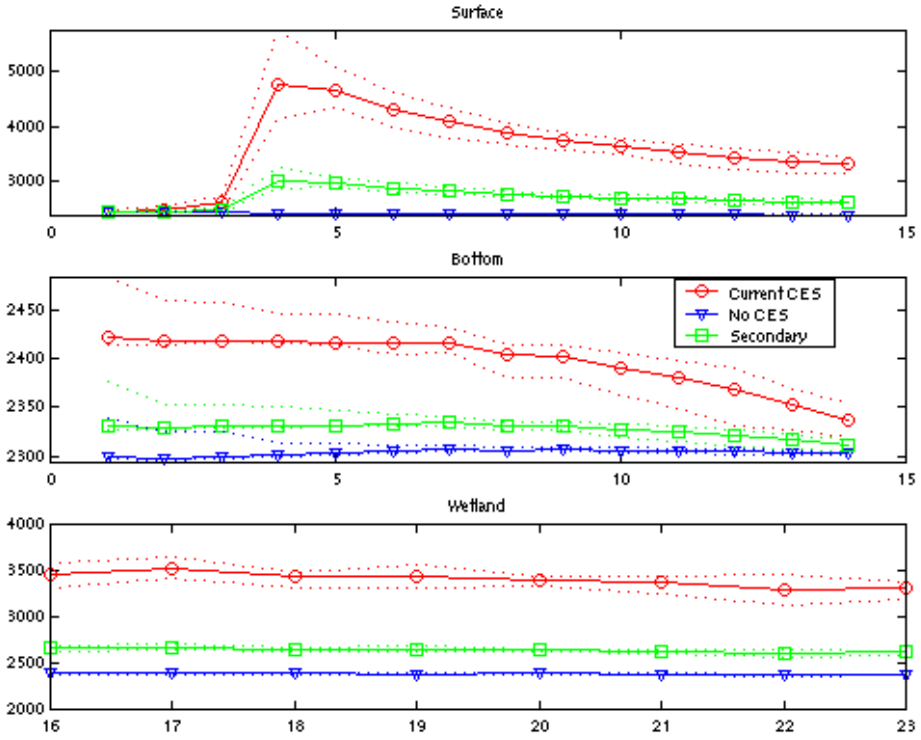

Fig. 6.3.1 b. 5%ile flow (Mar-Apr) scenarios, DOC (mg C m^{-3}) vs box #. Dashed lines indicate 5, 95%iles.

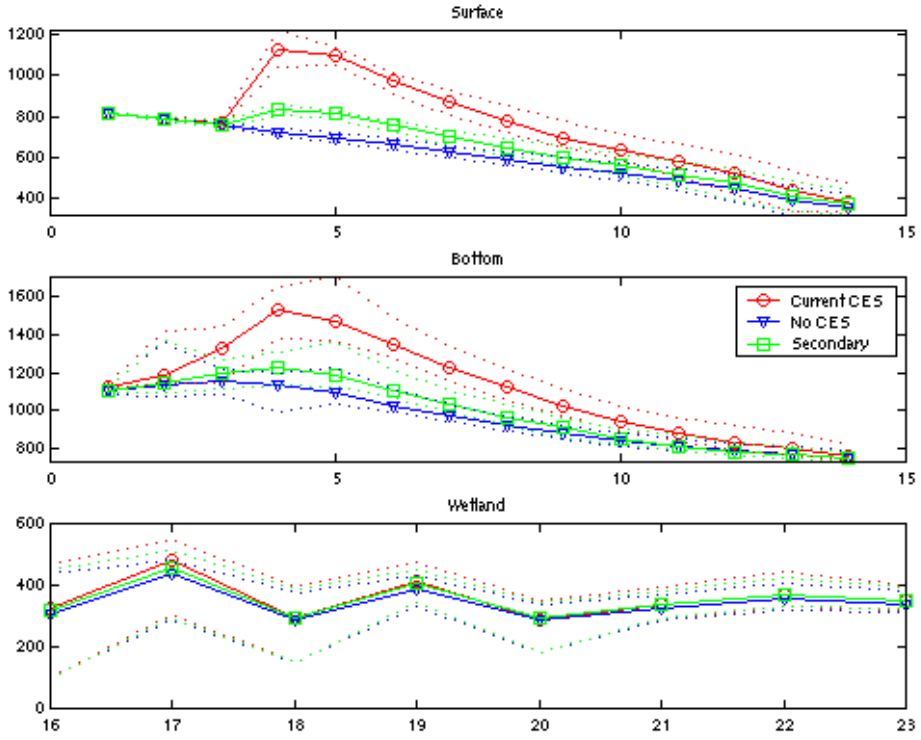

Fig. 6.3.2 a. Median flow (Nov-Dec) scenarios, POC (mg C m^{-3}) vs box #. Dashed lines indicate 5, 95%iles.

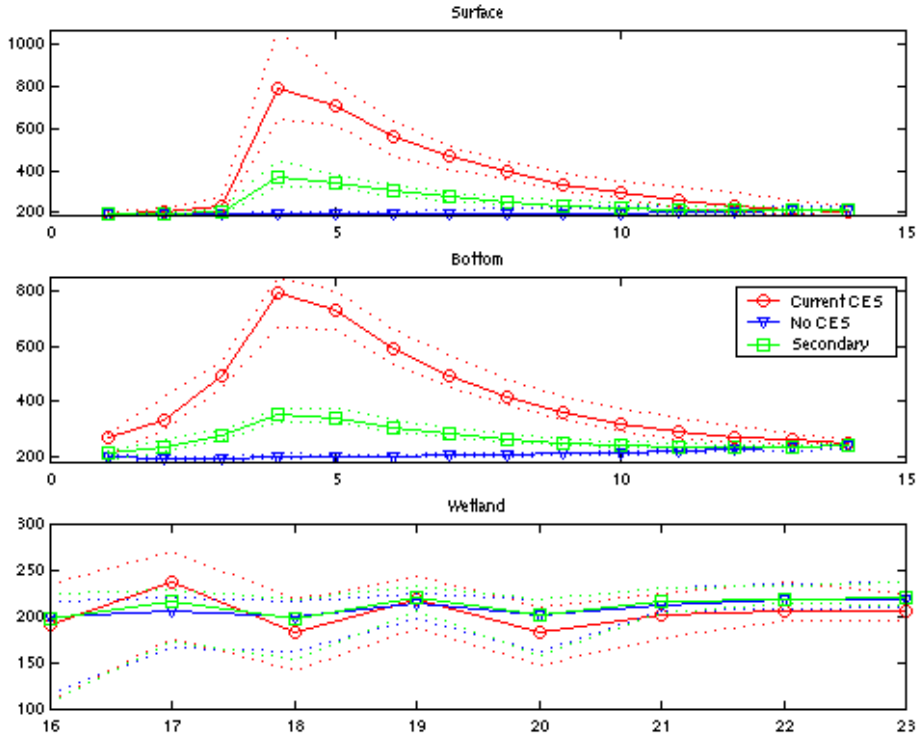

Fig. 6.3.2 b. 5%ile flow (Mar-Apr) scenarios, POC (mg C m^{-3}) vs box #. Dashed lines indicate 5, 95%iles.

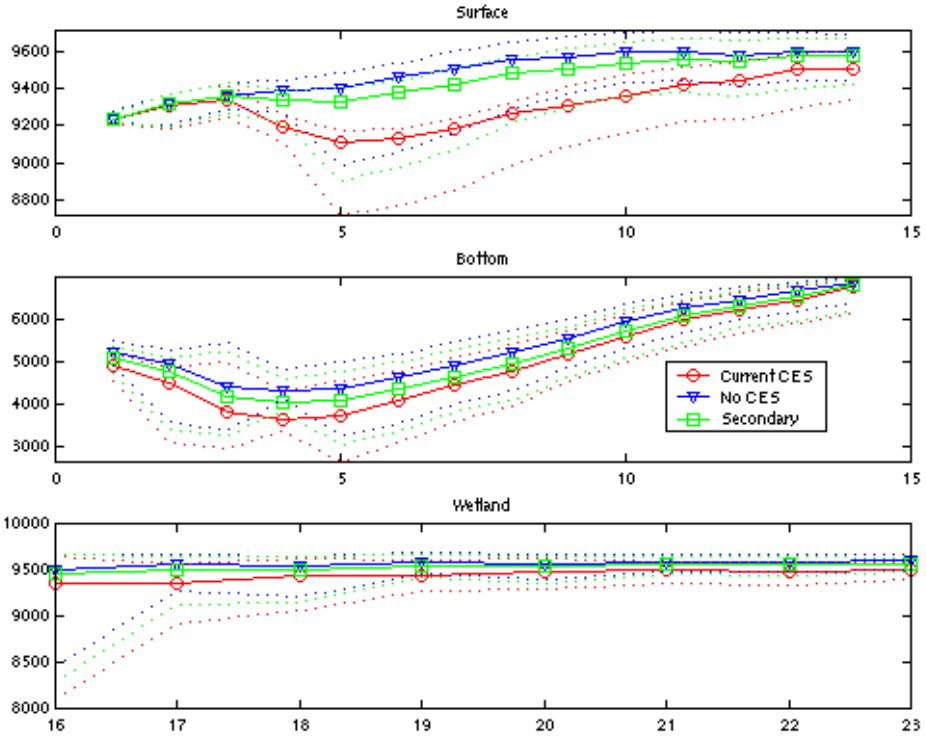

Fig. 6.3.3 a. Median flow (Nov-Dec) scenarios, Oxygen (mg O m^{-3}) vs box #. Dashed lines indicate 5, 95%iles.

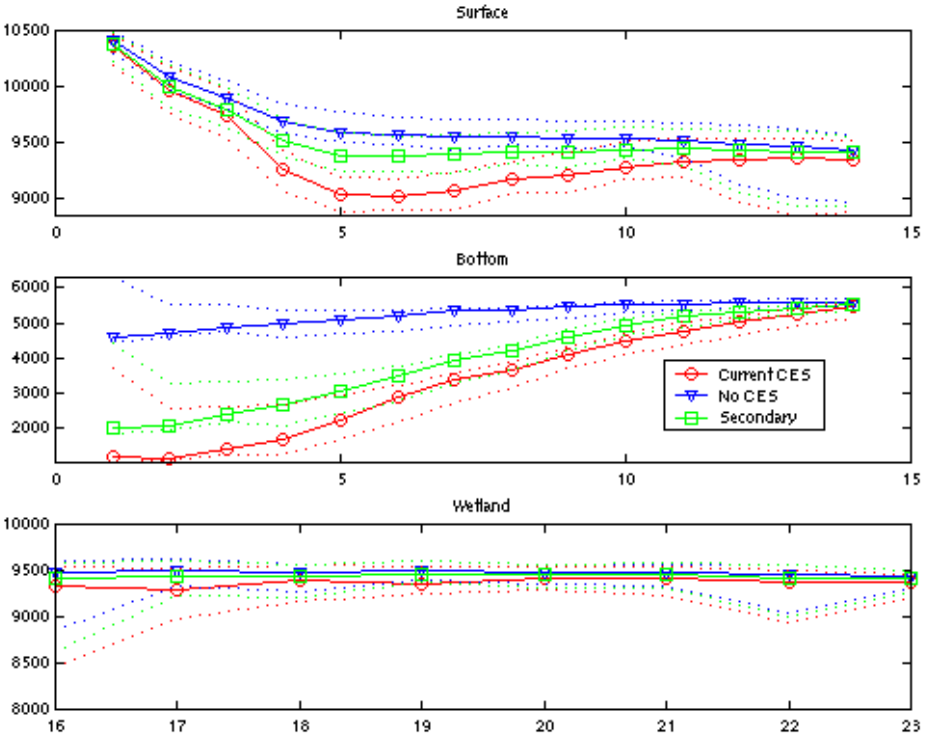

Fig. 6.3.3 b. 5%ile flow (Mar-Apr) scenarios, Oxygen (mg O m^{-3}) vs box #. Dashed lines indicate 5, 95%iles.

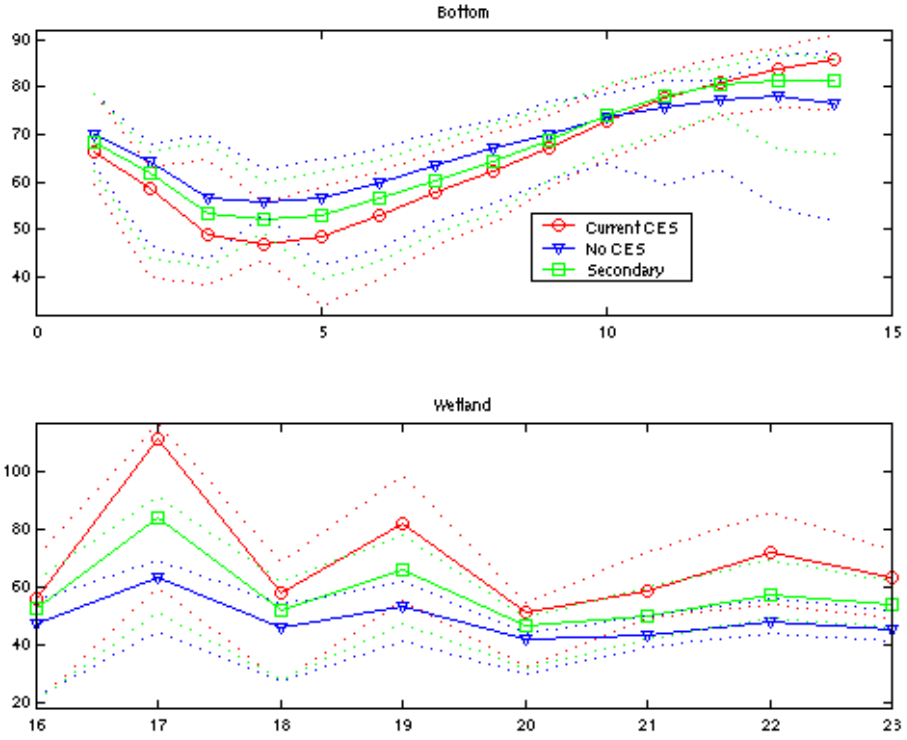

Fig. 6.3.4 a. Median flow (Nov-Dec) scenarios, Sediment Respiration (mmol O_2 m^{-2} d^{-1}) vs box #. Dashed lines indicate 5, 95%iles.

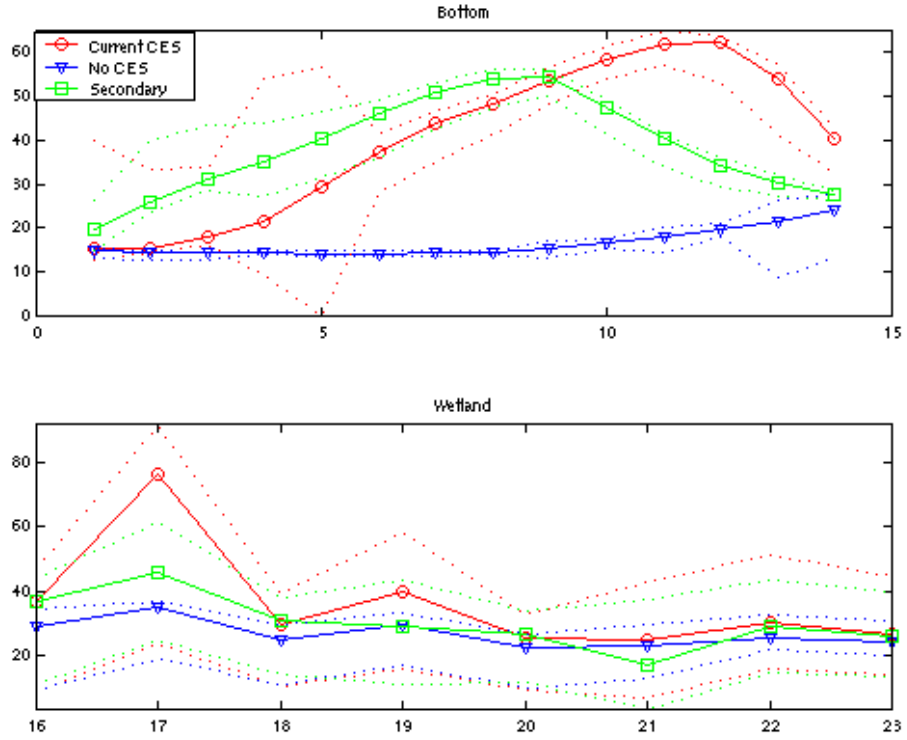

Fig. 6.3.4 b. 5%ile flow (Mar-Apr) scenarios, Sediment Respiration (mmol O_2 m^{-2} d^{-1}) vs box #. Dashed lines indicate 5, 95%iles.

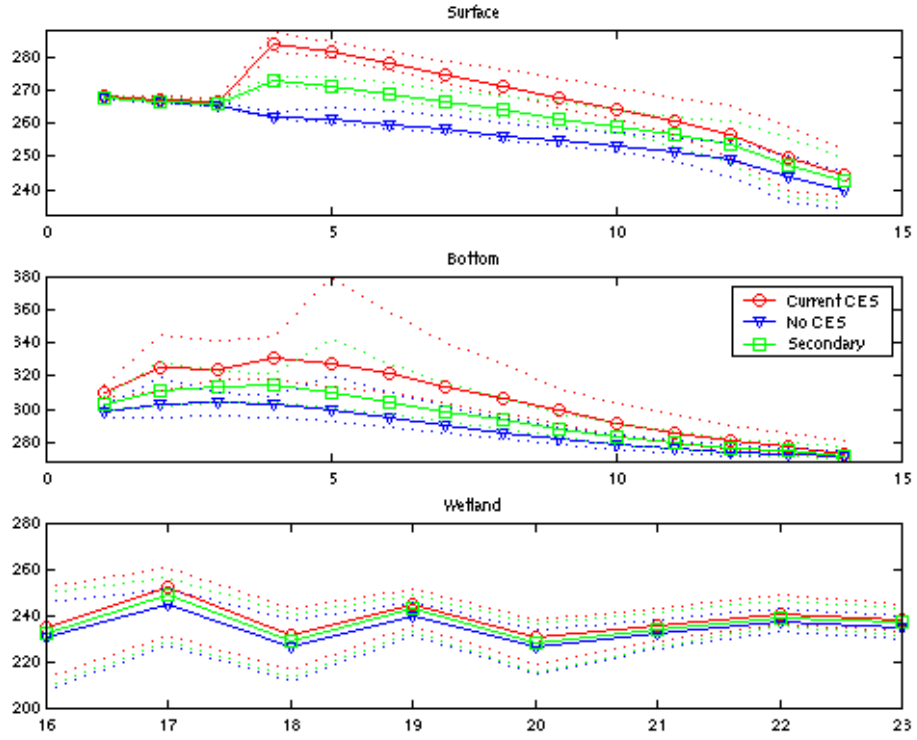

Fig. 6.3.5 a. Median flow (Nov-Dec) scenarios, TN (mg N m^{-3}) vs box #. Dashed lines indicate 5, 95%iles.

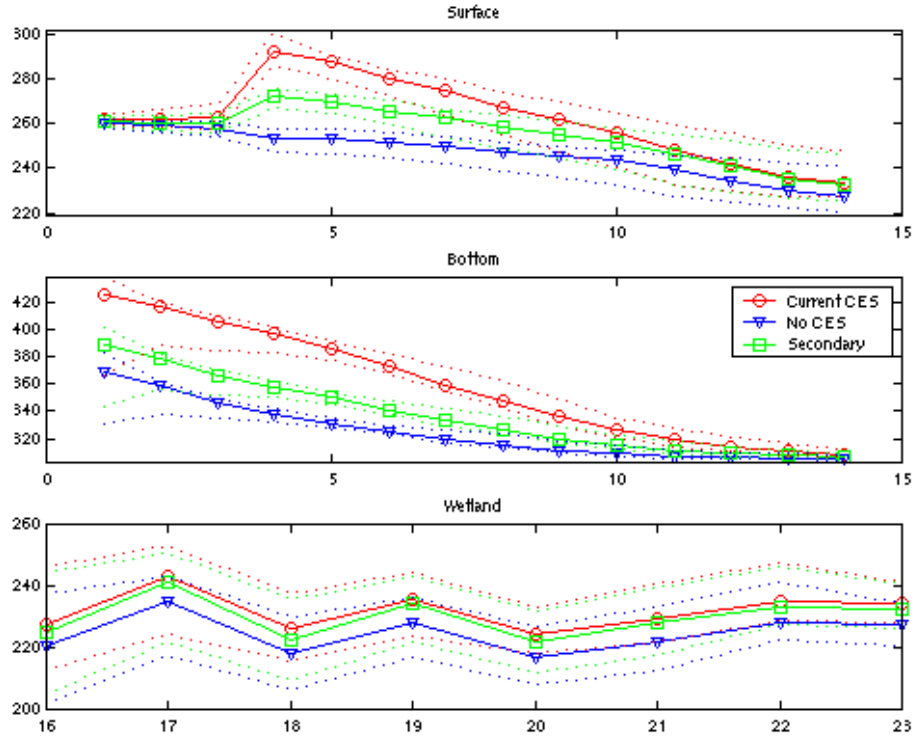

Fig. 6.3.5 b. 5%ile flow (Mar-Apr) scenarios, TN (mg N m^{-3}) vs box #. Dashed lines indicate 5, 95%iles.

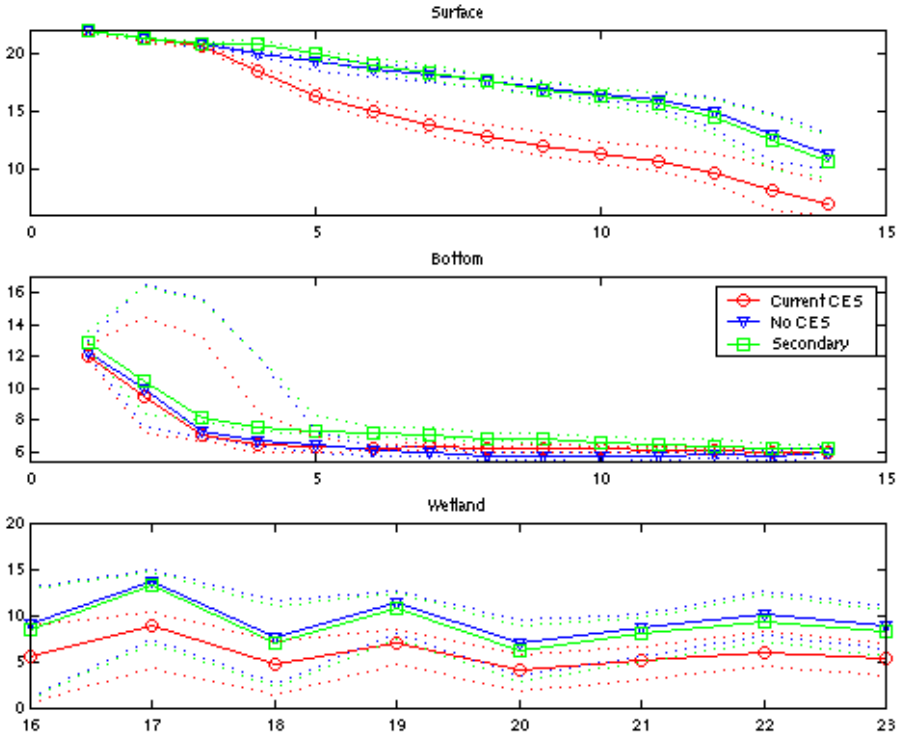

Fig. 6.3.6 a. Median flow (Nov-Dec) scenarios, NOx (mg N m^{-3}) vs box #. Dashed lines indicate 5, 95%iles.

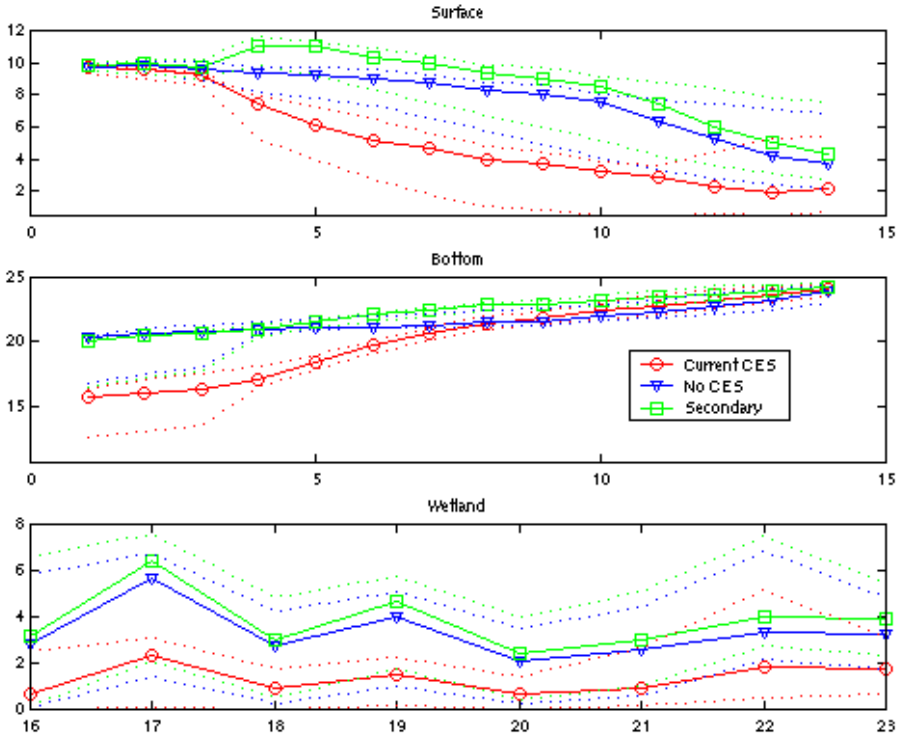

Fig. 6.3.6 b. 5%ile flow (Mar-Apr) scenarios, NOx (mg N m^{-3}) vs box #. Dashed lines indicate 5, 95%iles.

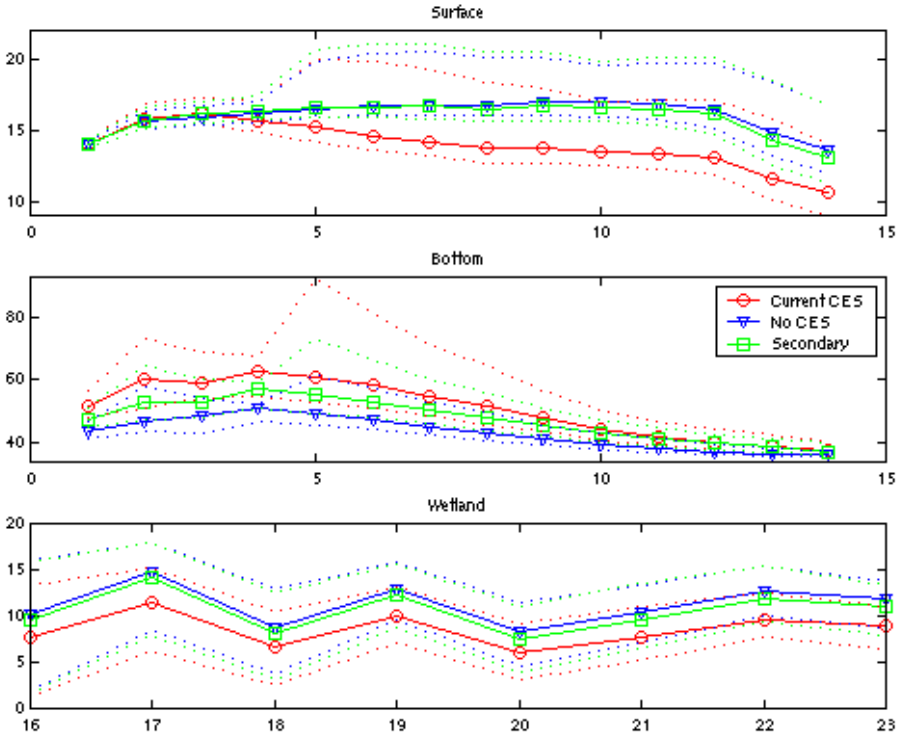

Fig. 6.3.7 a. Median flow (Nov-Dec) scenarios, NH_3 (mg N m^{-3}) vs box #. Dashed lines indicate 5, 95%iles.

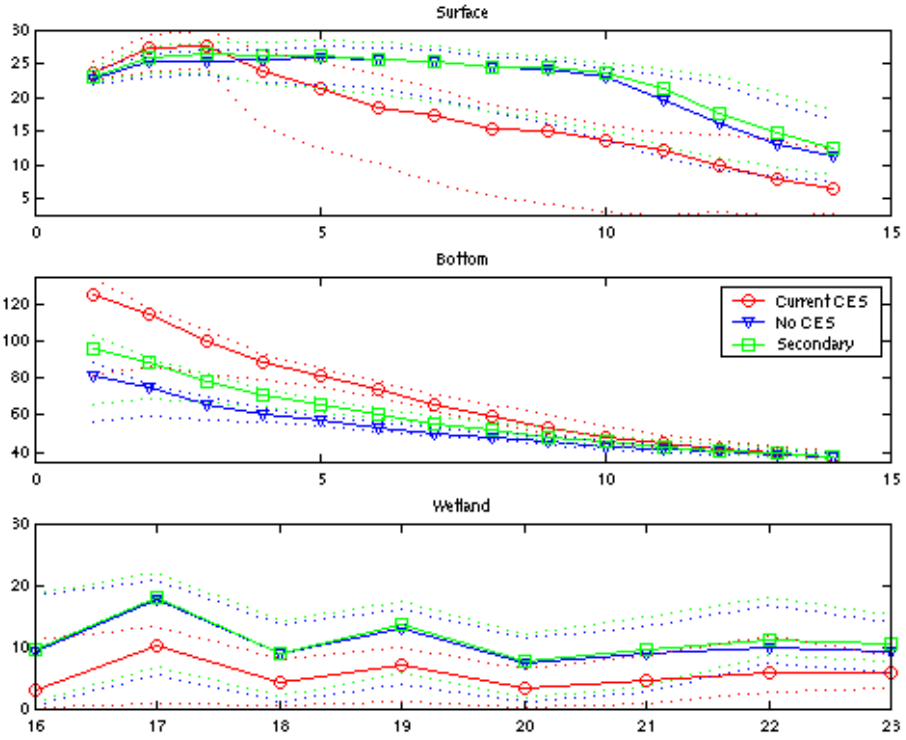

Fig. 6.3.7 b. 5%ile flow (Mar-Apr) scenarios, NH_3 (mg N m^{-3}) vs box #. Dashed lines indicate 5, 95%iles.

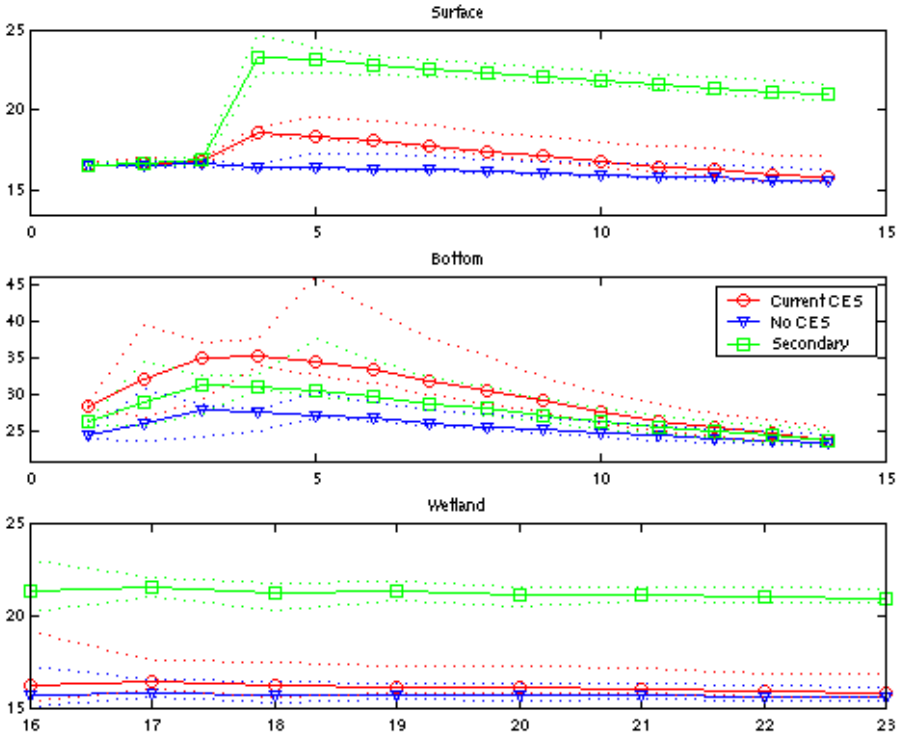

Fig. 6.3.8 a. Median flow (Nov-Dec) scenarios, TP (mg P m^{-3}) vs box #. Dashed lines indicate 5, 95%iles.

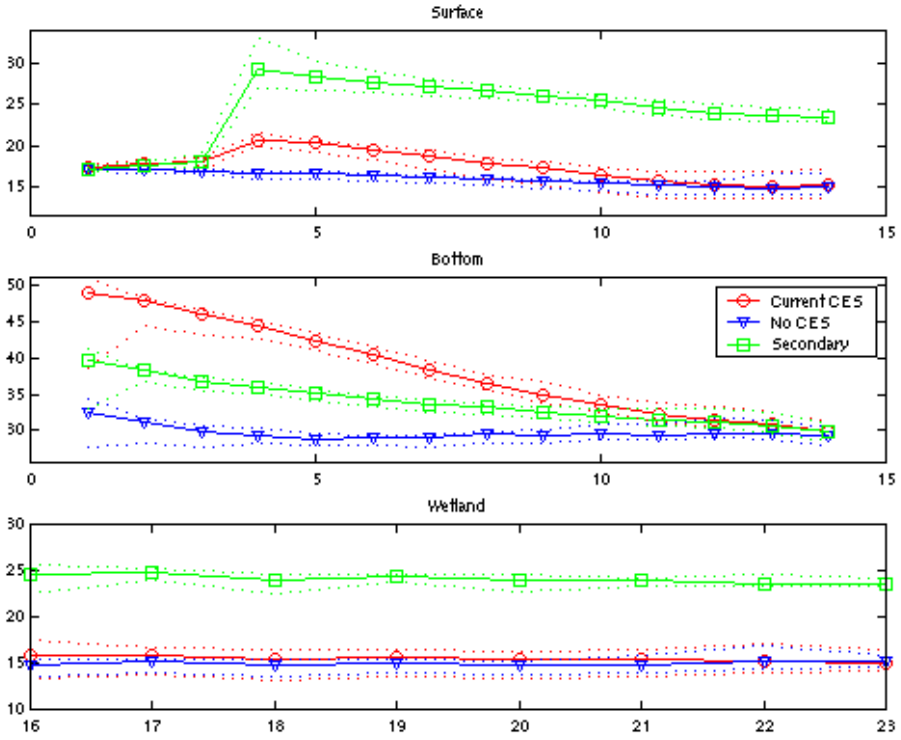

Fig. 6.3.8 b. 5%ile flow (Mar-Apr) scenarios, TP (mg P m^{-3}) vs box #. Dashed lines indicate 5, 95%iles.

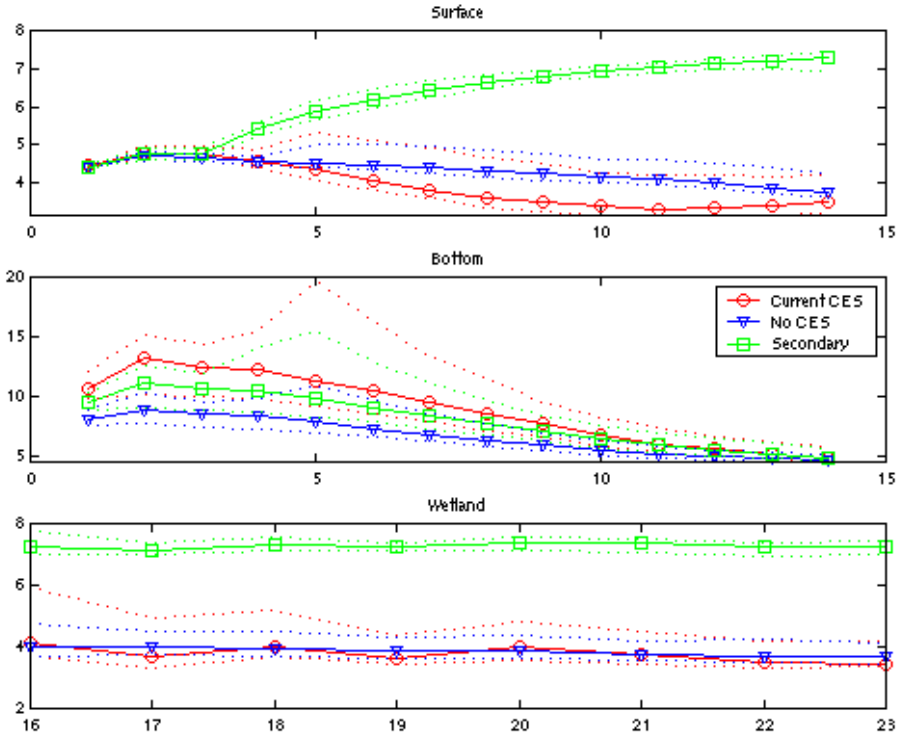

Fig. 6.3.9 a. Median flow (Nov-Dec) scenarios, PO_4 (mg P m^{-3}) vs box #. Dashed lines indicate 5, 95%iles.

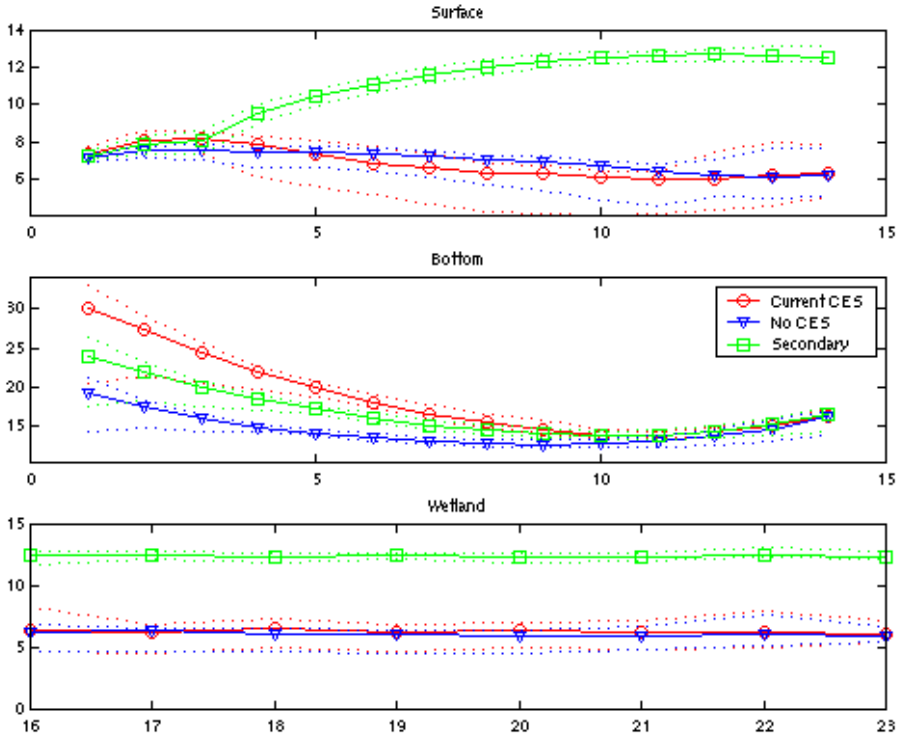

Fig. 6.3.9 b. 5%ile flow (Mar-Apr) scenarios, PO_4 (mg P m^{-3}) vs box #. Dashed lines indicate 5, 95%iles.

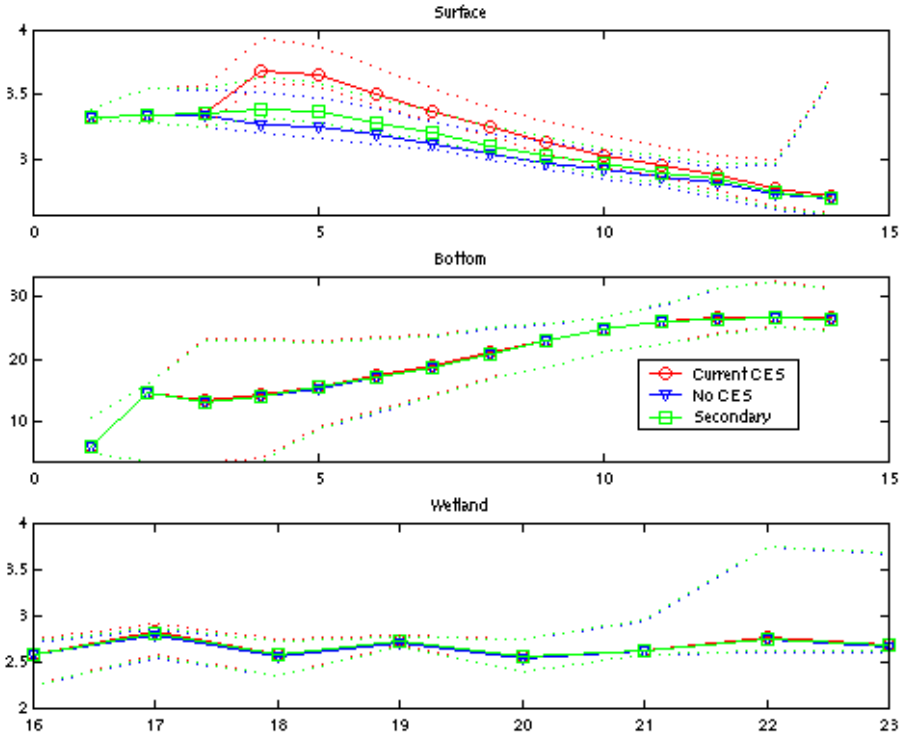

Fig. 6.3.10 a. Median flow (Nov-Dec) scenarios, SPM (mg C m^{-3}) vs box #. Dashed lines indicate 5, 95%iles.

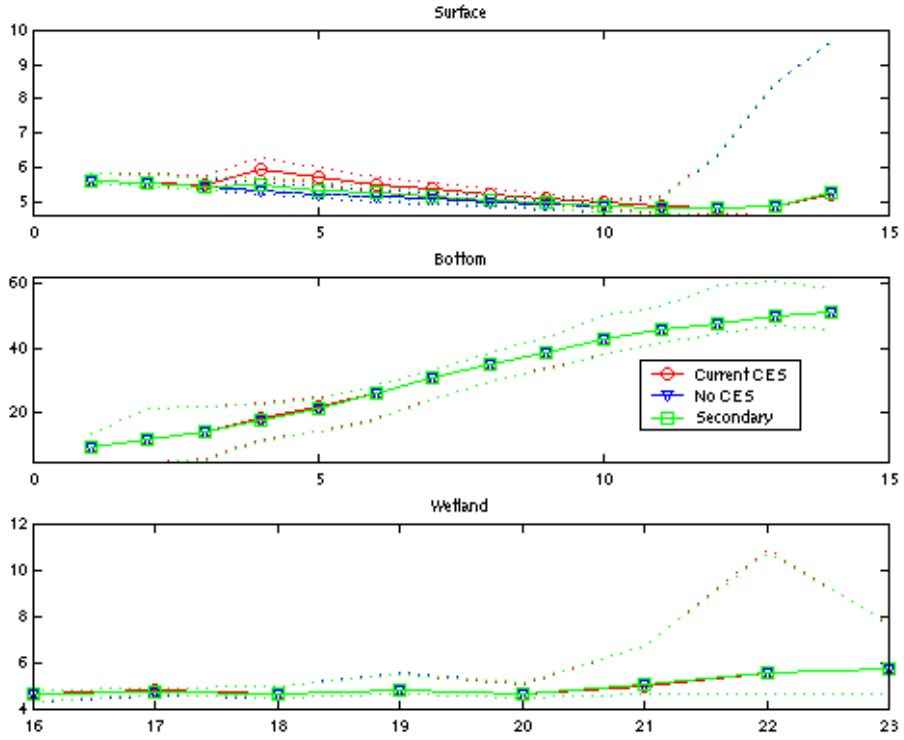

Fig. 6.3.10 b. 5%ile flow (Mar-Apr) scenarios, SPM (mg C m^{-3}) vs box #. Dashed lines indicate 5, 95%iles.

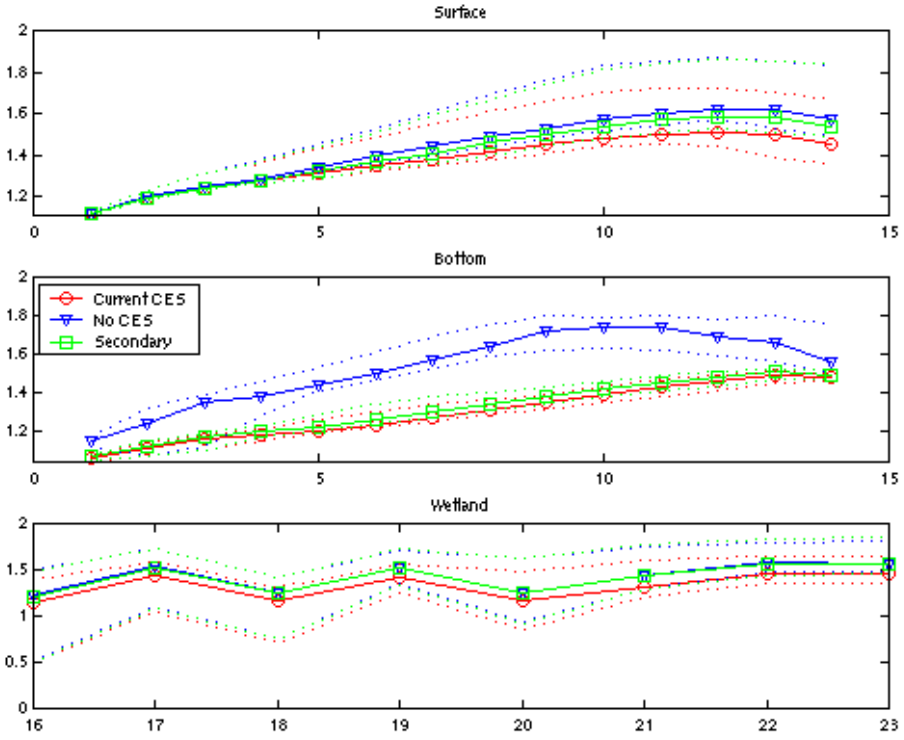

Fig. 6.3.11 a. Median flow (Nov-Dec) scenarios, Chl a (mg Chl a m^{-3}) vs box #. Dashed lines indicate 5, 95%iles.

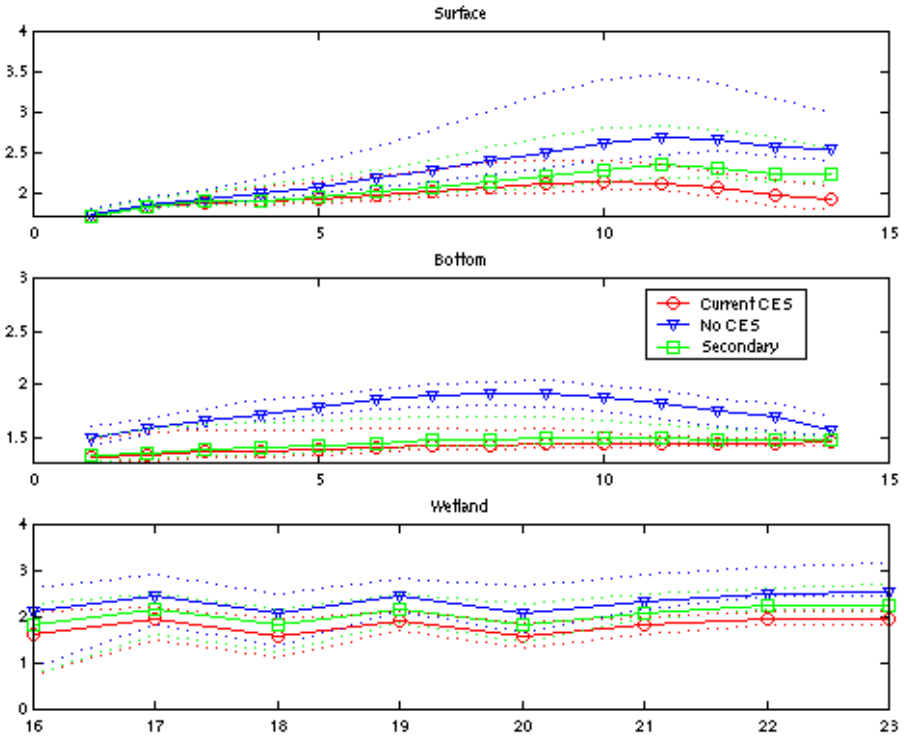

Fig. 6.3.11 b. 5%ile flow (Mar-Apr) scenarios, Chl a (mg Chl a m^{-3}) vs box #. Dashed lines indicate 5, 95%iles.

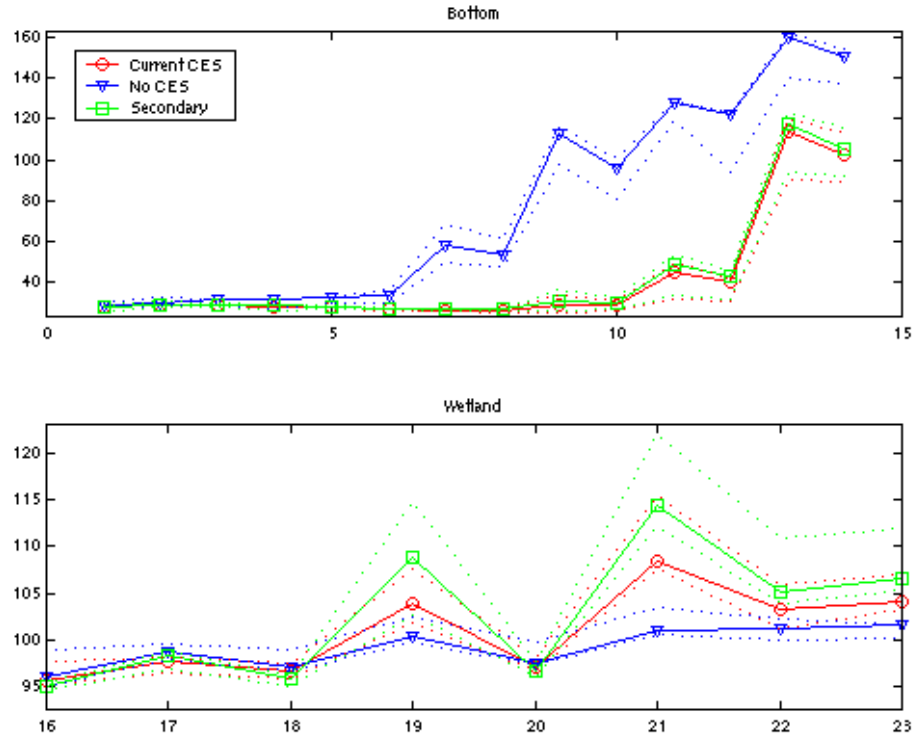

Fig. 6.3.12 a. Median flow (Nov-Dec) scenarios, MPB (mg Chl a m^{-2}) vs box #. Dashed lines indicate 5, 95%iles.

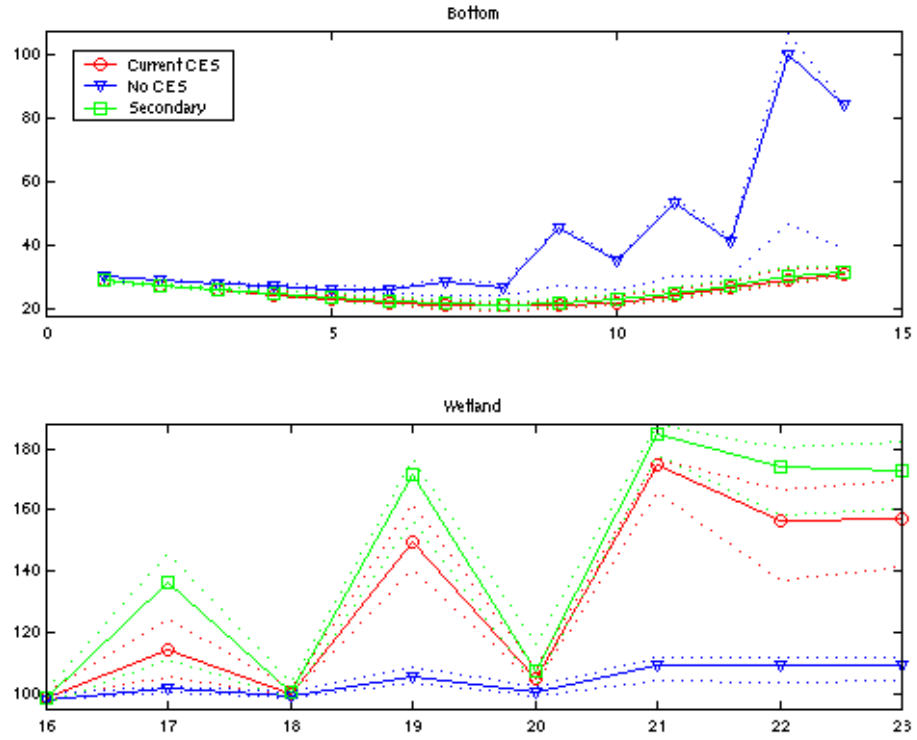

Fig. 6.3.12 b. 5%ile flow (Mar-Apr) scenarios, MPB (mg Chl a m^{-2}) vs box #. Dashed lines indicate 5, 95%iles.

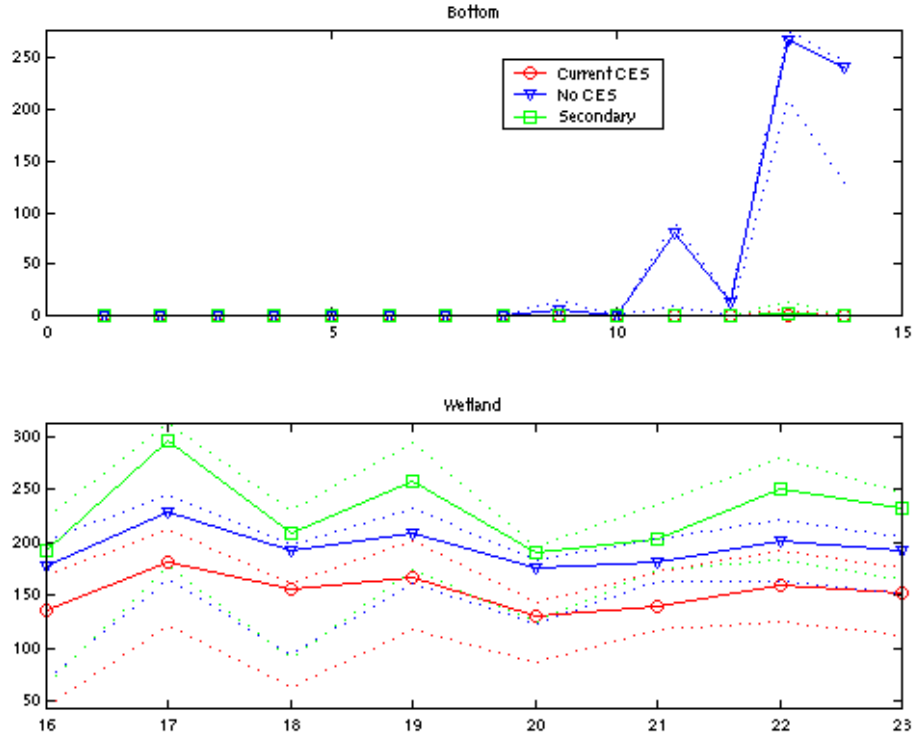

Fig. 6.3.13 a. Median flow (Nov-Dec) scenarios, Macroalgae (g wet wt m^{-2}) vs box #. Dashed lines indicate 5, 95%iles.

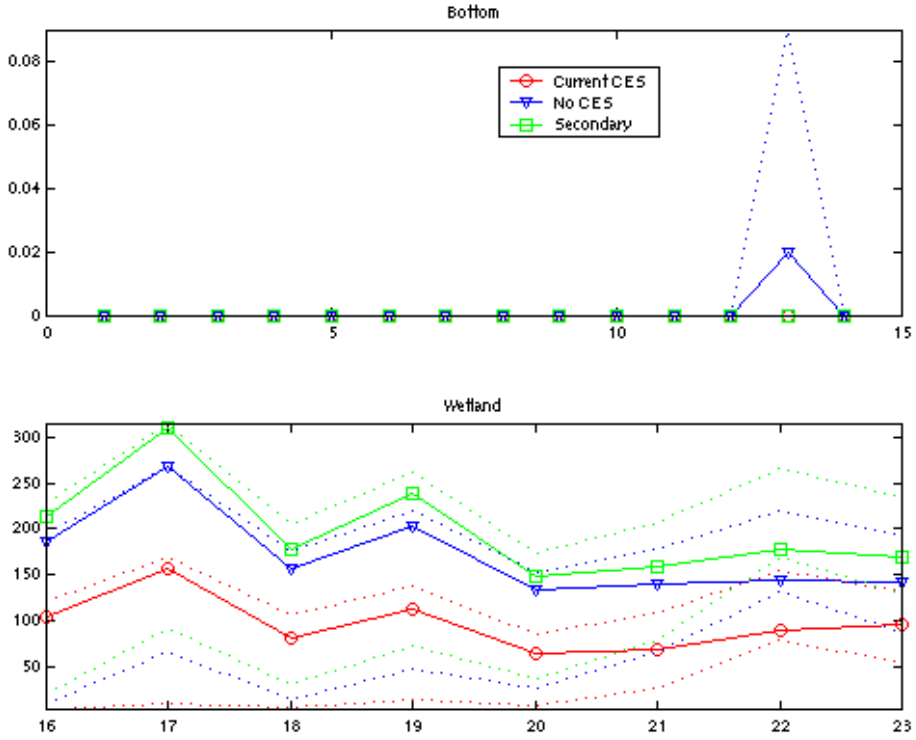

Fig. 6.3.13 b. 5%ile flow (Mar-Apr) scenarios, Macroalgae (g wet wt m^{-2}) vs box #. Dashed lines indicate 5, 95%iles.

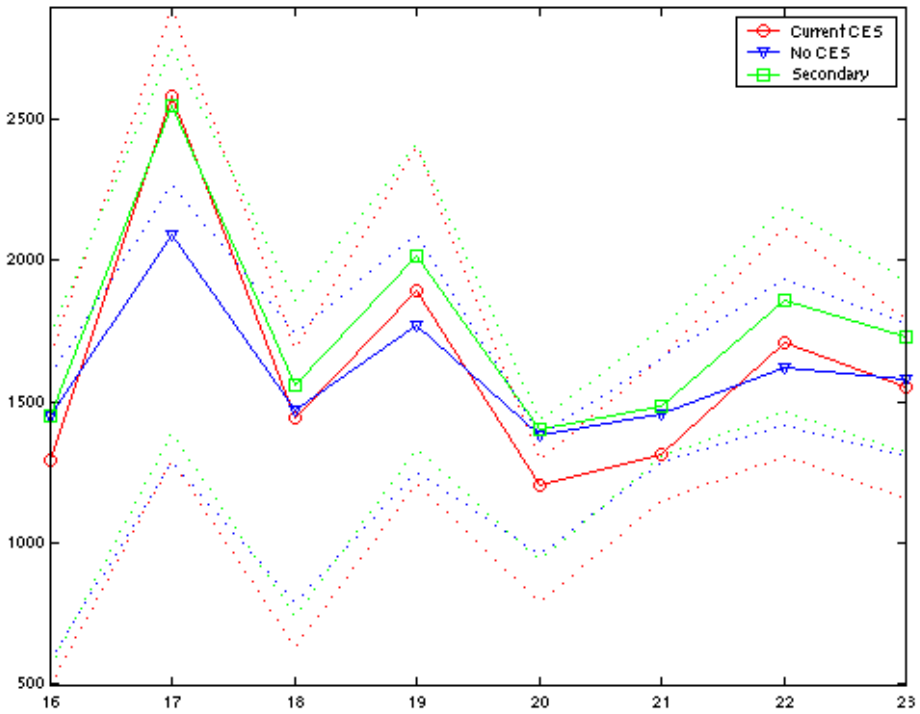

Fig. 6.3.14 a. Median flow (Nov-Dec) scenarios, Seagrass (g wet wt m^{-2}) vs box #. Dashed lines indicate 5, 95%iles.

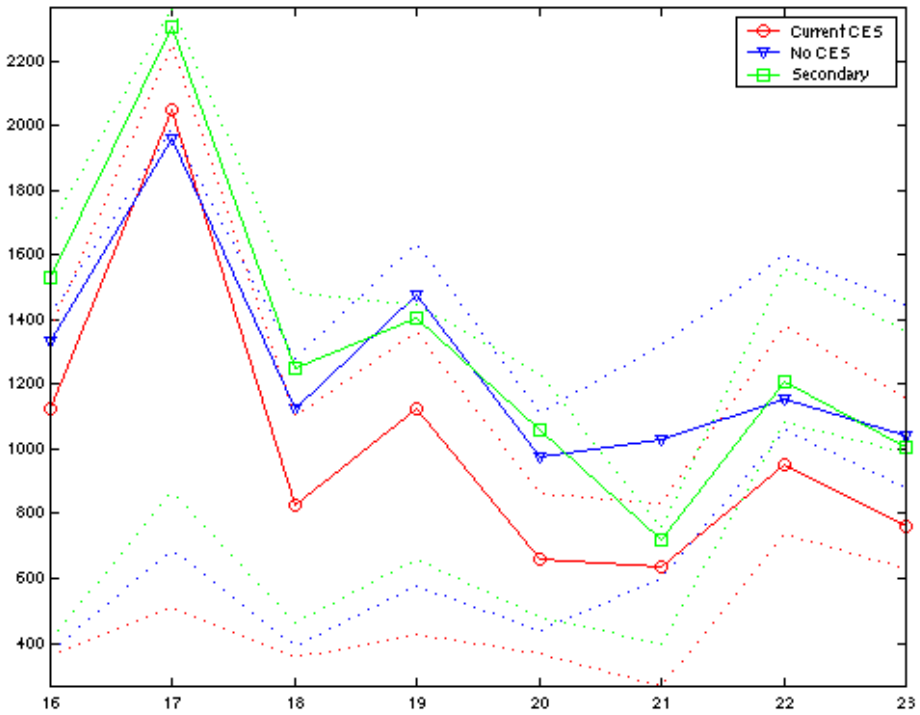

Fig. 6.3.14 b. 5%ile flow (Mar-Apr) scenarios, Seagrass (g wet wt m^{-2}) vs box #. Dashed lines indicate 5, 95%iles.